October 2021

Simulating the Effects of Floating Platforms, Tilted Rotors, and Breaking Waves for Offshore Wind Turbines

Hannah Johlas
University of Massachusetts Amherst

SIMULATING THE EFFECTS OF FLOATING PLATFORMS, TILTED ROTORS, AND BREAKING WAVES FOR OFFSHORE WIND TURBINES

A Dissertation Presented

by

HANNAH JOHLAS

Submitted to the Graduate School of the
University of Massachusetts Amherst in partial fulfillment
of the requirements for the degree of

DOCTOR OF PHILOSOPHY

September 2021

Mechanical Engineering

SIMULATING THE EFFECTS OF FLOATING PLATFORMS, TILTED ROTORS, AND BREAKING WAVES FOR OFFSHORE WIND TURBINES

A Dissertation Presented

by

HANNAH JOHLAS

Approved as to style and content by:

David P. Schmidt, Co-chair

Matthew A. Lackner, Co-chair

Sanjay R. Arwade, Member

Sundar Krishnamurty, Department Head
Mechanical and Industrial Engineering

ACKNOWLEDGMENTS

Thank you to both my advisors, David and Matt, for your guidance and wisdom during my Ph.D. journey. I deeply appreciate your supportive advising relationships and advocacy. Thank you also to my collaborator and third committee member, Professor Sanjay Arwade, for your insights and advice throughout my research career.

I also want to thank my collaborators Tony Martínez-Tossas and Matt Churchfield from the National Renewable Energy Laboratory, who I view as my unofficial advisors for large portions of my Ph.D. Thank you also to all my other collaborators, including Spencer Hallowell, Sam Roach, Andy Myers, and Pedro Lomonaco. Thank you especially to Convergent Science for your extensive software development support, particularly Shengbai Xie, Priyesh Srivastava, and Meizhong Dai.

I would like to acknowledge the support of a Graduate Research Fellowship from the National Science Foundation, a grant from the Bureau of Ocean Energy Management (contract E16PC00008), and a Kenneth A. Lloyd Fellowship from my department. This research used the Extreme Science and Engineering Discovery Environment (XSEDE) funded by National Science Foundation grant ACI-1548562, as well as National Renewable Energy Laboratory computational resources sponsored by the U.S. Department of Energy. A special thank you to Mahidhar Tatineni at the San Diego Supercomputing Center for his patient and prompt assistance.

Finally, I am so grateful for all the communities who provided support and friendship during my Ph.D.: my labmates, the IGERT and Wind Energy Fellow groups, the researchers at the National Wind Technology Center, my Graduate Women in STEM sisters, and the folk dance community. I am especially thankful for the continual support from my friends and family, who truly sustained me through this degree.

ABSTRACT

SIMULATING THE EFFECTS OF FLOATING PLATFORMS, TILTED ROTORS, AND BREAKING WAVES FOR OFFSHORE WIND TURBINES

SEPTEMBER 2021

HANNAH JOHLAS

B.A., MACALESTER COLLEGE

Ph.D., UNIVERSITY OF MASSACHUSETTS AMHERST

Directed by: Professor David P. Schmidt and Professor Matthew A. Lackner

Offshore wind energy is a rapidly expanding source of renewable energy worldwide, but many aspects of offshore wind turbine behavior are still poorly understood and are not accurately captured by low-cost engineering models used in the design process. To help improve these models, computational fluid dynamics (CFD) can provide valuable insight into the complex fluid flows that affect offshore wind turbine power generation and structural loads. This research uses CFD simulations to examine three main topics important to future offshore wind development: how breaking waves affect structural loads for fixed-bottom wind turbines; how platform motions affect power generation, wake characteristics, and downwind turbine behavior in floating wind turbines; and how rotor tilt angles affect wake characteristics when interacting with earth's surface. These high-fidelity simulations can help inform future improvements to engineering models like wake models, power prediction models, and breaking wave

models, which are integral to designing and financing both offshore turbines and offshore wind farm arrays.

First, breaking wave limits and slam force models are evaluated using CFD simulations of shoaling and breaking waves impacting monopile foundations, for environmental conditions representative of U.S. East Coast offshore wind sites. Second, floating turbine wakes are characterized by the velocity deficit, turbulent kinetic energy, and wake centerline location using large eddy simulations (LES) coupled via an actuator line model to the multidynamics turbine modeling tool OpenFAST. These wake metrics are compared for different floating platform types, atmospheric stability types, and environmental conditions. Third, the power generation of spar and semisubmersible floating turbines is simulated using OpenFAST with LES inflow, with different platform motions isolated. These power results inform a new analytical model for power generation in floating turbines. Fourth, downwind turbines with different platforms are simulated in OpenFAST using an upwind floating turbine's LES wake as inflow, to study how floating-turbine wakes affect a downwind turbine's power, blade loads, and towertop displacements. Finally, LES with an actuator disk model of a tilted wind turbine are performed for different tilt angles and blade-to-surface gaps, to characterize tilted rotor wakes and how they interact with the sea or ground surface.

TABLE OF CONTENTS

LIST OF TABLES

Table **Page**

LIST OF FIGURES

Figure **Page**

LIST OF SYMBOLS

Γ	Circulation	m^2/s
α	Angle between wind and wave directions (turbine simulations)	$^\circ$
α	Void fraction: 0.0 = water, 1.0 = air (wave simulations)	
β	Momentum damping coefficient	s^{-1}
η	Water surface elevation above still water level	m
η_i	Water surface elevation at time of slamming impact	m
κ	von Karman constant	
λ	Curling factor in slam force models	
μ	Dynamic viscosity of air	Ns/m^2
ν_T	Turbulent or eddy (kinematic) viscosity	m^2/s
ω	Frequency in sine approximation for $\dot{x}_{RC}$	rad/s
ϕ	Angle between rotor normal vector and wind vector	$^\circ$
ϕ_t	Rotor tilt angle	$^\circ$
ϕ_{RC}	Rotor pitch angle due to platform displacements	$^\circ$
ϕ_y	Nacelle yaw angle, not including θ_{RC}	$^\circ$
ψ	Thermal stratification correction in Monin-Obukhov similarity theory	
ρf_i	Rotor force in actuator models	N
ρ	Density of air	kg/m^3
ρ_w	Density of water	kg/m^3
τ_{ij}^R	Reynolds stress tensor (RANS)	m^2/s^2
τ_{ij}^{SGS}	Subgrid-scale stress tensor (LES)	m^2/s^2
θ	Angular polar coordinate for curled wake edges	$^\circ$
θ	Potential temperature	K
θ_{RC}	Rotor yaw angle due to platform displacements	$^\circ$
A	Rotor area	m^2
a	Horizontal fluid acceleration, in direction of wave propagation	m/s^2
C_d	Drag coefficient	
C_m	Inertia coefficient	
C_P	Power coefficient (turbine simulations)	
C_p	Wave celerity (wave simulations)	m/s
C_s	Slam coefficient	

C_T	Axial rotor thrust coefficient	
D	Monopile diameter (wave simulations)	m
D	Rotor diameter (rotor simulations)	m
d	Water depth	m
d_0	Nominal water depth	m
d_b	Water depth just before wave breaking	m
d_i	Water depth at time of slamming impact	m
F	Total force on monopile, in direction of wave propagation	N
F_D	Drag force on monopile, in direction of wave propagation	N
F_{inline}	See F	N
F_I	Inertia force on monopile, in direction of wave propagation	N
F_S	Slam force on monopile, in direction of wave propagation	N
g	Gravitational acceleration	m/s^2
H	Ocean wave height	m
H_0	Nominal or deep water wave height	m
H_{avg}	Average of H_{left} and H_{right}	m
H_b	Wave height just before wave breaks	m
H_i	Wave height at time of slamming impact	m
H_{left}	Wave height using left wave trough	m
H_{right}	Wave height using right wave trough	m
H_s	Significant wave height for irregular waves	m
$\hat{\imath}$	Unit vector in x-direction	
KC	Keulegan-Carpenter number	
k	Wavenumber	m^{-1}
L	Obukhov length of atmospheric boundary layer (turbine simulations)	m
L	Ocean wave wavelength (wave simulations)	m
L_0	Nominal or deep water wavelength	m
L_{avg}	Average of L_{left} and L_{right}	m
L_b	Wavelength just before wave breaks	m
L_i	Wavelength at time of slamming impact	m
L_{left}	Wavelength using left wave trough	m
L_{right}	Wavelength using right wave trough	m
P	Power produced by turbine rotor	W
P_{fb}	Power from fixed-bottom turbine	W
P_{wind}	Power available in wind	W
p	Pressure	Pa
R	Monopile radius (wave simulations)	m

R	Rotor radius (rotor simulations)	m
Re	Reynolds number	
r	Cylinder radius from Niedzwecki and Duggal experiments	m
r	Radial polar coordinate for curled wake edges	m
s	Seafloor slope	%
T	Wave period	s
T_p	Peak spectral wave period for irregular waves	s
TI	Turbulence intensity	
TI_{hh}	Turbulence intensity at hub height	
TKE	Turbulent kinetic energy	m^2/s^2
t	Time	s
t_s	Time since slamming impact	s
Δt_s	Slam force duration	s
U	Wind speed, often horizontal component only	m/s
ΔU	Difference in time-averaged wake velocity	m/s
U_∞	Free-stream wind speed	m/s
U_d	Velocity deficit in wake	m/s
U_{hh}	Wind speed at hub height	m/s
U_n	Wake velocity behind n^{th} turbine	m/s
U_{rel}	Relative wind velocity at rotor	m/s
u	Horizontal fluid velocity, in direction of wave propagation	m/s
u_i	Fluid velocity vector	m/s
u_*	Friction velocity	m/s
V_{RC}	Amplitude in sine approximation for $\dot{x}_{RC}$	m/s
w	Initial width of dammed water	m
x	Location coordinate, aligned with mean wind flow (turbine simulations)	m
x	Location coordinate, aligned with wave propagation (wave simulations)	m
x'	Downwind location, measured from turbine mean rotor displacement	m
x_b	Wave crest location just before wave breaks	m
x_i	Wave crest location at time of slamming impact (wave simulations)	m
x_i	Position vector (in Navier-Stokes equations)	m
x_{RC}	Downwind location of rotor center	m
$\dot{x}_{RC}$	Time derivative of x_{RC}	m/s
x_{WC}	Downwind location of wake center	m
y	Location coordinate, perpendicular to mean wind flow (turbine sims.)	m
y	Location coordinate, perpendicular to wave propagation (wave sims.)	m
y_{RC}	Cross-stream location of rotor center	m

y_{WC}	Cross-stream location of wake center	m
z	Location coordinate, in vertical direction (elevation)	m
z_0	Aerodynamic surface roughness height	m
z_{hh}	Hub-height elevation	m
z_{RC}	Vertical location of rotor center	m
z_r	Reference height in Monin-Obukhov similarity theory	m
z_{WC}	Vertical location of wake center	m

LIST OF ACRONYMS

ABL	Atmospheric boundary layer.
ADM	Actuator disk model.
ADM-R	Actuator disk model with rotation.
ALM	Actuator line model.
AMR	Adaptive mesh refinement.
BEM	Blade element momentum.
BiCGstab	Bi-conjugate gradient, stabilized.
C-A	Cointe-Armand slam force model.
C-W	Campbell-Weynberg slam force model.
CFD	Computational fluid dynamics.
CONVERGE	CFD software used in breaking wave simulations.
FA	Fore-aft.
FFT	Fast Fourier transform.
FLORIS	NREL's reduced-order wake modeling tool.
HRIC	High-resolution interface capturing.
IP	In-plane.
JONSWAP	Type of irregular wave spectrum.
LES	Large eddy simulation(s).
MUSCL	Monotonic upstream-centered scheme for conservation laws.
NOAA	National Oceanic and Atmospheric Administration (United States).
NREL	National Renewable Energy Laboratory (United States).
OoP	Out-of-plane.
OpenFAST	NREL's multi-dynamics engineering tool for modeling wind turbines.
OWT	Offshore wind turbine.
PISO	Pressure implicit with split operator.
PLIC	Piecewise linear interface calculation.
RANS	Reynolds-averaged Navier-Stokes.
RMS	Root-mean-square.
SDM	Standard dynamic model for eddy viscosity.
SGS	Subgrid scale.
SOR	Successive over-relaxation.
SOWFA	Simulator fOr Wind Farm Applications.
SS	Side-to-side.
VOF	Volume of fluid.
W-O	Wienke-Oumerachi slam force model.

CHAPTER 1

INTRODUCTION

Offshore wind energy as a renewable energy source has expanded rapidly in the last decade, increasing from 4.1 GW to 35.3 GW global installed capacity from 2011 to 2020 [1, 2]. This expansion is driven by better wind resources offshore and ambitious renewable energy goals in several countries, with additional benefits such as reduced visual impacts compared to onshore wind energy [3]. However, the complex offshore environment introduces many new engineering challenges to consider, when designing offshore wind turbines (OWTs) that will reliably produce power while minimizing cost. This research focuses on three such challenges: understanding loads due to breaking waves, understanding the behavior of floating turbines, and understanding wakes caused by tilted rotors.

1.1 Research motivation

Offshore wind energy design relies heavily on engineering models, from designing individual components of a turbine to optimizing the layout of a wind farm array. These engineering tools are computationally inexpensive which enables iterative design at reasonable timescales, but generally include many approximations and assumptions that must be informed and confirmed by higher-fidelity models, experimental data, and full-scale measurements. Unfortunately, full-scale measurements for most OWT phenomena are usually proprietary, if they exist at all. Experimental setups can be prohibitively expensive, especially when trying to capture the wide variety of environmental conditions an OWT will experience. High-fidelity models like

computational fluid dynamics (CFD) models can help gain a better understanding of fundamental physics of OWT phenomena, and identify topics for more targeted experimental or full-scale studies.

The three topics addressed in this dissertation (breaking wave loads, floating turbine effects, and tilted rotor wakes) are not yet well-understood for OWTs, and predictions from existing engineering models do not satisfactorily capture OWT behavior in these areas. However, all three topics are important for the design of offshore turbines or offshore wind farm arrays. For example, forces from breaking waves are expected to dictate foundation design for some fixed-bottom cases [4]. Also, as offshore wind energy moves into deeper waters beyond 50- to 60-m depth to access higher wind resources and new energy markets, floating platforms become more economical than fixed-bottom options [5, 6]. The additional rotor motion in floating turbines affects power generation and fatigue loads [7, 8]. Furthermore, in large wind farm arrays, wakes from upwind turbines reduce power production and increase fatigue loads in downwind turbines [9, 10]. Rotor tilt is considered a potential control strategy to increase power generation by reducing wake effects within offshore wind farm arrays [11–13]. The rotor angle of tilted turbines and the rotor motion of floating turbines change wake characteristics and therefore the power and loads of downwind turbines [11, 14, 15].

1.2 Research objectives

The goal of this research is to better describe breaking wave loads, floating turbine effects, and tilted rotor wakes using high-fidelity CFD simulations. Specifically, this work aims to:

1. Assess the performance of engineering models for breaking wave size and loads;
2. Identify how floating platform motions affect power generation and wake characteristics for a single turbine;

3. Identify how floating platform motions affect power generation and loads in downwind waked turbines; and

4. Characterize wakes behind tilted rotors and how these wakes interact with the ground or sea surface.

In addition to describing and quantifying the relevant phenomena, this work seeks to identify their underlying physical causes as well. These objectives promote improvement of engineering models, either by directly evaluating empirical models, or by identifying, describing, and explaining behavior that engineering models do not currently capture.

In achieving these research objectives, this dissertation makes the following novel contributions to the scholarly body of knowledge:

- Evaluates breaking wave limits and slam models for conditions at East Coast wind energy sites, finding that breaking limit accuracy depends on how wave characteristics are measured, and that slam force models make highly conservative predictions for breaking wave forces.

- Describes the far wake for floating wind turbines using high-fidelity models, finding that fixed-turbine wake models, especially curled wake models, are acceptable for modeling floating-turbine wakes as well.

- Studies power generation for floating turbines with stochastic environmental conditions, including determining that platform surge and pitch must be concurrently enabled to accurately predict power.

- Proposes a new, simple analytical model for power generation in floating wind turbines.

- Assesses how floating wakes affect downwind turbine power, including establishing that the downwind platform type is more important than the upwind wake

type, by using "mixed" cases with a fixed downwind turbine behind a floating upwind turbine.

- Examines the wake characteristics of tilted rotors for a larger 15 MW rotor as well as different surface-to-rotor gaps, documenting that downwind power gains in tilted wind farm arrays are caused by the wake location, rather than a faster deficit recovery within the wake.

- Identifies several measures to better quantify curled wakes, including counter-rotating vortex circulation and wake shape polar coordinates.

1.3 Outline of dissertation

The first chapter of this dissertation summarizes key background information relevant to this research, including several of the engineering models mentioned above, as well as CFD techniques related to the three research areas. Following this background information, Chapters 3–7 each address an individual subtopic, including a brief literature review, descriptions of the numerical model and simulation setups, a discussion of the study's results, and a summary of the conclusions for that topic.

Chapter 3 addresses breaking wave characteristics and breaking wave loads on fixed-bottom turbines. Next, Chapters 4 and 5 examine the wake characteristics and power generation of floating turbines, respectively. Chapter 6 continues this theme, addressing how wakes from floating turbines affect a downwind turbine's power generation and structural loads. Chapter 7 then studies the wake characteristics of wind turbines with tilted rotors, including how these tilted wakes interact with the surface. Most of the research presented in Chapters 3-7 is also published as conference or journal articles [16–20]. The dissertation concludes with an overview of the research findings, including describing its scholarly contributions in more detail. Possible directions for future work are also outlined.

CHAPTER 2

BACKGROUND

2.1 Offshore wind turbine foundation types

OWTs can be supported by a variety of foundation types, which are classified as either fixed-bottom or floating. Fixed-bottom designs attach directly to the seabed and are favored for water depths up to 50–60 m [5, 6]. Common fixed-bottom categories include gravity base, suction bucket, monopile, and jacket designs. This research uses a monopile structure for fixed-bottom foundations, illustrated in Figure 2.1.

Floating designs consist of a buoyant platform tethered to the seafloor by a system of mooring lines and anchors, which is more economical in deeper waters [5, 6]. Common floating categories include spar buoy, tension-leg platform, and semisubmersible

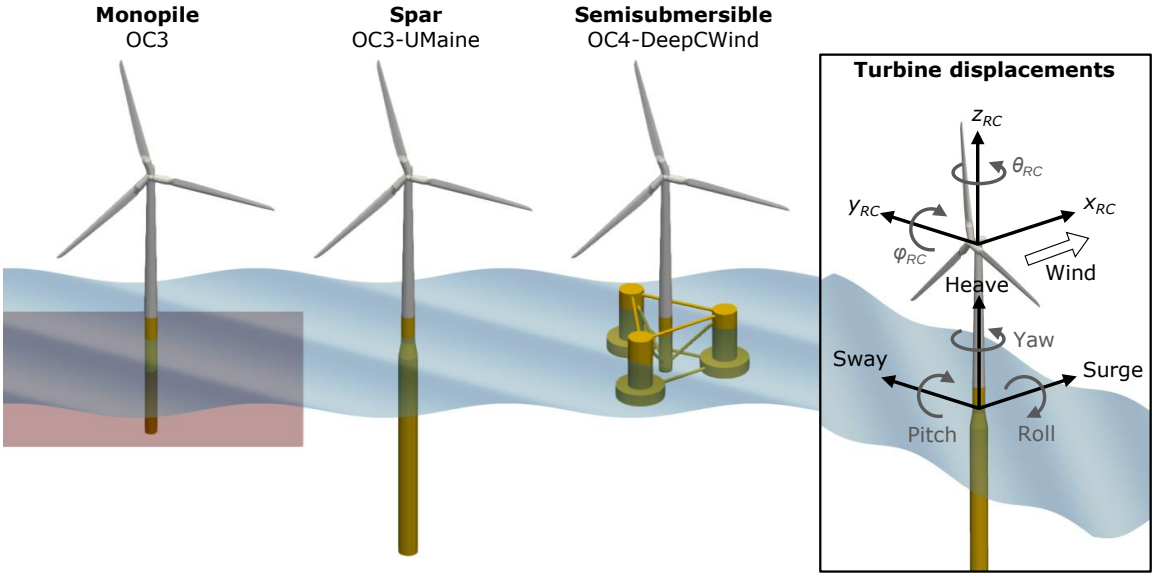

Figure 2.1. The NREL 5 MW reference turbine mounted on: the OC3 monopile, the OC3-UMaine/OC3-Hywind spar, and the OC4-DeepCWind semisubmersible. The subfigure defines platform displacements (surge, sway, heave, pitch, roll, and yaw) as well as rotor displacements (x_{RC}, y_{RC}, z_{RC}, ϕ_{RC}, and θ_{RC}) for floating turbines.

designs. This research uses spar and semisub platforms for floating foundations, illustrated in Figure 2.1. Unlike fixed-bottom foundations, floating platforms generally move with six degrees of freedom: surge, sway, heave, pitch, roll, and yaw. Figure 2.1 also shows these degrees of freedom, which are typically defined with respect to the wind direction (e.g. positive surge is downwind).

2.2 Engineering models for offshore wind energy

Numerous engineering models have been developed over the past several decades to analyze processes related to wind energy. Many of these models make simplifying assumptions that reduce their accuracy, but their low computational cost promotes their use in design and optimization. This section summarizes the most common engineering models used to analyze rotor aerodynamics, wind turbine wakes, and breaking waves, and briefly discusses the limitations of each.

2.2.1 Rotor aerodynamics and power

Rotor aerodynamics are crucial for many wind energy analyses, influencing power generation and loads on system components. Wind turbine aerodynamic performance is typically characterized by the power coefficient C_P, the ratio between the rotor power P and the power available in the wind P_{wind}. Engineering tools for predicting C_P and turbine aerodynamics typically utilize simplified theories for forces on the rotor and flow around the rotor. Nearly all rotor aerodynamics engineering tools make use of two theories: momentum theory, and the more advanced blade element momentum theory.

2.2.1.1 Momentum theory

The simplest approach to wind turbine aerodynamics is momentum theory, based on conservation of mass, axial and angular momentum, and energy in a control volume around an idealized rotor disk. The flow is assumed to be inviscid, incompressible, and

axisymmetric. In this framework, the rotor power depends on the power coefficient and the power available in the wind P_{wind}, given by the kinetic energy flux of the wind $\vec{U}_\infty$ through the rotor disk area $\vec{A}$:

$$\begin{aligned} P &= C_P P_{wind} \\ &= C_P \iint_A \frac{1}{2}|\vec{U}_\infty|^2 \left(\rho \vec{U}_\infty \cdot d\vec{A}\right) \\ &= C_P \frac{1}{2}\rho |\vec{U}_\infty|^2 \vec{U}_\infty \cdot \vec{A}, \text{ if } \vec{U}_\infty \text{ is uniform over } \vec{A}. \end{aligned} \tag{2.1}$$

For a uniform wind field of $\vec{U}_\infty = U_\infty \hat{\imath}$ and a stationary rotor plane perpendicular to the wind, this reduces to the well-known power formula

$$P = \frac{1}{2}\rho C_P A U_\infty^3. \tag{2.2}$$

Expanding on these ideas, Betz [21] developed a simple 1D momentum theory that predicts a maximum possible power coefficient of $C_P = 16/27 \approx 0.593$. This upper maximum, known as the Betz limit, is further reduced in physical turbines by wake rotation, aerodynamic drag, and blade tip losses. Glauert [22] extended 1D momentum theory by considering annular control volumes along the rotor radius and including wake rotation. In this case, the maximum possible C_P becomes a function of tip speed ratio, approaching the Betz limit for high tip speed ratios [3]. Further details of momentum theory are summarized by Sørenson [23] and Manwell *et al.* [3].

2.2.1.2 Blade element momentum theory

Building on momentum theory, Glauert [22] developed blade element momentum (BEM) theory as a practical engineering approach to analyzing wind turbine blades. BEM theory calculates the local aerodynamic forces on thin blade cross-sections (elements) using tabulated lift and drag coefficient data for 2D airfoils. Flow velocity and angle at these blade elements are predicted using momentum theory, typically

corrected by a tip-loss factor to account for the finite number of blades in physical rotors. Further modifications are required for unsteady or yawed inflow, operation in the turbulent wake state, and 3D airfoil effects [23]. Additional details of BEM theory are described by Sørenson [23] and Manwell *et al.* [3].

Despite BEM theory's simplifying assumptions and reliance on airfoil coefficient data, BEM-based models remain the most popular tools for wind turbine aerodynamic design due to their low computational cost [23, 24]. More advanced models, including some CFD approaches, combine higher-fidelity flow models with BEM theory's blade element approach (see Section 2.3.3).

2.2.2 Wake models

Because most modern wind turbines are arranged in large farms, turbine-to-turbine interaction through wake effects is also vital for predicting power production and loads for downstream turbines. Several engineering models have been proposed for predicting the large-scale characteristics of wakes behind a single turbine, as well as models for predicting wake behavior at the farm scale.

2.2.2.1 Single-turbine wake models

Numerous studies have examined the properties of wakes caused by single fixed-bottom wind turbines, as reviewed by Vermeer *et al.* [24] and Crespo *et al.* [25], with more recent reviews by Sørenson [23] and Stevens and Meneveau [10]. The classic theory for turbulent axisymmetric wake in laminar flow is not valid for wind turbine wakes, where mixing is heavily influenced by atmospheric boundary layer (ABL) turbulent structures and the wake is subject to the ABL's vertical velocity shear [10]. Instead, several engineering models have been proposed with varying levels of complexity specifically for single wind turbine wakes.

There are three popular analytic "kinematic" wake models. The Jensen (or Katic) model [26] assumes linear downstream expansion and an axisymmetric, uniform cross-

stream profile; it is recommended for $x > 3D$ [9]. The Larsen model [27] is based on self-similarity and Prandtl's turbulent boundary layer equations and assumes an axisymmetric, radially varying cross-stream profile; it is recommended for $x < 9.6D$ [9]. Finally, the Frandsen model [28] is based on self-similarity and a momentum control volume and assumes an axisymmetric, uniform cross-stream profile; it is recommended for $x < 10D$ [9].

Other common single-turbine wake models include the Bastankhah and Porté-Agel model [29], the Xie and Archer model [30], and the geometric model [31]. These wake models are discussed in more depth by Archer *et al.* [9] and Stevens and Meneveau [10].

More advanced wake models that solve simplified forms of the Reynolds-averaged Navier-Stokes (RANS) equations (see Section 2.3.1) are also gaining popularity as engineering tools [32]. For example, the Ainslie model [33] solves the axisymmetric parabolic Navier-Stokes equations and assumes an axisymmetric cross-section with a Gaussian inflow profile [23]; it is recommended for $x > 2D$ [32].

In general, more advanced wake models like the Ainslie model and its variations, which solve simplified versions of the RANS equations, can offer more accurate results than the early kinematic models of Jensen, Frandsen, and Larsen [32, 34]. However, these models are more computationally expensive and typically still include some limiting assumptions, such as axisymmetric wake profiles, that are not entirely realistic. Sanderse *et al.* [32] review these RANS-based wake models in more detail. Recent expansions to these RANS wake models include a curled wake model by Martínez-Tossas *et al.* [35, 36], which adds a vortex line to better model the curled wakes from angled rotors.

2.2.2.2 Farm-scale wake models

Often building on the single-turbine wake models described above, several methods have been proposed to model multiple wakes and their interactions at farm scales. A key feature of farm-scale wake effects is wake interaction, where multiple wakes overlap and combine. Superposition models mathematically superimpose the effects of individual wakes, typically through summing the velocity deficits or squared velocity deficits:

$$U - U_\infty = \sum \left(U_n - U_\infty\right), \text{ or} \tag{2.3}$$

$$(U - U_\infty)^2 = \sum \left(U_n - U_\infty\right)^2, \tag{2.4}$$

where U_n is the single-turbine wake velocity for the n^{th} turbine and U_∞ is the free-stream velocity [10, 34]. U_∞ can either be the true free-stream velocity outside the farm, or the inflow to turbine n. However, there is no consensus on which superposition model performs best, or even if such a velocity superposition approach is physically justified [10].

Wake interaction within very large arrays is also sometimes described as a wind turbine array boundary layer [37], where the wakes merge into a fully developed flow after 2-3 rows so that only vertical momentum and energy exchange is important [10, 34, 37]. Modeling this fully developed regime within the farm requires accurate modeling of the surrounding ABL, which may explain the inaccuracy of single-turbine wake superposition; most single-turbine wake models do not account for ABL properties [10].

In addition to wake interaction, wake meandering – the large-scale horizontal and vertical motion of a wake caused by ABL fluctuations – can also significantly affect downstream wind turbines. The dynamic wake meandering model [38] addresses this by superimposing the meandering of the wake center with a steady wake deficit from one of the single-turbine wake models described above [10].

Overall, engineering models for wind turbine wakes, particularly the interaction of wakes in large offshore farms, is an area of ongoing research and development (see, for example, the work of Walker *et al.* [39], Barthelmie *et al.* [40, 41] and the WAKEBENCH project [42]). In particular, there is no consensus on the validity of engineering wake models for floating OWT wakes or wakes due to tilted rotors. CFD simulations are valuable tools to better understand the physics of wake effects in offshore wind arrays, so that better engineering models can be developed and validated [34].

2.2.3 Breaking wave models

Engineering models are also used when designing OWT foundations, including when analyzing breaking wave loads on fixed-bottom OWTs. Two categories of engineering models are useful to understand how breaking waves interact with OWT foundations. First, empirical limits predict whether a wave will break given its characteristics. Second, slam models predict the impact force on structures due to a breaking wave. The most popular models within each category are described in the following sections.

2.2.3.1 Breaking wave limits

When designing support structures that can withstand breaking waves, inexpensive yet accurate models are needed for predicting whether a given wave will break. Many additional studies have examined numerical modeling of breaking wave kinematics, as summarized by Chella [43]. CFD models with two-phase flow have been recently favored for capturing the role of air during breaking [43], but are computationally expensive. Empirical breaking limit models offer an inexpensive alternative, and have been used to predict breaking for decades [44].

Numerous breaking limit models have been proposed, as summarized by Jensen [44] and Rattanapitikon and Shibayama [45]. The following four limits are commonly

used to predict the maximum wave steepness of a non-breaking wave:

$$\text{McCowan (1894):} \qquad \frac{H}{L} = 0.78\frac{d}{L} \tag{2.5}$$

$$\text{Miche (1944):} \qquad \frac{H}{L} = 0.142\tanh\left(2\pi\frac{d}{L}\right) \tag{2.6}$$

$$\text{Battjes (1978):} \qquad \frac{H}{L} = 0.142\tanh\left(\frac{0.8}{0.88}2\pi\frac{d}{L}\right) \tag{2.7}$$

$$\text{Goda (1974):} \qquad \frac{H}{L_0} = 0.17\left(1-\exp\left(-1.5\pi\frac{d}{L_0}\left(1+15s^{4/3}\right)\right)\right) \tag{2.8}$$

for wave height H (m), wavelength L (m), water depth d (m), seafloor slope s, and deep water wavelength L_0 (m) [44, 45]. These models predict that a wave will break if its steepness (H/L) exceeds these limits.

The McCowan, Miche, and Battjes limits were developed for water of constant depth d ($s = 0\%$). The McCowan formulation assumes solitary waves, and therefore includes no direct dependence on wavelength L. The Miche formulation assumes periodic waves, as does the Battjes limit which is adapted from the Miche limit. The Goda formulation was developed for waves on a sloped seafloor and assumes L_0 is the deep water (unshoaled) wavelength, while H and d are measured at breaking [44].

Rattanapitikon and Shibayama [45] evaluate twenty-four different breaking limits against a large collection of experimental datasets. They find that for the limits described in Equations 2.6 – 2.8, Miche is most accurate for $s > 7\%$, but Goda is most accurate for $s \leq 7\%$. All four models have higher errors with increasing seafloor slope [45]. However, there is little consensus on which breaking limit performs best for ocean conditions specific to OWT sites.

2.2.3.2 Slam force models

Empirical expressions are also used to predict loads on structures due to breaking waves. Wave loads on cylindrical structures like monopiles are typically calculated using the Morison equation with a drag term F_D and inertia term F_I. When a

breaking wave front slams into the cylinder, an additional slam term F_S is added to the Morison equation for the force in the direction of wave propagation [4, 46, 47]:

$$F(t) = F_D(t) + F_I(t) + F_S(t). \tag{2.9}$$

This slam term takes the form

$$F_S(t) = \lambda \eta_i \rho_w R C_p^2 C_s(t), \tag{2.10}$$

where λ is the curling factor, η_i is the surface elevation at impact, ρ_w is the density of water, R is the cylinder radius, C_p is the wave celerity, and $C_s(t)$ is the time-varying slam coefficient [4, 46]. The term $\lambda\eta_i$ measures how much of the cylinder's height is affected by the slamming force; values of 0.4 to 0.5 for λ for plunging breakers are typically cited from Goda *et al.*'s 1966 work [47, 48].

However, there are several disagreeing models for the slam coefficient $C_s(t)$. Four of the most popular are described in Table 2.1: Goda 1966, Campbell-Weynberg 1980 (C-W), Cointe-Armand 1987 (C-A), and Wienke-Oumerachi 2005 (W-O) [4, 46]. These four models predict different slam force durations Δt_s, different shapes for the $C_s(t)$ curve, and different values for the maximum slam force. All four models predict a peak C_s (and therefore a peak slam force) at the beginning of the slam force time history, when $t_s = 0$.

2.3 CFD models for offshore wind energy

Given the simplifying assumptions and limited accuracy of engineering models, CFD simulations offer a higher-fidelity method for gaining insight into OWT behaviors. However, simulating the coupled systems of the wind turbine and the surrounding atmospheric flow is a complex and computationally expensive problem.

Table 2.1. Common slam force models, their predicted slam durations, and their predicted slam coefficient time histories. Adapted from Tu *et al.* [46].

Model	Δt_s	$C_S(t)$: **peak value** is bolded
Goda	$\frac{R}{C_p}$	$\boldsymbol{\pi}\left(1-\frac{C_p t_s}{R}\right)$
C-W	$\frac{2R}{C_p}$	$\mathbf{5.15}\left(\frac{R}{R+9.5C_p t_s}+\frac{0.0535 C_p t_s}{R}\right)$
C-A	$\frac{3R}{C_p}$	$\mathbf{2\pi}\left(4.72-\ln\left(\frac{C_p t_s}{R}\right)\right)\sqrt{\frac{C_p t_s}{R}}$
W-O	$\frac{13R}{32C_p}$	$\begin{cases} \mathbf{2\pi}-2\sqrt{\frac{C_p t_s}{R}}\tanh^{-1}\left(\sqrt{1-\frac{C_p t_s}{4R}}\right), & \text{for } 0\le t_s\le \frac{R}{8C_p} \\ \pi\sqrt{\frac{R}{6C_p t_s'}}-\sqrt[4]{\frac{8C_p t_s'}{3R}}\tanh^{-1}\left(\sqrt{1-\frac{C_p t_s'}{R}\sqrt{\frac{6C_p t_s'}{R}}}\right), & \text{for } \frac{R}{8C_p}\le t_s\le \frac{13R}{32C_p}, \\ & \text{where } t_s'=t-\frac{R}{32C_p} \end{cases}$

A full discussion of all CFD methods used to simulate wind turbines is beyond the scope of this proposal; refer to the reviews of Sanderse *et al.* [32] and Mehta *et al.* [34] for additional discussion. This section provides a brief overview of several simplifying models that make simulating OWTs with CFD feasible, specifically turbulence models, atmosphere modeling, rotor models, wave modeling, and floating platform modeling.

Most CFD methods use the incompressible form of the Navier-Stokes equations to model wind turbine flow and wakes [24]. The incompressible Navier-Stokes equations in Einstein's index notation are

$$\frac{\partial u_i}{\partial x_i}=0, \text{and} \tag{2.11}$$

$$\begin{aligned}\frac{\partial(\rho_0 u_i)}{\partial t}+\frac{\partial(\rho_0 u_i u_j)}{\partial x_j}=&-\frac{\partial p}{\partial x_i}+\frac{\partial}{\partial x_j}\left(\mu\left(\frac{\partial u_i}{\partial x_j}+\frac{\partial u_j}{\partial x_i}\right)\right)\\ &+\rho_0 g_i\frac{\theta-\langle\theta\rangle}{\theta_0}+f_c\epsilon_{ij3}u_j+\rho_0 f_i,\end{aligned} \tag{2.12}$$

where t is time, u_i and x_i are the velocity and position vectors respectively, p is the pressure, and ρ_0 and θ_0 are the reference air density and temperature respectively. The buoyancy term $\rho_0 g_i(\theta - \langle\theta\rangle)/\theta_0$ is Boussinesq's approximation using the spatially averaged temperature $\langle\theta\rangle$, typically averaged over horizontal planes [34]. The Coriolis term $f_c \epsilon_{ij3} u_j$ is often neglected except for large wind farms [32, 49]. Finally, the term $\rho_0 f_i$ represents the force of the turbine rotor (and sometimes the tower and nacelle) on the flow; this rotor force is discussed in more detail in Section 2.3.3.

2.3.1 Turbulence models

Turbulence is a key feature of fluid flows in wind energy: turbulent inflow affects power production as well as turbine loads, and turbulence is the driving mechanism in wake behavior. There are three sources of turbulence in wind turbine wakes: atmospheric turbulence due to surface roughness and thermal effects; mechanical turbulence from the blades, tower, and nacelle; and wake turbulence due to the breakdown of tip vortices shed from the blades [32]. Unwaked turbines with "undisturbed" inflow still experience atmospheric turbulence as well.

Although Equations 2.11–2.12 fully describe turbulent flow for wind turbines, solving these equations directly is complicated by the nonlinear convection term and its associated range of time and length scales [34]. Resolving all these scales in direct numerical simulation is not feasible for most wind turbine studies: turbulent scales in the ABL range from 1 km to 1 mm, while scales in the blade boundary layer are even smaller [32]. Instead, turbulence models are used to model the unresolved scales for a less computationally expensive simulation.

2.3.1.1 RANS turbulence models

The Reynolds-averaged Navier-Stokes (RANS) turbulence model assumes turbulent variables (such as the velocity u_i) can be separated into an ensemble-averaged portion $\overline{u_i}$ plus a fluctuating portion u_i'. Substituting this decomposition into Equa-

tions 2.11–2.12 gives rise to the RANS equations (see [34]), which are solved for the averaged velocity $\overline{u_i}$, pressure $\overline{p}$, and temperature $\overline{\theta}$. In the RANS equations, the Reynolds stress tensor $\tau_{ij}^R = \overline{u_i' u_j'}$ must be modeled in terms of these known flow variables, creating the so-called closure problem [34].

The Boussinesq hypothesis (distinct from the Boussinesq approximation for density effects) is often used to model the Reynolds stress tensor based on a turbulent (or eddy) viscosity ν_T. Various models have been proposed to represent the turbulent viscosity ν_T, such as the popular $k-\epsilon$ and $k-\omega$ models and their variants. However, most of these models are not valid for the ABL's anisotropic turbulence or the wake shear layer's rapid changes in mean strain rate [32, 34]. The Reynolds stress model is an alternative approach to the Boussinesq hypothesis suitable for anisotropic flows, but is more expensive and typically relies on models that resemble the Boussinesq hypothesis for additional parameters [32].

In addition, numerical diffusion is typically employed to help stabilize RANS simulations, causing unrealistically rapid wake recovery unless model constants are carefully adjusted [50]. Despite these limitations, RANS models remain popular due to their reasonable accuracy and intermediate computational cost. Sanderse *et al.* [32], Mehta *et al.* [34], and Cabezón *et al.* [50] provide additional commentary on RANS models and their limitations for wind turbine flows.

2.3.1.2 LES turbulence models

Although many CFD studies of wind turbines still rely on RANS turbulence models, the large eddy simulation (LES) approach has emerged as a more sophisticated way to study the underlying physics of wind turbine flow phenomena, particularly in wakes. Fundamentally, LES resolves large energy-containing scales as well as intermediate inertial scales, modeling only the small Kolmogorov scales that are strongly influenced by molecular viscosity [34]. Mathematically, LES decomposes the turbu-

lence variables into a filtered (resolved) component $\widetilde{u_i}$ plus a subgrid (unresolved) component u_i'. Substituting this decomposition into Equations 2.11–2.12 introduces the filtered convection term $\widetilde{u_i u_j}$, which is usually modeled as

$$\widetilde{u_i u_j} = \widetilde{u_i}\widetilde{u_j} + \tau_{ij}^{SGS} \tag{2.13}$$

where τ_{ij}^{SGS} is the subgrid-scale (SGS) stress tensor [34], which physically represents how the unresolved scales affect the larger (resolved) scales [32].

Like the Reynolds stress tensor in RANS, there are many proposed models for the SGS stresses. The most popular SGS models for wind farm LES are eddy-viscosity models, which relate the SGS stresses to the resolved velocity field $\widetilde{u_i}$ through the local eddy viscosity ν_T using the Boussinesq hypothesis [32, 34]. Commonly used eddy-viscosity models for wind farm simulations include the Smagorinsky model and variants, as well as Germano's standard dynamic model (SDM) and variants like the scale-dependent dynamic model. Although SDM-type models can produce more accurate results than Smagorinsky-type models, their filter-based approach is only computationally feasible with pseudo-spectral CFD schemes [34]. Mehta *et al.* [34] provides an in-depth discussion of LES SGS models and their limitations for wind farm simulations.

Note that the most widely used LES closures do not model anisotropic turbulence (like the ABL) well, just like most RANS closures. Also, overly dissipative spatial and temporal discretizations can cause wake turbulence to decay too quickly in LES, just as in RANS. However, LES mesh refinement studies are often neglected in favor of energy spectrum comparisons, encouraging partial cancellation of numerical error with subgrid modeling error [32]. Despite its limitations and high computational cost, LES can capture the time evolution of turbulent eddies, allowing for realistic conditions like wind gusts and wake meandering [34].

2.3.1.3 Vortex methods for turbulence

Vortex methods offer a fundamentally different approach to modeling turbulent flow, assuming that the main flow features can be modeled as inviscid potential flow. This allows for linear superposition of uniform flow profiles and vortex lines, which are discretized into filaments and tracked as Lagrangian markers [15, 51, 52]. Free-wake vortex simulations often model the rotor blades as lifting lines that shed vorticity from their trailing edges, circumventing the actuator models described in Section 2.3.3 [52, 53]. Further details of vortex methods as applied to wind turbines are discussed by Sebastian and Lackner [15] and Farrugia *et al.* [51].

Vortex methods are sometimes considered mid-fidelity CFD models due to the assumption of inviscid potential flow, which does not accurately capture strong flow separation on the blade [7] and may not completely capture the complex rotor-wake interaction in floating OWTs [15]. Nonetheless, vortex methods are computationally much less expensive than LES or RANS simulations, and have been successfully used to analyze the aerodynamics and wakes of fixed-bottom and floating wind turbines (see, for example, [15, 51–54]).

2.3.2 Modeling the atmospheric boundary layer

Turbulence modeling is important for wind turbines in part because all wind turbine arrays are located in the turbulent atmospheric boundary layer (ABL), the lower section of the atmosphere affected by Earth's surface. Above the ABL, the atmospheric flow is characterized by a geostrophic velocity due to geostrophic balance, when the Coriolis accelerations are balanced by large-scale horizontal pressure gradients. Wind arrays are typically assumed to not affect the geostrophic balance, although large arrays can affect characteristics of the ABL [10].

ABL characteristics such as mean velocity profiles, turbulence intensity, and turbulence structures are determined by thermal stratification, measured by the vertical

gradient in (average) potential temperature $\partial\theta/\partial z$. Three broad categories are used to describe the ABL for different thermal stratifications: near-neutral ($\partial\theta/\partial z \approx 0$), stable ($\partial\theta/\partial z > 0$), and unstable ($\partial\theta/\partial z < 0$). Unstable conditions generally have higher turbulence than neutral conditions, with larger vertical structures due to convective mixing. Conversely, stable conditions have less turbulence with suppressed vertical structures [55].

In general, higher wind speeds correlate with more neutral conditions at offshore sites, although the distribution of stable, unstable, and neutral conditions varies widely by site [56–58]. Figure 2.2 shows the distribution of different atmospheric stability conditions at two offshore wind sites for different wind speeds. Due to the site-specific nature of this distribution, it is difficult to choose a representative offshore atmospheric stability when setting up simulations.

In terms of wind turbines, atmospheric stability affects wind speed at hub height, wind shear across the rotor, and turbulence properties, which in turn have a significant

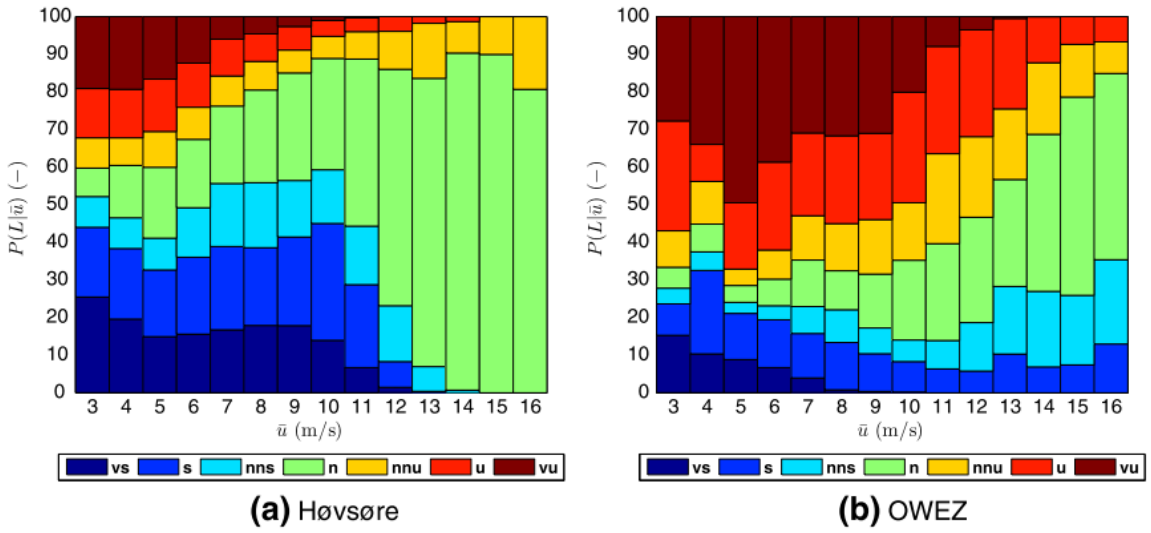

Figure 2.2. Distribution of atmospheric stability conditions at the Høvsøre (a) and Egmond aan Zee (b) offshore wind farms as a function of mean wind speed. Conditions are classified as very stable (vs), stable (s), near-neutral stable (nns), neutral (n), near-neutral unstable (nnu), unstable (u), or very unstable (vu). Reproduced from Sathe *et al.* [58].

impact on wind turbine power production [56], loads [55, 58], fatigue [57], and wake characteristics [55], particularly at farm scales.

2.3.2.1 Monin-Obukhov similarity theory

The most widely used ABL model is Monin-Obukhov similarity theory, derived from classic boundary layer theory, which gives the mean free-stream wind speed U_∞ as a function of elevation z:

$$U_\infty(z) = \frac{u_*}{\kappa}\left[\ln\left(\frac{z}{z_0}\right) - \psi\left(\frac{z}{L}\right)\right], \tag{2.14}$$

where $\kappa = 0.4$ is the von Karman constant, u_* is the friction velocity, z_0 is the aerodynamic surface roughness height, L is the Obukhov length, and $\psi(z/L)$ is an empirically based thermal stratification correction function [10, 57]. In practice, Equation 2.14 is often written in terms of a known wind speed at a reference height z_r:

$$U_\infty(z) = U_\infty(z_r)\frac{\ln\left(\frac{z}{z_0}\right) - \psi\left(\frac{z}{L}\right)}{\ln\left(\frac{z_r}{z_0}\right) - \psi\left(\frac{z_r}{L}\right)}, \tag{2.15}$$

so that the wind speed profile can be calculated using only the reference height wind speed (often the hub-height wind speed), the surface roughness z_0, and the Obukhov length L (for non-neutral stability) [57]. Sathe and Bierbooms [57] provide further details on Monin-Obukhov similarity theory.

Monin-Obukhov similarity theory requires the aerodynamic surface roughness z_0, which depends on the terrain. For offshore sites in particular, there is little consensus on an appropriate model for z_0; commonly used models include assuming a constant z_0, the simple Charnock relation, and more complicated wave-dependent models based on wave age [56, 59, 60]. However, work by Motta *et al.* [56] and Lange *et al.* [60] suggests that using different surface roughness models have negligible effect on OWT wind resource assessment, likely because roughness model errors only become

significant at high wind speeds, where the turbine power curve is flat [60]. On the other hand, studies by Churchfield *et al.* [55] and Lee *et al.* [61] indicate that different values for z_0 can produce significantly different turbine loads and waked turbine power production, due to differences in turbulence.

2.3.2.2 Modeling the offshore ABL in CFD

There are two main approaches when simulating the offshore ABL for CFD studies of OWTs, differentiated by their approach to the offshore environment's wind-wave coupling. The first approach is to decouple the wind and waves by using Monin-Obukhov similarity theory for the bottom boundary condition (see, for example, [12, 55, 61, 62]). This method avoids simulation of the waves, depending only on the sea surface roughness z_0, making it computationally more efficient. It also permits parameter studies to independently vary wave properties and wind properties.

The second approach is to simulate both the wind and waves using CFD, allowing for better wind-wave coupling. This approach often features fully two-phase simulations where the air and water phases are concurrently simulated using a single solver (see, for example, [7, 63]). Alternatively, sometimes the air and water phases are partially or fully coupled through surface elevation, velocity, and pressure despite using different solvers (see, for example, [64, 65]). In general, simulating both phases is more computationally expensive and these studies tend towards smaller domains focusing on single-turbine behavior. However, this approach is popular for simulating floating platforms, where accurate wind-wave coupling can affect turbine aerodynamics.

Regardless of the wind-wave coupling approach, CFD simulations must provide appropriately turbulent inflow boundary conditions and initial conditions for the air phase. RANS simulations can generally use Monin-Obukhov similarity theory to prescribe velocity profiles and turbulence characteristics. However, the time-varying nature of LES requires one of two techniques for generating unsteady inflow. First,

a synthetic turbulent field based on the desired turbulence characteristics can be prescribed, although this approach often neglects the effects of the ground.

Alternatively, a precursor simulation can be used to generate a turbulent velocity field that accurately includes the effect of the ground and is furthermore a solution to the Navier-Stokes equations. However, precursor simulations are more expensive and cannot easily be adjusted to acquire the desired turbulence characteristics [32]. Sanderse *et al.* [32] provides a more detailed review on initial conditions and boundary conditions in CFD simulations of the ABL.

2.3.3 Modeling turbine rotors

In most RANS and LES studies of wake behavior, rotors are modeled by actuator disks or lines rather than resolving the flow around each blade. This avoids simulating the blade boundary layer with CFD, which greatly reduces the meshing requirements around the rotor, both in complexity and number of mesh elements. Also, directly simulating the blade geometry can require solving the compressible Navier-Stokes equations, to capture compressability effects at the blade tips of large turbines. Therefore, actuator models significantly lower the computational cost compared to blade-resolved CFD [32]. Given current computing limitations, it remains unfeasible to simulate a many-turbine array using a blade-resolved approach; actuator models are the preferred alternative for CFD studies of wakes [34].

In an actuator model, the rotor is represented as a momentum sink and a turbulence source in the flow equations, to account for the force exerted on the flow by the rotor as well as the mechanical turbulence created by the blades [32]. The two main classes of actuator models (disk and line) differ in the form of the momentum sink term ρf_i in Equation 2.12, with a trade-off of accuracy and computational cost.

2.3.3.1 Actuator disk models

The actuator disk model (ADM) represents the rotor as a disk with swept area A. The uniformly loaded ADM assumes the rotor force ρf_i is constant across the rotor disk, expressed as a function of a "reference" velocity and the thrust coefficient C_T. However, this reference velocity is poorly defined for yawed turbines or turbines in disturbed flow, including wakes [32]. An alternative is non-uniformly loaded disks, which assume the rotor force varies with radial position, but is constant across an annular section of the disk. As in BEM theory, blade lift and drag coefficients are used to predict the force for each annulus. Unlike BEM theory, the local flow velocity is interpolated from the surrounding CFD flow field [32].

In addition to allowing axially non-uniform loading, the ADM with rotation (ADM-R) adds tangential forces to consider rotational effects. The work of Wu and Porté-Agel [66, 67] suggests that the uniformly loaded ADM significantly underpredicts the wake deficit and wake turbulence intensity compared to the ADM-R (with non-uniform loading). Consequently, the ADM-R approach better predicts the power output of a large wind farm, where wake effects are important [67]. Additional ADM variations and their performance are summarized by Sanderse *et al.* [32].

2.3.3.2 Actuator line models

Sørenson and Shen [68] extended the non-uniformly loaded ADM to the actuator line model (ALM), where the rotor force ρf_i is represented as line forces at each blade. The blade forces vary with radial position and are again based on airfoil lift and drag coefficients. Due to the ALM's reliance on 2D airfoil data, corrections are implemented to account for centrifugal, Coriolis, and tip effects [32].

Unlike ADM variations, the ALM can capture blade tip vortices and generally performs better in the near wake ($x < 3D$) than the ADM [68, 69]. As shown in Figure 2.3, the ALM and ADM-R are of comparable accuracy, though both perform better

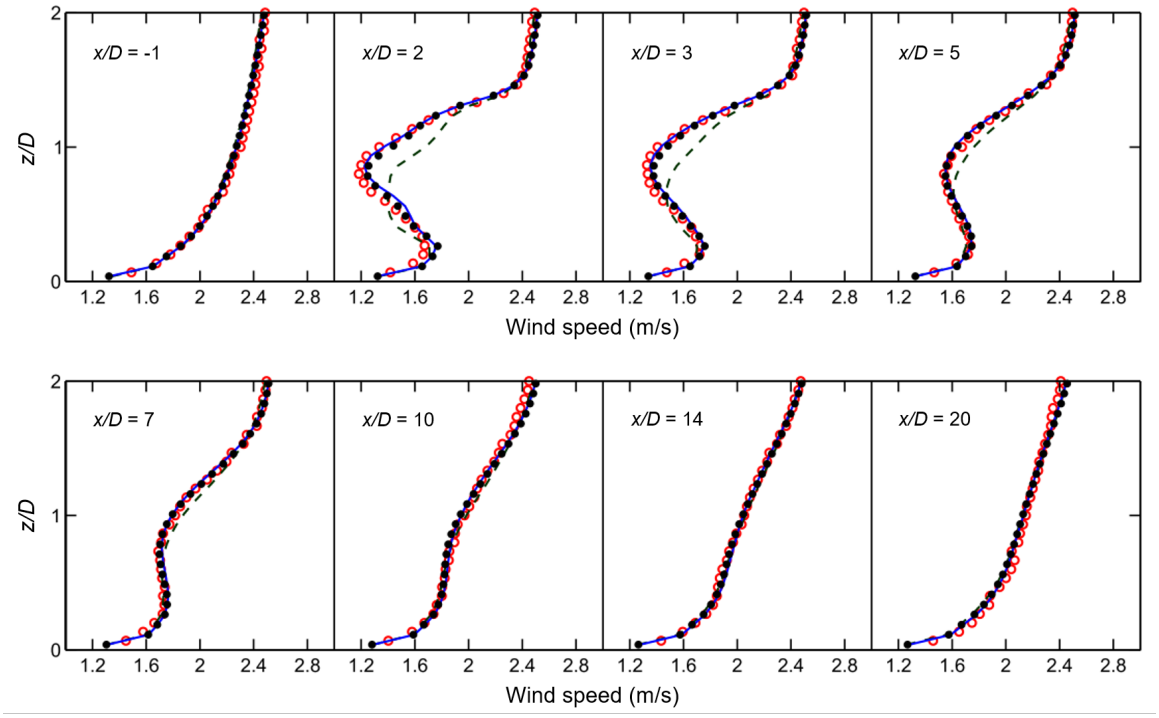

Figure 2.3. Comparison of average horizontal velocity as a function of height z at different downstream locations x for ADM (−−), ADM-R (−), ALM (●), and experiment (○). Adapted from Sanderse *et al.* [32] and Porté-Agel *et al.* [49].

than the ADM in the near wake. However, the ALM generally requires higher mesh resolution across the rotor diameter than either ADM approach [32, 70]. Furthermore, work by Stevens *et al.* [69] and Wu and Porté-Agel [66, 67] indicates that the ADM approach is preferable to ALM for large farm studies; ADM-R in particular can satisfactorily predict flow within the farm at a lower computational cost.

However, these comparisons between the ADM and ALM have thus far been conducted only for fixed-bottom turbines. Floating platform motion induces non-axisymmetric variations in relative velocity across the rotor disk. These variations can only be captured by the ALM and not by the ADM or ADM-R, which at best assume constant loading across each disk annulus. It is unclear if these velocity variations cause significant wake differences far enough downstream to favor ALM-based simulations for floating turbine farm studies.

In addition to modeling the rotor, an ALM-like body force approach can be used to model the effect of the tower and nacelle on the flow. This method is more easily implemented than an immersed boundary method and less computationally expensive than resolving the structures [71]. Including tower and nacelle effects typically improves wake predictions, particularly in the near wake [71, 72]. Santoni *et al.* examines tower and nacelle effects on the wake in more detail [72].

2.3.3.3 Models with flexible rotors

If the rotor force is simulated using a blade-resolved approach, ALM, or vortex method lifting lines, the blades can be modeled as either rigid bodies or with an elastic structural model, creating a so-called flexible rotor. Manolas *et al.* [53] and Lee *et al.* [14] conducted CFD simulations of floating OWTs with flexible rotors. Work by Rodriguez and Jaworski [52] indicates that flexible rotors cause earlier breakdown of the tip vortices in the near wake. However, flexible rotors require an additional elastic structural model, adding complexity.

2.3.4 Modeling wave hydrodynamics

There are two main approaches to modeling ocean hydrodynamics within CFD simulations for offshore wind energy. The first approach is to solve the Navier-Stokes equations for the water phase as well, requiring a two-phase CFD model. The Volume of Fluid (VOF) method is often used for these multi-phase simulations, which can be extremely computationally expensive. Two-phase VOF is used when simulating the areodynamics of floating OWTs (see [7, 63, 65, 73]) as well as breaking waves for fixed-bottom OWTs (see [43]).

The second approach is to rely on engineering models based on potential flow or strip theory, such as OpenFAST's HydroDyn module [74]. This decouples the simulated wind from the waves, but is much less expensive computationally. This

approach is frequently used for CFD simulations focused on rotor aerodynamics or turbine wakes, especially when simulating multiple turbines.

2.3.5 Modeling turbine foundations

CFD simulations of OWTs also sometimes require models for the turbine foundation, whether fixed or floating. The foundations of fixed-bottom OWTs are either assumed to be rigid and stationary, or an elastic structural model is employed to capture the structural deformation and dynamics. The rigid foundation approximation is popular for CFD studies focused on breaking wave kinematics or turbine wakes. However, simulating OWTs mounted on floating platforms introduces the complexity of accurately modeling floating platform motion. Approaches to including floating platform motion in CFD simulations fall into two categories: prescribed or coupled platform motion.

2.3.5.1 Prescribed platform motion

The easiest approach to simulating a floating platform in CFD is to prescribe platform motion (see, for example, [15, 51, 52, 54, 64, 65, 75, 76]). Often only 1-3 degrees of freedom – typically surge, heave, pitch, or yaw depending on the floating platform type – are retained to simplify analysis. The complexity of the prescribed motion ranges from simple sinusoidal motion in a single degree of freedom, to platform displacement time histories from simulations in engineering tools like OpenFAST [15].

Unfortunately, many current studies do not thoroughly justify their prescribed motion. In general, the amplitude and period of prescribed sinusoidal motion should be well-justified for the particular platform, wind speed, and wave characteristics through comparison to simulations, experiments, or field measurements that include the effects of aerodynamic loading on the platform motion. For example, studies by Sebastian and Lackner [15] and Farrugia *et al.* [51] prescribe bi-sinusoidal platform motion based on fits to platform displacement time histories simulated in OpenFAST.

Although easily implemented, prescribed platform motion only allows one-way coupling between the platform motion and the aerodynamic loading. In reality, the platform motion is affected by aerodynamic loading, which is in turn dependent on platform motion [7, 15]. This two-way coupling cannot be accurately replicated using prescribed platform motion, although it can be approximated if the prescribed motion is informed by methods that do include the two-way coupling.

2.3.5.2 Coupled platform motion

Instead of prescribing platform motion, several CFD studies have coupled the platform motion to the aerodynamic and hydrodynamic loading (see, for example, [7, 14, 53, 63, 65, 73]). This approach is widely used by studies that use VOF CFD for the water phase [7, 63, 65, 73], since the hydrodynamic forces are easily calculated without resorting to models like the Morison equation. However, less expensive possibilities include coupling aerodynamic CFD to engineering tools for hydrodynamic loads, as done by Manolas *et al.* [53] and Lee *et al.* [14].

Regardless of how the hydrodynamic forces are modeled, coupled platform motion also requires an accurate mooring line model. VOF simulations tend to use in-house mooring line models, which are often validated against engineering tools like OpenFAST [7, 63, 65, 73]. Alternatively, engineering tools can provide mooring models packaged with hydrodynamic load models, controls models, and elastic structural models [14, 53].

2.4 Background summary

In offshore wind energy models, high-fidelity and detailed results usually come at the cost of increased computational expense. Engineering models for rotor power, turbine wakes, and breaking wave loads are used in design and optimization due to their low costs. CFD simulations can offer a better understanding of these phenomena,

and in some cases more accurate predictions, which can inform future improvements to the engineering models.

Even within CFD simulations of OWTs, computational cost is often reduced by limiting detailed accuracy when modeling turbulence, the ABL, turbine rotors, wave hydrodynamics, and fixed or floating foundations. However, this trade-off is required depending on the focus of study: higher-fidelity simulations like RANS or LES of a blade-resolved turbine with two-phase VOF and coupled platform motion cannot simulate beyond the near wake due to computational cost, even with cost-saving numerical schemes (see for example [7, 63]). Though computational power continues to improve, CFD simulations still require properly applied models to remain valuable tools for understanding OWT aerodynamics, wakes, and wave loads.

CHAPTER 3

BREAKING WAVES FOR FIXED-BOTTOM TURBINES

Fixed-bottom OWTs in shallower water depths are likely to experience breaking waves due to bottom interaction, particularly during severe sea states [77, 78]. Breaking waves can cause significant loads on offshore structures [79] and are expected to drive the design of OWT support structures for some design cases [4].

Numerous experimental and numerical studies have examined breaking wave loads on fixed-bottom OWT support structures (see, for example, the work of the Wave Loads project [80], the Wave Impact on Fixed Foundations Joint Industry Project [79], Chella [43], Stansby *et al.* [81], and Marino *et al.* [82]). Other studies have addressed breaking wave loads on similar slender cylindrical structures (see, for example, the work of Wienke and Oumeraci [47], Luck and Benoit [83], and Irschik [84]). These studies mainly focus on modeling breaking wave kinematics and loads, rather than predicting if waves are breaking or non-breaking.

In the first component of this research, the performance of four breaking limits (McCowan, Miche, Battjes, and Goda from Equations 2.5–2.8) is evaluated and compared for regular wave trains shoaling over sloped bottoms in conditions representative of potential wind energy development sites off the U.S. Atlantic Coast. To provide a basis for comparison, nonlinear regular wave trains are simulated using CFD for numerous combinations of wave height, wavelength, water depth, and seafloor slope. Shoaling regular waves are selected as cleanly representative of breaking due to bottom interaction and seafloor slope, but this neglects breaking due to superposition of irregular wave train components [44].

In the second component of this research, the performance of four slam force models (Goda, Campbell-Weynberg, Cointe-Armand, and Wienke-Oumerachi from Table 2.1) is evaluated and compared using CFD simulations of regular wave trains shoaling over a sloped seafloor until the waves break on or shortly before monopile foundations. A total of four different combinations of wave height, wavelength, and monopile size are considered.

In this chapter, the CFD model used to simulate the wave trains is described first. The model is then verified against analytical solutions and validated against experimental data for four cases: a dam break case, nonlinear wave propagation, nonlinear wave shoaling experiments, and nonlinear wave force experiments. The CFD simulations for evaluating the breaking wave limits are then described, and their results compared to the four limits. Finally, the CFD simulations for evaluating the slam force models are described, and their results compared to the four slam models.

3.1 Numerical models

The regular wave trains are simulated using a two-phase finite-volume CFD model that solves the 3D incompressible Navier-Stokes equations. The air-water interface is modeled using a VOF approach with a void fraction solution method with Piecewise Linear Interface Calculation (PLIC) interface reconstruction. The model is implemented in CONVERGE version 2.4.15, a commercial CFD software with adaptive meshing capabilities [85].

The CFD model uses the Pressure Implicit with Split Operator (PISO) solver algorithm with Rhie-Chow interpolation, using SOR and BiCGstab matrix solvers for the momentum and pressure terms respectively. For the momentum advection term, the CFD model uses a blended Monotonic Upstream-Centered Scheme for Conservation Laws (MUSCL) interpolation scheme, with a van Leer flux limiter [85].

The CFD model does not include a turbulence model or wall functions, although the mesh resolution is not fine enough to resolve the boundary layer on the domain bottom. However, various turbulence models were found to add too much dissipation in the validation cases and did not agree well with experimental results.

3.1.1 Wave generation and absorption

In the simulations used to evaluate the breaking limits and slam force models, the regular wave trains are generated by prescribing the appropriate surface elevation and water velocity at one domain boundary, as an adaptation of a traditional inlet boundary condition. The surface elevation and water velocity values are calculated using 25th order stream function theory [86]. The prescribed wave kinematics slowly increase from zero to the full values over one wave period at the beginning of the simulation.

The domain boundary opposite this wave generation boundary is an adaption of a traditional outlet boundary condition. At this boundary, a hydrostatic pressure distribution is prescribed with a Neumann condition on velocity. To prevent nonphysical reflections off this boundary, a momentum damping zone suppresses the waves before they reach the boundary. The damping region is implemented by adding a sink term $\beta\rho_w u_i$ to the momentum equation. The positive sink coefficient β increases quadratically from the beginning of the damping zone to create a smooth transition between the damped and non-damped regions.

3.2 Model verification and validation

Before using the CONVERGE CFD model for evaluating the breaking wave limits and slam force models, it must first be validated and verified against experimental data and accepted analytical models for cases relevant to breaking wave forces on

fixed-bottom OWTs. Each of the following four cases provides confirmation for a different aspect of modeling breaking wave forces on offshore wind support structures:

1. **Dam break**: capture structure of breaking water front
2. **Nonlinear wave propagation**: generate, propagate, and absorb waves
3. **Nonlinear wave shoaling**: capture shoaling and produce breaking waves
4. **Nonlinear wave forces**: predict forces on cylinders from regular waves

The process of validating and verifying these four cases also develops a set of "best practice" guidelines for setting parameters in the CONVERGE CFD model for wave applications (like solver parameters, interface reconstruction models, mesh resolution, turbulence models, etc.).

3.2.1 Dam break

The first case is the single-sided 2D dam break described by Whitman [87], where the flow is assumed to be incompressible, inviscid, and without surface tension. A column of water with height d_0=50 cm and width w=3 m is initially confined on the left side of a 10 m by 60 cm domain. The column is released at the beginning of the simulation (t=0 s) and allowed to collapse towards the right under the influence of gravity g.

The CFD domain is bounded by slip walls on the left and right sides as well as the bottom, with the top open to atmospheric pressure. The CFD mesh has a base cell size of $w/150$ by $d_0/100$ and adaptive mesh refinement at the interface down to a cell size of $w/300$ by $d_0/200$. The timestep size is adjusted throughout the simulation to maintain a Courant number of 0.4, with a first-order upwinding advection scheme.

The water depth d, as a function of distance x from the left edge of the domain and time t, is compared to the analytical solution based on potential flow theory, as discussed by Whitman [87]:

$$\sqrt{gd} = \frac{1}{3}\left(2\sqrt{gd_0} - \frac{x-w}{t}\right), \text{ for } -\sqrt{gd_0} \leq \frac{x-w}{t} \leq 2\sqrt{gd_0}. \tag{3.1}$$

Figure 3.1 shows the depth d across the domain length at two different times, comparing the CFD results to the analytical solution. As Figure 3.1 shows, the CFD interface shape is in excellent agreement with the analytical solution, particularly at later times when the potential flow solution is more accurate [87]. The verification of this dam break case against analytical results indicates that the CFD model can accurately simulate a collapsing water front, like those found in breaking waves.

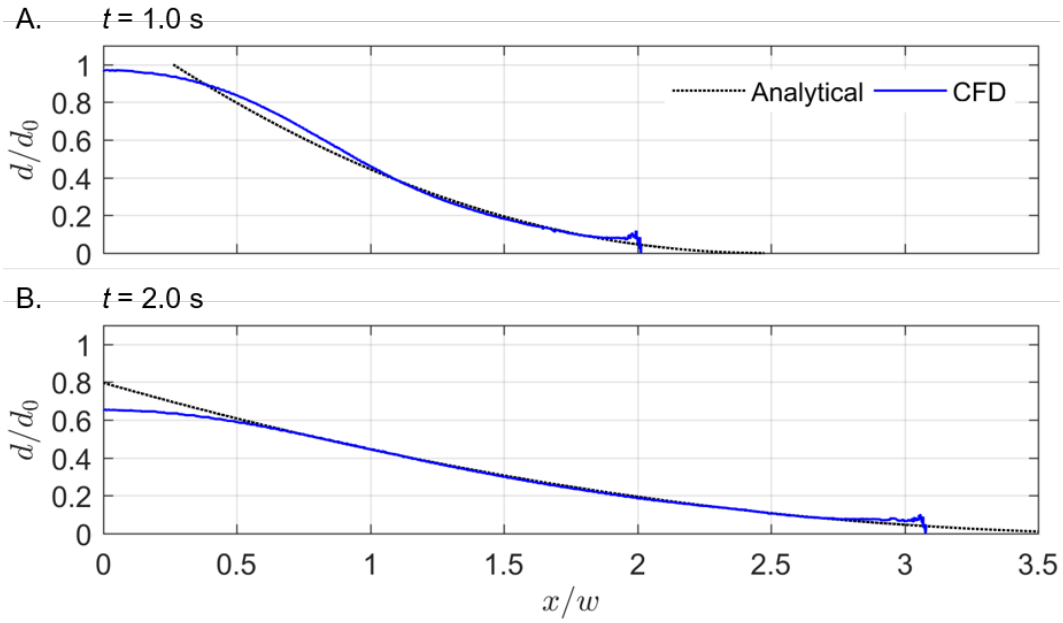

Figure 3.1. CFD results (solid blue) and analytical results based on potential flow theory (dotted black) for a collapsing water column, initially w=3 m wide and d_0=50 cm tall. Water depth d is plotted versus distance from the left tank wall x at times of 1 s (A) and 2 s (B).

3.2.2 Nonlinear wave propagation

The second verification case is the generation and propagation of 2D nonlinear regular waves. Nonlinear waves of height H=10 cm, period T=1.0 s, and wavelength L=1.62 m are generated in a constant water depth of d=1.0 m. The waves kinematics are defined by 5th order Stokes wave theory, described by Fenton [88, 89], rather than the more general 25th order stream function theory. Figure 3.2 shows the case setup.

The CFD domain is 5 m long and 1.5 m tall, with slip walls on the top and bottom. The waves are generated using the wavemaker boundary approach described in Section 3.1.1. A momentum damping region in the rightmost 1 m of the domain absorbs the waves before they reach the outlet boundary condition, as described in Section 3.1.1.

The CFD mesh has a base cell size of $L/20$ by $d/12.5$, with adaptive mesh refinement at the interface down to a cell size of $L/160$ by $H/10$. The timestep was adjusted to maintain a Courant number of 0.75. As with the dam break case, first-order upwinding is used for the advection scheme.

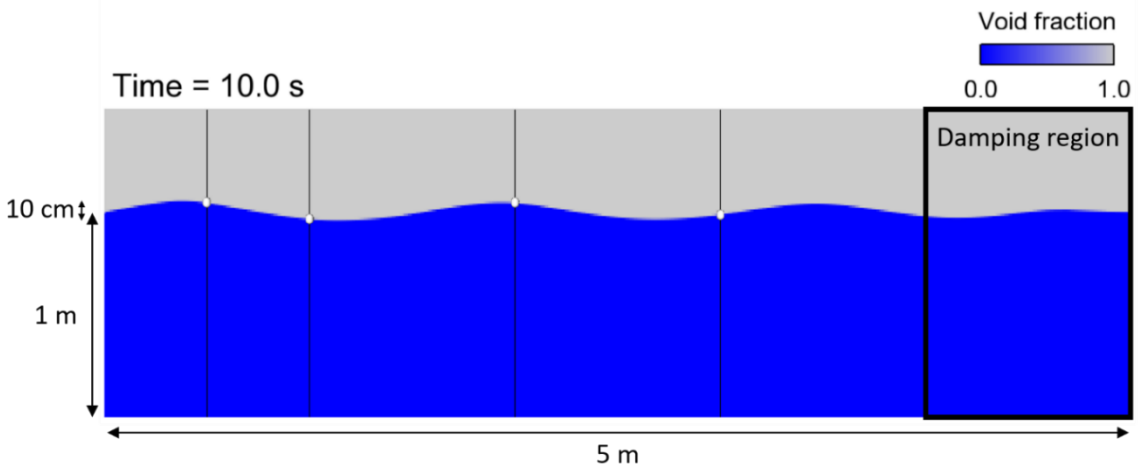

Figure 3.2. CFD simulation of 5th order Stokes waves (H=10 cm, d=1 m, T=1 s) shown at time 10 s. The 2D domain is 5 m long, with a 1 m momentum damping region at the right boundary. The surface elevation is measured at 0.5, 1, 2, and 3 m from the wave generation boundary on the left (indicated by white dots).

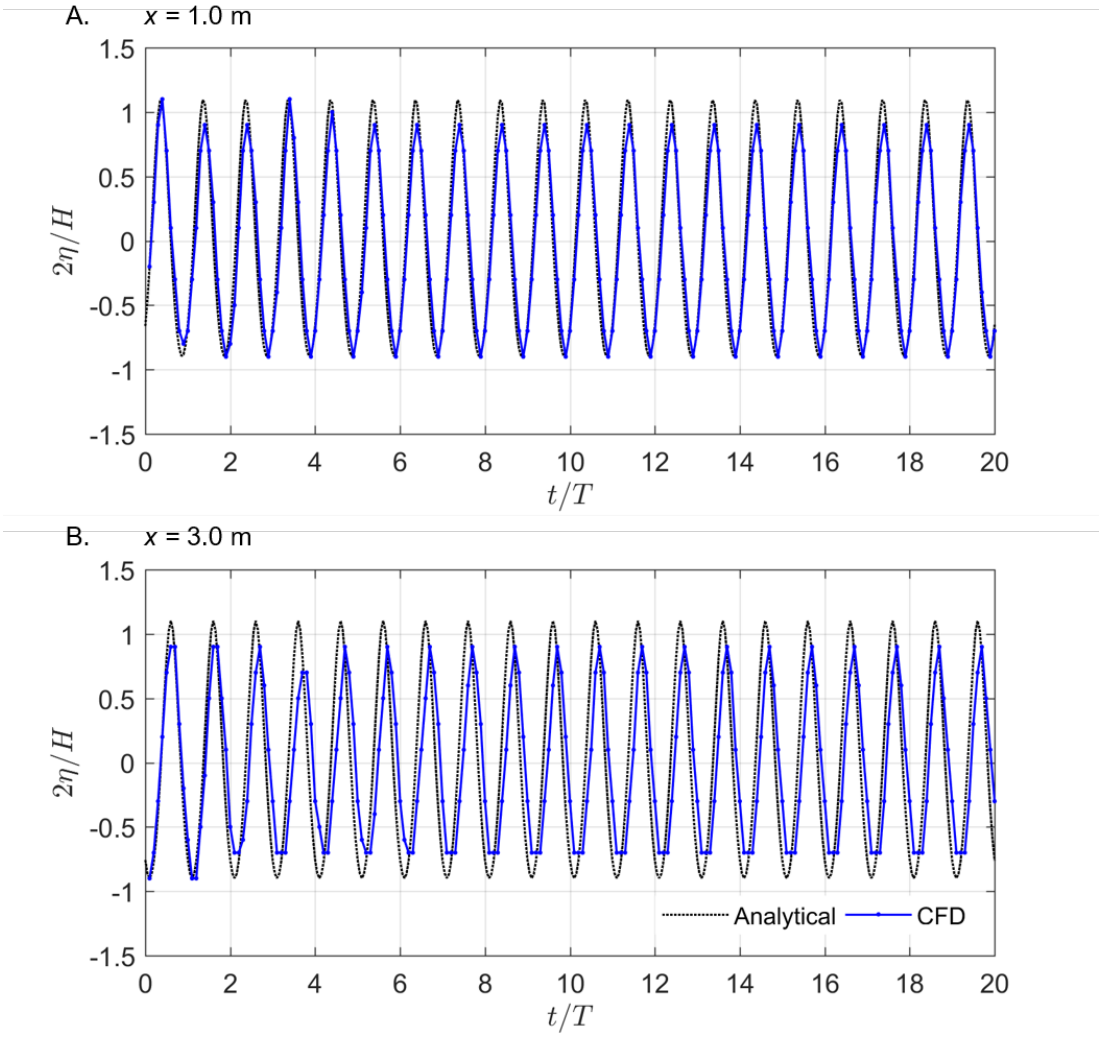

Figure 3.3. Time history of the surface elevation η for 5th order Stokes waves, at locations 1 m (A) and 3 m (B) from the wave generation boundary. CFD results are plotted in solid blue while analytical results are in dotted black.

Figure 3.3 shows the surface elevation η as a function of time t at x=1 m=0.62L from the left wave generation boundary (Figure 3.3A) and at x=3 m=1.85L from the left wave generation boundary (Figure 3.3B). As shown in Figure 3.3, the CFD surface elevations match the analytical 5th order Stokes solution within the size of one cell (0.1H), though the agreement deteriorates farther from the left wave generation boundary, likely due to the numerical viscosity introduced by the first-order advection scheme. Similar trends are observed in the surface elevations for locations 0.5 m and 2 m from the inlet.

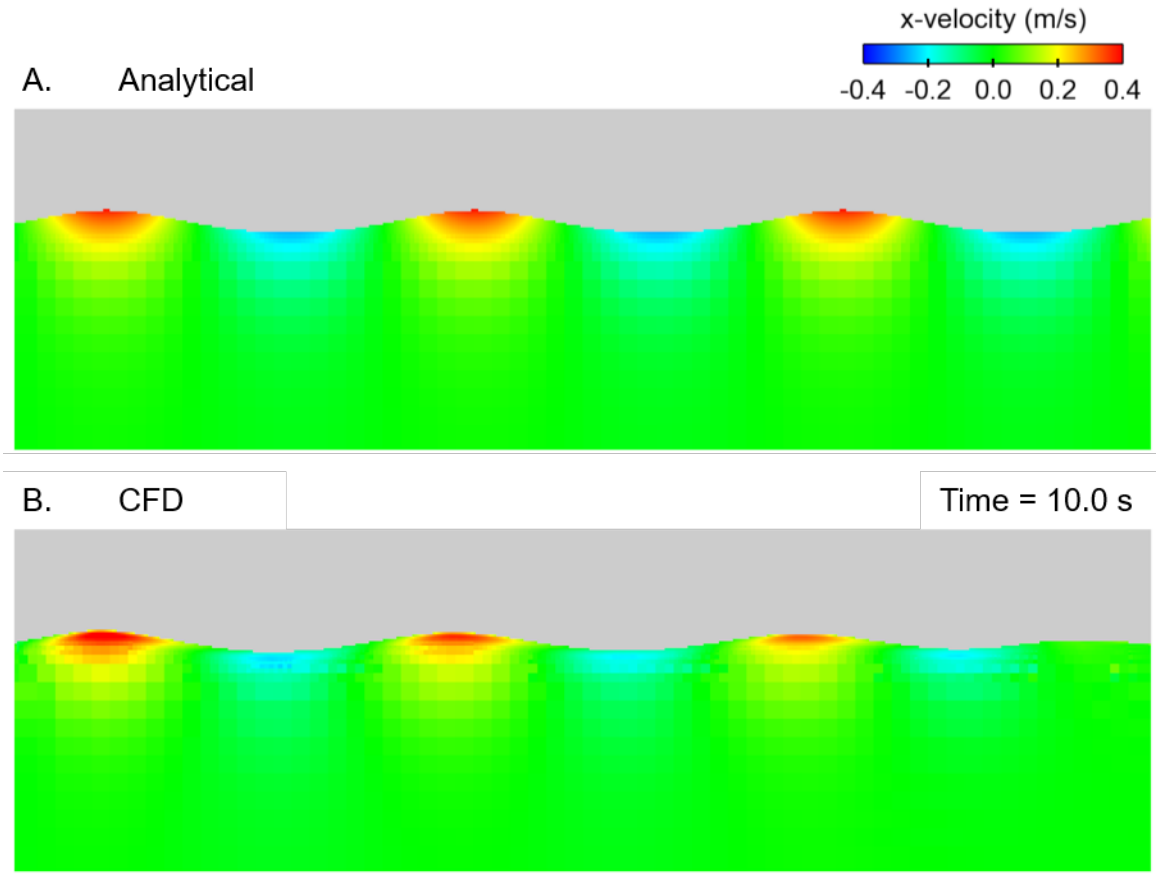

Figure 3.4. Horizontal fluid velocity at time t=10 s according to the analytical 5th order Stokes solution (A) and the CFD results (B).

Figure 3.4 shows the satisfactory agreement between analytical (Figure 3.4A) and CFD (Figure 3.4B) results for horizontal particle velocity at t=10 s. As with the surface elevation, the CFD velocity profile becomes less accurate farther from the left wave generation boundary. The vertical particle velocity and pressure distribution also show reasonable agreement between the CFD and analytical results, again with poorer agreement far from the wave generation boundary.

Overall, the CFD results agree reasonably well with the analytical solution derived from 5th order Stokes wave theory. This case confirms the CFD model's ability to generate and propagate nonlinear waves accurately, including the absorption of nonphysical waves by a momentum damping region. However, the decreasing accuracy far from the inlet could likely be improved by using a higher-order advection

scheme. A similar wave generation and propagation case was also performed using 25th order stream function theory, as described by Fenton [86], to generate highly nonlinear waves. This case verified the approach of prescribing wave kinematics from stream function theory.

3.2.3 Nonlinear wave shoaling

The third case considers regular and solitary waves shoaling over a sloped floor, including a breaking solitary wave. The simulated surface elevations are validated against experimental data from two tests conducted in the Large Wave Flume at the O.H. Hinsdale Wave Research Facility at Oregon State University.

3.2.3.1 Validation domain

The experimental flume is 87 m long and 3.7 m wide, with a piston wavemaker at one end for generating unidirectional waves. The flume bathymetry features an 8.3% slope starting at x=14.07 m from the wavemaker, followed by a horizontal plateau at $43.33 < x < 79.91$ m which is raised 1.75 m above the flume floor. An 8.3% slope beyond the plateau acts as an artificial beach for wave absorption.

The CFD domain replicates the experimental bathymetry along the entire length and is 3.0 m tall from top to bottom at the wavemaker. Although the CFD model solves the 3D Navier-Stokes equations, a 2D domain is created by a domain width of one cell and symmetry boundary conditions on the domain sides. The 2D approximation is appropriate because the experimental waves are unidirectional and have a uniform cross-flume profile.

The CFD wavemaker wall generates waves by moving horizontally according to the experimental wavemaker displacement time history, which had a maximum error of 0.39% at the most recent instrument calibration. The CFD wavemaker, floor, and beach wall are treated as no-slip walls, while the top of the domain is set to

atmospheric pressure. Figure 3.5 shows the simulated validation domain, with the wavemaker on the left.

These validation simulations use High-Resolution Interface Capturing (HRIC) interface reconstruction, rather than the PLIC reconstruction used in the other wave simulations. Although PLIC interfaces are less diffuse than HRIC interfaces [90], PLIC is unsuitable for the validation cases because it does not conserve mass in cases with moving walls [85]. Improving upon the previous verification cases, the momentum interpolation uses a blended MUSCL interpolation scheme, with a van Leer flux limiter [85].

Two validation cases are simulated: first, nonlinear regular waves of height H=16 cm, period T=2.5 s, and wavelength L=8.8 m are generated in a water depth of d=2.15 m at the wavemaker. Second, an error function solitary wave of height H=51 cm and time width T=10 s is generated in a water depth of d=2.00 m, shown in Figure 3.5 at the time of breaking.

For the regular waves case, the CFD mesh consists of Cartesian base cells sized $L/110$ by $d/215$, producing an aspect ratio of 1:8 and ensuring that the still water depth on the plateau is spanned by 40 cells. The time-evolving air-water interface is refined to cells of size $L/440$ by $H/64$ using adaptive mesh refinement (AMR). CONVERGE's adaptive meshing also allows mesh deformation at the wavemaker's

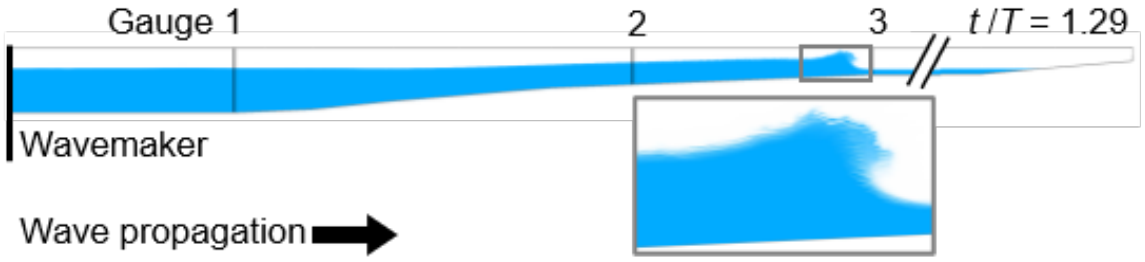

Figure 3.5. Partial CFD domain for the solitary wave validation case at time of breaking, including the wavemaker (left) and three wave gauges.

moving wall boundary [85]. The same mesh settings are used for the solitary wave case, so that the solitary wave interface is refined to $H/204$.

For both validation cases, the timestep is adaptively adjusted to maintain a Courant number of 0.2. This produces timesteps on the order of 0.9 ms=$T/2800$ for the regular waves case and 0.4 ms=$T/25{,}000$ for the solitary wave. For the solitary wave, the simulated time is 18.9 s, from the start of the wavemaker motion to when the wave has propagated onto the plateau. For the regular waves, the simulated time is 48.4 s, from the start of the wavemaker motion to when three full-sized waves have propagated onto the plateau.

3.2.3.2 Surface elevation analysis

The CFD and experimental surface elevations $\eta(t)$ are compared at the three wave gauges shown in Figure 3.5, located at x=14.172 m, 32.326 m, and 43.431 m from the wavemaker respectively. The experimental wave gauges are calibrated pairs of surface-piercing wire resistance gauges. During the calibrations before and after the two validation tests, the standard deviation on minute-long wave gauge measurements ranged from 0.02 cm to 1.13 cm, with an average standard deviation of 0.65 cm. This may be considered an estimation for the uncertainty on the experimental wave gauge measurements. The water level in the flume also varies by about 3 mm over a 5-10 minute cycle during the tests, as water leaks behind the wavemaker and is pumped back into the flume.

The CFD surface elevations are inherently imprecise because the interface is diffused over several cells. The reported diffuse interface includes all cells with void fractions α between 0.01 and 0.99. These cells are neither fully water (α=0.0) nor fully air (α=1.0). When using HRIC interface reconstruction, the reported interface location is the average location of all cells with α=0.5. For PLIC's smaller interface band, the reported surface elevation is the average location of all cells in the uncer-

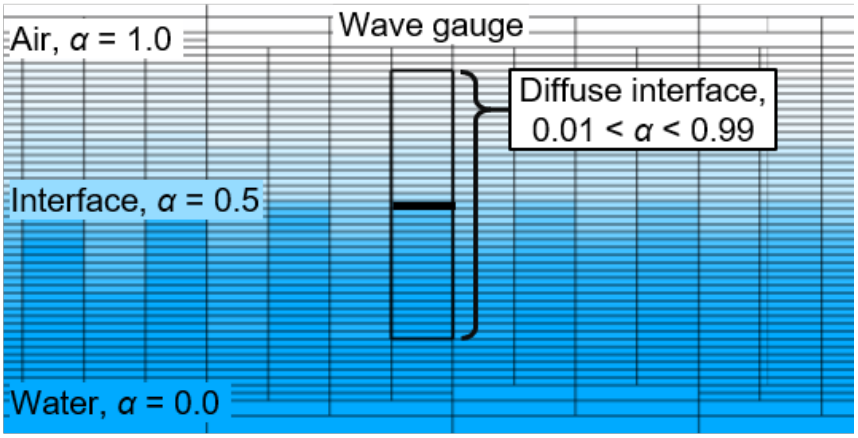

Figure 3.6. Close-up of diffuse air-water interface at wave gauge 3, with reported HRIC interface location (black cell) and diffuse interface band (outlined cells).

tainty band, because typically no cell has α=0.5 exactly. Figure 3.6 illustrates the diffuse interface and reported HRIC interface location at wave gauge 3 for the solitary wave simulation.

3.2.3.3 Shoaling validation results

The CFD and experimental time histories of surface elevation $\eta(t)$ are compared at the three wave gauges for the regular waves validation case in Figure 3.7. At each wave gauge, the CFD and experimental surface elevations agree within the CFD diffuse interface band, although the CFD model tends to overpredict the surface elevation. The CFD model accurately captures the wave shoaling, correctly predicting the change in period and wave height across the wave gauges. Note that the experimental wave gauge 3 is unable to measure $\eta < 0$ due to its placement and therefore cannot capture the wave troughs.

Similarly, Figure 3.8 compares the CFD and experimental surface elevation time histories $\eta(t)$ at the three wave gauges for the solitary wave validation case. Again, the CFD model overpredicts the surface elevation, though the peak height is within the CFD diffuse interface band at wave gauges 1 and 2. The CFD wave also exhibits

reasonable shoaling, but the CFD model slightly overpredicts the celerity so that the CFD wave arrives sooner at a given location than in the experiment.

Table 3.1 quantifies the difference between the CFD and experimental results at each wave gauge for the solitary and regular waves validation cases. Positive values indicate that the CFD prediction exceeds the experimental data. The difference in the regular waves' period and wave height are the averaged differences from three

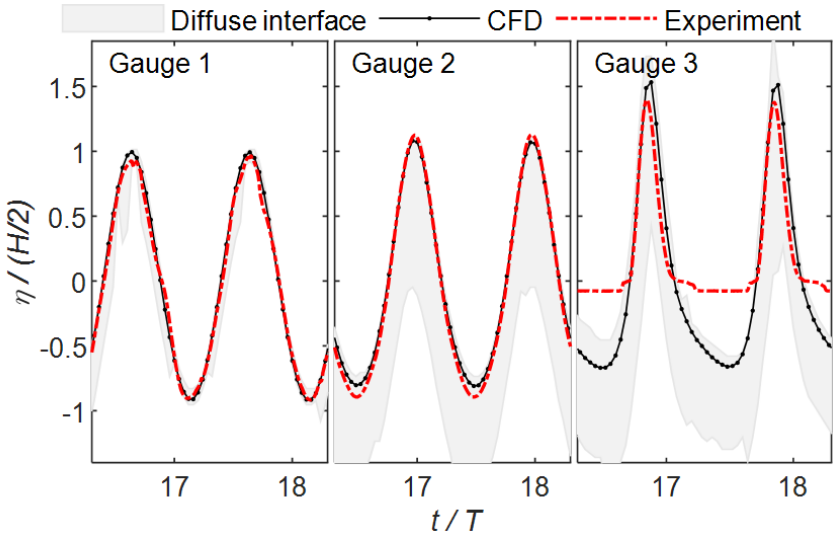

Figure 3.7. CFD and experimental time histories for regular waves surface elevation at three gauge locations.

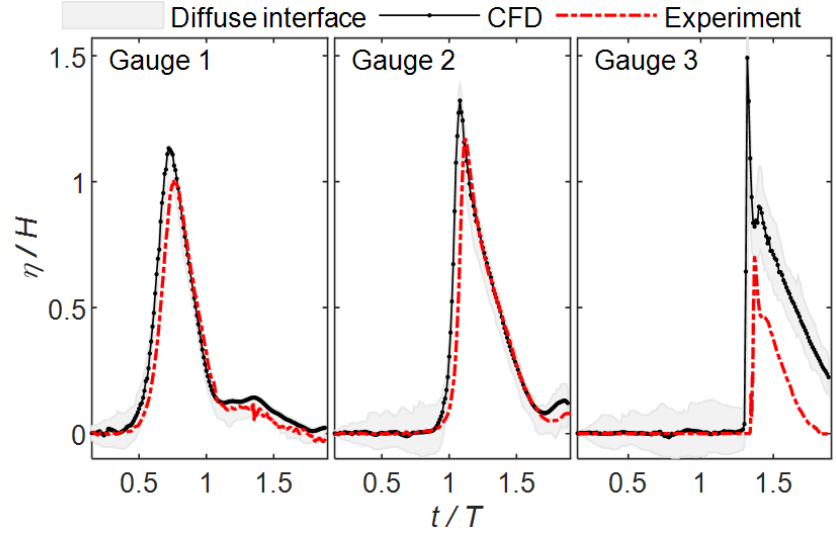

Figure 3.8. CFD and experimental time histories for solitary wave surface elevation at three gauge locations.

Table 3.1. Difference between CFD and experiment for wave height H, period T, and peak surface elevation η at each wave gauge.

Gauge	Regular waves ΔH (cm)		Regular waves ΔT (ms)		Solitary wave Δ(peak η) (cm)	
1	0.5	(+3.5%)	45.0	(+1.8%)	6.4	(+12.5%)
2	-1.1	(+3.5%)	0.2	(+0.01%)	7.8	(+13.1%)
3	1.0	(+9.5%)	0.0	(+0.0%)	40.2	(+112%)

waves. For gauge 3, the regular waves' peak surface elevation is substituted for wave height because the experimental troughs are not captured (see Figure 3.7). Table 3.1 also lists the difference in the solitary wave's peak surface elevation.

In Figure 3.8 and Table 3.1, the CFD and experimental surface elevations at wave gauge 3 show poor agreement for the solitary wave, particularly at the peak. At this gauge location, the wave is a plunging breaker in the process of collapsing. The collapsing wave produces spray, an air-water mixture that the experimental gauge struggles to capture. The CFD diffuse interface includes the modeled version of this spray. The diffuse interface band is therefore larger at gauge 3, when the wave is breaking, than at gauges 1 or 2 (see Figure 3.8). In this case, the bottom of the CFD diffuse interface band is a better approximation for the experimental gauge measurement, which largely neglects the spray. When the diffuse interface bottom is used for the CFD surface elevation, the CFD overpredicts solitary wave peak elevation by 14.2 cm (+39.4%).

The CFD model's overprediction of surface elevation and celerity could indicate a need for a well-tuned turbulence model to add more dissipation, although initial efforts to add turbulence models added too much dissipation and did not match the experimental data. Additional validation simulations indicate that applying a slip wall boundary condition on the CFD floor rather than a no-slip condition could also improve the CFD predictions in the absence of a turbulence model.

Overall, the CFD model satisfactorily predicts the surface elevation for regular nonlinear and solitary waves shoaling over a sloped bottom. In the solitary wave case, the CFD model also predicts a breaking wave due to shoaling at approximately the correct location and time. The CFD regular wave heights are correct at each gauge within experimental uncertainty, given the diffuse interface (see Figure 3.7 and Table 3.1). The CFD regular wave periods are also satisfactorily accurate. The CFD solitary wave peak surface elevation is correct within experimental uncertainty given the diffuse interface for gauges 1 and 2, although the CFD model overpredicts the surface elevation of a wave in a late stage of breaking (see Figure 3.8 and Table 3.1). These validation cases indicate that the CFD model can accurately capture a shoaling nonlinear wave train and produce a breaking wave due to shoaling.

3.2.4 Nonlinear wave forces

The fourth and final case validates the CFD force on a cylinder due to regular waves against experimental work by Niedzwecki and Duggal [91]. Niedzwecki and Duggal measure the inline forces on a cylinder of radius r=5.7 cm subjected to regular waves with periods T=0.5–1.5 s and wave heights H=1.04–12.69 cm. The experiments are carried out in a wave flume 37 m long, 0.91 m wide, and 1.22 m tall, filled to a water depth d=0.91 m with wave absorption provided by a 1:3.5 slope placed after the cylinder.

In the CFD simulations, the domain is reduced to 5–6 wavelengths long, 0.91 m wide, and 1.0 m tall, in order to reduce computational cost. The simulations include a dynamic Smagorinsky LES turbulence model with a Werner-Wengle wall model on the cylinder. The domain bottom and cross-flow sides are no-slip walls, with the top open to atmospheric pressure.

The regular waves are generated in the CFD simulations by prescribing the velocity and void fraction at a location at the boundary located 1–2 wavelengths upstream

of the cylinder, according to 5th order Stokes wave theory [88, 89]. The domain is also initialized with velocity, pressure, and void fraction distributions according to 5th order Stokes wave theory. Wave absorption is provided by a momentum damping region 1–2 wavelengths long, located 2–3 wavelengths downstream of the cylinder. These methods for wave generation and absorption are described in Section 3.1.1 and verified by the wave propagation case described in Section 3.2.2.

The CFD mesh consists of base cells with an approximate size of $L/10$ by $L/10$ by $d/22$. AMR adds cells of size $L/180$ by $L/180$ by $H/20$ at the interface, and four layers of $r/45$ by $r/45$ by $H/80$ cells are also added to the cylinder surface. This mesh is selected after a brief mesh convergence study shows that halving the dimensions of the base and cylinder cells yields minimal improvements to the force results, while doubling the cell dimensions creates significant noise in the force results. Like in the previous validation and verification cases, the timestep is adjusted to maintain a Courant number of 0.4 and first-order upwinding is used for the advection scheme with the HRIC interface tracking scheme.

The CFD simulations focus on five of the fifteen wave parameter combinations studied by Niedzwecki and Duggal [91]. Each CFD case simulates waves of a different period, with wave heights in the range described by Niedzwecki and Duggal for that period. See Table 3.2 for a summary of the five CFD wave parameter combinations. Niedzwecki and Duggal characterize the waves by the scatter parameter kr, the product of the wavenumber k and the cylinder radius r, representing a ratio of cylinder size to wavelength.

The force on the cylinder is characterized by the maximum inline force F on the cylinder, averaged over several waves, in keeping with Niedzwecki and Duggal. Figure 3.9 plots the maximum inline force against the scatter parameter kr from the CFD simulation, Niedzwecki and Duggal's experiments, and the results of linear diffraction theory as described by Niedzwecki and Duggal [91].

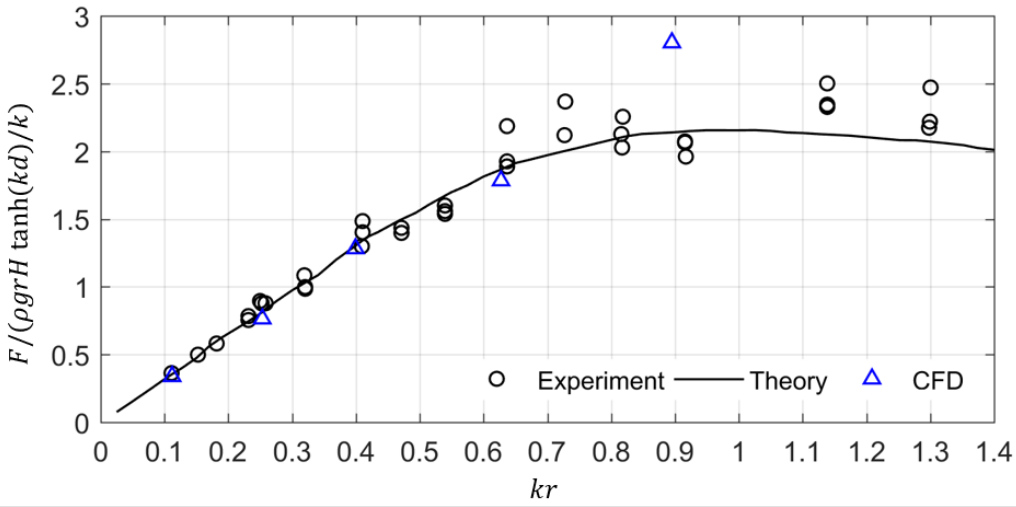

Figure 3.9. The maximum inline force F on a cylinder due to regular waves, plotted versus the product of wavenumber and cylinder radius kr. The CFD results ($\triangle$) agree well with experimental values ($\bigcirc$) from Niedzwecki and Dugal [91], as well as results from linear diffraction theory ($-$), particularly for $kr < 0.7$.

As shown in Figure 3.9, the CFD force agrees very well with the experimental and theoretical values for kr less than about 0.7. For larger kr, the CFD force is significantly larger than the experimental and theoretical results. However, note that the experimental results vary considerably for a given kr depending on the wave height, although the CFD kr=0.895 case is outside the experimental range given for nearby kr. Despite this, the CFD model's success at low kr is encouraging, since ocean waves for OWTs tend to have low kr due to their large wavelengths compared to the scales of OWT monopiles.

Table 3.2. Wave parameters for the five CFD regular wave force validation cases. Wavelength and wavenumber are calculated according to 5th order Stokes wave theory.

Scatter parameter kr	0.112	0.253	0.399	0.627	0.895
Wave period T (s)	1.47	0.947	0.749	0.595	0.498
Wave height H (cm)	4.93	4.65	4.43	3.29	2.25
Wavelength L (m)	3.12	1.41	0.897	0.571	0.400
Wavenumber k (m^{-1})	1.96	4.44	7.00	11.0	15.7

Overall, the validation of CFD regular wave forces against experimental data indicates that the CFD model accurately predicts the forces on cylindrical structures due to wave trains, especially for scales relevant for offshore wind energy.

3.3 Breaking wave limits

Using the validated CFD model, thirty-nine shoaling regular wave trains are simulated with various wave parameter combinations representative of wind energy development sites off the U.S. Atlantic Coast. This set of simulations provides a basis for evaluating the performance of the McCowan, Miche, Battjes and Goda empirical breaking limits described in Equations 2.5–2.8. This section describes the CFD simulation setup, discusses how the simulated waves are analyzed, and finally evaluates the performance of the four empirical breaking limits using the simulated waves.

3.3.1 Simulation setup

Each shoaling regular wave train is simulated using the best-practice CFD settings identified while verifying and validating the CFD model, as described in Section 3.2.

3.3.1.1 Simulation domain

Each wave train is generated in a 2D computational domain with a floor of some slope s. The domain is one cell wide with symmetry boundary conditions on the sides, creating a 2D domain although the Navier-Stokes equations are solved in 3D. The top of the domain is open to atmospheric pressure and the floor is modeled as a no-slip wall.

For cases with s=0, the domain floor is horizontal, with a constant water depth d_0. For cases with s <0, the domain floor slopes upward from a water depth of $1.75d_0$ at the left end of the domain to a depth of $0.25d_0$ at the right, with the nominal depth d_0 occurring at the midpoint of the slope. Figure 3.10 illustrates the simulated

domain for a case with nominal depth d_0=35 m, nominal wavelength L_0=315 m, and slope s=6%.

The CFD mesh consists of Cartesian base cells sized $L_0/100$ by $d_0/160$ or smaller, maintaining an aspect ratio of 1:8 based on the vertical cell size. The vertical cell size ensures that the shallowest still water depth is spanned by at least 40 cells. One level of AMR is added at the evolving air-water interface, producing cells sized $L_0/200$ by $H_0/110$ or smaller at the interface.

A brief mesh convergence study is carried out for a case with nominal depth d_0=35 m, slope s=6%, nominal wavelength L_0=315 m, nominal wave height H_0=17.5 m, and nominal period T_0=15.1 s. Three mesh resolutions are considered: base cells sized $L_0/187$ by $d_0/166$ as described above, base cells twice this size, and base cells half this size. One level of interface AMR is added to each mesh's base cells. Figure 3.11 compares each mesh's surface elevation time history at x=$L_0/2$ for the first wave generated. As shown in Figure 3.11, there is little difference between the three meshes, although the coarsest mesh predicts a slightly lower wave height than the other two meshes. The middle mesh is therefore selected for this study, as described above.

The adaptive timestep is adjusted to maintain a Courant number of 0.2 throughout each simulation, creating timesteps on the order of 0.2–4 ms. The simulated time ranges from about 20 s to 100 s, depending on the wave train and domain.

The regular wave trains are generated at the left domain boundary using 25th order stream function theory [86], as described in Section 3.1.1. The stream function

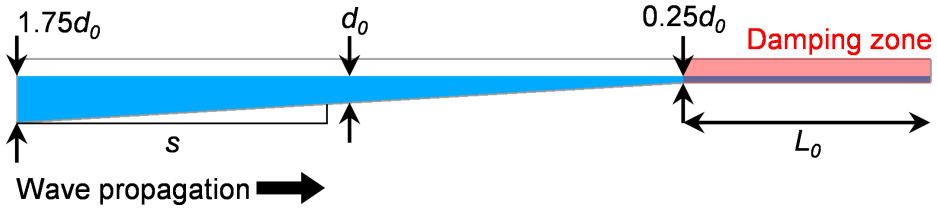

Figure 3.10. Sample CFD domain for shoaling regular wave trains, including wave generation boundary (left) and momentum damping zone (right).

wave kinematics are calculated for a nominal wave height H_0 and nominal wavelength L_0, assuming a constant water depth of d_0 for s=0 or $1.75d_0$ for $s > 0$. The waves propagate to the right into the initially still domain, shoaling over the sloped floor. For wave absorption, a momentum damping zone is added on an L_0-long horizontal plateau at the right domain boundary, as shown in Figure 3.10 and described in Section 3.1.1.

3.3.1.2 Wave parameters

Each simulated wave train is characterized by four parameters: the seafloor slope s, the nominal depth d_0, the nominal wave height H_0, and the nominal wavelength L_0. Simulated values for the nominal depth d_0 and the seafloor slope s are chosen based on representative ranges for potential U.S. offshore wind energy development sites off Maine, New Jersey, and Georgia. Table 3.3 summarizes the depth and slope ranges for the three sites as well as the simulated wave trains. The water depths for the three sites in Table 3.3 are derived from the U.S. Coastal Relief Model from

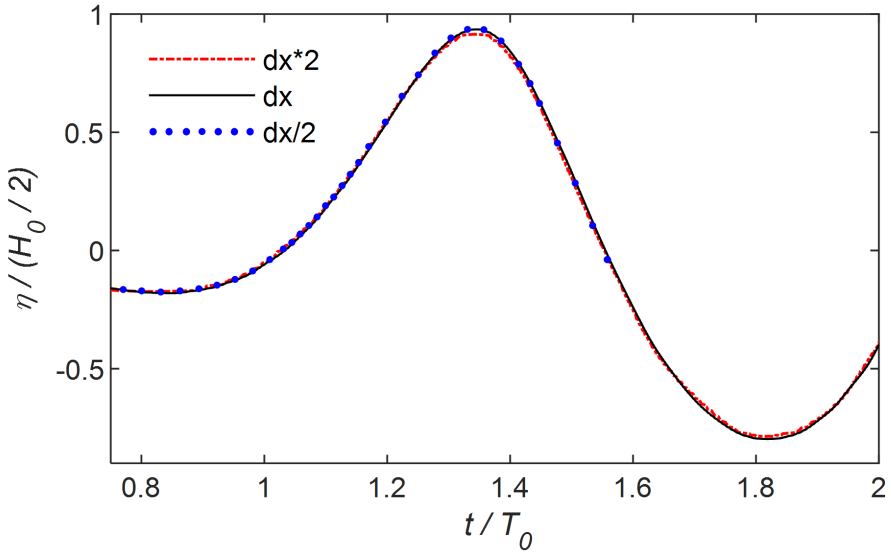

Figure 3.11. Surface elevation time histories at x=$L_0/2$ for three meshes: the cell size used in this study (−), cells twice this size (−−), and cells half this size (●).

the National Oceanic and Atmospheric Administration (NOAA), with further details documented in Johlas *et al.* [16].

While the simulated water depths and slopes are based on the U.S. site data, the nominal wave heights H_0 and wavelengths L_0 are selected to create breaking waves. Values for H_0 and L_0 are chosen so that some, but not all, of the generated wave trains exceed the McCowan, Miche, Battjes, and Goda breaking limits at the nominal depth d_0. This is accomplished using the ranges $0.50 \leq H_0/d_0 \leq 1.15$ and $5 \leq L_0/d_0 \leq 14$. This range for H_0/d_0 produces some simulated wave heights that exceed expected extreme wave heights for the three U.S. sites. However, these large heights are necessary to obtain breaking waves for use in evaluating the breaking limits. A total of 39 different regular wave trains are simulated. Table 3.4 summarizes the nominal wave train parameters d_0, s, H_0, and L_0 for each of these simulations.

3.3.2 Analysis of simulated waves

The 39 simulated wave trains yield a collection of 25 breaking waves and 19 non-breaking waves. To evaluate the four empirical breaking limits using this collection of simulated waves, the simulated waves must be characterized by parameters used in the breaking limits.

3.3.2.1 Characterization of breaking waves

Although each simulated wave train is defined by the nominal parameters d_0, s, H_0/d_0, and L_0/d_0, individual waves within that train develop new characteristic

Table 3.3. Water depth and seafloor slope ranges for potential U.S. wind energy development sites, compared to CFD ranges.

	Depth (m)	Slope (%)
Maine	$2 \leq d \leq 50$	$0 \leq s \leq 12$
New Jersey	$2 \leq d \leq 20$	$0 \leq s \leq 2$
Georgia	$12 \leq d \leq 25$	$0 \leq s \leq 1$
Simulations	$5 \leq d_0 \leq 50$	$0 \leq s \leq 12$

values as they shoal and break. Therefore, each individual wave is characterized using local, instantaneous values d, H, and L rather than the wave train's nominal values. The seafloor slope s is consistent between the nominal wave train and each individual wave.

Within some wave trains, one or more individual waves break during the simulated time. In this study, the breaking waves are mostly plunging breakers, with some spilling breakers [43]. It is difficult to capture the exact instant of breaking, so the local instantaneous parameters d, H, and L are averaged from two times: immediately before the wave tongue curls over, and as the wave tongue begins to curl over. For wave trains where no waves break within the simulated time, the local instantaneous parameters are taken from the steepest non-breaking wave at the end of the simulation.

Table 3.4. Summary of 39 wave trains for breaking wave simulations, listed by nominal depth d_0, slope s, generated wave height H_0, and generated wavelength L_0.

s (%)	d_0 (m)	H_0/d_0	L_0/d_0	s (%)	d_0 (m)	H_0/d_0	L_0/d_0
0	5	1.10	11	6	25	0.80	11
0	10	0.55	14	6	35	0.50	9
0	20	0.70	6	8	10	1.15	8
0	25	0.50	13	8	20	1.00	10
0	30	0.85	10	8	30	0.70	12
0	35	0.65	7	8	40	0.55	6
0	40	1.00	8	8	50	0.85	14
0	45	0.80	9	9	5	0.50	5
0	50	1.15	12	9	15	0.80	7
2	10	0.70	10	9	25	0.95	9
2	30	0.55	8	9	45	0.65	11
2	40	0.85	12	11	20	0.55	12
3	5	0.65	9	11	40	1.15	10
3	15	0.50	11	11	50	0.70	8
3	45	0.95	13	12	5	0.80	13
5	20	0.85	8	12	15	1.10	9
5	40	0.70	14	12	25	0.65	5
5	50	0.55	10	12	35	0.95	11
6	5	0.95	7	12	45	0.50	7
6	15	0.65	13				

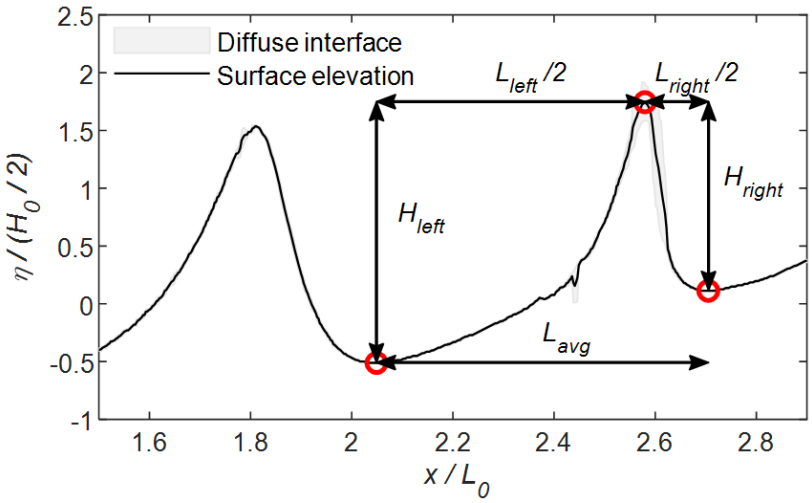

Figure 3.12. Instantaneous surface elevation of a CFD wave about to break, with its peak and troughs circled and different options for wavelength and height characterizations labeled.

3.3.2.2 Ambiguity of H and L

The simulated waves are highly nonlinear and often asymmetric, as illustrated in Figure 3.12. Although the PLIC diffuse interface band is relatively small in Figure 3.12, characterizing the local instantaneous d, H, and L is still ambiguous due to the wave's asymmetry. The depth d is defined as the still water depth at the location of the wave's peak. The height H can be defined in three ways:

1. H_{left}, the vertical distance between the left trough and the peak of the wave,
2. H_{right}, the vertical distance between the right trough and the peak, or
3. H_{avg}, the average given by $(H_{left} + H_{right})/2$.

The vertical arrows in Figure 3.12 illustrate H_{left} and H_{right}. Similarly, the wavelength L can be defined as:

1. L_{left}, twice the horizontal distance between the left trough and the wave peak,
2. L_{right}, twice the horizontal distance between the right trough and the peak, or
3. L_{avg}, the horizontal distance between the left and right troughs.

The horizontal arrows in Figure 3.12 illustrate L_{left}, L_{right}, and L_{avg}. Of these three options, L_{avg} is most consistent with observations of physical asymmetric waves, since measuring trough-to-trough makes no assumptions about the symmetry of the wave.

3.3.3 Performance of empirical breaking limits

The McCowan, Miche, Battjes, and Goda breaking limits are evaluated against the shoaling and breaking regular wave trains simulated using the CFD model. First, how the characterization of individual CFD waves affects model performance is discussed. Second, the key metrics for evaluating breaking limit performance are described. Next, the apparent tendency of the breaking limits to underpredict the breaking steepness is examined. Finally, the performance of each limit is evaluated and compared.

3.3.3.1 Effect of H and L choice

Different options for wave height and wavelength characterizations produce decidedly different results, as shown in Figure 3.13. Figure 3.13 plots the steepness H/L against the relative depth d/L for each simulated wave: breaking and non-breaking waves are filled and non-filled circles respectively. The limits predicted by the McCowan, Miche, and Goda (for s=0% and s=12%) breaking criteria are also shown; the breaking region is above the limit lines. Figure 3.13 compares the accuracy of the criteria for different combinations of H and L characterizations. The Battjes limit predicts a slightly lower breaking limit than Miche for all d/L, but is nearly identical to Miche and is therefore not included in Figure 3.13 for visual clarity.

Choosing the average options H_{avg} and L_{avg} (top, Figure 3.13) works reasonably well for all four breaking limits. The left options H_{left} and L_{left} (middle, Figure 3.13) and the right options H_{right} and L_{right} (bottom, Figure 3.13) do not agree as well with the four criteria, although the left options still agree acceptably with the Miche, Battjes, and McCowan limits. Additionally, using H_{right} with L_{avg} also agrees

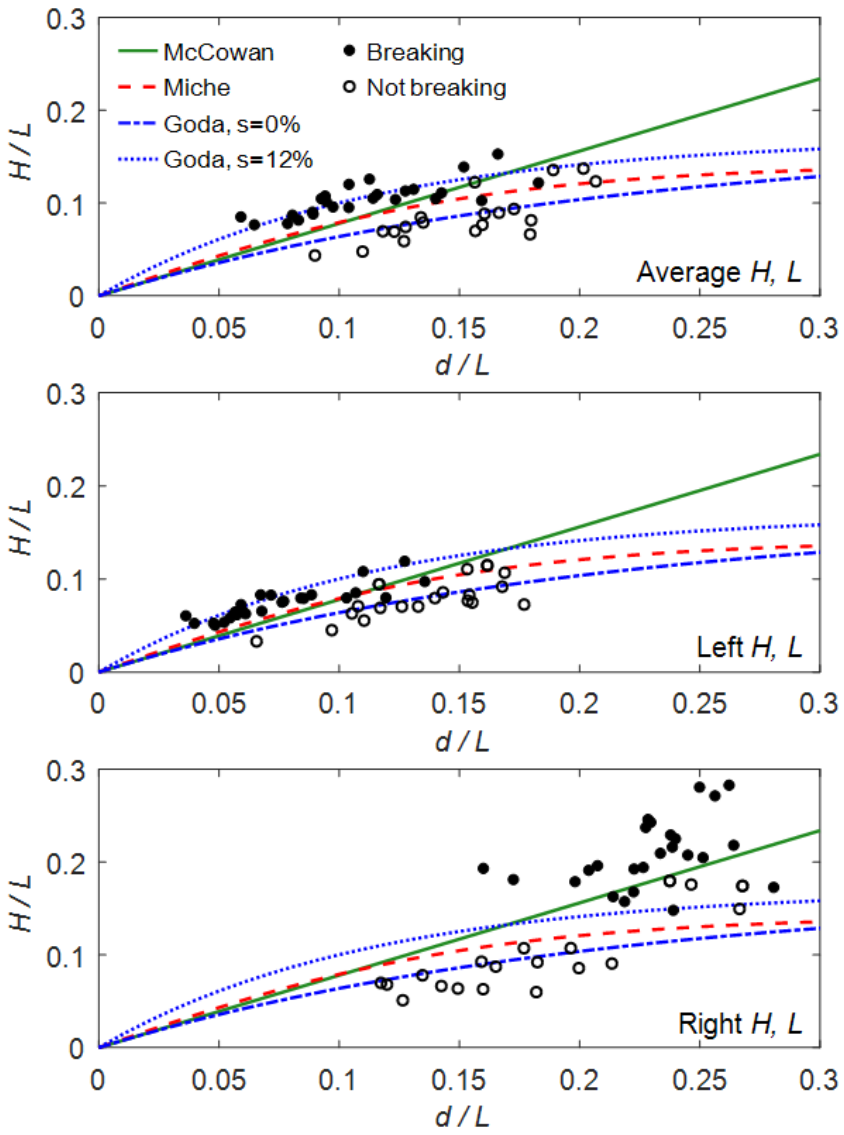

Figure 3.13. Breaking (●) and non-breaking (○) CFD waves with McCowan, Miche, and Goda breaking limits (lines). Waves are characterized by the average, left, or right L and H (top, middle, or bottom plot).

reasonably well with all four limits. For the remainder of the analysis, the average options H_{avg} and L_{avg} are used unless otherwise noted.

It is expected that the trough-to-trough wavelength characterization L_{avg} agrees the best with the four limits, since this is the only wavelength option with real physical meaning. The average or right height characterizations (H_{avg} or H_{right}) are also compatible with typical experimental measurements of waves, which are usually time histories of surface elevation taken at single-location wave gauges.

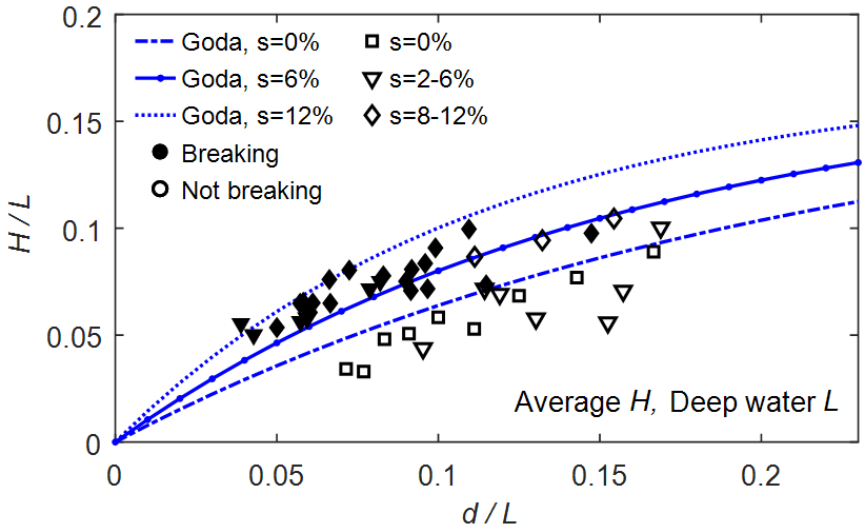

Figure 3.14. Breaking and non-breaking CFD waves (filled and unfilled markers) with Goda breaking limit (lines) for different slopes s. Waves are characterized by the deep water wavelength L_0 and average height H.

3.3.3.2 Goda with deep water L

Although Figure 3.13 uses the local, instantaneous wavelength L, the Goda limit was originally derived for the deep water wavelength L_0 rather than the local wavelength L [44, 45]. Figure 3.14 compares the Goda limit to the simulated waves using H_{avg} and the deep water wavelength L_0, for different slope ranges s. The Goda limit matches the CFD results better when the deep water L_0 is used rather than the local L, but only for seafloor slopes $s \leq 8\%$. This slope-dependent accuracy is comparable to the results of Rattanapitikon and Shibayama [45]. In general, the local L is an acceptable alternative in the Goda limit and is preferable for larger seafloor slopes.

3.3.3.3 Breaking limit performance metrics

The performance of the McCowan, Miche, Battjes, and Goda breaking limits is evaluated by comparing the breaking limit predictions to the CFD simulation results, using the average wavelength and wave height. Figure 3.15 compares the McCowan, Miche, and Goda breaking limits to the breaking and non-breaking CFD waves, grouped by seafloor slope s. Note that the Battjes formulation predicts a

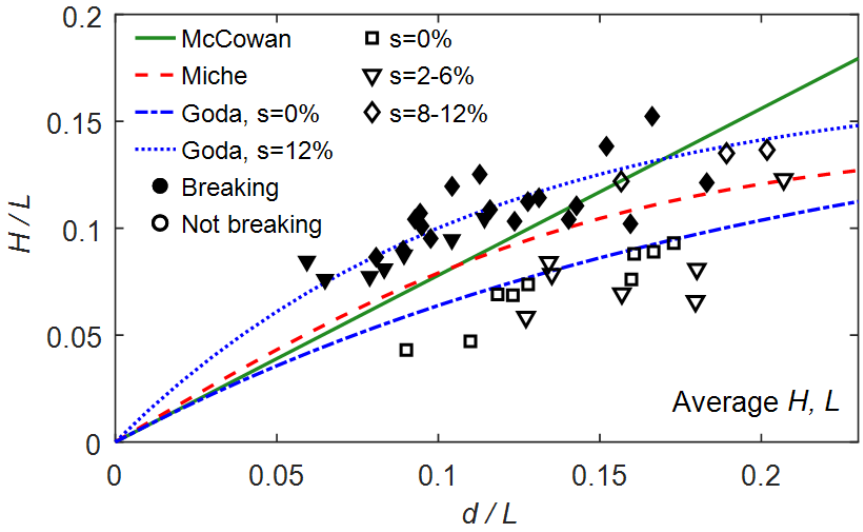

Figure 3.15. Breaking and non-breaking CFD waves (filled and unfilled markers) with McCowan, Miche, and Goda breaking limits (lines) for different seafloor slopes s. Waves are characterized by average wavelength and height.

slightly lower limit than the Miche limit, but again is not included in Figure 3.15 for visual clarity. Appendix A also summarizes the data in Figures 3.14–3.15, and indicates disagreement between the CFD wave and each limit for each wave. When evaluating the four limits' performance in relation to the simulated waves, it is convenient to examine three main ways a limit may be inaccurate when compared with a CFD wave.

First, the limit may predict that a wave should break, although the simulated wave does not. The limit then produces a false positive. Second, the limit may predict that a wave should not break, but the simulated wave does break, producing a false negative. False positives are preferable to false negatives for conservative design purposes, because breaking wave loads are generally higher than non-breaking wave loads [43].

Third, the limit may underpredict the steepness H/L at which a wave breaks, even if it correctly predicts the CFD wave's status at the end of the simulation. This underprediction is quantified by the ratio of the CFD wave's steepness to the limit steepness for a given d/L. Appendix A also uses this ratio to indicate if the

breaking limit prediction agrees with the CFD wave. This steepness underprediction is illustrated when the simulated breaking waves significantly exceed the breaking criteria's predictions, as shown in Figure 3.15 and Appendix A, which requires further examination.

3.3.3.4 Steepness underprediction

In this analysis, waves are identified as breaking when the wave tongue curls over. A few timesteps before a shoaling wave is identified as breaking, the wave had a larger d and L but lower H. Therefore, this slightly earlier version of the simulated wave is not yet breaking, yet still exceeds the breaking limit. There are two possible explanations for this behavior:

1. Breaking is truly initiated significantly before the wave tongue curls over, so the simulated wave continues to shoal throughout the process of breaking, or
2. The breaking limits underpredict the steepness H/L at which a wave breaks for a given d/L.

A combination of both explanations is most likely.

Conversely, the simulated non-breaking waves are often significantly below the breaking limits, as shown in Figure 3.15 and Appendix A. This behavior is physical and expected, since the limits predict an upper bound on non-breaking wave size. For the $s > 0\%$ non-breaking waves, the relatively small waves shown in Figure 3.15 are simply an artifact of when these waves are measured, at the end of the simulation. With additional domain space and simulation time, presumably these waves would continue to shoal and eventually break.

For s=0% waves there are no shoaling effects, so that if a wave does not immediately break when generated, it will never break during the simulation. Several of the s=0% wave trains are in fact unstable or breaking when initially generated at the left domain boundary, as predicted by the breaking limits. However, these waves are not

included in the breaking wave group because the wave kinematics are prescribed by stream function theory, which is inaccurate for breaking waves [86], rather than being allowed to develop naturally during the simulation. The stable, smaller waves that form after these initial waves break are recorded as non-breaking, so all simulated s=0% waves are non-breaking.

3.3.3.5 Breaking limit performance

Table 3.5 compares the McCowan, Miche, Battjes, and Goda limits based on the occurrence of these three kinds of inaccuracy. The percentage of all recorded waves that are false negatives and false positives are presented for each limit in the first two rows of Table 3.5. The last row shows the average steepness underprediction as a percentage of the CFD breaking steepness.

As shown in Table 3.5, none of the limits perform well across all three metrics of accuracy. The Battjes limit has no false negatives and is therefore the most conservative, but tends to significantly underpredict the breaking steepness. The Miche limit also has an acceptably low false negative rate but a lower intermediate false positive rate and steepness underprediction than the Battjes limit. In terms of conservative predictions for design purposes that work for all seafloor slopes, the Battjes and Miche limits have the best overall performance.

The Goda limits with L and the McCowan limit have higher false negative rates than the Miche and Battjes limits, but lower false positive rates (see Table 3.5). The Goda limit with L_0 has the highest false negative rate, although these false negatives only occur for seafloor slopes $s \geq 8\%$, as illustrated in Appendix A. The Battjes and

Table 3.5. Comparison of breaking limit performance based on false negatives, false positives, and steepness underprediction.

CFD wave breaks?	**McCowan**	**Miche**	**Battjes**	**Goda, L**	**Goda, L_0**
Yes, limit says no	9.1%	2.3%	0.0%	9.1%	60.0%
No, limit says yes	0.0%	9.1%	21.0%	6.8%	0.0%
Mean H/L underprediction	23.2%	21.1%	26.6%	13.3%	11.8%

Miche limits are therefore preferable to the McCowan and Goda limits for conservative predictions for design, particularly for large seafloor slopes. However, the Goda limit is preferable for conservative predictions for lower seafloor slopes (see Appendix A), like those found in most of the shallow to intermediate depths off the U.S. East Coast.

Aside from each limit's accuracy, external factors may also influence which limit is best-suited for the design of OWTs. For example, it may be difficult to collect data on the deep water wavelength and sea floor slope required for the full deep water Goda limit with L_0. The Miche and Battjes models' dependence on local wave parameters, without the slope, is advantageous in this respect.

Furthermore, initial attempts to slightly modify the Battjes and Goda limits did not yield improvements in overall performance. For example, adjusting the coefficients or adding a slope dependence to the Battjes limit may reduce the average steepness overprediction, but increase the number of false negatives. Therefore, the Goda limit with the deep water wavelength should be used for seafloor slopes $s < 8\%$, and the Battjes limit for seafloor slopes $s \geq 8\%$.

3.4 Breaking wave forces

Having addressed whether a given wave will break, the second component of this research examines the force on a monopile OWT due to a breaking wave. Specifically, this study compares four empirical slam force models (Goda, Campbell-Weynberg, Cointe-Armand, and Wienke-Oumerachi from Table 2.1) to CFD simulations of breaking waves impacting monopile OWTs. CFD simulations are performed for regular wave trains shoaling over a sloped floor until the waves break on or shortly before the monopile. A total of four different combinations of wave height, wavelength, and monopile size are considered. This section describes the simulation setup, presents the CFD results for wave characteristic and peak slam force, and finally compares the simulated forces to predictions from the empirical slam force models.

3.4.1 Simulation setup

3.4.1.1 Monopile foundation descriptions

Two different monopile designs are examined: a monopile for the DTU 10 MW reference turbine [92] and the UpWind reference monopile for the UpWind 5 MW turbine [93]. The simulated 5 MW and 10 MW untapered monopiles have diameters D of 6 m and 9 m respectively [92, 93], and are designed for 25 m of water depth. The D=6 m monopile has the same diameter as the OC3 monopile for the NREL 5 MW reference turbine, although the design water depth is slightly deeper (25 m instead of 20 m).

Both monopiles are simulated as fixed rigid bodies, removing the need to simulate each structure's below-mudline embedded pile. The simulations also do not include any transition pieces, platform decks, or towers, in favor of isolating the breaking wave interaction with the substructure. Both monopiles are extended at a constant diameter to a length of 45 m above the sea floor, to capture impact forces from the large breaking waves. Although this extended height is larger than the height specified in the original designs [92, 93], it represents well-designed structures that avoid deck slamming during the highest wave.

3.4.1.2 Simulation domains

The wave trains are simulated in a 3D computational domain with a sloping floor dictated by seafloor slope s. The setup of each individual simulation is determined by the support structure type. The water depth at the structure is chosen to be 25 m $\pm$ 5 m for the monopiles to reasonably match the design depth for each structure. This monopile depth is also very reasonable for the U.S. East Coast when compared to the site ranges in Table 3.3. The depth at the left end of the domain is 40 m. The seafloor slopes upward to a depth of 20 m at the right end of the domain, as illustrated in Figure 3.16.

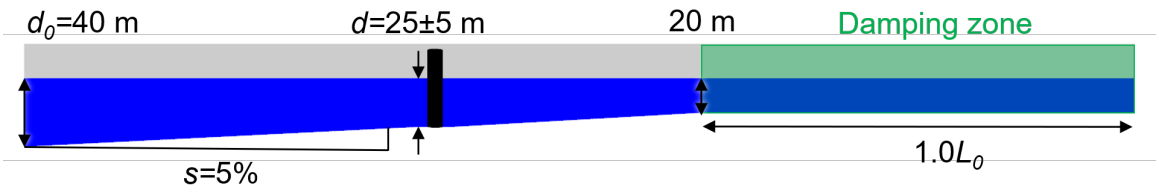

Figure 3.16. Side view of the 3D domain for a simulation with the 10 MW monopile. Waves are generated at the left domain boundary, with a momentum damping zone before the right domain boundary.

As described in Section 3.1.1, wave trains are generated in the initially still domain by prescribing the surface elevation and fluid velocity at the left domain boundary, according to 25th order stream function theory [86]. The wave generation kinematics are for a wave of height H_0 and wavelength L_0 in water of constant depth d_0=40 m (see Figure 3.16). The unshoaled wave height H_0 and wavelength L_0 are selected to produce breaking near the design depth of 25 m, based on breaking wave simulations from Section 3.3. As described in Section 3.1.1, an L_0-long momentum damping zone with a horizontal floor is added to the right end of a domain (see Figure 3.16).

The width of the 3D domain is based on the structure width; the domain width is five times the monopile diameter D. The prescribed wave kinematics are uniform across the width of the domain, creating waves that are largely 2D until they interact with the structure. Symmetry boundary conditions are applied to the domain sides to minimize the sides' effect on the simulation.

For these simulations, the momentum interpolation scheme is full upwinding with a Courant number of 0.9, due to improvements to the VOF portion of the CONVERGE model after the simulations in Section 3.3 were completed. No turbulence model is included due to the numerical diffusion supplied by the full upwinding scheme. Slip wall boundary conditions are then applied to the domain floor and the structure, which neglects the viscous force on the structure. This is justified by the validation case of regular waves on cylinders (see Section 3.2.4), which indicates

that pressure forces are significantly larger than viscous forces, even for waves with no slamming impact force.

The CFD mesh resolution is similar to the resolution used in the breaking wave simulations described in Section 3.3.1. The base cell size is approximately $L_0/120$ by $L_0/120$ by $d/150$ or smaller, with $L_0/240$ by $L_0/240$ by $H_0/170$ or smaller cells at the interface. Additional refinement is added around the monopile, creating cells of width $D/120$ for the 10 MW monopile and $D/80$ for the 5 MW monopile. These cell sizes create meshes with about 14 million cells.

3.4.1.3 Simulation workflow

Preliminary 2D simulations without monopiles are conducted with different seafloor slopes s, for each unique combination of water depth, wave height H_0, and wavelength L_0. Based on these preliminary simulations, the chosen value of s=5% is found to produce breaking waves near the desired depths, with reasonable values for the wave height at breaking H and the wavelength at breaking L.

The preliminary simulations also estimate the location where waves break for a given wave height H_0, wavelength L_0, and support structure type. For the 3D simulations, the upstream edge of the structure is located at this estimated breaking location (for waves breaking on the structure), or two structure widths downstream of this estimated breaking location (for waves breaking before the structure).

3.4.1.4 Summary of cases

Table 3.6 summarizes the domain parameters for each of the four simulations. The 5 MW and 10 MW monopiles are subjected to the same wave train, in order to compare the effect of structure size. Similarly, the 10 MW monopile is subjected to the same wave at different locations relative to the 2D predicted breaking location, in order to compare the effect of breaking location. Finally, the 10 MW monopile is subjected to two different wave trains, in order to compare the effect of wave size.

Table 3.6. Summary of four breaking wave force simulations, including monopile type, unshoaled wave characteristics, and wave characteristics just before breaking and at impact on the monopile. The last row lists the maximum inline force, when the slam impact occurs.

Case	1	2	3	4
Structure	10 MW mono.	10 MW mono.	10 MW mono.	5 MW mono.
d_0 (m)	40	40	40	40
H_0 (m)	20	20	25	20
L_0 (m)	250	250	250	250
s (%)	5	5	5	5
2D break loc.	On mono.	Before mono.	On mono.	On mono.
d_b (m)	32.01	32.00	31.01	31.68
H_b (m)	18.19	18.19	18.27	17.69
L_b (m)	198.0	197.4	203.5	201.7
d_i (m)	31.06	31.06	29.86	31.06
H_i (m)	16.79	15.65	17.20	16.84
L_i (m)	199.8	178.1	217.8	202.2
$x_i - x_b$ (m)	36.21	54.00	18.25	28.00
Max. F (MN)	22.00	24.49	17.88	11.30

3.4.2 Simulation results

During each simulation, a time history of the force vector on the structure is recorded. Snapshots of the surface elevation around the monopile, pressure on the monopile, and fluid velocity within the wave are also captured throughout the simulations. Table 3.6 lists the wave characteristics derived from these surface elevation snapshots at the time just before breaking and the time of impact on the structure. These values for H and L are the average values H_{avg} and L_{avg} (see Section 3.3.2).

The horizontal location of the peak x_b at the moment just before it breaks (when d_b, H_b, L_b are measured) and the horizontal location of the peak x_i at the moment of impact (when d_i, H_i, L_i are measured) are also compared for the full 3D simulations. The values of x_i–x_b reported in Table 3.6 therefore reflect the horizontal distance between when the wave starts to break and when the wave impacts the structure.

Figure 3.17 shows a 2D side view of each wave just before it impacts the structure. Runup on the leading edge of the cylinder is evident in all four cases. Most notably,

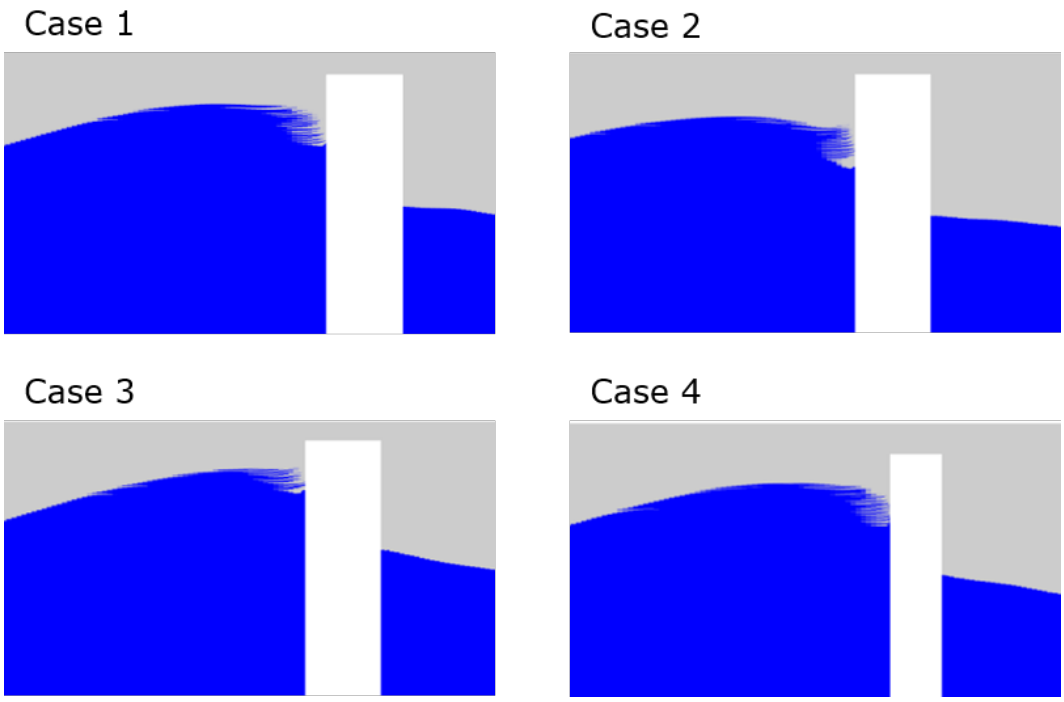

Figure 3.17. Side view of breaking waves just before impact for four slam force cases. Water is shaded blue, air is grey, and the monopile is white.

however, cases 2 and 3 are farther along in the breaking process than cases 1 and 4, so that more of the wave crest is moving as a vertical wall of water.

The maximum force caused by each breaking wave is also included in Table 3.6. These peak forces occur when the breaking wave front impacts the front of the structure. Time histories of the inline force on the structure are shown and discussed further in the next section.

3.4.3 Comparison to empirical slam force models

The breaking wave force simulations summarized in Table 3.6 are compared to the predictions made by the four empirical slam force models in Table 2.1, in conjunction with the Morison equation with slam force term F_S (see Equations 2.9–2.10).

3.4.3.1 Calculating drag and inertia terms

Although the slam force is separated from the drag and inertia forces in the Morison equation (see Equation 2.9), the simulated CFD force is the combined total

inline force (in the direction of wave propagation). The inline drag and inertia forces must therefore also be predicted using the Morison equation in order to compare the slam coefficient models to the CFD force. This approach would also be used in design, to predict the total load a monopile would experience due to a breaking wave of known characteristics.

The inline drag force on the cylindrical monopile is predicted from the CFD horizontal fluid velocities $u(z,t)$, by summing up the inline force per unit length over dz-tall segments of the cylinder. The total inline drag force on the cylinder is then given by

$$F_D(t) = \sum_{z=floor}^{z=interface} \Big(\big(1-\alpha(z,t)\big)\rho_w R u(z,t)|u(z,t)|C_d \; dz \Big), \tag{3.2}$$

where the water density ρ_w is weighted by the void fraction α to account for cells that are not fully water ($\alpha > 0.0$). The drag coefficient C_d is estimated for each of the four slam force simulations by extrapolating from the commonly cited Sarpkaya experimental curves, which give C_d as a function of Reynolds number Re and Keulegan-Carpenter number KC [94].

The CFD $u(z,t)$ is measured at the x-location of the monopile's leading edge, at a y-location of $4R$ from the structure center. Since the wave form is mostly uniform in y until it interacts with the structure, this approximates the wave kinematics at the structure location as if no structure existed. This approach is akin to obtaining breaking wave kinematics for a known wave (from measurements, wave theory approximations, or CFD) and predicting the force on a theoretical structure using the Morison equation. Using the structure leading edge as the x-location for the $u(z,t)$ measurement, rather than the structure center, was found to better capture the gradual rise in force prior to the slamming impact.

The inline inertia force on the cylinder is predicted from the CFD horizontal fluid acceleration $a(z,t)$ using a similar summing approach as the drag force:

$$F_I(t) = \sum_{z=floor}^{z=interface} \Big(\big(1-\alpha(z,t)\big)\rho_w \pi R^2 a(z,t)|u(z,t)|C_m \; dz \Big), \tag{3.3}$$

where the inertia coefficient C_m is again estimated for each CFD wave using Sarpkaya's experimental $C_m(Re, KC)$ curves [94]. The CFD $a(z,t)$ is estimated from the same $u(z,t)$ used in the drag calculation, using a central difference approximation for the derivative. This represents the undisturbed horizontal acceleration at the location of the structure's leading edge.

Table 3.7 summarizes the parameter values used to calculate the predicted drag and inertia force for each CFD wave, including the cylinder segment height dz, Reynolds number Re, Keulegan-Carpenter number KC, and the estimated drag and inertia coefficients C_d and C_m. For each simulated wave, the cylinder segment height dz=0.075 m is equal to the cell size at the air-water interface. The wave celerity C_p and surface elevation at impact η_i used to calculate the predicted slam force in Equation 2.10 are also included in Table 3.7. Values for C_p and η_i are calculated from CFD surface elevation snapshots, again located at y=4R to approximate a wave without a structure. A value of λ=0.4 is used for the curling factor for all four simulated waves.

Table 3.7. Parameter values used to calculate drag, inertia, and slam forces for each simulated breaking wave force case.

Case	Max. CFD F (MN)	Re	KC	C_D	C_M	C_p (m/s)	η_i (m)
1	22.00	1.8 x 10^8	33	0.71	1.74	17.44	13.03
2	24.49	1.8 x 10^8	32	0.71	1.74	17.98	12.22
3	17.88	1.9 x 10^8	31	0.71	1.74	18.88	13.82
4	11.30	1.2 x 10^8	48	0.68	1.76	17.48	13.01

3.4.3.2 Comparison of force time histories

Using Equations 3.2–3.3 and the values listed in Table 3.7, the drag and inertia forces predicted by the Morison equation are calculated for each simulated CFD wave. The slam force is also calculated for each CFD wave, using each of the four slam coefficient models listed in Table 2.1. The predicted total inline force time history (drag plus inertia plus slam) is then compared to the CFD total inline force time history for each wave. Figures 3.18–3.21 compare the CFD (black curve) and predicted total force time histories for the four slamming coefficient models (colored curves), for each of the four CFD simulations. The predicted drag and inertia force time histories are also included in Figures 3.18–3.21.

As shown in Figures 3.18–3.21, the predicted total inline force matches the CFD total force reasonably well for the times leading up to the impact in each case. The inertia force dominates the predicted total force until the times immediately before impact, when the fast-moving wave crest contributes to a larger predicted drag force.

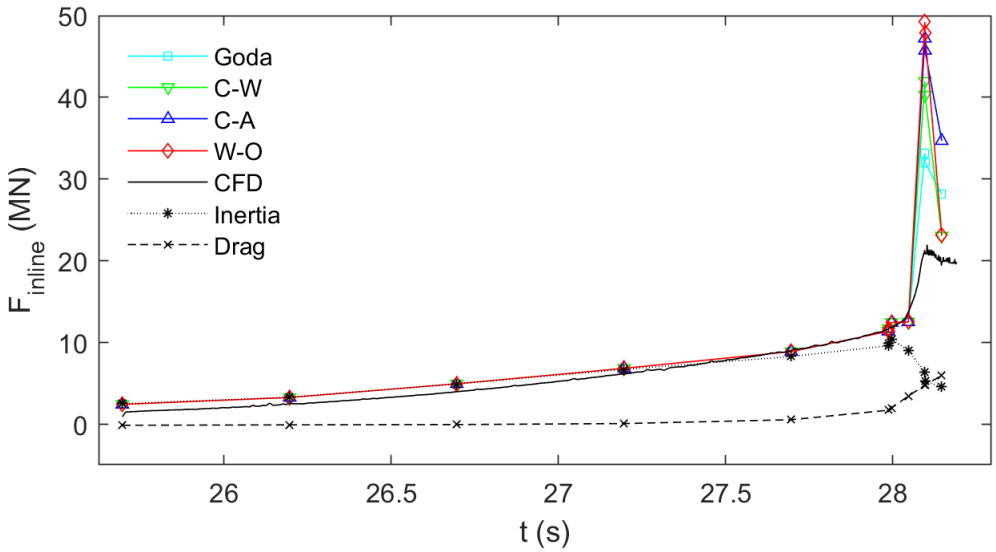

Figure 3.18. Inline force time history for case 1 (10 MW monopile), including CFD total force (−), predicted inertia and drag (dashed ∗ and ×), and predicted total force using Goda (□), Campbell-Weynberg (▽), Cointe-Armand (△), and Wienke-Oumerachi (◇) slam coefficient models.

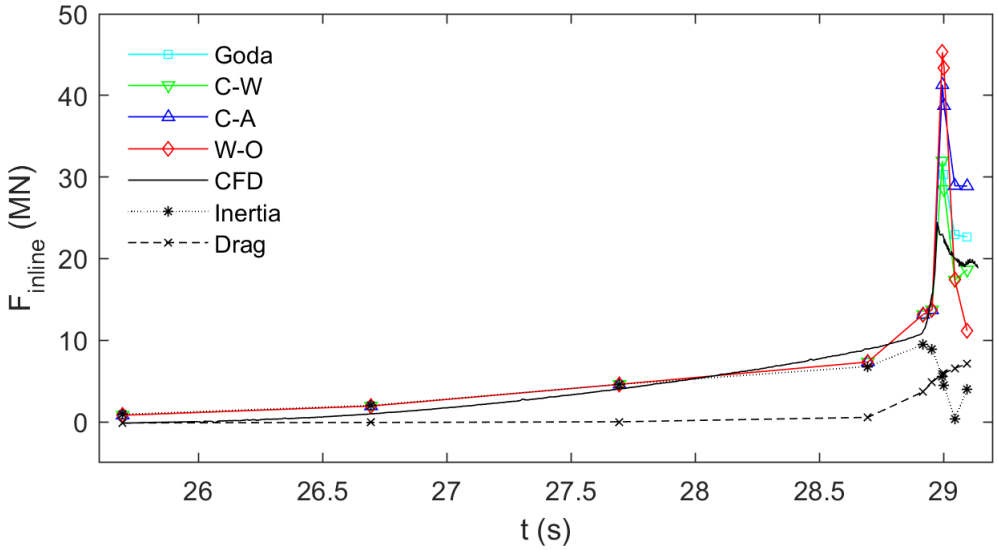

Figure 3.19. Inline force time history for case 2 (10 MW monopile), including CFD total force (−), predicted inertia and drag (dashed ∗ and ×), and predicted total force using Goda (□), Campbell-Weynberg (▽), Cointe-Armand (△), and Wienke-Oumerachi (◇) slam coefficient models.

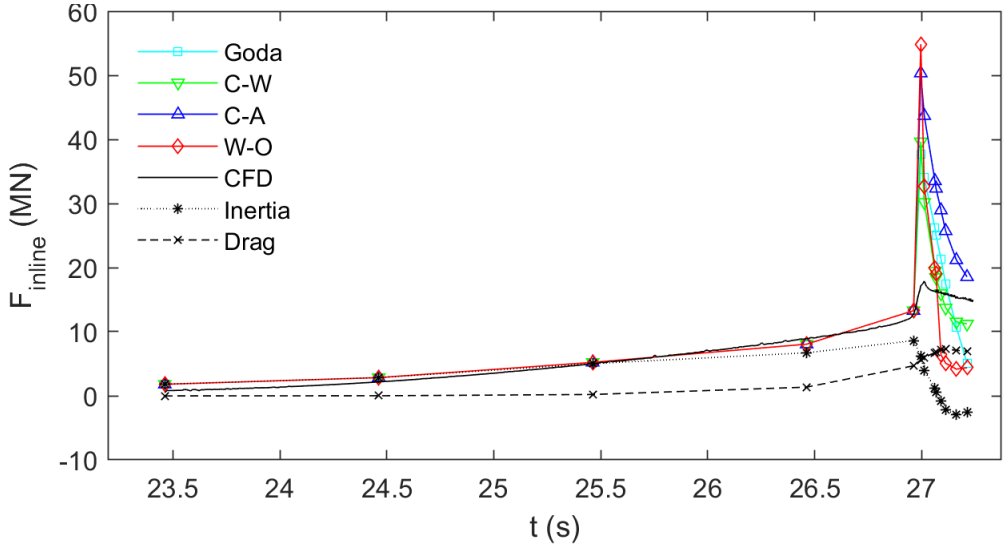

Figure 3.20. Inline force time history for case 3 (10 MW monopile), including CFD total force (−), predicted inertia and drag (dashed ∗ and ×), and predicted total force using Goda (□), Campbell-Weynberg (▽), Cointe-Armand (△), and Wienke-Oumerachi (◇) slam coefficient models.

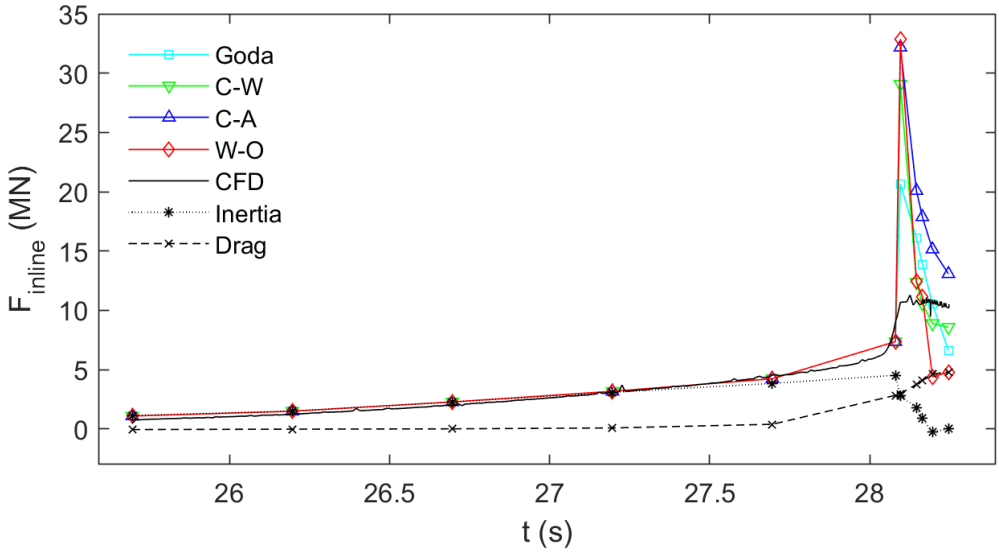

Figure 3.21. Inline force time history for case 4 (5 MW monopile), including CFD total force (−), predicted inertia and drag (dashed ∗ and ×), and predicted total force using Goda (□), Campbell-Weynberg (▽), Cointe-Armand (△), and Wienke-Oumerachi (◇) slam coefficient models.

At impact, all four slam coefficient models predict a higher peak total force than the CFD model, although Goda is the closest with the lowest peak slam coefficient (see Figures 3.18–3.21). This could partially be caused by numerical dispersion in the wave crest in the CFD simulations, where the fast-moving crest is artificially spread out (see Figure 3.17) which causes the slam force to be lower in magnitude but longer in duration.

After the initial impact, the four slam models vary significantly due to their different slam durations (see Figures 3.18–3.21). For example, the W-O slam model tends to predict a total force lower than the CFD force after the initial impact due to its short slam duration, while the C-A slam model tends to predict a higher post-impact force than the CFD, due to C-A's longer slam duration.

Of the four CFD simulations, some feature a distinct slam force more clearly than others. In particular, case 2 most clearly displays a sharp slam force (Figure 3.19), and a smaller slam force is also evident in case 3 (Figure 3.20). Cases 1 and 4 (Figures 3.18 and 3.21) also show a sharp increase in force when the wave front impacts the

structure, although it does not decay quickly after impact as would be expected with a slam force. However, this increase in force is only partially captured using drag and inertia models alone, indicating that some slam force is present.

The differences in CFD force time history between the four simulated waves are strongly dependent on wave structure at the time of impact. As shown in Table 3.6, the four waves are extremely similar just before breaking. However, the waves are still in the process of breaking when they impact the structures; the stage of breaking has a significant effect on the force. As discussed in Section 3.4.2, cases 2 and 3 are farther along in the breaking process than cases 1 and 4, so that more of the crest is moving as a vertical wall of water (see Figure 3.12). This creates the more distinct slamming force peak, and is consistent with the idea that the highest force occurs when the crest has turned into a vertical wall of water impacting the cylinder [47].

3.4.3.3 Comparison of slam coefficients

To gain additional insight into how the slam coefficient models compare to each other and to the CFD results, a CFD-based slam coefficient $C_s(t)$ is calculated for each case using the total CFD force and the predicted drag and inertia forces. Figure 3.22 plots the slam coefficient time histories for the four slam coefficient models (colored curves) alongside the CFD-based $C_s(t)$ (black circles). Markers indicate the times where drag and inertia forces are calculated, limited to the times of recorded snapshots of the CFD fluid velocity $u(z,t)$.

As illustrated in Figure 3.22, none of the four models for $C_s(t)$ capture the CFD force beyond the predicted drag and inertia terms well. Cases 3 and 4 in particular feature a sustained, slightly increasing CFD force beyond the initial time of impact. None of the four $C_s(t)$ models fit this shape, likely because the sustained CFD force is caused less by the slamming impact and more due to a continued imbalance in surface elevation across the cylinder. This sustained elevated force can also be seen for all

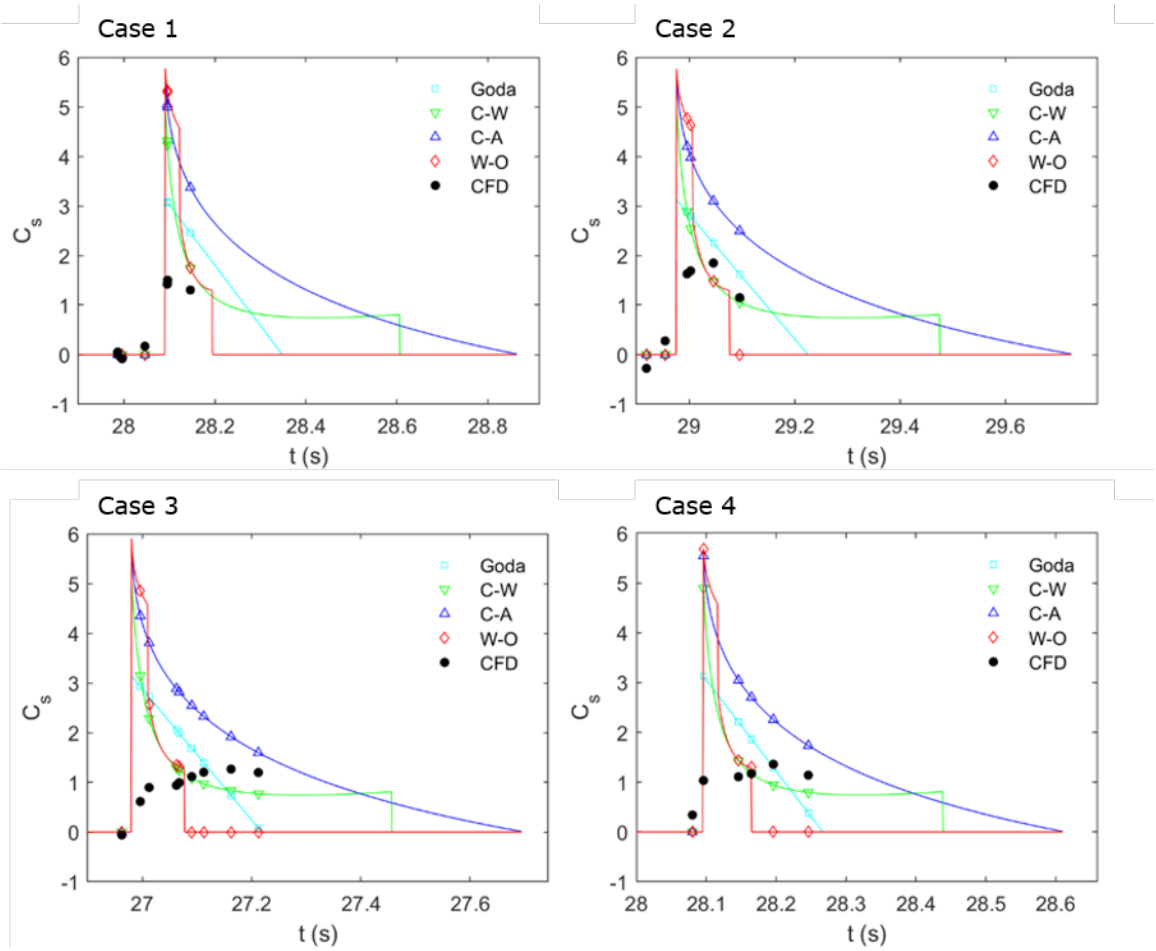

Figure 3.22. Slam coefficient time histories for all four breaking wave force cases, calculated using the Goda (□), Campbell-Weynberg (▽), Cointe-Armand (△), and Wienke-Oumerachi (◇) models, as well as based on the CFD total force (●).

the simulated waves (see Figures 3.18–3.21), even those with identifiable slam force (see Figures 3.19–3.20). Improved models for drag and inertia, or perhaps adding an additional term to the Morison force equation, may address this portion of the force better than any slam-focused model.

Aside from the shape of the slamming coefficient time history, the maximum total force should also be accurately predicted by the slamming coefficient models when used in conjunction with the Morison equation. However, as noted in Figures 3.18–3.21), the maximum CFD total force is significantly below the predicted peak force using the four slam models, even for the simulations with clear slam forces. Table 3.8

Table 3.8. Comparing maximum values for CFD total force, CFD slam force, and predicted slam force. Slamming coefficient and single fit parameter λC_s are reported based on CFD slam force. Values in parentheses are relative to CFD slam force.

Case	CFD F (MN)	CFD F_S (MN)	Goda F_S (MN)	C-W F_S (MN)	C-A, W-O F_S (MN)	CFD C_S, λ=0.4	CFD λC_S
1	22.00	11.81	22.41 (1.9x)	36.74 (3.1x)	44.82 (3.8x)	1.66	0.662
2	24.49	11.95	22.34 (1.9x)	36.62 (3.1x)	44.67 (3.1x)	1.68	0.673
3	17.88	7.96	27.87 (3.5x)	45.68 (5.7x)	55.73 (5.7x)	0.897	0.359
4	11.30	5.67	14.98 (2.6x)	24.56 (2.6x)	29.97 (4.3x)	1.19	0.476

compares the peak inline force for the total CFD force, the CFD slam force based on interpolated values for the predicted drag and inertia, and the predicted slam force using all four slamming coefficient models. The ratio between the predicted slam force and the CFD slam force is reported in parentheses for each model and each simulated wave.

A CFD-based maximum C_s is also included in Table 3.8, based on the peak CFD C_s using the same λ=0.4 used throughout this research. The last column in Table 3.8 factors out the curling factor λ to give a single dimensionless parameter λC_s that is theoretically constant across all waves.

As Table 3.8 illustrates, all four models predict a peak slam force several times larger than the CFD peak slam force. Goda is the closest to the peak CFD slam force, followed by Campbell-Weynberg, followed by Cointe-Armand and Wienke-Oumerachi.

3.4.3.4 Limitations of existing slam models

As indicated in Table 3.8 as well as Figures 3.18–3.22, the existing slam models significantly disagree with the simulated forces for these four breaking waves. According to the CFD peak slam forces, a lower value for the peak C_s should be used (see Table 3.8), or perhaps a lower value for the factor λC_s since very little guidance is given on the curling factor. The variation in the peak λC_s across the four simulated

waves indicates that one or more important factors are neglected in the existing slam model formulations.

For instance, cylinder runup is not explicitly accounted for in the existing slam models, although it is present in all four simulations (see Figure 3.17). Using the horizontal velocity $u(z,t)$ and acceleration $a(z,t)$ as measured at the cylinder leading edge (rather than the cylinder center) for Morison drag and inertia does capture the effect of runup acceptably, at least before wave impact, as shown in Figures 3.18–3.21. However, the effects of runup post-impact could explain the sustained elevated force post-impact observed in all four simulated waves. None of the four existing models for slam capture this effect, as shown in Figures 3.18–3.22.

Additionally, the existing slam models assume the breaking wave is a plunging breaker, with the moment of impact occurring when the wave front is vertical. While this scenario produces the highest peak force, it does not address breaking waves at other stages of breaking, as reflected in Table 3.8 and Figures 3.18–3.22.

Overall, these CFD simulations indicate that the existing slam force models provide a strongly conservative prediction for the peak inline force due to breaking waves. However, the predicted time history of the total breaking force could be further improved by including runup effects. These four slam force models in conjunction with traditional Morison drag and inertia do not account for the variety of breaking wave shapes and impact timings, but provide a conservative estimate for most breaking waves.

3.5 Summary and conclusions

In summary, four breaking wave limits and four slam force models are evaluated using CFD simulations of breaking waves with characteristics representative of potential East Coast offshore wind energy sites. The CFD model used in the simulations is first developed in a series of validation and verification studies, including wave gen-

eration and absorption, wave shoaling and breaking, and wave forces on a cylinder. In the first component of this research, four breaking wave limits (McCowan, Miche, Battjes, and Goda) that predict if a wave will break are evaluated using thirty-nine CFD simulations of shoaling and breaking waves. In the second component of this research, four slam force models (Goda, Campbell-Weynberg, Cointe-Armand, and Wienke-Oumerachi) that predict the force on a cylinder due to breaking waves are evaluated using four CFD simulations of waves shoaling and breaking on monopiles designed for 5 and 10 MW OWTs.

When examining the breaking wave limits, this research concludes that:

- The Goda limit is the most accurate breaking limit for low seafloor slopes ($s < 8\%$), which are common at East Coast sites suitable for fixed-bottom offshore wind farms.
- The Miche and Battjes limits are acceptable conservative alternatives that perform reasonably for a wider range of seafloor slopes.
- Simple modifications to the Goda and Battjes limits do not yield improved overall performance.
- The performance of each limit depends on how the wave height and wavelength are measured in an asymmetric shoaling wave.

Regarding the force predictions from slam force models, this research indicates that:

- All four slam force models are conservative and assume the "worst case" shape for the breaking wave during impact. Less conservative models should account for different wave shapes during impact by adjusting the value of λC_S.
- When predicting peak impact force, the Goda slam model is generally the least conservative, while the Cointe-Armand and Wienke-Oumerachi slam models are generally the most conservative.

- All four slam force models do not capture the total force time history well after the initial impact, potentially due to neglecting the effects of runup on the monopile.

In conclusion, this work indicates that the Goda breaking wave limit should be used to predict if a wave will break for seafloor slopes less than 8%, and the Battjes limit should be used to conservatively predict if a wave will break for seafloor slopes greater than 8%. Furthermore, the Wienke-Oumerachi or Cointe-Armand slam force models are good choices for highly conservative predictions of the peak impact force due to a breaking wave.

CHAPTER 4

WAKE CHARACTERISTICS FOR FLOATING TURBINES

Wind turbine wake effects can decrease power generation and increase turbine loads in wind farm arrays. A better understanding of floating OWT wake physics allows for improved engineering wake models used in design. Wakes of floating OWTs are particularly complex because they are generated by a rotor that moves with the floating platform. This research examines how downstream wake characteristics differ between fixed and floating turbines, and specifically how these differences depend on floating platform type and environmental conditions.

Floating OWT wakes are difficult to accurately model, due in part to the coupled nature of floating OWT rotor aerodynamics and platform motion. To meet this challenge, LES coupled with reasonable platform motions are increasingly used to study floating OWT rotor aerodynamics and wakes [14, 95, 96]. For instance, Wang *et al.* [95] compared LES to experimental results for the wake of a multi-turbine platform with prescribed motion. Lyu *et al.* [64] also used LES to briefly examine floating OWT behavior for prescribed motion. However, this type of study is limited by prescribed platform motion, which only partially captures the aerodynamic-platform coupling. An improved approach is demonstrated by Lee *et al.* [14], where the responses of waked downwind floating OWTs are examined using LES coupled to a turbine dynamics solver.

Floating OWT wake behavior depends on environmental conditions, just like fixed-bottom turbine wakes. However, most current studies of floating OWT wakes do not thoroughly examine the effects of environmental conditions like wind speed, wave

height, or wind-wave alignment, regardless of methodology [15, 97]. Although existing studies examine how platform type affects floating OWT loads and rotor aerodynamics (see [15, 98–100]) and how atmospheric stability affects onshore turbine wakes (see [55, 101–103]), the effects of platform type and atmospheric stability on floating OWT wakes require further study, particularly in the mid-to-far wake where downstream turbines would typically be placed.

In this research, the wake of a floating OWT is simulated with high-fidelity LES in the Simulator fOr Wind Farm Applications (SOWFA), coupled to the turbine simulator OpenFAST using an ALM. Wake characteristics are compared among a fixed-bottom turbine, a spar floating OWT, and a semisubmersible floating OWT for different wind speeds, wave heights, wind-wave alignments, rotor yaw angles, and atmospheric stability conditions.

4.1 Numerical models

Wakes of individual floating OWTs are simulated in SOWFA [104], a CFD tool developed by the National Renewable Energy Laboratory (NREL) based on the OpenFOAM v2.4 toolbox [105]. The SOWFA simulations of the wake and surrounding ABL flow include an ALM for the turbine rotor, loosely coupled with NREL's aeroelastic turbine simulator OpenFAST v1.0.0 [106] for the motion of the rotor, tower, and platform. OpenFAST's submodules model the effects of the hydrodynamics, mooring lines, and turbine controllers on the turbine motion. The SOWFA-OpenFAST model used in this work is briefly described below, with a more extensive description provided by Churchfield *et al.* [55]. Past validation and verification of the SOWFA framework includes recent work by Doubrawa *et al.* [107], Martínez-Tossas *et al.* [108], Mirocha *et al.* [109], and Churchfield *et al.* [110], with Fleming *et al.* [12] summarizing prior efforts.

4.1.1 Simulation workflow

The wake simulation workflow in this study consists of three main steps. First, LES of the ABL is performed using SOWFA for a large domain with no turbine, which develops the wind shear profile and large turbulent structures within the ABL. Second, this "precursor" simulation is continued for additional simulation time, which generates and records boundary condition time histories. Third, LES of the turbine wake is performed using SOWFA, coupled to OpenFAST via the rotor ALM. This third SOWFA simulation is initialized using ABL flow field data generated by the first step and uses the boundary condition histories generated during the second step. Figure 4.1 illustrates this three-step workflow, which is is similar to that used by Lee *et al.* [14], among other studies.

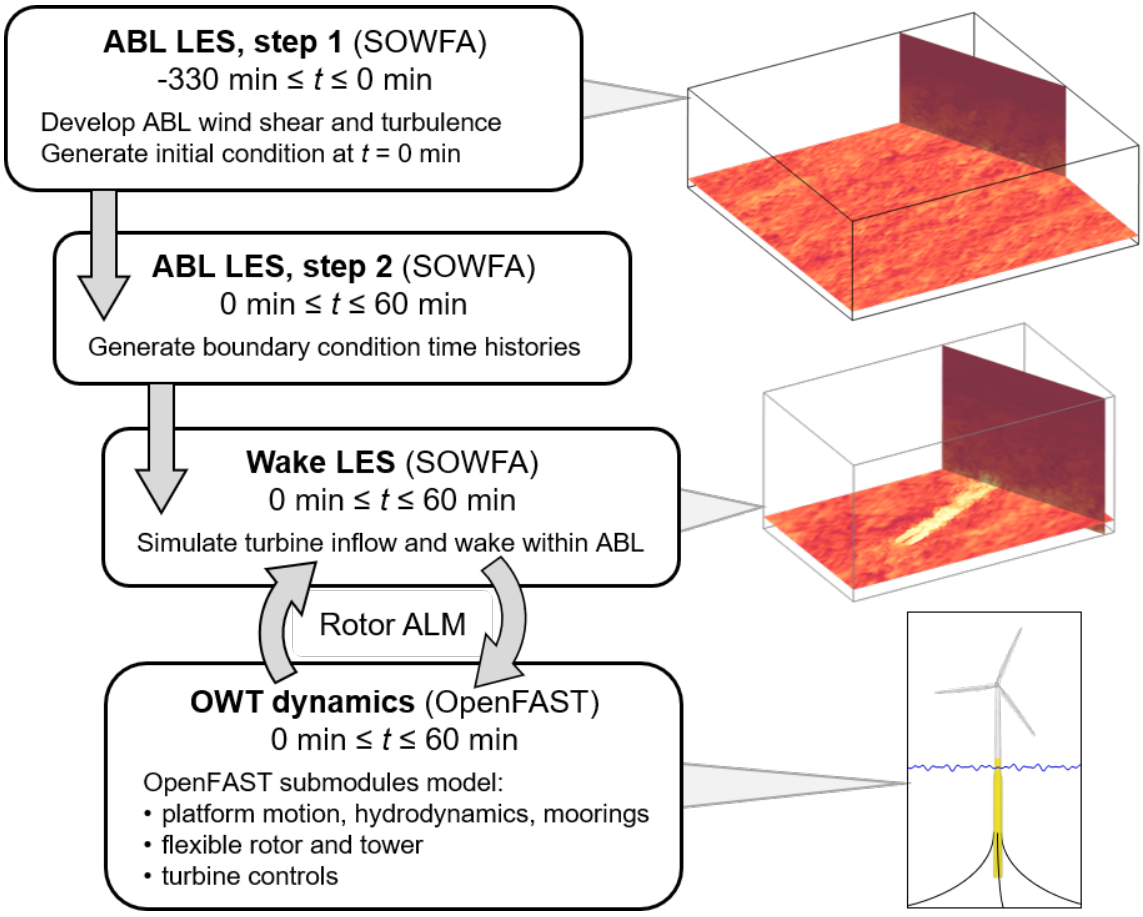

Figure 4.1. Three-step workflow for LES of turbine wakes within the atmospheric boundary layer, coupled to floating turbine motions through an actuator line model.

4.1.2 SOWFA

SOWFA solves the filtered incompressible Navier-Stokes equations using a finite-volume method. The momentum equations include Coriolis effects due to the Earth's rotation and incorporate buoyancy effects using the Boussinesq approximation, adding a temperature transport equation [55]. The PISO algorithm [111] is used with Rhie-Chow interpolation [112] to avoid pressure-velocity decoupling. The Deardorff-Lilly one-equation model [113] is used as the LES subgrid-scale model.

The lower boundary is treated using the rough-wall shear stress model of Schumann [114]. Monin-Obukhov similarity theory is used [115] to relate the friction velocity to the flow adjacent to the surface, the surface roughness height z_0, and the surface heat flux, as is common practice in ABL LES [55]. The upper boundary is located in the geostrophic region above the ABL and is therefore modeled as a stress-free, rigid lid. The four side boundary conditions are laterally periodic for precursor ABL simulations, but are inflow or outflow for turbine-wake simulations. The inflow values are based on the recorded boundary conditions from the precursor ABL simulations, while a zero normal gradient condition is used for outflow boundaries.

4.1.3 Actuator line model

For the turbine-wake simulations, the ALM of Sørenson and Shen [68] is used to model each turbine blade as a line of distributed forces. The drag and lift forces are projected onto the LES flow field as body forces in the momentum equation, using a 3D Gaussian kernel at each blade line element. The width of this Gaussian projection is set to slightly more than twice the local cell size to maintain numerical stability, as Troldborg [116] and Churchfield *et al.* [55] recommend.

The traditional turbine ALM models how the rotor influences the LES flow, but does not account for the effects of the tower or nacelle. However, work by Santoni *et al.* [72] indicates that including tower and nacelle models can moderately affect the

wake up to $6D$ downstream, although their unusually large nacelle may exaggerate the importance of the tower and nacelle. To account for these effects, SOWFA has the capability to include ALM-based tower and nacelle models as described by Churchfield *et al.* [71]. A preliminary study conducted for 8 m/s hub-height wind speed and a fixed platform indicates that the SOWFA tower and nacelle models significantly influence only the near wake, with little effect by $4D$ downstream. Although these models could use improvement [71] and do not appear to affect the far wake, these simulations implement SOWFA's ALM-based tower and nacelle models, in addition to the traditional ALM rotor model.

4.1.4 OpenFAST

In the coupled SOWFA-OpenFAST turbine simulations, OpenFAST computes the time-varying motion of the turbine blades, tower, and platform. The structural dynamics of the flexible blades and tower are modeled with the ElastoDyn submodule, while variable-speed and blade-pitch control is included using the ServoDyn submodule. The rotor yaw degree of freedom is disabled so that the rotor yaw angle can be set without depending on a yaw controller. The HydroDyn submodule models the hydrodynamic loading on the platform, while the mooring lines are modeled with the MoorDyn submodule. Additional details on the underlying OpenFAST solvers are described by Jonkman and Buhl [117], and in the OpenFAST documentation [118].

4.2 Simulation setup

4.2.1 Platform types

This study simulates the NREL 5 MW reference turbine (diameter D=126 m, hub height z_{hh}=90 m, rated wind speed 11.4 m/s, and shaft tilt ϕ_t=5°) [119] mounted on two floating platforms: the OC3-UMaine spar [98] and the OC4-DeepCWind semisubmersible [120] (see Figure 2.1). The OC3-UMaine spar is identical to the OC3-Hywind

spar [121], but with the catenary mooring lines adjusted to match the semisub's water depth of 200 m [98]. For comparison, an equivalent fixed-bottom turbine is also simulated by disabling all platform degrees of freedom to remove any foundation motion or deflections.

4.2.2 Environmental conditions

The OWTs are simulated for various combinations of environmental conditions. Common attributes across the simulations include unidirectional, irregular JONSWAP waves and sheared, turbulent wind from the southwest. The OWTs are simulated for two different atmospheric stability conditions: neutral and stable.

4.2.2.1 Neutral atmosphere

First, a neutral atmosphere is simulated with no surface cooling and a strong capping inversion at an elevation of z=750 m. The surface roughness height z_0 is based on the Charnock model with α=0.011, as recommended by International Electrotechnical Commission standard 614000-3 [122]. This z_0 model is selected because preliminary studies indicate that it creates turbulence intensities at z=90 m (hub height) and z=30 m that best match those measured at the FINO1 platform [123].

Two different hub-height wind speeds are examined for these neutral conditions, U_{hh}=8 m/s and U_{hh}=15 m/s, requiring two different neutral precursor ABL simulations. The wind shear and temperature profiles for both neutral precursor ABL simulations are shown in Figure 4.2.

4.2.2.2 Stable atmosphere

Second, a stable atmosphere is also simulated with a surface cooling rate of 0.25 K/h and an initial temperature inversion starting at z=250 m, based on the canonical GABLS1 case, as described by Beare *et al.* [124] but with the initial inversion

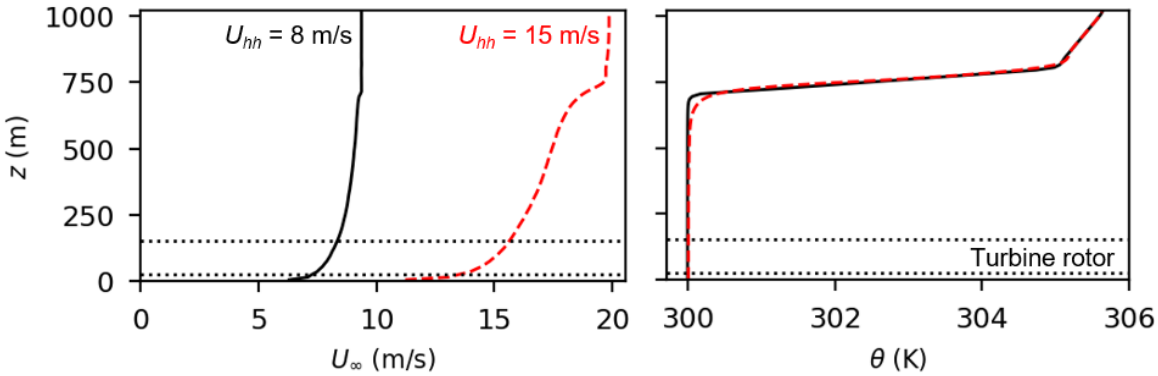

Figure 4.2. Horizontally averaged wind speed U_∞ and potential temperature θ plotted against elevation z for neutral simulations with hub-height wind speeds U_{hh} of 8 m/s (—) and 15 m/s (– –). The turbine rotor location is marked by dotted horizontal lines.

raised above the rotor disk. The surface roughness height is identical to the neutral atmosphere simulations.

Only a hub-height wind speed of U_{hh}=8 m/s is simulated for the stable atmosphere. As shown in Figure 4.3, the stable atmosphere exhibits higher wind shear, higher wind veer, and lower turbulence intensity across the rotor disk than the neutral atmosphere with the same wind speed. Figure 4.3 compares the neutral and stable atmospheres for U_{hh}=8 m/s, showing the vertical profiles of the potential temperature θ, free-stream horizontal wind speed U_∞, free-stream horizontal wind direction, and turbulence intensity (TI), averaged over time and across the domain.

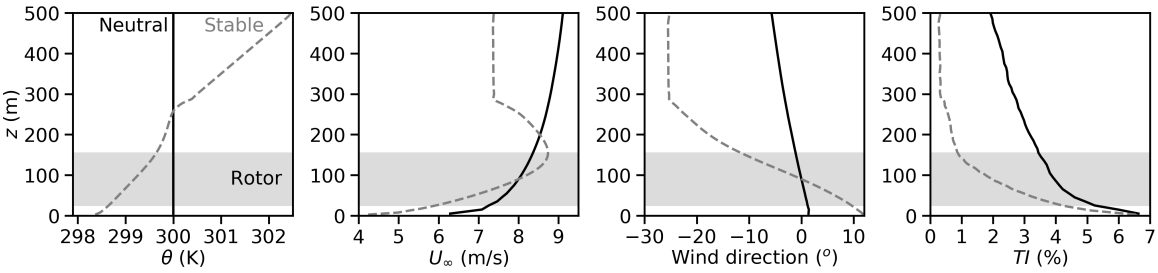

Figure 4.3. Potential temperature, wind speed, wind direction, and turbulence intensity plotted against elevation for neutral (—) and stable (– –) atmosphere simulations with U_{hh}=8 m/s, averaged over time and across the domain. The shaded region indicates the rotor disk elevation.

4.2.3 Simulated domains

The size and mesh resolution of each CFD domain depends on if the simulation is a precursor or turbine-wake simulation, and on if atmospheric stability is neutral or stable. The neutral precursor simulations develop the neutral ABL over 5.5 hours, in a 3 km by 3 km by 1.02 km domain on a 10 m uniform cubic mesh, for a total of 9.2 million cells. The stable precursor simulations develop the stable ABL over 10 hours in a 2 km by 2 km by 0.5 km domain on a 5 m mesh, for a total of 16 million cells.

For the turbine-wake simulations, the neutral domain size is reduced to 2 km by 1–1.2 km by 1.02 km with a base cell size of 10 m, to reduce computational cost. The stable domain size is likewise reduced to 2 km by 1 km by 0.5 km, with a base cell size of 5 m. For both the neutral and stable turbine-wake simulations, a wake refinement region at 2.5 m resolution extends from $4D$ upstream to $10.3D$ downstream of the turbine. Also, a rotor refinement region at 1.25 m resolution extends from $0.5D$ upstream to $1.5D$ downstream. The rotor, wake, and base resolutions are comparable to those used in other SOWFA studies [12–14, 55, 125]. For these simulations in particular, halving the cell size in the wake refinement region has negligible effects on the floating turbine wakes, although small changes in the resolved turbulent kinetic energy are observed. In total, the neutral and stable turbine simulation cell counts are 18.3 and 23.8 million cells, respectively.

Figure 4.4 illustrates the key features of the CFD domains, using the neutral precursor and turbine-wake simulations as an example. Figure 4.4 includes slices through the turbine-wake domain mesh at the rotor plane (for 0° rotor yaw) and at hub height, colored by instantaneous velocity magnitude. For all simulations, the domain sides and Cartesian mesh are aligned with the cardinal directions, while the average wind U_∞ blows from the southwest at 245° (measured clockwise from north). This means that the precursor's lateral periodic boundaries are not aligned with the wind direction, to avoid spurious periodicity. The coordinate system is defined so

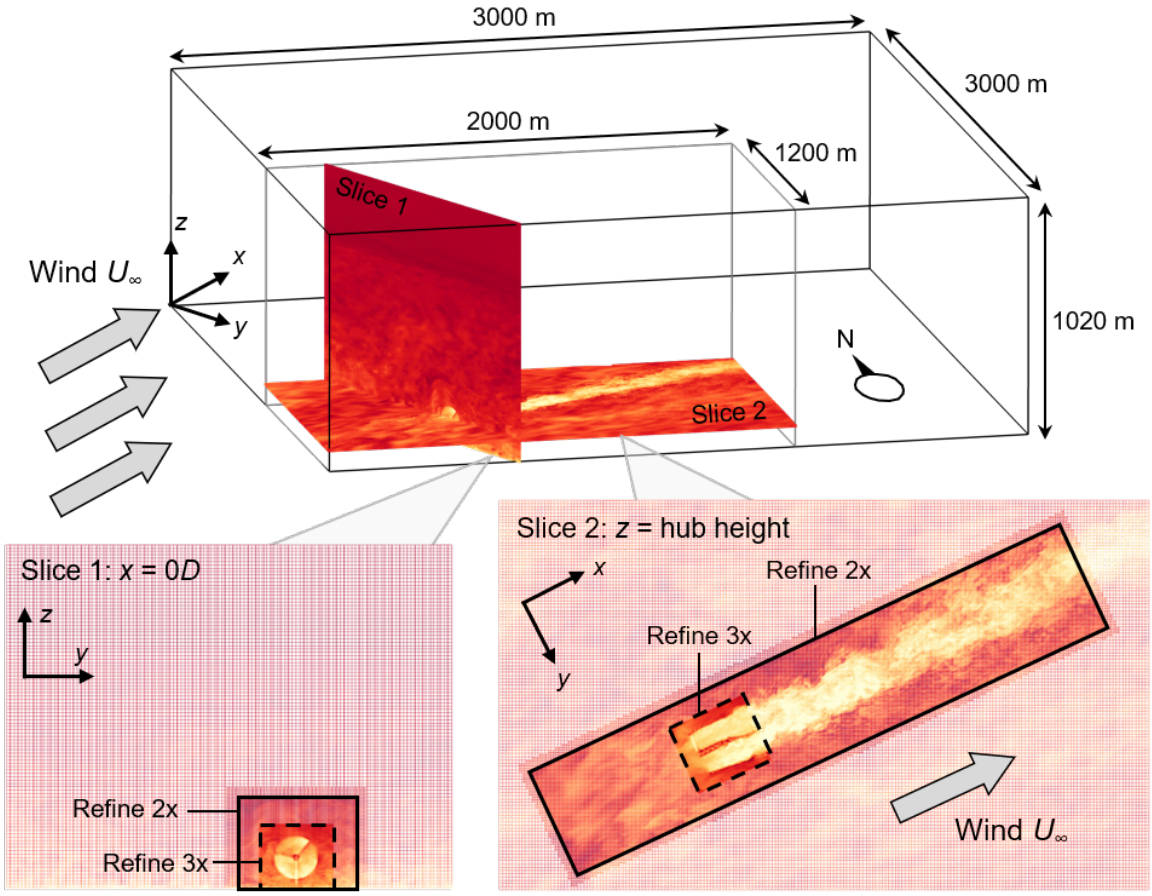

Figure 4.4. Domains for the ABL simulations (3 km by 3 km by 1.02 km) and SOWFA-OpenFAST turbine-wake simulations (2 km by 1.2 km by 1.02 km), with an average wind direction from the southwest. For the turbine-wake domain, mesh slices colored by instantaneous wind speed are shown at the rotor plane ($x = 0D$) and at hub height, including wake and rotor refinement regions (solid and dashed boxes).

that the x axis is aligned with the average wind flow U_∞, the y axis is aligned with the rotor plane (for 0° rotor yaw), and the z axis points in the upward direction.

4.2.4 Case descriptions

Two groups of turbine-wake simulations are performed. First, the spar and fixed-bottom OWTs are compared in a neutral atmosphere, for different wind speeds, wave heights, wind-wave alignments, and rotor yaw angles. Second, spar, semisub, and fixed-bottom OWTs are compared in neutral and stable atmospheres, for a single combination of wind speed/wave height/wind-wave alignment/rotor yaw angle.

For the first group of cases, the wind speeds are either U_{hh}=8 m/s or 15 m/s, representing below-rated or above-rated operating conditions. The significant wave heights are either H_s=4 m or 8 m, with peak spectral periods of T_p=10 s and 14 s, respectively. Wind-wave alignments of α=0° and 30° are also compared. Finally, rotor yaw angles of $\phi_y = 0°$ and 10° are compared. The nacelle yaw angle is held constant at the nominal yaw, but variations in wind direction and platform yaw motion cause the instantaneous wind-rotor alignment to fluctuate about this average angle.

In this first group, starting with a baseline floating OWT simulation with U_{hh}=8 m/s, H_s=8 m, α=0°, and ϕ_y=0°, eight cases allow each parameter – wind speed, wave height, wind-wave alignment, and rotor yaw – to be studied individually. Table 4.1 enumerates each case in this first group.

For the second group of cases, all simulations use U_{hh}=8 m/s, H_s=8 m, α=25°, and ϕ_y=0°. This combination represents conditions most likely to accentuate wake differences between fixed and floating turbines. In this second group, wake characteristics are compared across spar, semisub and fixed-bottom turbines in both the neutral and stable atmospheres. Table 4.1 also lists the cases in this second group.

4.3 Simulation results

To understand how environmental conditions and platform type affect the differences between fixed and floating OWT wakes, each floating case in Table 4.1 is compared to the equivalent fixed-bottom case. The wake and turbine behavior are examined after discarding the initial 10 minutes of transient behavior, producing 50 minutes of usable data for the first group of cases and 60 minutes for the second group.

Table 4.1. Summary of cases for two groups of turbine-wake simulations.

Case	Platform	Atmosphere	U_{hh} (m/s)	H_s (m)	α (°)	ϕ_y (°)
1.1	Fixed	Neutral	8	–	–	0
1.2	Spar	Neutral	8	8	0	0
1.3	Spar	Neutral	8	4	0	0
1.4	Spar	Neutral	8	8	30	0
1.5	Fixed	Neutral	8	–	–	10
1.6	Spar	Neutral	8	8	0	10
1.7	Fixed	Neutral	15	–	–	0
1.8	Spar	Neutral	15	8	0	0
2.1	Fixed	Neutral	8	–	–	0
2.2	Spar	Neutral	8	8	25	0
2.3	Semisub	Neutral	8	8	25	0
2.4	Fixed	Stable	8	–	–	0
2.5	Spar	Stable	8	8	25	0
2.6	Semisub	Stable	8	8	25	0

4.3.1 Platform displacements

The nuances of platform motion are key to understanding how floating platforms affect wakes. In addition to the inherent time-varying motion, non-zero mean displacements of floating platforms also affect the wake. Figure 4.5 summarizes the platform displacements for all floating cases in the first group. The time-averaged displacement is reported, as well as the root-mean-square (RMS), minimum, and maximum of the time-varying displacement, for each degree of freedom.

In Figure 4.5, the large mean surge and pitch displacements are caused by the rotor aerodynamic thrust, which increases with wind speed. As expected, the smaller wave height produces less time variation (smaller RMS) in all degrees of freedom. Also, the larger wind-wave misalignment increases the time variation (larger RMS), especially in sway, roll, and yaw.

Figure 4.6 similarly shows platform displacements for the second group of cases, and also includes rotor center displacements (Δx_{RC}, Δy_{RC}, Δz_{RC}). For each floating

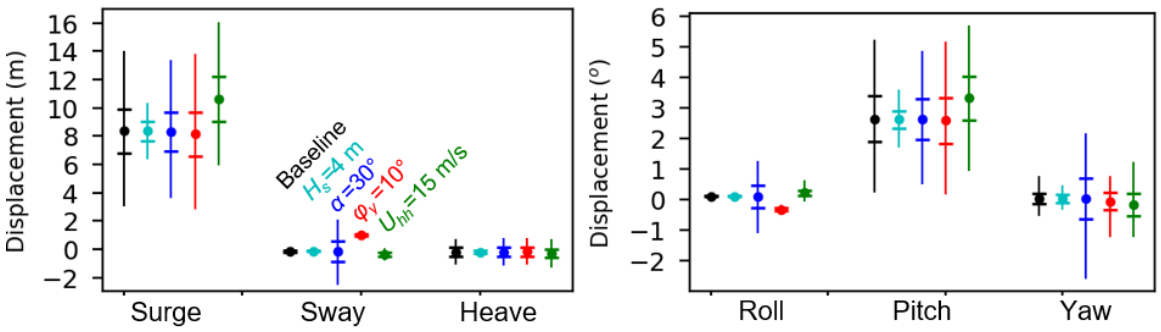

Figure 4.5. Floating platform displacements in each degree of freedom, including displacement mean (circles), root-mean-square (−), and minimum-maximum (vertical lines). The baseline floating simulation (case 1.2 in Table 4.1) is compared to the other floating cases in the first group.

case, the time-averaged displacement is again reported alongside the RMS, minimum, and maximum of the displacement time history.

Comparing the spar to the semisub (for a neutral atmosphere) in Figure 4.6, the spar exhibits a larger mean surge, larger mean pitch, larger yaw RMS, and smaller heave RMS than the semisub. Although the spar and semisub have similar surge and pitch RMS, the phasing of these motions differs significantly between the two platforms. Surge and pitch are in phase for the spar but out of phase for the semisub, so that the spar Δx_{RC} RMS is more than twice the semisub RMS. The spar and

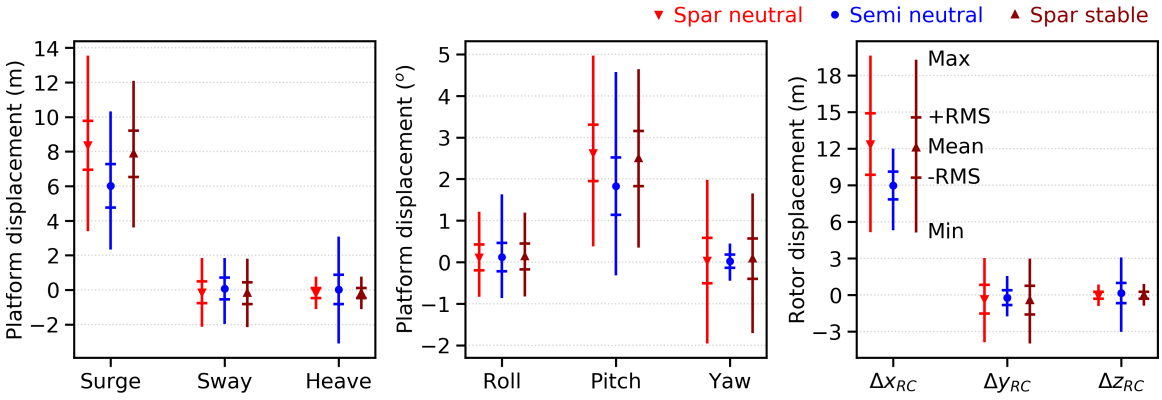

Figure 4.6. Floating turbine displacements for spar neutral (▼), semisubmersible neutral (●), and spar stable (▲) cases from the second group. The mean (symbols), root-mean-square (−), and minimum/maximum (vertical lines) are shown for six platform motions as well as rotor center displacements.

semisub also have similar sway and roll RMS values, but the spar's larger yaw RMS causes a larger Δy_{RC} RMS because the rotor center is offset from the yaw axis. The spar's smaller heave RMS translates directly into smaller Δz_{RC} RMS.

Comparing the neutral atmosphere to the stable atmosphere (for the spar) in Figure 4.6, the stable atmosphere creates slightly smaller RMS variations in most degrees of freedom, as expected for the stable atmosphere's lower turbulence intensity. The neutral mean surge and pitch are slightly larger than the stable mean values, but the mean displacements are generally similar between the neutral and stable atmospheres. The overall similarity in platform displacements between the neutral and stable atmospheres indicates that atmospheric stability plays little role in platform motion for these conditions.

4.3.2 Time-averaged wake characteristics

Wakes are typically characterized by the streamwise velocity deficit $U_d = U - U_\infty$ as well as increased turbulent kinetic energy (TKE). The time-averaged results for these quantities are presented in this section, for both groups of cases.

4.3.2.1 Wake characteristics for cases 1.1–1.8

Figures 4.7 and 4.8 plot the wake velocity deficit U_d against elevation z and cross-stream coordinate y at downstream locations of x/D=1, 3, 6, and 9, for the first group of cases. The top row compares the fixed-platform case with U_{hh}=8 m/s and 0° yaw (case 1.1) to similar floating-platform cases (cases 1.2–1.4) with different wave heights H_s and wind-wave alignments α. The middle row compares the fixed and floating cases with U_{hh}=8 m/s and 10° yaw (cases 1.5–1.6). The bottom row compares the fixed and floating cases with U_{hh}=15 m/s and 0° yaw (cases 1.7–1.8).

As expected, all wake deficits recover with downstream distance, with the higher wind speed cases recovering faster, partially due to their slightly higher ambient turbulence intensities TI_{hh} and lower thrust coefficients C_T. The deficit profiles in

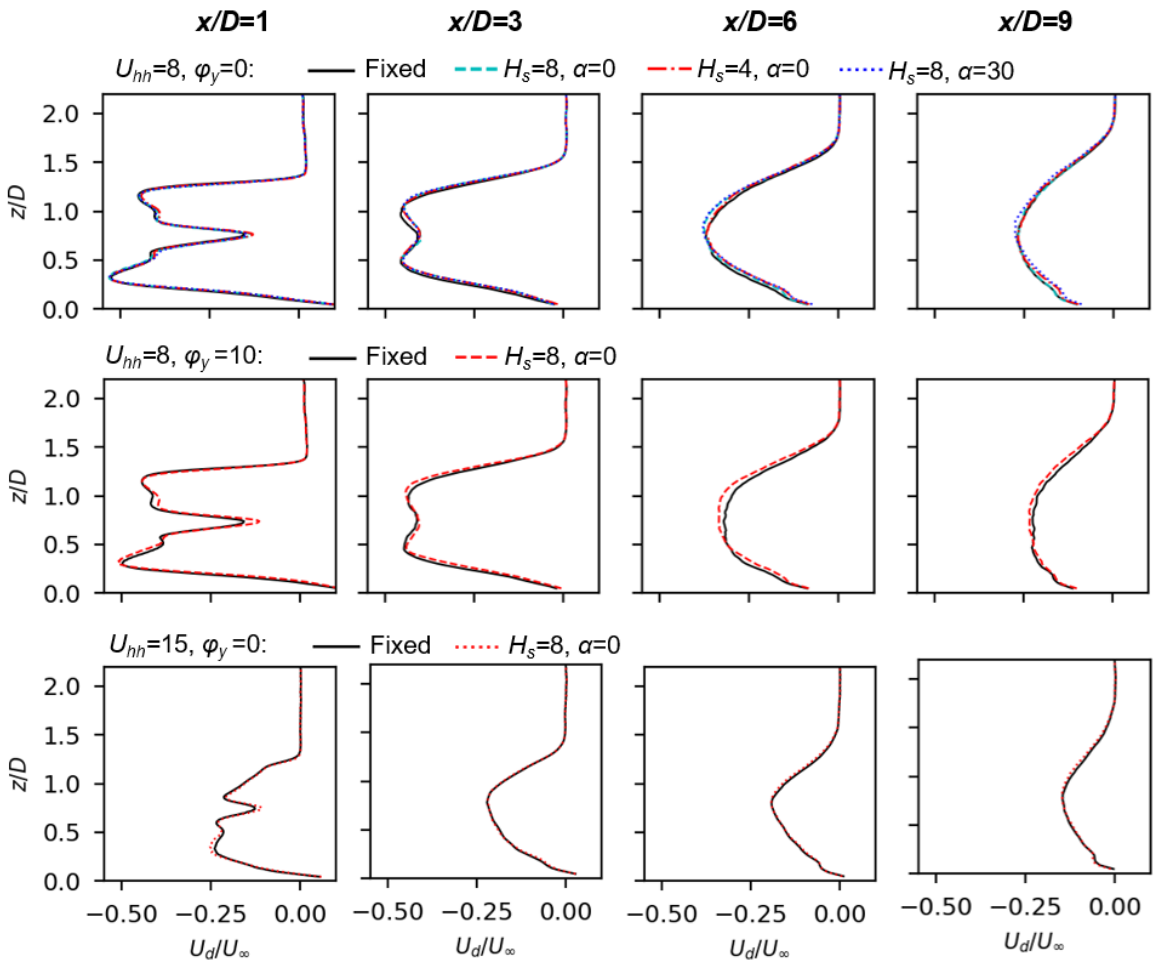

Figure 4.7. Temporally averaged wake velocity deficit U_d plotted against elevation z at different downstream locations x. Fixed and floating platforms are compared for different wave heights H_s (top), wind-wave alignments α (top), rotor yaw angles ϕ_y (middle), and wind speeds U_{hh} (bottom).

the yawed cases are slightly distorted due to the wake veer caused by the yawed rotor, as expected. In general, floating- and fixed-platform wakes are very similar in shape. As illustrated in Figure 4.8, the floating-platform wake deficits are nearly identical to the fixed-platform wake deficits in the cross-stream direction, especially as the distance downstream increases. However, the wake deficit elevation profiles in Figure 4.7 show that the floating-platform wakes are generally deflected upward compared to the fixed platform, though this effect is reduced for higher wind speeds or lower wave heights.

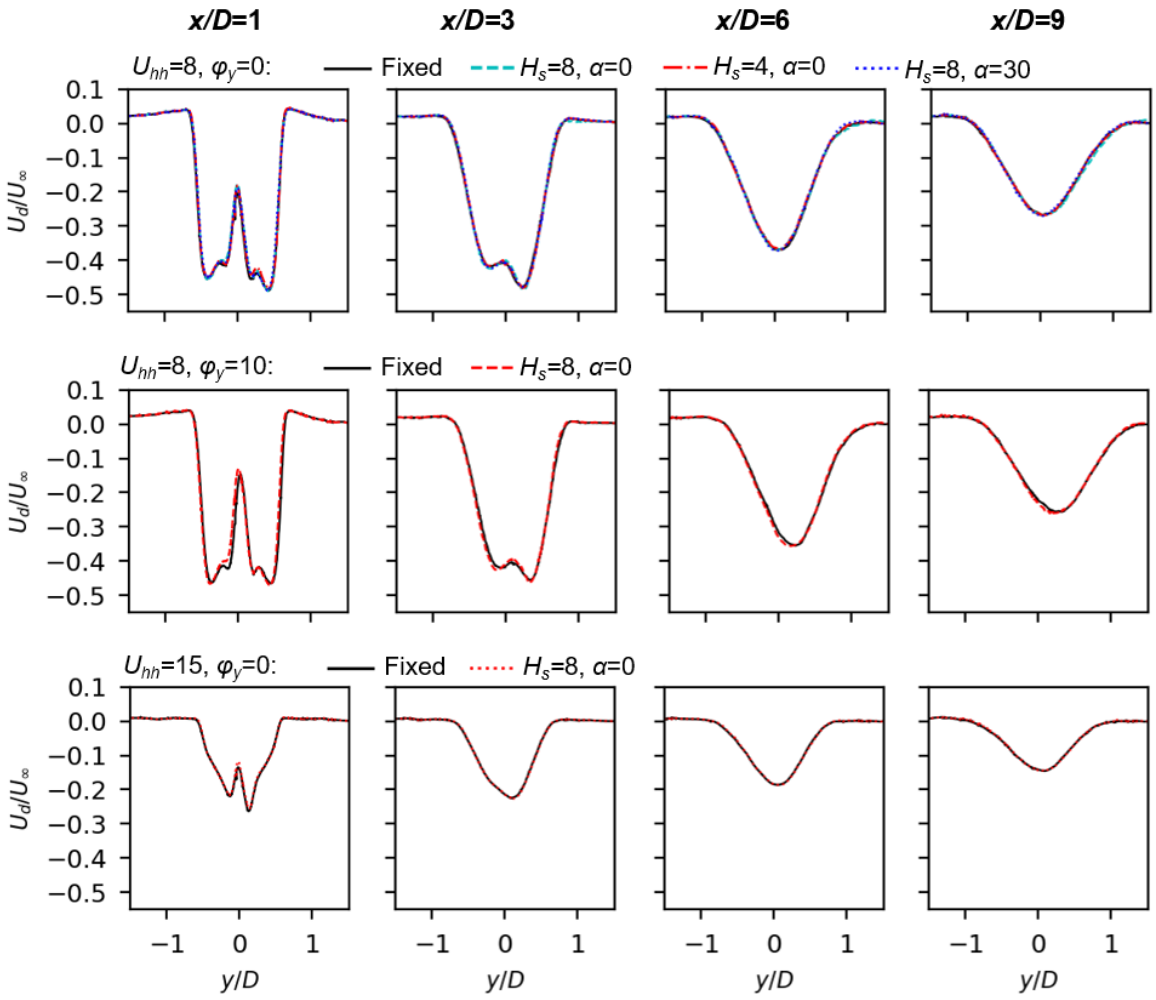

Figure 4.8. Temporally averaged wake velocity deficit U_d plotted against cross-flow coordinate y at different downstream locations x. Refer to Figure 4.7.

Figures 4.9–4.10 plot the TKE profiles in the wake, in a manner similar to Figures 4.7–4.8. The high-turbulence regions at the blade tips and nacelle decay downstream, with faster recovery for the higher wind speed cases (again, due to lower C_T and higher TI_{hh}). As with the wake deficit, the fixed and floating platforms produce similar TKE profiles. However, the floating platforms produce increased TKE in the wake shear layer compared to the fixed cases, though this effect is lessened for smaller wave heights and higher wind speeds (see in particular Figure 4.10).

Based on Figures 4.5 and 4.7, the floating-platform wakes are deflected upward due to the mean platform pitch, as observed in other studies [14, 97]. This vertical

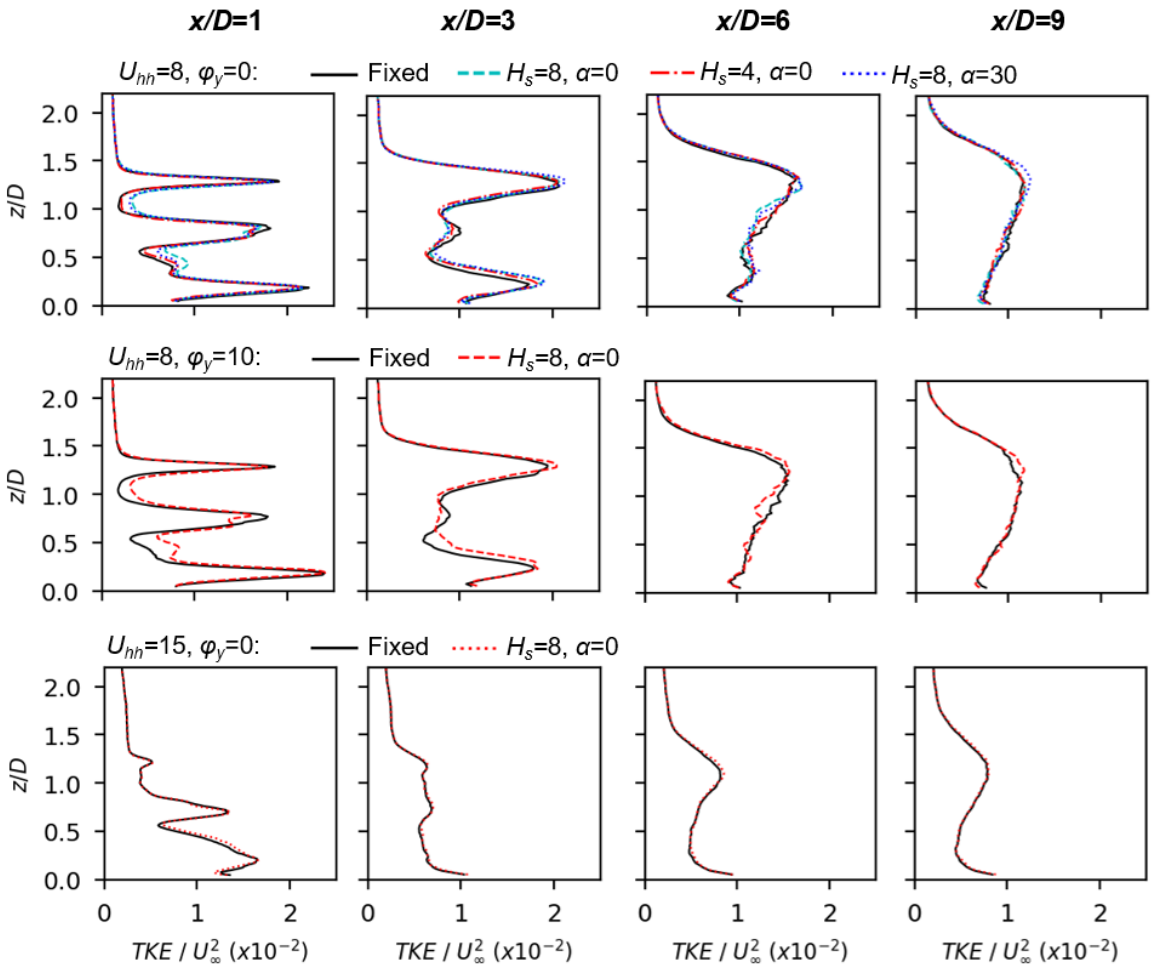

Figure 4.9. Temporally averaged turbulent kinetic energy plotted against elevation z at different downstream locations x. Refer to Figure 4.7.

deflection is similar to the well-known horizontal wake veer due to rotor yaw. Also, the mean platform surge may explain the slight differences in wake deficit shape at x/D=1: x is measured from a 0 m surge, so that the floating platform's x/D=1 (as reported) is effectively slightly upstream compared to the fixed platform. The importance of this mean surge effect decreases farther downstream.

In addition, based on Figures 4.5 and 4.7–4.10, the increased TKE in the wake shear layer for floating platforms is associated with time-varying platform motion. More platform movement results in more rotor motion, which triggers instability in the wake shear layer faster than in fixed-platform cases. This idea is supported by the

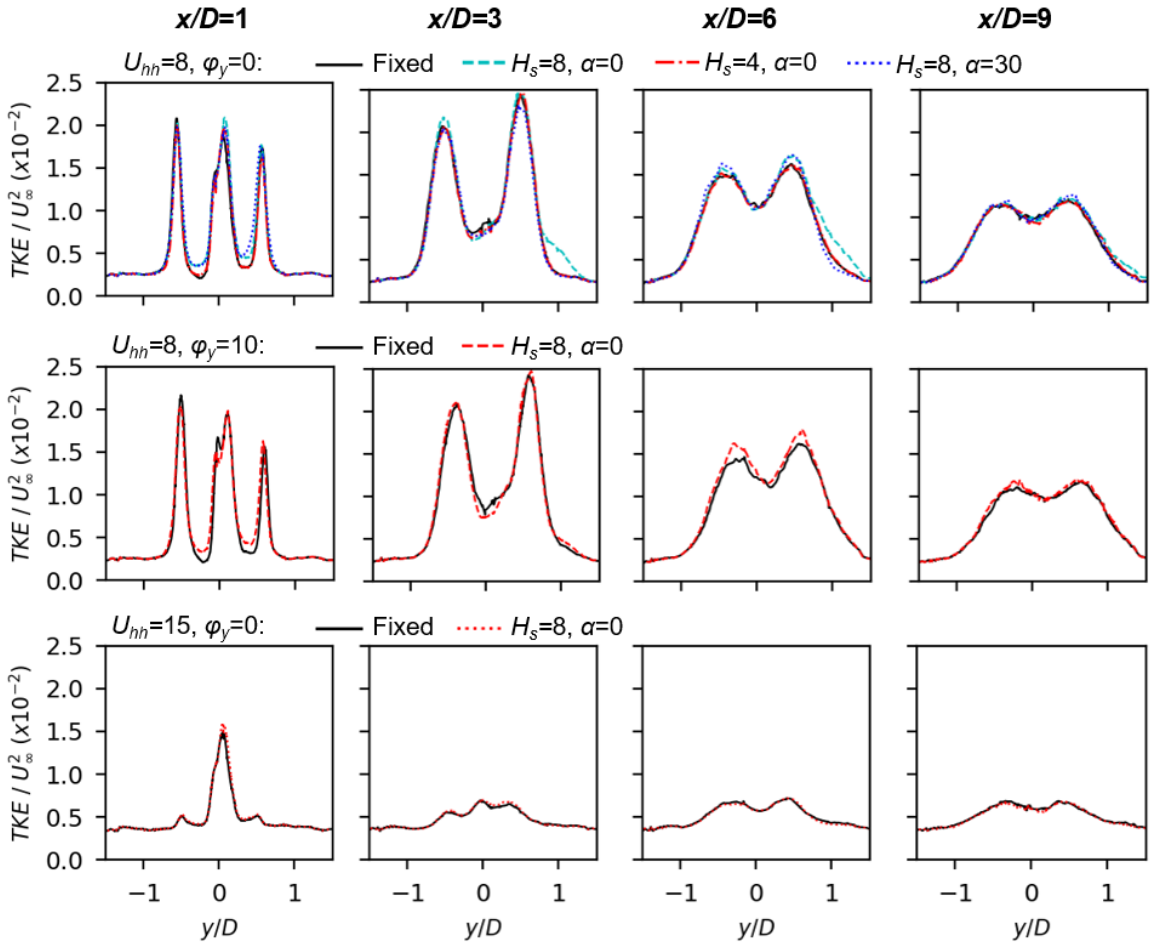

Figure 4.10. Temporally averaged turbulent kinetic energy plotted against cross-flow coordinate y at different downstream locations x. Refer to Figure 4.7.

H_s=4 m case, where smaller time-varying platform motions cause smaller increases in TKE in the wake shear layer.

Overall, Figures 4.5 and 4.9–4.10 indicate that the wake deficit shape is altered by mean platform displacements, specifically shifting the elevation of the peak wake deficit upwards by up to 10%. Also, peak TKE in the wake shear layer is increased up to 6% due to time-varying platform motion. These effects are relatively small in this study, especially for higher wind speeds and lower wave heights. However, because the platform motion is on the order of the simulation cell size, it is unclear if this study adequately resolves the full effects of floating-platform motion on the wake. Although higher mesh resolution remains computationally prohibitive, suffi-

ciently high-resolution data from experiments or field measurements are also difficult to obtain.

4.3.2.2 Wake characteristics for cases 2.1–2.6

Figure 4.11 shows U_d versus elevation z at different downstream locations for the fixed, spar, and semisub turbines in neutral (A) and stable (B) atmospheres. For each simulation, the downstream location x' is measured from the turbine's mean rotor center displacement such that x' = x - Δx_{RC}. Similarly, Figure 4.12 plots the resolved TKE against elevation z at different downstream locations x'.

As shown in Figures 4.11–4.12, all wakes recover with downstream distance as expected, indicated by reduced wake deficits and turbulence levels. The double-peak wake shape at $x'/D = 1, 3$ is caused by the low-thrust region near the blade roots. Figures 4.11–4.12 also show that the fixed-turbine wakes are similar to the floating-turbine wakes for both neutral and stable atmospheres.

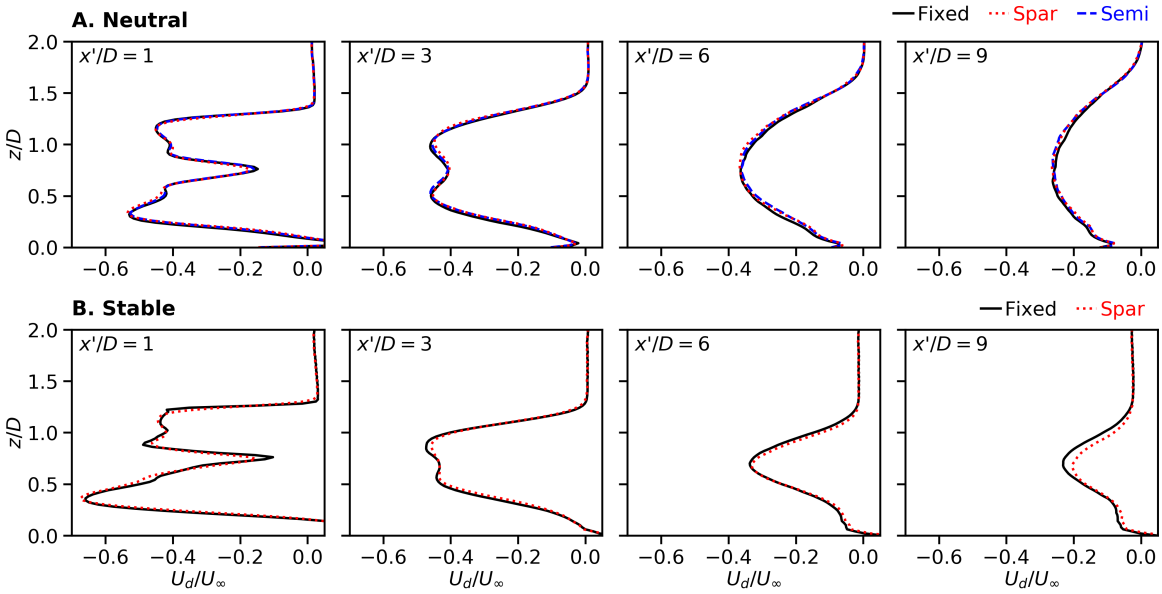

Figure 4.11. Time-averaged velocity deficit plotted against elevation at several downstream locations. Fixed and floating turbines are compared in neutral (A) and stable (B) atmospheres. The downstream locations are measured from the mean rotor displacement.

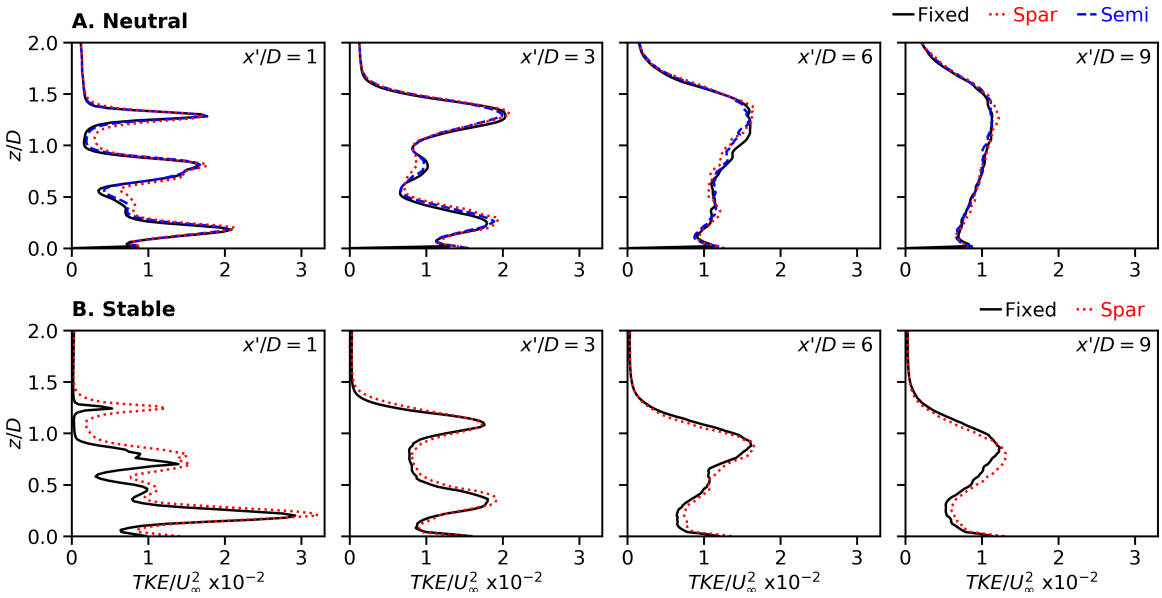

Figure 4.12. Turbulent kinetic energy plotted against elevation at several downstream locations. Fixed and floating turbines are compared in neutral (A) and stable (B) atmospheres. The downstream locations are measured from the mean rotor displacement.

4.3.3 Wake velocity differences for cases 2.1–2.6

To better illustrate the small differences between the fixed-turbine wakes and floating-turbine wakes, Figure 4.13 displays contours of the difference in time-averaged streamwise velocity, ΔU, at several cross-stream planes. Specifically, velocity differences are shown: between the spar and the fixed turbine in the neutral atmosphere (top), between the semisub and the fixed turbine in the neutral atmosphere (center), and between the spar and the fixed turbine in the stable atmosphere (bottom). The downstream locations x' are again measured from the mean rotor displacement, and an outline of the undisplaced rotor disk is included for reference.

The most prominent feature of the time-averaged velocity difference contours in Figure 4.13 is the positive ΔU near the bottom of the wake paired with a negative ΔU near the top of the wake. This is caused by the floating-turbine wakes deflecting upward compared to the fixed-turbine wakes: the floating wake is shifted upwards, creating a higher-velocity region near the bottom of the rotor disk and a lower-velocity

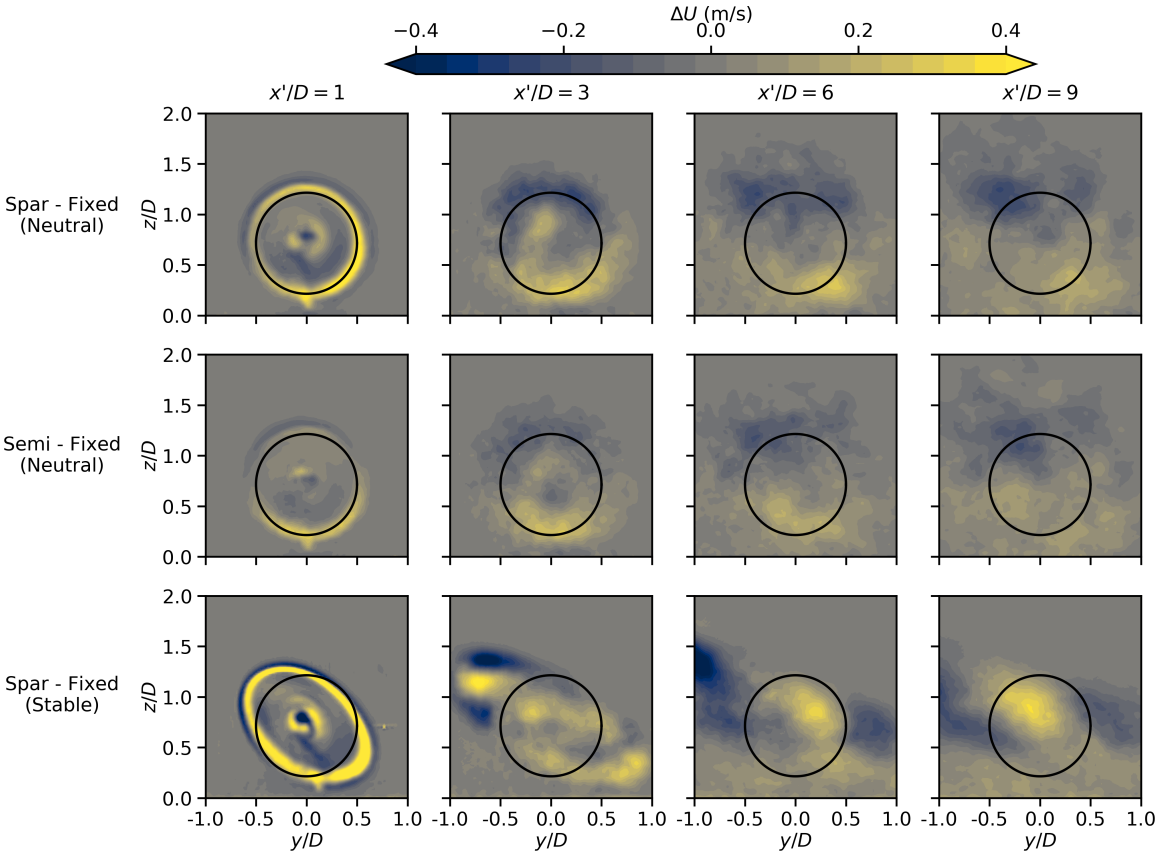

Figure 4.13. Differences in time-averaged wake velocity between fixed and floating simulations at downstream locations of $x'/D = 1, 3, 6, 9$. The downstream locations are measured from the mean rotor displacement. The undisplaced rotor disk is outlined for reference.

region near the top. At $x'/D = 1$ and 3, the alternating positive-negative ΔU areas inside the rotor outline are caused by the upwards deflection of the double-peak wake shape shown in Figures 4.11–4.12. The differences between the semisub and the fixed turbine are smaller than between the spar and the fixed turbine, although the same upwards deflection appears for both floating platforms. For the stable simulations, the higher wind veer skews the wake more, causing the positive-negative ΔU pattern to be stretched diagonally.

This upwards deflection of floating-turbine wakes is caused by the mean platform pitch backwards, creating a vertically curled wake, as also observed by Lee *et al.* [14] and Rockel *et al.* [97]. This curled wake resulting from platform pitch is similar to curled wakes caused by rotor tilt [11–13, 126], and is also analogous to horizontally

curled wakes caused by nacelle yaw. Although the vertical deflection is measurable for these floating-turbine wakes, the curled shape distortion is relatively weak because of the low effective rotor tilt angles (5° shaft tilt plus 1-3° mean platform pitch), especially beyond the near wake, $x'/D > 1$.

To further illustrate the reason why floating-turbine wakes are deflected upward compared to fixed-turbine wakes, Figure 4.14 shows a contour at $x'/D = 3$ of the difference in time-averaged streamwise velocity ΔU between a fixed turbine with a 10° nacelle yaw angle (case 1.5) and a fixed turbine with a 0° yaw angle in the neutral atmosphere (case 1.1). The horizontal positive-negative ΔU pattern in Figure 4.14 is similar to the vertical positive-negative ΔU in Figure 4.13, including the effects of the double-peak wake shape inside the rotor outline. This similarity to the wake differences between two fixed turbines (one yawed and one without yaw) suggests that the floating-turbine wakes' upward deflection is mostly caused by the mean platform pitch displacement, rather than any time-varying motions due to the floating platform.

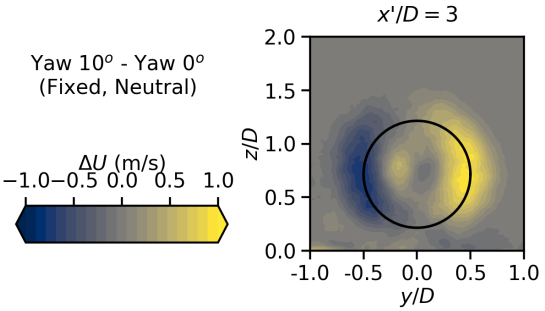

Figure 4.14. Differences in time-averaged wake velocity between a fixed turbine with 10° rotor yaw and a fixed turbine with 0° rotor yaw, at a downstream location of $x'/D = 3$. The undisplaced rotor disk is also outlined.

In contrast to the time-averaged wake velocity differences in Figure 4.13, the instantaneous wake velocity differences between the floating and fixed turbines (not shown) do not show recognizable patterns over time or space. Although the instantaneous streamwise velocity in the wake is noticeably different (1-2 m/s) at any given time between the fixed and floating simulations, these differences represent a different realization of wake turbulence and do not form spatial or temporal patterns that would affect a downstream turbine.

4.3.4 Wake centerline locations for cases 2.1–2.6

To further investigate how floating-turbine wakes differ from fixed-turbine wakes, the wake center is tracked over time for cases in the second group. The wake center at each downstream location is identified every 1 s, using the SAMWICH toolbox [127] by fitting a 2D Gaussian to the streamwise velocity deficit and taking the Gaussian center as the wake center. This method can track the wake center up to $x'/D = 6$, but results farther downstream are omitted because of spurious wake center locations.

Figure 4.15 shows the wake center cross-stream coordinate y_{WC} and vertical coordinate z_{WC} at different downstream slices x' for each platform type in neutral (A) and stable (B) atmospheres. The time-averaged wake center is shown with the RMS, minimum, and maximum of the wake center time history. The downstream location x' is measured from the mean rotor displacement.

The mean wake center elevations z_{WC} in Figure 4.15 confirm that the floating-turbine wakes are deflected upwards, compared to the fixed-turbine wakes. However, even the fixed-turbine wakes are somewhat deflected upward, due to the 5° shaft tilt

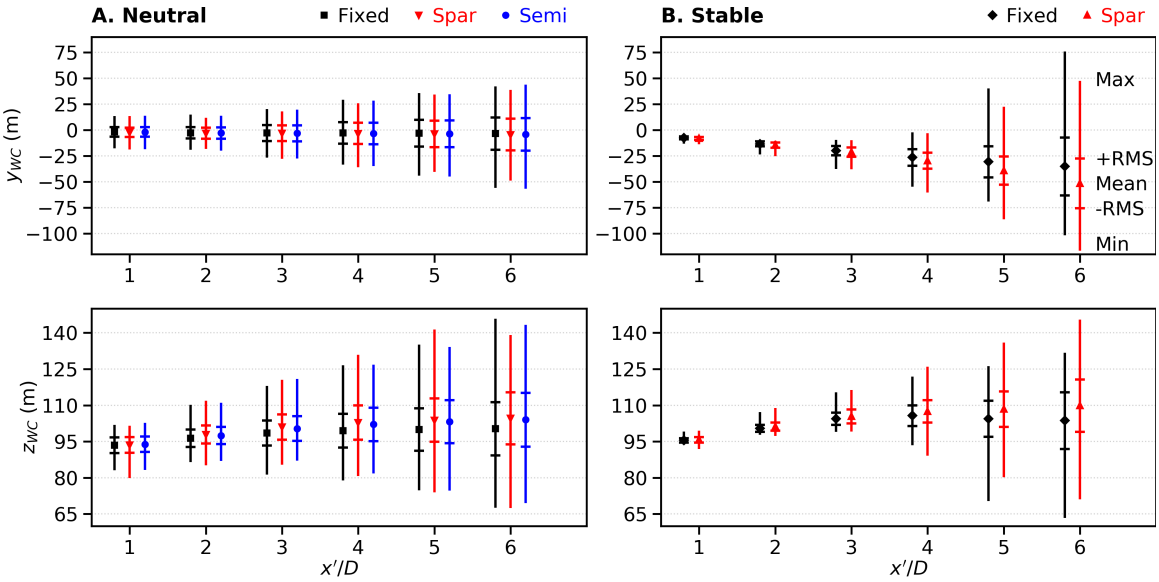

Figure 4.15. Wake center coordinates y_{WC}, z_{WC} versus downstream location in neutral (A) and stable (B) atmospheres. The mean (symbols), root-mean-square (−), and minimum/maximum (|) are shown for the fixed (■, ◆), spar (▼, ▲), and semisubmersible (●) platforms.

[119]. The spar wake center is deflected upward more than the semisub wake center, which is consistent with the spar's larger wake velocity differences in Figure 4.13. This trend is caused by the spar's larger mean platform pitch (see Figure 4.6). Comparing atmospheric stabilities, the stable spar wake is deflected more than the neutral spar, suggesting that floating-turbine wake deflection is influenced by wind shear.

The mean wake center cross-stream locations y_{WC} in Figure 4.15 are generally similar between fixed and floating turbines for the neutral atmosphere, with differences less than $1\%D$. Since the stable atmosphere has higher wind veer, the stable wakes are deflected more than the neutral wakes in the cross-stream direction. Furthermore, the stable floating-turbine wakes are deflected more in the cross-stream direction than the stable fixed-turbine wakes (up to $13\%D$). This is caused by the vertical wake deflection interacting with the stable atmosphere's wind veer.

The time-varying fluctuations in wake center location in Figure 4.15 are generally similar between the fixed and floating turbines. For both y_{WC} and z_{WC}, the RMS differences between fixed and floating wake center locations are mostly less than $1\%D$. However, the stable atmosphere's low TI increases the importance of the platform motion's effect on the wake, creating a $3\%D$ difference in horizontal RMS between the stable fixed and floating cases at $x'/D = 6$. Differences in the RMS y_{WC} and z_{WC} between the stable and neutral atmospheres are generally larger than the RMS differences between fixed and floating turbines, indicating that atmospheric flow influences wake center variations more than floating platform motion.

4.3.5 Quantifying floating-fixed differences for cases 2.1–2.6

Table 4.2 summarizes the key differences between fixed and floating turbines presented in Figures 4.6 and 4.11–4.15, illustrating how floating platform motion and rotor center displacements translate into differences in wake center locations. As indicated in Table 4.2, mean platform pitch values of 1.8-2.6° result in increased vertical

Table 4.2. Differences in mean and root-mean-square values between floating and fixed turbines. Differences are shown for key platform motions; rotor center displacements; and wake center locations at three downstream locations.

	Spar vs. Fixed (Neutral)		Semi vs. Fixed (Neutral)		Spar vs. Fixed (Stable)	
Difference	Mean	RMS	Mean	RMS	Mean	RMS
Surge (m)	8.36	1.41	6.02	1.26	7.87	1.34
Heave (m)	−0.19	0.29	0.02	0.85	−0.18	0.29
Pitch (°)	2.63	0.68	1.83	0.69	2.49	0.66
Yaw (°)	0.04	0.55	0.03	0.16	0.08	0.49
Δx_{RC} (m)	12.21	2.52	8.82	1.12	11.92	2.46
Δy_{RC} (m)	−0.33	1.16	−0.20	0.58	−0.41	1.15
Δz_{RC} (m)	−0.05	0.26	0.13	0.81	−0.05	0.26
y_{WC}						
x'/D=1	−0.37%D	−0.03%D	−0.11%D	−0.01%D	−0.45%D	0.00%D
x'/D=3	−0.20%D	−0.01%D	−0.25%D	−0.05%D	−1.17%D	0.04%D
x'/D=6	−0.70%D	−0.30%D	−0.67%D	0.03%D	−12.97%D	−3.05%D
z_{WC}						
x'/D=1	0.12%D	0.04%D	0.30%D	−0.04%D	0.21%D	0.18%D
x'/D=3	1.96%D	0.03%D	1.47%D	−0.03%D	0.77%D	0.33%D
x'/D=6	3.42%D	−0.16%D	2.95%D	0.08%D	4.93%D	−0.66%D

wake deflections of 3-5%D at x'$/D$=6, with the stable atmosphere increasing the vertical wake deflection. Increased rotor displacement RMS values of 1-3 m result in negligible (mostly less than 1%D) changes in wake center location RMS, though the stable atmosphere creates larger differences (up to 3%D) in horizontal wake center fluctuations between the fixed and floating cases.

4.4 Summary and conclusions

In summary, floating OWTs are simulated using LES with an ALM in a coupled SOWFA-OpenFAST framework for different wind speeds, wave heights, wind-wave alignments, rotor yaw angles, floating platform types, and atmospheric stability conditions. Wake characteristics such as velocity deficit U_d, TKE, and wake centerline locations are compared between the floating OWTs and an equivalent fixed-bottom turbine.

For the simulated conditions, floating OWT wakes generally have similar characteristics to fixed-platform wakes. The primary difference is that floating-turbine wakes are deflected upwards because of mean platform pitch angles in all simulations. This vertical wake deflection for floating turbines is similar to horizontal wake deflection caused by nacelle yaw in fixed turbines (see Figures 4.13–4.14). Across the different environmental conditions studied in cases 1.1–1.8, mean platform pitch deflected the wake upwards by 5–10%. Based on cases 2.1–2.6, the spar platform produces larger upwards wake deflections than the semisub, because of the spar's larger mean platform pitch (see Table 4.2). The stable atmosphere produces larger vertical and horizontal deflections than the neutral atmosphere (see Table 4.2), indicating that wind shear and wind veer interact with this pitch-driven wake deflection.

In addition, small variations in turbulence are associated with time-varying platform motions, particularly a 1–6% increase in peak TKE in the wake shear layer. These differences persist into the far wake 6 to $9D$ downstream, but are reduced for higher wind speeds or lower wave heights. Rotor yaw angle and wind-wave alignment only minimally affect the differences between fixed- and floating-platform wakes. Due to mesh resolution limitations, these results may not capture all floating-platform wake effects.

Floating-turbine wake fluctuations in time do not significantly differ from fixed-turbine wake fluctuations, even for conditions selected to accentuate floating wake differences (high wave height, below-rated wind speed, and wind-wave misalignment). The RMS fluctuations in wake center location differ by less than $1\%D$ between fixed and floating turbines in most cases, although the stable atmosphere's low turbulence intensity allows the floating platform motion to have a larger effect on horizontal wake center fluctuations (see Figure 4.15 and Table 4.2).

These conclusions suggest that reduced-order wake models for fixed turbines can reasonably apply to floating-turbine wakes, especially curled wake models that cap-

ture upwards wake deflection caused by mean platform pitch. Additional adjustments may be necessary for vertical wake deflections interacting with wind shear and wind veer, for some conditions.

CHAPTER 5

POWER GENERATION FOR FLOATING TURBINES

Accurately predicting the power generation for floating turbines is vital for designing and financing large-scale floating wind projects. In floating OWTs, the coupling of platform mobility to aerodynamic loads on the turbine rotor affects the power generation, structural loads, and wind flow around the turbine [7, 8]. It is important to understand how and why power generation differs between floating turbines and fixed-bottom turbines, so that appropriate adjustments can be made to power prediction models used in project design and planning.

Floating platform displacements are described by six degrees of freedom: surge, sway, heave, pitch, roll, and yaw, as illustrated in Figure 2.1. These platform displacements cause displacements of the rotor, also shown in Figure 2.1: the three linear displacements of the rotor center, x_{RC}, y_{RC}, and z_{RC}, as well as the rotor "pitch" and "yaw" angles due to platform displacements, ϕ_{RC} and θ_{RC}. In general, both rotor and platform displacements may include both fluctuating motions ("dynamic displacements") and nonzero time-averaged positions ("time-averaged displacements").

Previous studies examine how specific types of dynamic platform displacements affect a floating turbine's power generation. In particular, dynamic motions in surge and pitch typically increase time-averaged power generation: the associated rotor motions upwind-downwind change the relative wind speed experienced by the rotor, which results in a power gain when averaged over time. This phenomenon is observed for isolated pitch motions, isolated surge motions, and combinations of surge and

pitch motions in studies by Huang and Wan [128], Karimian Aliabadi and Rasekh [129], Lin *et al.* [76], Sant *et al.* [130], Shen *et al.* [131], and Wen *et al.* [132–134].

Other studies also document that statically angling the rotor relative to the wind decreases power generation. Specifically, static rotor yaw reduces a turbine's power generation [13, 135], with a power loss coefficient typically predicted by a $\cos^n$ model [135]. Similarly, static rotor tilt decreases a turbine's power generation [13]. For floating turbines, platform yaw and pitch directly cause an angled rotor, which may act like static rotor yaw or tilt and decrease power [128]. Additionally, platform roll and heave may affect power by causing vertical rotor displacements within the wind shear profile, though the vertical displacements may be too small relative to the wind shear to create a substantial effect.

Although platform displacements are the underlying reason behind power gains or losses in floating turbines, previous studies rarely use representative displacement values. A realistic floating turbine's platform displacements are driven by stochastic environmental loads from irregular waves and turbulent wind, with possible coupling between different platform degrees of freedom [99]. Despite this, simulated platform displacement time histories are often approximated as prescribed sinusoids with time-averaged values of zero, and individual platform degrees of freedom are often studied in isolation [95, 129, 131–134, 136]. Direct comparisons between multiple common floating platform types are also rare, limiting the ability to generalize trends across platform types. Notable exceptions include Sebastian and Lackner [99], who examined barge, spar, and tension-leg platforms with dynamic behavior under irregular waves and steady wind, as well as Huang and Wan [128], who examined a spar platform with dynamic behavior under regular waves and steady wind.

This research aims to provide upper estimates for power gains or losses due to floating platform displacements for two common floating platform types, the spar and semisubmersible. Furthermore, this research seeks to link these power gains

or losses to rotor displacement patterns, and in doing so, identify the underlying physical phenomena that cause differences in average power between floating and fixed-bottom turbines. Specifically, this study focuses on determining which types of realistic platform behavior most affect the average power for below-rated conditions, by addressing the following questions:

- Do any dynamic rotor or platform displacements significantly affect power?
- Do any time-averaged rotor or platform displacements significantly affect power?
- Which rotor and platform degrees of freedom affect power the most?
- How does average power generation differ between spar and semisub platforms?

To answer these questions, floating turbines are simulated using OpenFAST [106] and SOWFA [104]. Section 5.1 describes the simulation setup, including details on the simulation models, platform types, environmental conditions, and case descriptions. Section 5.2 presents the simulated results for platform displacements and average power generation. In Section 5.3, a new analytical model for floating power generation is proposed and evaluated against the simulated results. Finally, Section 5.4 summarizes this work's conclusions about how specific platform displacements affect average power generation in floating turbines.

5.1 Simulation setup

This study simulates the power generation of the NREL 5 MW reference turbine, which has a diameter of D=126 m, a hub height of z_{hh}=90 m, a rated wind speed of 11.4 m/s, and a shaft tilt of ϕ_t=5° [119]. The simulated turbine is mounted on two floating platforms: the OC3-UMaine spar [98] and the OC4-DeepCWind semisubmersible [120] (see Section 4.2.1). For comparison, a fixed-bottom version of the NREL 5 MW turbine is also replicated by disabling all platform displacements for a spar simulation, as described in Section 4.2.1.

5.1.1 Environmental conditions

This study considers the power generation under one combination of environmental conditions. The turbulent wind conditions represent an offshore ABL with neutral stability, capped by a stable inversion at an elevation of 750 m. At hub height, the wind speed is 8 m/s and the turbulence intensity is 4%, with a wind shear of 0.008 m/s/m and a wind veer of 0.02°/m across the rotor height. Figure 5.1 shows the average horizontal wind speed, wind direction, and turbulence intensity as a function of elevation in the simulated ABL. Additional characteristics of a similar neutral boundary layer are described in more detail in Sections 4.2.2–4.2.4. The 8-m/s wind speed is in the turbine's below-rated operating region, where tip-speed ratios are high and power generation is most influenced by platform behavior [76, 129].

The wave conditions are irregular, unidirectional JONSWAP waves in a water depth of 200 m. The irregular waves have a significant wave height of H_s=8 m and a peak spectral period of T_p=14 s. The wave propagation direction is aligned with the hub-height wind direction. These environmental conditions represent an unusual combination of below-rated wind speeds and very large waves; a more typical 10-year significant wave height might be 4.5-5 m for this wind speed [100]. Previous studies indicate that this combination increases the platform displacements [17, 100] while remaining in the below-rated control regime where power is most affected by platform motions, therefore giving an upper estimate for the power gains or losses due to floating platform displacements.

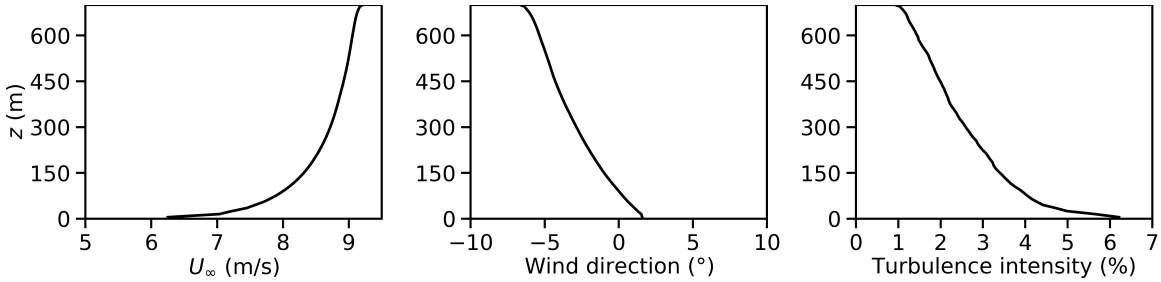

Figure 5.1. Free-stream horizontal wind speed U_∞, wind direction, and turbulence intensity in the simulated ABL, averaged horizontally and over time.

5.1.2 Simulation models

The spar, semisubmersible, and fixed-bottom turbines in these environmental conditions are simulated using OpenFAST v2.3.0 [106], NREL's modular aeroelastic engineering tool that models the platform motion, rotor motion, rotor aerodynamic performance, and power generation. Variable-speed control and blade-pitch control are included using OpenFAST's ServoDyn module, but the blade pitch remains at 0° due to the below-rated wind speed. The HydroDyn module models the irregular wave conditions. The turbulent inflow wind is generated by LES of the ABL flow. This LES is performed with SOWFA [104], described in Section 4.1.2, which models the wind flow around the turbine.

The majority of the OpenFAST simulations in this chapter use a prerecorded time history of the inflow wind field. This prerecorded inflow is generated by sampling on a plane in the SOWFA LES, producing a time series of 2D slices of the instantaneous wind field at 16 Hz. These slices are then converted to HAWC-format binary files, and marched past the turbine in OpenFAST to recreate the SOWFA flow field time history at the rotor plane. This approach of using prerecorded SOWFA slices as inflow wind to a stand-alone OpenFAST simulation is documented further by Lee *et al.* [14].

Although computationally efficient, this prerecorded inflow field does not fully capture the two-way interaction between the floating rotor motion and the surrounding flow. To address this shortcoming, additional simulations are performed by directly coupling the OpenFAST turbine with a simultaneous SOWFA LES of the surrounding wind flow. The two-way coupling between the OpenFAST turbine and the SOWFA flow field is achieved via an ALM and is updated every time-step to capture the feedback between rotor motion and the surrounding fluid flow. This coupled SOWFA-OpenFAST model is described further in Section 4.1.

The simulation workflow in this study follows three main stages, as illustrated in Figure 5.2. First, a precursor LES in SOWFA establishes the stably-capped neutral ABL with no turbine present. This precursor simulation develops the turbulent structures and wind shear profile over 5.5 hours, on a uniform 10-m cubic mesh in a domain with dimensions of 8 km by 2 km by 1 km and lateral periodic boundaries (see Figure 5.2). This precursor simulation provides the initial condition and boundary condition time histories for the next simulation stage.

In the second stage, SOWFA simulations capture the flow surrounding the turbine for 70 minutes. These turbine-focused simulations are carried out in a smaller domain with dimensions 1.8 km by 1 km by 1 km, with inflow/outflow x boundaries and periodic y boundaries. These SOWFA simulations contain either an ALM with the

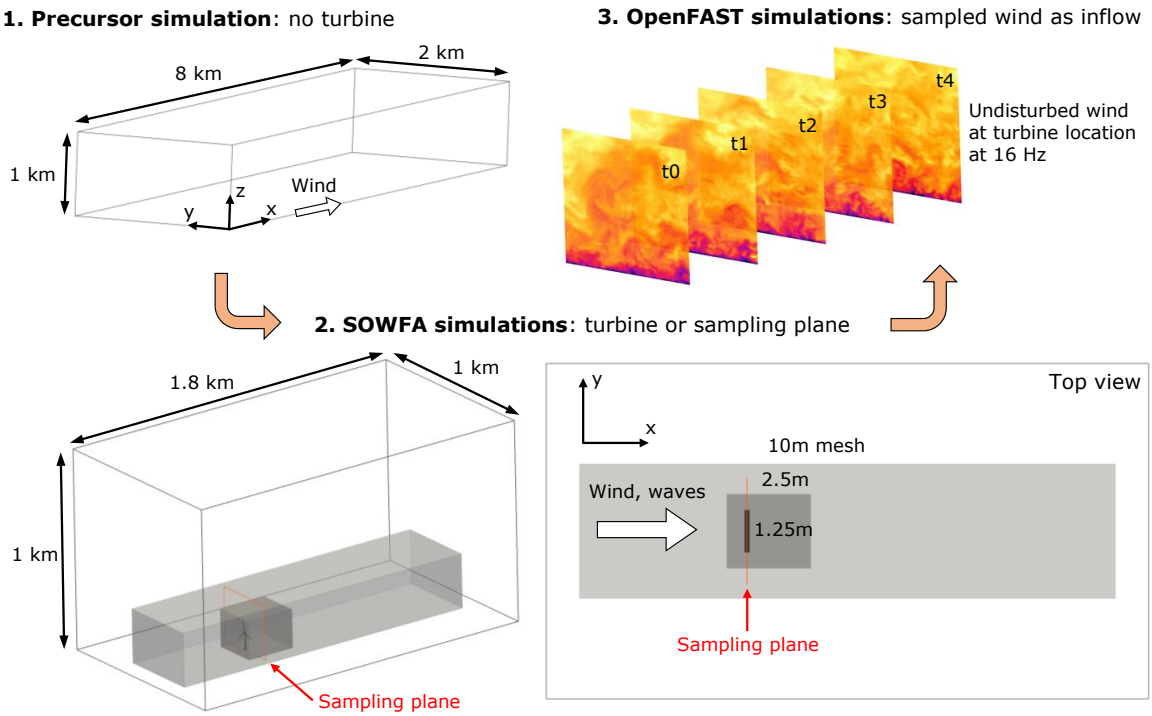

Figure 5.2. Three-stage simulation workflow: 1) a "precursor" LES in SOWFA that develops the ABL, 2) SOWFA LES that contain either a coupled OpenFAST turbine or a sampling plane at the rotor, and 3) stand-alone OpenFAST turbine simulations using the sampled SOWFA time series as inflow wind. The SOWFA simulation domain, mesh refinement regions, and sampling plane location are illustrated, including a top view.

coupled OpenFAST turbine (for the coupled inflow approach), or a sampling plane at the hypothetical rotor's undisplaced location (for the prerecorded inflow approach). In both situations, the uniform cubic 10-m mesh is refined to 1.25 m around the rotor, with a larger refinement region to 2.5 m in the turbine wake region. Figure 5.2 illustrates this domain, the mesh refinement regions, and the sampling plane location. The third stage consists of stand-alone OpenFAST simulations of the turbine over 70 minutes, using the prerecorded SOWFA inflow wind time series as described above. Similar precursor simulations and similar coupled SOWFA-OpenFAST simulations are described in further detail in Chapter 4.

5.1.3 Case descriptions

To study how power generation is affected by floating platform displacements, a total of 36 simulations of an individual turbine are performed using the same inflow wind from SOWFA. The baseline case represents a fixed-bottom turbine, with all platform displacements set to a constant value of zero. All values for power generation by floating turbines are compared to this baseline case. To better understand how platform type affects power generation and to identify underlying physical effects that can be generalized for any platform type, all cases with floating turbines are repeated for both the spar and semisubmersible platforms. The main floating case represents a typical floating turbine, with platform displacements in all six degrees of freedom (surge, sway, heave, pitch, roll, and yaw) causing rotor displacements in x_{RC}, y_{RC}, z_{RC}, ϕ_{RC}, and θ_{RC}. These displacements generally consist of dynamic motion ("dynamic displacement") around some time-averaged value ("time-averaged displacement"). The all-displacements floating case (for the spar and semisubmersible) and the fixed-bottom baseline case are performed using both the prerecorded inflow slices approach and the two-way coupled inflow approach. To limit computational

cost, the remaining cases discussed next are performed using the prerecorded inflow approach only.

To better understand how individual platform degrees of freedom affect power generation, an additional set of cases restricts platform displacements to one or two degrees of freedom. For these cases, the nonactive degrees of freedom are set to a constant displacement of zero, with motion disabled in that direction. Each platform degree of freedom (surge, sway, heave, pitch, roll, and yaw) is simulated in isolation in this manner, as well as a case with both surge and pitch enabled together, for both platforms. Within this simulation framework, it is not possible to isolate individual rotor displacements directly, only platform displacements. Still, some of these cases can serve as proxies for isolating rotor displacements: for example, the surge-only case produces only x_{RC} displacements.

The floating cases described so far include both dynamic and time-averaged displacements. To better separate the effects of these two categories of displacement, another set of cases isolates the time-averaged displacement by disabling dynamic platform motions. For this set, each of the floating cases described above is repeated, but with the active degrees of freedom set to a constant displacement equal to the mean value from the previous cases. Conversely, the dynamic motion effect cannot be isolated in this simulation framework; this would require artificially prescribing displacement time histories with the time-averaged value subtracted out. However, the other floating cases that include both dynamic and time-averaged displacements still provide insight into the dynamic displacement effect.

5.2 Simulation results

Each simulated case described in Section 5.1.3 produces 70-minute time histories for power generation, platform displacements, and rotor displacements. The first 10 minutes of each time history are discarded to remove any transient startup effects,

producing time histories of 60 minutes for analysis. In this section, the rotor and platform displacements that affect power generation are identified. The important rotor and platform displacements are then compared across platform type and across inflow approach. The difference in power generation between the floating cases and the fixed-bottom turbine is then linked to specific types of rotor displacements, explaining the underlying physical reasons for power losses or gains associated with floating wind turbines.

5.2.1 Negligible effect of crosswind and vertical displacements

For the simulated conditions with both wind and waves aligned with the x-axis, power generation is unaffected by crosswind and vertical rotor displacements, specifically y_{RC}, z_{RC}, and θ_{RC}. The associated platform displacements in sway, heave, roll, and yaw are small for the simulated conditions, and cause rotor displacements that are too small to significantly affect the average power. Comparing the case with all displacements enabled to the case with surge and pitch enabled, the average power agrees within 0.3%, indicating that the other displacements do not significantly affect the power. These unimportant displacements and results from cases that isolate the corresponding platform degrees of freedom are not discussed further, but are documented in Appendix B. Instead, the analysis focuses on displacements that do affect the power: the downwind rotor displacement x_{RC} and the rotor "pitch" angle ϕ_{RC}, caused by platform surge and pitch.

5.2.2 Platform and rotor displacements

Understanding power generation in floating wind turbines requires understanding the underlying platform and rotor displacements that ultimately affect that power. The OpenFAST simulations record platform displacements, which are used to calculate rotor displacements based on simple geometry. For example, the downwind rotor displacement x_{RC} and rotor "pitch" angle ϕ_{RC} are calculated from the platform surge

and pitch, neglecting the small platform yaw displacement and tower bending effects:

$$\begin{aligned} x_{RC} &= Surge + z_{hh} \sin(Pitch) \\ \phi_{RC} &= Pitch, \end{aligned} \tag{5.1}$$

where z_{hh} is the distance between the platform origin and rotor center (90 m for the NREL 5 MW reference turbine [119]).

Figure 5.3 presents partial time histories for the rotor and platform displacements that affect power: platform surge, rotor angle ϕ_{RC} (equivalent to platform pitch), rotor center location downwind x_{RC}, and the resulting rotor center speed $\dot{x}_{RC}$. The time histories shown are for the case with prerecorded inflow and all displacements enabled. Additionally, the entire 60-minute time histories are summarized using four metrics: the time-average, the root-mean-square (RMS), the minimum, and the maximum. Figure 5.3 includes summary metrics for four different cases: all displacements enabled with coupled inflow, all displacements enabled with prerecorded inflow, only average $\overline{\phi}_{RC}$ (via platform pitch) displacement with prerecorded inflow, and only x_{RC} displacements (via platform surge) with prerecorded inflow.

As shown in Figure 5.3, the coupled inflow case (grey circle) has nearly identical platform and rotor displacements as the prerecorded inflow case (black square). For example, the average values for ϕ_{RC} and x_{RC} agree within 1.5%, and the RMS values for ϕ_{RC}, x_{RC}, and $\dot{x}_{RC}$ agree within 1%. This is expected, because both cases use OpenFAST to compute the platform displacements regardless of inflow approach. In contrast, the displacements in Figure 5.3 vary significantly between the other cases, and between the spar and semisubmersible.

Differences between the spar and semisubmersible displacements in Figure 5.3 are largely caused by the platforms' different geometries and center of mass locations. The spar center of mass is 89.9 m below still water level [121], but the semisubmersible center of mass is much higher at only 13.5 m below still water level [120]. In Figure

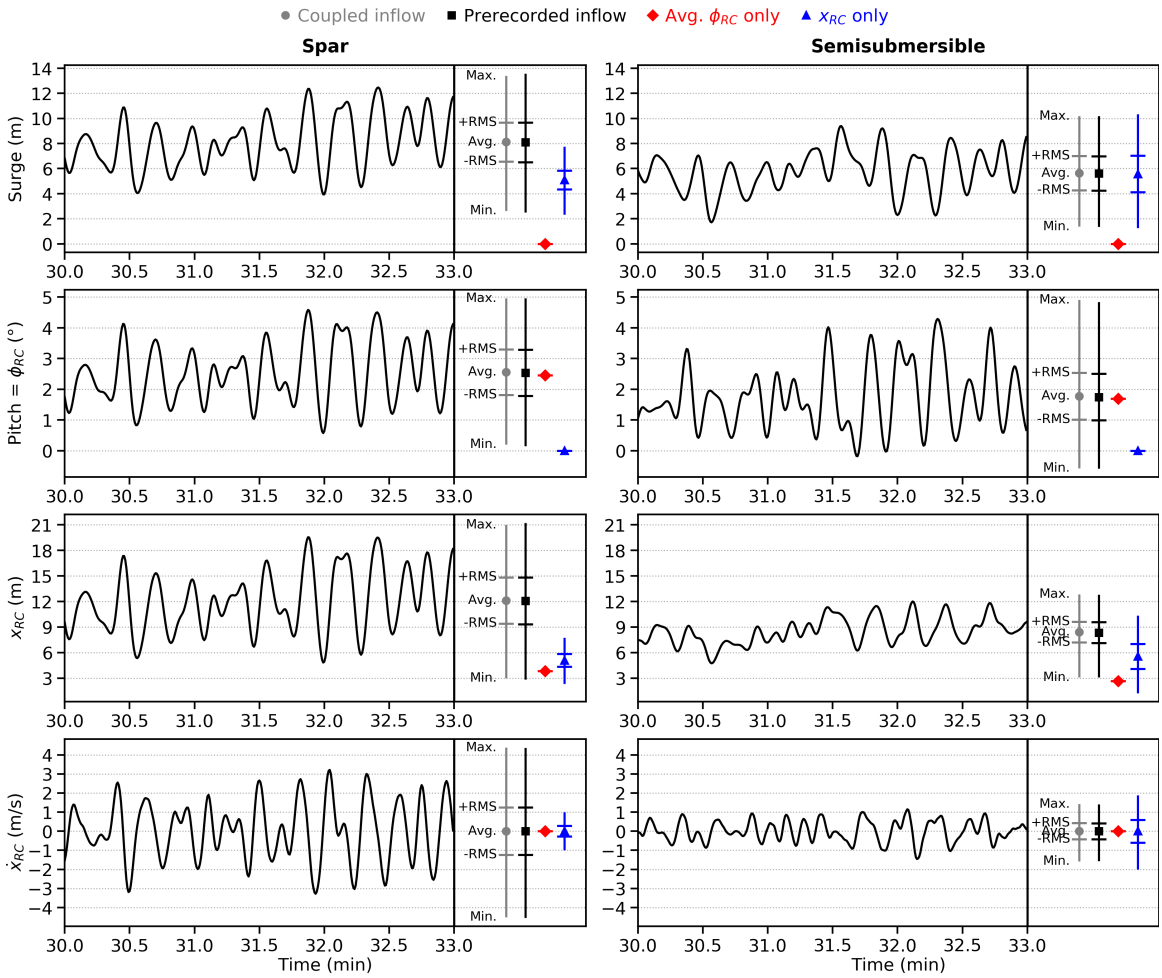

Figure 5.3. Partial time histories of platform surge, rotor angle ϕ_{RC}, rotor center location x_{RC}, and rotor center speed $\dot{x}_{RC}$ from the prerecorded inflow case for spar (left) and semisubmersible (right) floating platforms. Key metrics of the entire time history, including the average, root-mean-square, minimum, and maximum values, are shown for four cases, including cases where the displacements are restricted to only the time-averaged $\overline{\phi}_{RC}$ value or only x_{RC} displacements.

5.3, the rotor aerodynamic thrust causes the nonzero averages for ϕ_{RC} and x_{RC}, as also observed by Liu *et al.* [7]. However, the spar average $\overline{\phi}_{RC} = 2.5°$ is 45% larger than the semisubmersible average $\overline{\phi}_{RC} = 1.7°$.

In Figure 5.3, the two platforms have similar RMS values for ϕ_{RC}, but the spar RMS values for x_{RC} and $\dot{x}_{RC}$ are 1.5 m (125%) larger and 0.8 m/s (197%) larger for the semisubmersible. This is partially because the lower center of mass for the spar creates a longer rotation arm to the rotor center, compared to the semisubmersible.

So, similarly sized RMS platform pitch values are amplified into larger RMS x_{RC} values for the spar than for the semisubmersible. In fact, platform pitch rotation is the dominant driver of x_{RC} displacements for the spar, but not for the semisubmersible: the spar has a 99% correlation between the pitch and x_{RC} time histories, but the semisubmersible only has a 36% correlation. These different correlation levels between x_{RC} and pitch (or ϕ_{RC}) are also evident in the time histories in Figure 5.3.

The center of mass location also helps explain correlation patterns between platform surge and pitch. The spar platform surge is strongly positively correlated to platform pitch at a +97% correlation coefficient, so that large positive pitch variations occur at the same time as positive surge variations (see Figure 5.3). In contrast, the semisubmersible platform surge is somewhat negatively correlated to platform pitch at a -56% correlation coefficient, so that large positive pitch variations occur at the same time as negative surge variations (see Figure 5.3). This is partially because OpenFAST reports platform displacements with respect to a platform origin at still water level [118], rather than the center of rotation. Therefore, the reported platform surge is partly caused by platform rotation, rather than a purely linear displacement of the center of rotation.

Figure 5.4 illustrates the scenario where platform pitch rotation, about the center of rotation, causes a reported platform surge and x_{RC} rotor displacement. The spar center of rotation is far below still water level, so that positive pitch angles significantly increase the reported platform surge at still water level. In contrast, the semisubmersible center of rotation is much closer to still water level because of its high center of mass, so that positive pitch angles do not affect the reported platform surge as much.

The influence of platform pitch on both x_{RC} and reported platform surge also explains why the surge-only case has different x_{RC} displacements than the cases with all displacements enabled. In Figure 5.3, the x_{RC}-only case (blue triangle) is sim-

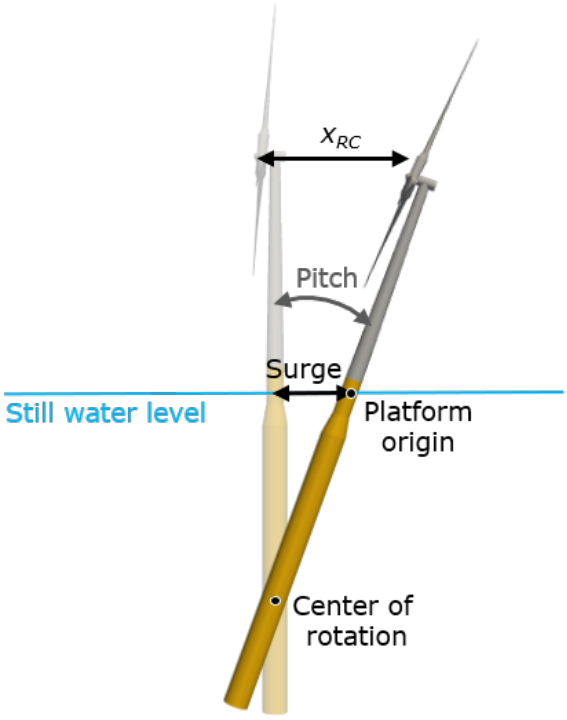

Figure 5.4. Side view of a scenario where pitch rotation, about the center of rotation, creates a reported platform surge because of the distance from the center of rotation to the platform origin, where surge is reported. Similarly, this pure platform rotation creates a linear displacement x_{RC} at the rotor center.

ulated by enabling surge platform displacements only and is therefore missing the contribution of platform pitch to reported surge and x_{RC}. So, the x_{RC} and $\dot{x}_{RC}$ RMS values are significantly different between this case and the other cases: the spar has x_{RC} and $\dot{x}_{RC}$ RMS values that are 2.0 m (72%) and 1.0 m/s (77%) smaller for this case, whereas the semisubmersible values are 0.2 m (20%) and 0.2 m/s (41%) larger for this case.

Finally, both surge and pitch must be enabled concurrently to obtain realistic rotor displacements, because isolating surge or pitch changes their displacement metrics and x_{RC} results from both surge and pitch. Still, power is directly affected by rotor displacements, so power effects are best explained by focusing on rotor displacements

x_{RC} and ϕ_{RC}, with the awareness that x_{RC} displacements are caused by a combination of platform surge and pitch.

5.2.3 Power generation

The turbine displacements summarized in Figure 5.3 affect the power generation of the floating wind turbine. Figure 5.5 presents the difference in power between floating turbine cases and an equivalent fixed-bottom turbine baseline case, where the solid bars represent the simulation results. The striped bars represent results from the proposed analytical model and are discussed in Section 5.3. These power differences are compared across four different cases: all displacements enabled with coupled inflow, all displacements enabled with prerecorded inflow, only average $\overline{\phi}_{RC}$ displacement with prerecorded inflow, and only x_{RC} displacements with prerecorded inflow.

Figure 5.5 illustrates that coupled inflow (grey) and prerecorded inflow (black) generate slightly different amounts of power, despite agreeing well on rotor displacements (see Figure 5.3). Specifically, the prerecorded inflow approach predicts lower

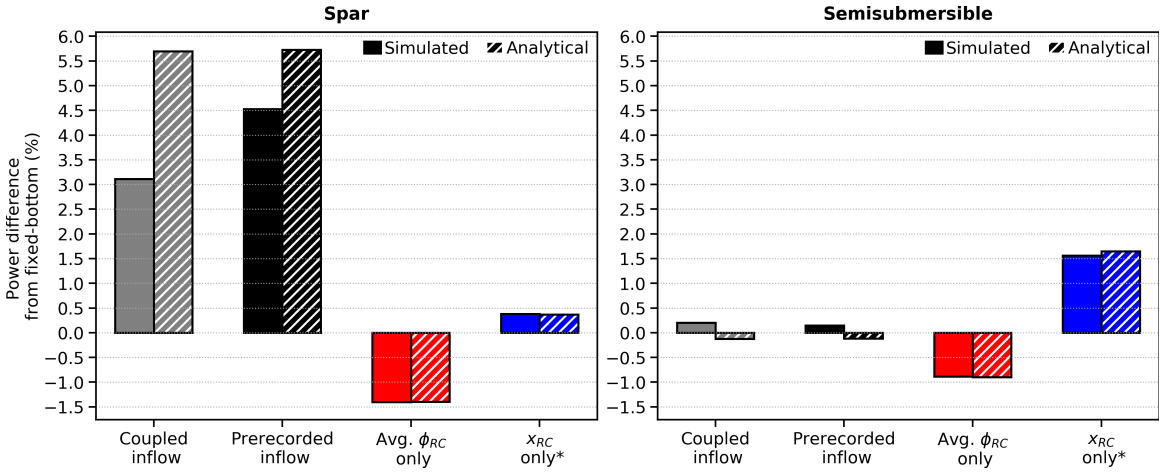

*The x_{RC} only case has different rotor displacements than other cases, see Figure 5.3.

Figure 5.5. Percent difference in power generation, relative to an equivalent fixed-bottom turbine, of spar (left) and semisubmersible (right) floating wind turbines. Simulated power gains/losses (solid bars) are compared to predictions from the analytical model (striped bars) for four cases.

power generation than the coupled approach for all three platform types: the prerecorded cases' power predictions are 2.0%, 3.4%, and 3.3% smaller than the coupled cases' for the spar, semisubmersible, and fixed-bottom platforms, respectively. This power difference is caused by the two inflow methods' models for rotor-flow interactions. Although both inflow approaches rely on an ALM, the prerecorded inflow method uses AeroDyn's dynamic blade element momentum theory model to estimate rotor wake and induction effects [106]. In contrast, the coupled inflow approach directly captures these effects by allowing the blade node forces to affect the surrounding flow [55].

5.2.3.1 Time-averaged displacement effect on power

To examine how average rotor angle $\overline{\phi}_{RC}$ affects the average power, compare the prerecorded inflow case with all displacements enabled to the case with only average $\overline{\phi}_{RC}$ in Figure 5.5. The nonzero average $\overline{\phi}_{RC}$ causes a 0.9%-1.4% power loss compared to the fixed-bottom case, because it increases the angle of the relative wind and therefore reduces aerodynamic performance. In contrast, the nonzero average x_{RC} displacement does not affect the power, because statically shifting the rotor downwind does not affect its aerodynamic performance: the case with only average x_{RC} displacement (not pictured) produces the same power as the fixed-bottom case (see Appendix B). Comparing between the two platforms, the spar power loss is 1.6 times the semisubmersible power loss for the average-$\overline{\phi}_{RC}$-only case, because the spar average $\overline{\phi}_{RC}$ angle is 1.4 times the semisubmersible average $\overline{\phi}_{RC}$ (see Figure 5.3).

5.2.3.2 Dynamic displacement effect on power

In general, dynamic displacements in x_{RC} create power gains compared to the fixed-bottom case, because it adds a relative rotor velocity $\dot{x}_{RC}$ to the inflow wind speed. Though $\dot{x}_{RC}$ can take both positive and negative values, the additional motion causes a net power gain when averaged over time. Although dynamic displacements

cannot be simulated separately from time-averaged displacements in this simulation framework, the case with only x_{RC} displacements (both average and dynamic) does offer evidence that dynamic x_{RC} displacements cause power gains. Average x_{RC} does not affect the power, implying that the entire 0.4%-1.6% power gain for the x_{RC} case (see Figure 5.5) is caused by the dynamic x_{RC} displacements. Comparing between the two platforms, the semisubmersible power gain caused by dynamic x_{RC} is 4.1 times the spar power gain (see Figure 5.5), because the x_{RC} and $\dot{x}_{RC}$ variations are larger for the semisubmersible, as measured by the RMS values (see Figure 5.3).

5.2.3.3 Total floating effect on power

The total effect of floating platforms on power is a balance between the time-averaged and dynamic displacement effects, specifically a balance between the power loss due to average $\overline{\phi}_{RC}$ and the power gain due to dynamic x_{RC} displacements. This balance explains why the all-displacement case results in a large 4.1%-4.5% power gain for the spar, but a negligible 0.1%-0.2% power gain for the semisubmersible (see Figure 5.5): the spar $\dot{x}_{RC}$ variations are 197% larger than for the semisubmersible, which outweighs the 45% larger average $\overline{\phi}_{RC}$ to create a substantially larger power gain.

In Figure 5.5, it appears that the power gains in the all-displacement cases are not a simple superposition of the average $\overline{\phi}_{RC}$-only power loss and the x_{RC}-only power gain. However, the x_{RC}-only case has substantially different x_{RC} displacements than the all-displacement cases, as discussed in Section 5.2.2, so power gains should not be directly compared between the x_{RC}-only case and the all-displacement cases.

Finally, these power results are all based on a below-rated wind speed of 8 m/s. When the turbine is operating at above-rated wind speeds in control region 3, power loss caused by average $\overline{\phi}_{RC}$ may be insignificant, because the turbine is capped at rated power regardless. For above-rated wind speeds, the size of any power gain

caused by dynamic x_{RC} displacements likely depends on how the blade pitch controller interacts with the displacement frequencies. However, the trends in platform displacements, rotor displacements, and power generation discussed in this section generally hold true for nonaligned wind and waves, as indicated by similar simulations with 30° misalignment between the wind and wave directions conducted previously. The simulated results are also generally consistent with limited field measurements from the Hywind Demo and WindFloat WF1 projects, as reported in Roddier *et al.* [137]. In particular, the WF1 semisubmersible generated power on par with an equivalent fixed-bottom turbine [137]. Also, the Hywind Demo spar required introducing a platform control system for above-rated wind speeds to reduce unacceptably large platform pitch displacements, although how this affected power generation is not documented [137].

5.3 Analytical models for power generation

Based on the simulation results in Section 5.2, simple analytical models are proposed for estimating the power generation from floating wind turbines in the below-rated operating region. As discussed in Section 5.2, the total floating effect on power generation is a combination of the effects of average $\overline{\phi}_{RC}$ displacement and dynamic x_{RC} displacement (caused by surge and pitch). The final proposed analytical model is a combination of two analytical submodels for each of these effects.

The proposed analytical models predict the difference between a floating wind turbine and an equivalent fixed-bottom turbine using basic momentum theory. First, recall the derivation for a fixed-bottom turbine's power, given by Equation 2.1. The power P_{fb} produced by a fixed-bottom turbine with no rotor displacement, in a uniform wind field of $\vec{U} = U\hat{\imath}$, is given directly from Equation 2.2:

$$P_{fb} = \frac{1}{2}\rho C_P A U^3. \tag{5.2}$$

If the rotor is moving or angled with respect to the wind, Equation 2.1 can be adapted by considering the reference frame of the turbine, where the rotor area $\vec{A}$ remains unchanged but the wind vector $\vec{U}$ becomes the relative wind velocity $\vec{U}_{rel}$. The instantaneous power coefficient C_P is also altered due to modified aerodynamic performance, but the simple analytical models presented here assume that C_P is constant over time, and also consistent between floating and fixed turbines.

5.3.1 Average ϕ_{RC} displacement model

The first model considers a rotor at an angle ϕ relative to a uniform wind field with wind speed U. In the reference frame of the rotor, the relative wind vector is $\vec{U}_{rel} = U\cos\phi\hat{\imath}$ and the rotor area is $\vec{A} = A\hat{\imath}$. Assuming a constant power coefficient C_P in Equation 2.1, the angled turbine's power is

$$P(\phi) = \frac{1}{2}\rho C_P \iint_A (U\cos\phi)^3 dA = P_{fb}\cos^3\phi. \tag{5.3}$$

If the angle ϕ is static over time, then Equation 5.3 directly gives the time-averaged power, assuming U is steady. This variety of $\cos^n\phi$ model is commonly used for angled rotors (especially rotors at a constant yaw) throughout the literature [135, 138], with $n = 3$ as a common exponent [135]. Different experiments suggest values of n varying from 1 to 5 for yawed rotors [135, 139].

On the other hand, if ϕ varies in time, the entire $P_{fb}\cos^3\phi$ term should be averaged to get the time-averaged $\overline{P}(\phi)$. Despite this, the proposed average pitch model assumes that the effect of a dynamically varying rotor angle $\phi(t)$ can be approximated by a constant rotor angle at the time-averaged value $\overline{\phi}$:

$$\overline{P}(\phi) = \overline{P}_{fb}\cos^3\overline{\phi}. \tag{5.4}$$

Equation 5.4 can be used to model how average rotor "pitch" $\overline{\phi}_{RC}$ changes power generation in floating wind turbines. In this case, the overall angle $\overline{\phi}$ between the

wind vector and the rotor disk should incorporate both the platform-induced angle ϕ_{RC} and the shaft tilt angle ϕ_t (5° for the NREL 5 MW reference turbine [119]). The shaft tilt angle is typically ignored in yawed rotor analysis, or implicitly included in P_{fb}. However, for a rotor with an average angle caused by platform pitch, the power is better modeled by explicitly including the shaft tilt angle as a constant rotor angle, for both the the floating turbine and the fixed-bottom turbine. In this situation, Equation 5.4 becomes

$$\overline{P}_{fb} = \overline{P}(\phi = 0)\cos^3\phi_t \tag{5.5}$$

for the fixed-bottom turbine and

$$\begin{aligned}\overline{P}(\overline{\phi}_{RC} + \phi_t) &= \overline{P}(\phi = 0)\cos^3(\overline{\phi}_{RC} + \phi_t) \\ &= \overline{P}_{fb}\cos^3(\overline{\phi}_{RC} + \phi_t)/\cos^3\phi_t\end{aligned} \tag{5.6}$$

for the turbine with an average pitch displacement. The shaft tilt angle can similarly be incorporated into a yawed rotor model. Note that this model predicts that a positive ϕ_{RC} always works to decrease the average power generation, which is consistent with the simulated results. Equation 5.6 is the proposed analytical model for describing the effect of average rotor angle ϕ_{RC} on power generation.

5.3.2 Dynamic x_{RC} displacement model

The second model considers a rotor perpendicular to the steady wind vector $\vec{U} = U\hat{\imath}$, moving forward and backward into the wind with motion $x_{RC}(t)$. The relative wind vector is $\vec{U}_{rel} = (U - \dot{x}_{RC})\hat{\imath}$ and the rotor area is $\vec{A} = A\hat{\imath}$. Assuming a constant power coefficient C_P in Equation 2.1, the moving turbine's power is

$$P(t) = \frac{1}{2}\rho C_P \iint_A (U - \dot{x}_{RC})^3 dA = \frac{1}{2}\rho C_P A(U - \dot{x}_{RC})^3, \text{ if } U \text{ is uniform over } A. \tag{5.7}$$

To further simplify the model, let the rotor velocity $\dot{x}_{RC}$ be modeled as a sine curve with angular frequency ω and amplitude V_{RC}, such that $\dot{x}_{RC} = V_{RC}\sin(\omega t)$. The time-averaged power is then obtained by integrating over one period:

$$\begin{aligned}\overline{P} &= \frac{\omega}{2\pi}\frac{1}{2}\rho C_P A \int_{-\pi/\omega}^{\pi/\omega} (U - \dot{x}_{RC})^3 dt \\ &= \frac{\omega}{2\pi}\frac{1}{2}\rho C_P A \int_{-\pi/\omega}^{\pi/\omega} \big(U - V_{RC}\sin(\omega t)\big)^3 dt \\ &= \frac{1}{2}\rho C_P A U^3 \left(1 + \frac{3}{2}\frac{V_{RC}^2}{U^2}\right) = \overline{P}_{fb}\left(1 + \frac{3}{2}\frac{V_{RC}^2}{U^2}\right),\end{aligned} \tag{5.8}$$

since the odd-powered sine terms in the cubic expansion integrate to zero. Note that this model predicts that x_{RC} motions always work to increase time-averaged power, which is consistent with the simulated results. The model given by Equation 5.8 is similar to analytical models proposed by Wen *et al.* for sinusoidal platform surge and sinusoidal pitch [132, 133]. However, the models by Wen *et al.* separate surge from pitch, rather than considering the rotor center velocity $\dot{x}_{RC}$ caused by both surge and pitch together. Wen *et al.*'s pitch model also explicitly assumes ϕ_{RC} is small enough that $\cos(\phi_{RC}) \approx 1$, which neglects the average pitch effect modeled by Equation 5.6.

Equation 5.8 can be used to model how dynamic x_{RC} displacements affect power generation for floating platforms. Numerical differentiation of $x_{RC}(t)$ produces a time history for the rotor center x-velocity $\dot{x}_{RC}(t)$, which can be approximated by a sine curve with amplitude V_{RC}, as in Equation 5.8. For these simulations, the $\dot{x}_{RC}(t)$ time history does not directly fit a sine curve well (see Figure 5.3). So, a proxy V_{RC} amplitude is computed from the RMS of the $\dot{x}_{RC}(t)$ time history using $V_{RC} = \sqrt{2}$ RMS$(\dot{x}_{RC})$, where the factor of $\sqrt{2}$ is determined by the ratio of amplitude to RMS for all sine curves. Equation 5.8 with the RMS approximation for V_{RC} is the proposed analytical model for describing the effect of dynamic x_{RC} displacements on power generation.

5.3.3 Total floating model: dynamic and time-averaged displacements

The final model considers a floating wind turbine's rotor that is free to move under the influence of all six platform degrees of freedom. As discussed in Section 5.2, the power generation of this rotor is predominantly affected by both the time-averaged rotor angle $\overline{\phi}_{RC}$ and dynamic x_{RC} displacements, caused by platform surge and pitch. To model the overall power difference between this floating turbine and an equivalent fixed-bottom turbine, the analytical model for average $\overline{\phi}_{RC}$ displacement (Section 5.3.1) is combined with the analytical model for dynamic x_{RC} displacements (Section 5.3.2).

Specifically, this total floating model treats the rotor as translating horizontally according to x_{RC}, while also angled at a constant value given by the time-averaged ϕ_{RC} (plus shaft tilt). In the reference frame of the rotor, the relative wind vector is then

$$\vec{U}_{rel} = \left(U + \dot{x}_{RC}\right) \cos(\overline{\phi}_{RC} + \phi_t)\hat{\imath} \tag{5.9}$$

and the rotor area is $\vec{A} = A\hat{\imath}$. Note that the $\cos(\overline{\phi}_{RC} + \phi_t)\hat{\imath}$ term in Equation 5.9 does not vary in time, so it can be moved outside the time integral when calculating the time-averaged power generation. Following similar steps as in Sections 5.3.1 and 5.3.2, the time-averaged power generated by this floating wind turbine is

$$\overline{P} = \overline{P}_{fb}\left(1 + \frac{3}{2}\frac{V_{RC}^2}{U^2}\right) \cos^3(\overline{\phi}_{RC} + \phi_t) / \cos^3 \phi_t, \tag{5.10}$$

assuming a constant C_P, an average rotor angle of $\overline{\phi}_{RC}$, a shaft tilt of ϕ_t, and a sine curve model for the rotor center velocity: $\dot{x}_{RC} = V_{RC} \sin(\omega t)$.

Equation 5.10 is the proposed model for how a floating wind turbine's power generation compares to a fixed-bottom turbine's power overall, including effects from both average rotor angle as well as dynamic x_{RC} displacements. For no rotor motion ($V_{RC} = 0$), this total floating model reduces to the average rotor angle model in

Equation 5.6. For no average rotor angle ($\overline{\phi}_{RC} = 0$), this total floating model reduces to the dynamic x_{RC} displacement model in Equation 5.8.

5.3.4 Analytical model performance

Figure 5.5 compares power gain predictions from the total-floating-effect analytical model in Equation 5.10 (striped bars) to the simulated power results discussed in Section 5.2 (solid bars), for both the spar and semisubmersible. The analytical model agrees with the simulations that the all-displacement spar cases show a significant power gain, although the semisubmersible only shows a small power difference (see Figure 5.5). However, this basic analytical model does not perfectly agree with the magnitude of the simulated power gains/losses.

For the case with only average $\overline{\phi}_{RC}$, the analytical model performs well, with a ratio of 0.99-1.02 between the analytical and simulated power losses (see Figure 5.5). This indicates that the analytical model can reasonably predict how a constant ϕ_{RC} angle affects power generation. For the case with only x_{RC} displacements, the analytical model also performs well, with a ratio of 0.96-1.06 between the analytical and simulated power losses (see Figure 5.5). This indicates that the dynamic displacement model with the RMS approximation for $\dot{x}_{RC}$ amplitude reasonably captures the simulated power gain due to dynamic x_{RC} displacements.

However, for the all-displacement cases which are more representative of a real turbine, the analytical model does not perfectly predict the power gain/loss magnitude, with ratios of 0.81-1.83 between the analytical and simulated power gains/losses (see Figure 5.5). This disagreement in power gain/loss magnitude indicates that the analytical model does not fully capture some simulated effect. Several adjustments to the model were attempted to address this disagreement:

- **Removing the sine approximation for $\dot{x}_{RC}$**: the simulated time history for $\dot{x}_{RC}$ was used in Equation 5.9 instead of using the sine curve approximation,

and then this time history was averaged over time to replace the $3V_{RC}^2/2U^2$ term in Equation 5.10.

- **Removing the constant-angle approximation for the average pitch effect**: as well as using the time history for $\dot{x}_{RC}$, the simulated ϕ_{RC} time history replaced the time-averaged angle $\overline{\phi}_{RC}$ in Equation 5.9 and then the entire term $(U + \dot{x}_{RC})\cos(\phi_{RC} + \phi_t)$ was averaged over time.

- **Removing the steady wind approximation**: the simulated time history for U at hub height was used instead of assuming steady wind, and then the entire term $(U + \dot{x}_{RC})\cos(\phi_{RC} + \phi_t)$ was again averaged over time using simulated time histories for U, $\dot{x}_{RC}$, and ϕ_{RC}.

However, these attempted adjustments did not clearly improve the model performance for power gain/loss magnitude. Possible reasons for the continued disagreement include assuming that C_P is constant, although C_P actually varies in time as the relative inflow wind fluctuates. This effect is difficult to capture with a model of comparable simplicity, but one possibility is to adjust the instantaneous C_P using an empirical relationship between C_P and tip speed ratio (possibly filtered and with a time delay to account for the variable-speed controller). Precursory attempts to predict the instantaneous power using the instantaneous platform or rotor displacements were not successful, possibly because of the influence of the variable-speed controller. The disagreement between the simulated and modeled average power may also be partially caused by only including the effect of instantaneous rotor angle ϕ_{RC} at the rotor center, rather than across the height of the rotor disk. This could explain why the analytical model performs better for the x_{RC}-only case, where platform pitch does not contribute to the x_{RC} displacements.

5.4 Summary and conclusions

In summary, OpenFAST simulations of the NREL 5 MW reference turbine are performed for three platform types: the OC3-UMaine spar, the OC4-DeepCWind semisubmersible, and a fixed-bottom counterpart with no platform displacements. These simulations examine how platform and rotor displacements, both dynamic and time-averaged, affect the average power generation of floating wind turbines for a single combination of a below-rated wind speed and extreme wave height. The main conclusions of this study are:

- Overall power gains or losses in floating OWTs are primarily caused by a balance between two competing effects:
  - Power decreases caused by average rotor pitch angle ($\overline{\phi}_{RC}$) driven by platform pitch, and
  - Power increases caused by dynamic rotor motions upwind-downwind (x_{RC}) driven by platform surge and pitch motions, which change the relative wind velocity at the rotor.
- Rotor displacements caused by platform sway, heave, roll, and yaw do not significantly affect the average power.
- Contrary to the common practice of isolating platform surge or pitch when studying floating platforms, surge and pitch must be enabled concurrently to accurately capture the power generated by floating OWTs, for two reasons:
  - Isolating surge or pitch changes displacement characteristics, and
  - Both surge and pitch contribute to the dynamic rotor motions upwind-downwind (x_{RC}).
- The spar's lower center of mass creates larger, pitch-dominated rotor motions upwind-downwind, which outweigh its larger average rotor pitch angle to cause

a 3.1%-4.5% power gain compared to a fixed-bottom wind turbine (for this below-rated wind speed).

- The semisub has smaller rotor motions upwind-downwind, which barely outweigh the smaller average rotor pitch angle to cause an insignificant (0.1%-0.2%) power gain.

- The simple analytical model proposed in Equation 5.10 reasonably predicts power differences caused by floating platforms, but the magnitude of the predicted gain/loss can be improved.

Overall, although predicting floating-turbine power is vital for floating wind farm design and economics, this study indicates that floating platforms do not provide universally significant power gains compared to fixed-bottom wind turbines; a closer analysis of details in the platform's displacement behavior is required for such a prediction. Future research in this area should examine additional environmental conditions, especially near-rated wind speeds and lower wave heights, which are expected to reduce the power gains observed for the spar. The trends observed here should be confirmed by field measurements, when available. Field measurements, experiments, and additional simulations with simplified environmental conditions could also inform significant improvements to the proposed analytical model, with a focus on a time-varying power coefficient and instantaneous pitch angle effects.

CHAPTER 6

FLOATING-TURBINE WAKE EFFECTS ON DOWNWIND TURBINES

The previous two chapters describe how wake characteristics behind a single turbine differ between floating and fixed-bottom OWTs (Chapter 4) and how power generation of a single turbine differs between floating and fixed-bottom OWTs (Chapter 5). Having identified that power generation is significantly affected by floating platform displacements, and that floating OWTs wakes have slightly different characteristics in the far wake (e.g. wake deflection upwards and higher TKE in the wake shear layer), a natural continuation is to consider the power generation and loads of a downwind floating OWT when placed in the wake of an upwind floating OWT. This extends the research from single-turbine behavior to multi-turbine interactions, which are vital to designing a floating wind farm array.

Recently, a small number of other studies explore the response of a waked downwind offshore OWT. Manolas *et al.* [53] simulate a partially-waked spar OWT using a free vortex method coupled with the engineering tool hGAST, while Lee *et al.* [14] conduct LES coupled with FAST for a partially and fully waked spar OWT. Wise and Bachynski [140] simulate fully waked spar, semisub, and tension-leg platform floating OWTs using FAST.Farm, a mid-fidelity tool that combines OpenFAST with dynamic wake meandering models.

Wise and Bachynski observe that yaw motions are excited by wake meandering when the downwind turbine is fully waked, but surge and pitch motions are also affected by upwards deflection in wake deficit due to time-averaged platform pitch

[140]. Both Manolas *et al.* [53] and Lee *et al.* [14] also observe that partially waked spar OWTs are excited in the yaw degree of freedom at rotor rotational frequencies. Lee *et al.* further conclude that partial waking also reduces power production and changes platform response beyond yaw [14].

Wise and Bachynski conclude that fatigue loads do not increase when fully waked at rated wind speed [140], but Lee *et al.* and Manolas *et al.* disagree, concluding that fatigue loads do increase when fully or partially waked [14, 53]. Lee *et al.* also note that fatigue loads are increased by placing the downstream turbine to the left of the wake rather than to the right, due to wake asymmetry [14].

Taken together, these studies indicate the need for high-fidelity simulations of fully- and partially-waked downwind floating OWTs, for multiple platform types. Although Wise and Bachynski simulate multiple floating platform types in turbulent sheared inflow, their wake characteristics are generated by engineering models rather than full LES, and they do not consider partial waking [140]. Manolas *et al.* use mid-fidelity vortex methods for partial waking, but are limited to a single platform type [53]. Lee *et al.* use high-fidelity LES for partial waking, but are also limited to a single platform [14].

Although these studies all examine a downwind OWT's platform displacements and structural loading, only Lee *et al.* address power generation [14], indicating the need for research into how wakes affect power generation for floating OWTs. These studies also use various turbines with different rated powers ranging from 3 MW to 10 MW, so further research for other turbine capacities could help identify universal trends as well.

The primary goal of this study is to identify how downwind floating and fixed-bottom OWTs differ in their power generation and structural loads, when placed in the wake of an upwind turbine. Key questions include:

- Do the floating wake differences described in Chapter 4 translate into significant differences in a downwind turbine's power generation or structural loads?
- Are differences in downwind power or loads caused predominantly by floating wake differences, or by the downwind platform's ability to move?
- Does the downwind turbine's location in the wake affect power or load differences between floating and fixed-bottom OWTs?
- Does floating platform type affect the downwind turbine's response?

6.1 Simulation setup

In this chapter, the NREL 5 MW reference turbine [119] is simulated in OpenFAST [106]. The turbine is mounted on the same three platforms simulated in Chapter 4: the OC3-UMaine spar [98], the OC4-DeepCWind semisubmersible [120], and a fixed-bottom baseline represented by disabling all platform displacements (see Section 4.2.1). These simulated turbines represent a downwind turbine within a wind farm array, located behind an upwind turbine. The upwind turbine is simulated in coupled SOWFA-OpenFAST LES, then the LES wake flow field is used as the inflow to OpenFAST simulations of the downwind turbine.

The SOWFA-OpenFAST simulations of the upwind turbine are the coupled LES simulations described in Section 5.1, with the same environmental conditions of turbulent, sheared, veered wind with 8 m/s hub-height wind speed and 8 m JONSWAP irregular waves. The wake from the upwind turbine is sampled at $7D$ downwind using a similar prerecorded inflow approach described in Section 5.1: a time series of 2D slices of the instantaneous velocity field is sampled at 16 Hz, converted to HAWC-format binary files, and then marched past the downwind turbine in OpenFAST to recreate the SOWFA wake flow field at the downwind rotor plane. The downwind turbine is simulated in the newer OpenFAST v2.5.0, but otherwise the downwind simulation inputs are the same as those described in Section 5.1. The downwind turbine

in OpenFAST is subjected to the same wave conditions as the upwind turbine, but with a different realization of a wave train with the same JONSWAP characteristics.

6.1.1 Case descriptions

A total of ten different two-turbine configurations are simulated. Three simulations are performed where the upwind and downwind turbines are mounted on matching platform types: spar-spar, semisub-semisub, and fixed-fixed. An additional two simulations use inflow from spar and semisub upwind turbines, but with a fixed downwind turbine; this mixed configuration addresses whether any differences in the downwind turbine response are caused primarily by floating wake characteristics, or by the downwind platform type. For all five of these upwind-downwind configurations, one case simulates the downwind turbine located directly downwind of the upwind turbine, representing a fully-waked downwind turbine. A second case shifts the downwind turbine $0.5D$ to the right, representing a half-waked downwind turbine. Table 6.1 summarizes these ten different cases.

Table 6.1. Summary of cases for two-turbine simulations.

Case	Upwind platform	Downwind platform	Downwind location
1a / 1b	Fixed	Fixed	Fully-waked / Half-waked
2a / 2b	Spar	Spar	Fully-waked / Half-waked
3a / 3b	Semisub	Semisub	Fully-waked / Half-waked
4a / 4b	Spar	Fixed	Fully-waked / Half-waked
5a / 5b	Semisub	Fixed	Fully-waked / Half-waked

6.2 Simulation results

For each simulated case in Table 6.1, the downwind turbine behavior is analyzed through time histories of its power generation, blade loads, and towertop displacements. The first 10 minutes of each simulation are discarded to remove transient start-up effects, leaving the remaining 60 minutes for analysis. These 60-minute

time histories are quantified by their average, minimum, and maximum values. The root-mean-square (RMS) is also calculated for each time history to help quantify the amplitude of fluctuations over time, similar to the analysis performed in Chapters 4 and 5. The frequency contents are also compared using Fourier analysis.

6.2.1 Downwind power and loads

Figure 6.1 plots the time-averaged value of the downwind turbine's power generation, in-plane blade root bending moment, out-of-plane blade root bending moment, towertop fore-aft displacement, and towertop side-to-side displacement. The left column compares the fully-waked cases with different upwind-downwind configurations: for example, 1:spar/2:fixed refers to the case with an upwind spar turbine and downwind fixed turbine. The right column compares the half-waked cases. For each case, the minimum-maximum spread of the time history is represented by vertical lines, and the RMS values are shown as horizontal bars added and subtracted from the average value. Note that the towertop displacements do not include the contribution from floating platform motions, and the blade root moments are from one blade.

Table 6.2 also quantifies how the average values differ between the baseline fixed-fixed case and the other cases, using the percent difference from the fixed-fixed value. Table 6.3 similarly examines the percent difference of the RMS values compared to the baseline fixed-fixed case. As indicated in Figure 6.1 and Table 6.2, the time-averaged values of the generated power, blade root loads, and towertop displacements are fairly similar for all cases with a fixed downwind turbine: the average values for the spar-fixed and semisub-fixed cases are within 3.5% of the fixed-fixed value. For the spar-fixed and semisub-fixed cases, the fully waked configuration produces larger differences from the baseline than the half-waked configuration does, but only in the towertop displacements.

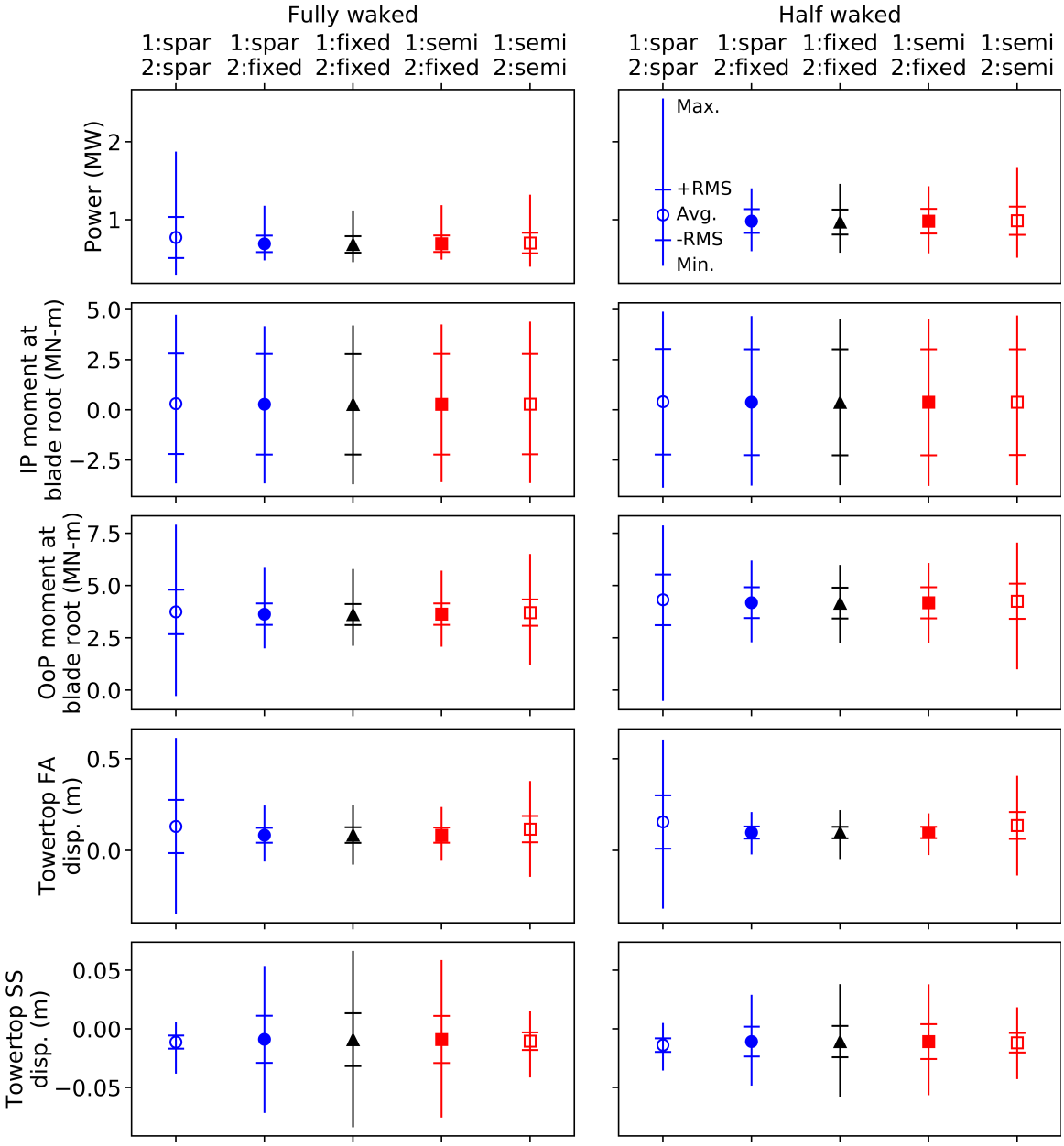

Figure 6.1. The average (symbols), root-mean-square (−), and minimum-maximum (vertical lines) of time histories for power generation, blade root bending moments, and towertop displacements (not including platform displacements) of the downwind turbine for different simulated cases.

In contrast, cases with a floating downwind turbine have average values that differ significantly from the fixed-fixed baseline, especially for the spar-spar case and for towertop displacements. In particular, the spar-spar case generates up to 13.0% more average power than the baseline fixed-fixed case, due to the downwind spar turbine

Table 6.2. Percent difference in time-average value compared to the baseline case with fixed platforms for both upwind and downwind turbines.

	Fully waked				**Half waked**			
Upwind platform	spar	spar	semi	semi	spar	spar	semi	semi
Downwind platform	spar	fixed	fixed	semi	spar	fixed	fixed	semi
Power	13.0%	1.1%	1.4%	2.7%	9.5%	1.3%	1.2%	1.8%
IP blade root moment	11.0%	1.7%	1.7%	3.7%	7.2%	1.2%	1.1%	1.8%
OoP blade root moment	3.5%	0.4%	0.5%	2.5%	3.8%	0.6%	0.4%	2.2%
Towertop FA disp.	55.7%	-1.3%	-0.5%	38.2%	59.1%	0.3%	0.3%	39.6%
Towertop SS disp.	22.8%	-3.5%	-1.7%	13.8%	28.0%	-0.5%	-0.1%	9.4%

Table 6.3. Percent difference in root-mean-square (RMS) value compared to the baseline case with fixed platforms for both upwind and downwind turbines.

	Fully waked				**Half waked**			
Upwind platform	spar	spar	semi	semi	spar	spar	semi	semi
Downwind platform	spar	fixed	fixed	semi	spar	fixed	fixed	semi
Power	149.8%	0.1%	0.2%	25.2%	102.7%	-4.6%	-1.2%	13.5%
IP blade root mom.	-0.2%	0.0%	-0.1%	-0.2%	-0.5%	-0.1%	-0.1%	-0.4%
OoP blade root mom.	111.4%	2.0%	2.2%	25.3%	64.6%	-0.2%	0.8%	14.0%
Towertop FA disp.	242.1%	-4.2%	-2.7%	69.2%	365.8%	6.1%	-1.1%	134.8%
Towertop SS disp.	-75.3%	-11.0%	-11.0%	-66.8%	-56.8%	-4.9%	11.4%	-37.8%

gaining additional rotor velocity as documented in Chapter 5. The in-plane blade root bending moment is likewise up to 11.0% larger in the spar-spar case than in the baseline fixed-fixed case. In general, the percent difference between the spar-spar case and the baseline case is an order of magnitude larger than the percent difference between the spar-fixed case and the baseline case (see Table 6.2). This indicates that for the spar, the floating platform motions of the downwind turbine have a much larger influence on the downwind turbine behavior than any changes to the wake initiated by an upwind floating turbine.

However, the floating motions of the downwind semisub only moderately increase the average power gain and in-plane blade root bending moment, with the semisub-semisub case generating up to 2.7% more power than the baseline versus the semisub-fixed case generating up to 1.4% more power than the baseline already. Still, the semisub-semisub out-of-plane blade root bending moment and towertop displacements

increase much more significantly compared to the baseline: the percent difference between the semisub-semisub case and the baseline is again an order of magnitude larger than the difference between the semisub-fixed case and the baseline, for these load and displacements average value (see Table 6.2). The platform motions of the downwind turbine again significantly influence the downwind turbine's behavior, but are comparable to the floating wake's influences on power generation and in-plane blade root moments only.

Comparing between the half-waked and fully waked cases, the platform type of the downwind turbine affects the downwind power and loads slightly more in fully waked cases. This suggests that the downwind platform type is even more important, compared to the upwind platform type and associated wake characteristics, for a fully waked configuration.

As shown in Figure 6.1 and Table 6.3, the RMS values also differ from the baseline case significantly more for cases with a floating downwind turbine, compared to cases with a fixed downwind turbine. For example, the spar-spar case power RMS is 150% larger than the baseline fixed-fixed power RMS, while the spar-fixed power RMS is only 0.1% larger. A similar trend occurs for the semisub cases, although not as drastically. This indicates that the large RMS values in the floating-floating cases are caused mainly by the platform motions of the floating downwind turbine. These RMS trends hold true for power, out-of-plane blade root bending moment, and the towertop displacements, but not for the in-plane blade root bending moment RMS which is virtually identical across all cases.

Comparing between the half-waked and fully waked cases, the upwind turbine type affects the RMS power more for half-waked cases. For example, the spar-fixed power RMS is only 0.1% larger than the baseline for the fully waked configuration, but is 4.6% smaller than the baseline for the half-waked configuration. However, this observation does not consistently hold true for blade moment or towertop displace-

ment RMS values. In general, there is not a universal trend in how half-waked versus fully waked placements affect the RMS differences from the baseline case.

Overall, the downwind platform motions affect the downwind turbine average and RMS behaviors much more than any wake changes caused by a floating upwind turbine. One exception is the semisub average power, which is affected only slightly more by the downwind platform type than by the upwind wake type.

6.2.2 Frequency analysis of downwind turbine behavior

In addition to the average and RMS values, the time history frequencies of the power, blade root bending moments, and towertop displacements are also compared across the different cases. For example, Figure 6.2 plots a Fourier transform of the out-of-plane blade root bending moment time history for each different case.

As shown in Figure 6.2, cases with fixed downwind turbines have similar frequency responses in this blade root moment, with the expected peak at the 1P blade passing frequency. There are not substantial differences in frequency content between the downwind fixed cases with floating upwind turbines and the baseline fixed-fixed case. However, cases with floating downwind turbines, i.e. the spar-spar and semisub-semisub cases, have additional frequency content due to the downwind platform motions. A similar trend is observed in Fourier transform results for the power generation (see Figure 6.3), in-plane blade root bending moments (see Figure 6.4), and both towertop displacements (see Figures 6.5 and 6.6): cases with fixed downwind turbines have very similar frequency content, regardless of upwind turbine type, and the frequency content of some downwind behaviors only differs when the downwind turbine is floating.

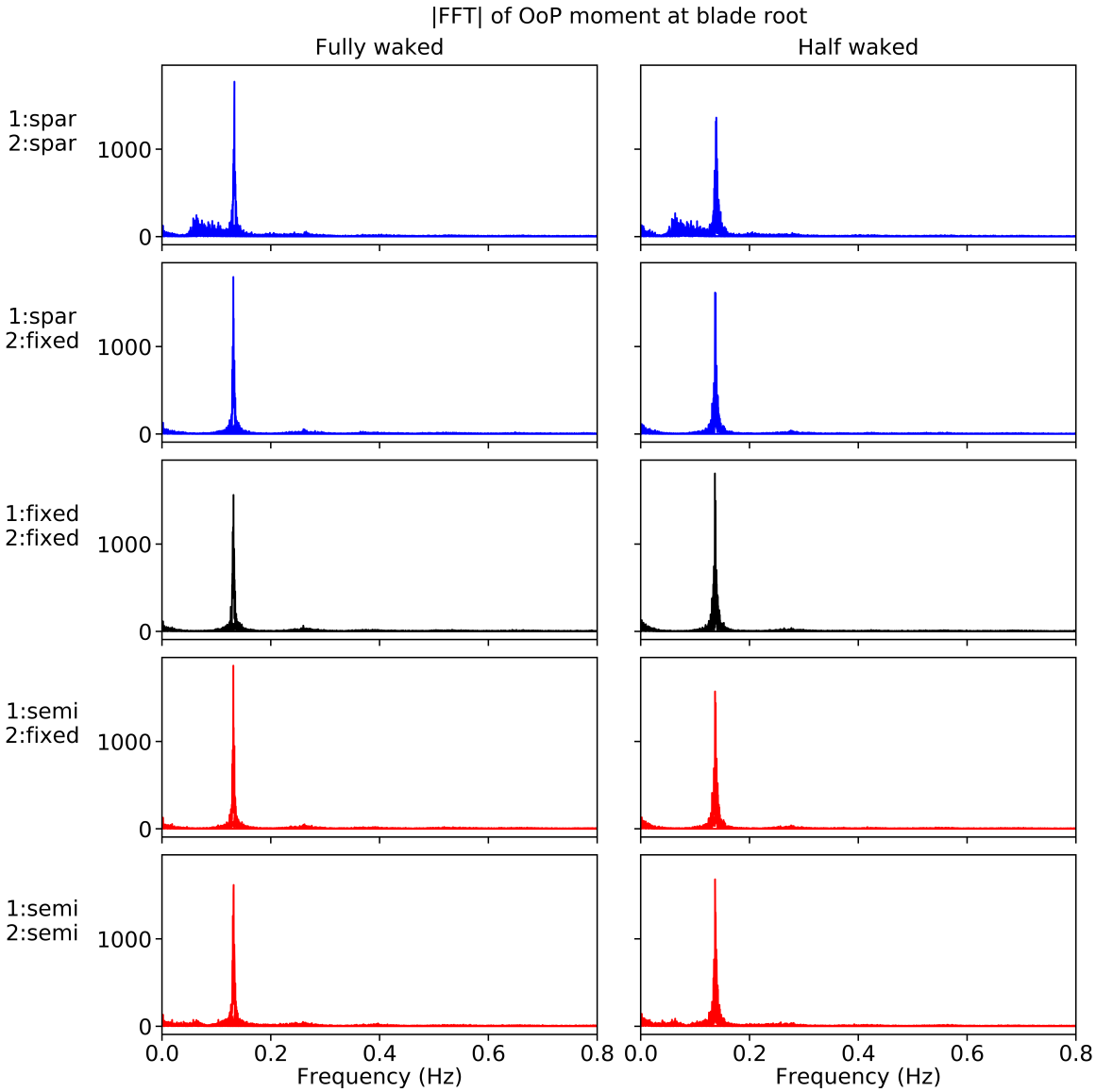

Figure 6.2. Fourier transform of the out-of-plane blade root bending moment time history for each simulated case.

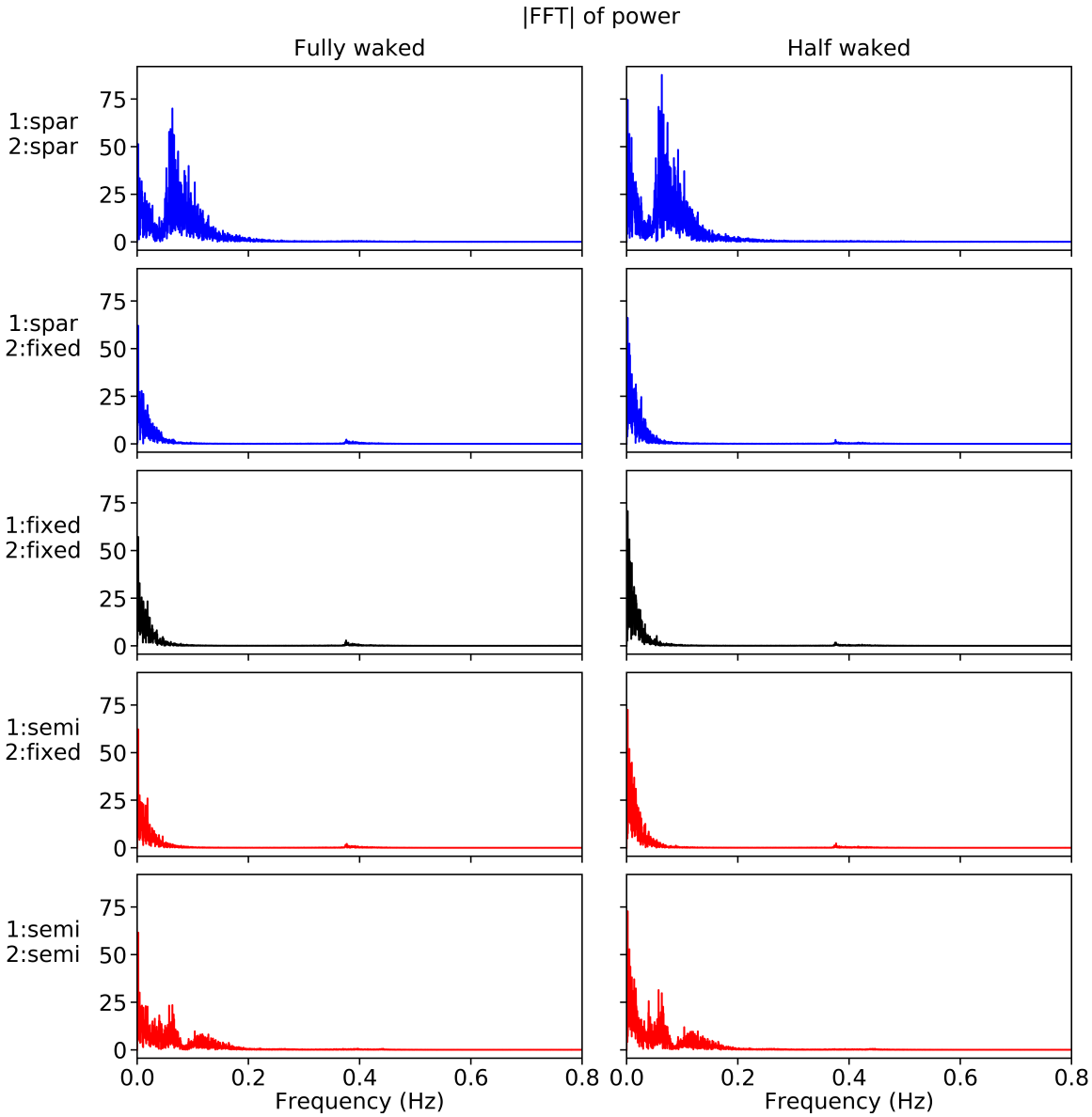

Figure 6.3. Fourier transform of the power generation time history for each simulated case.

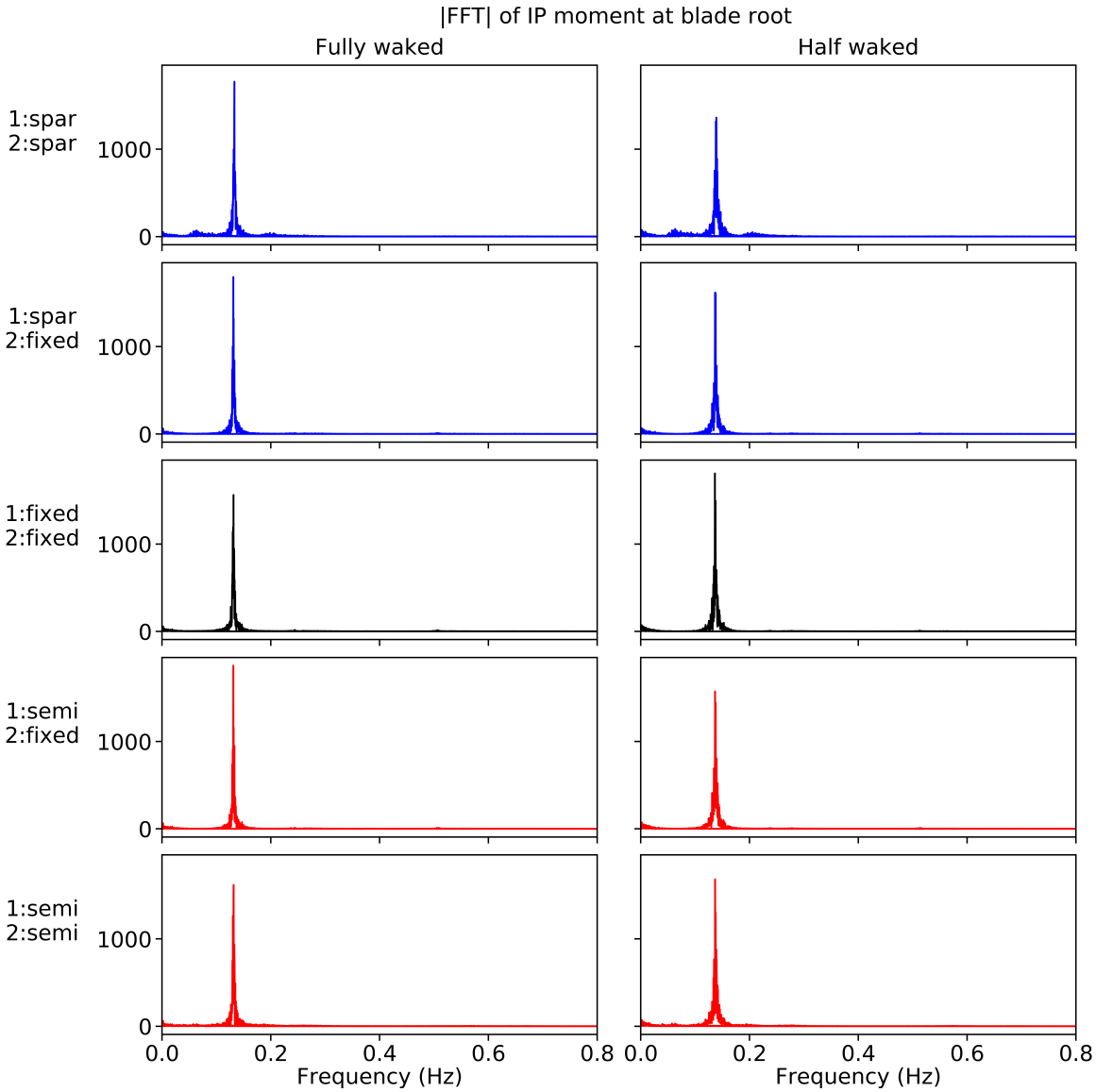

Figure 6.4. Fourier transform of the in-plane blade root bending moment time history for each simulated case.

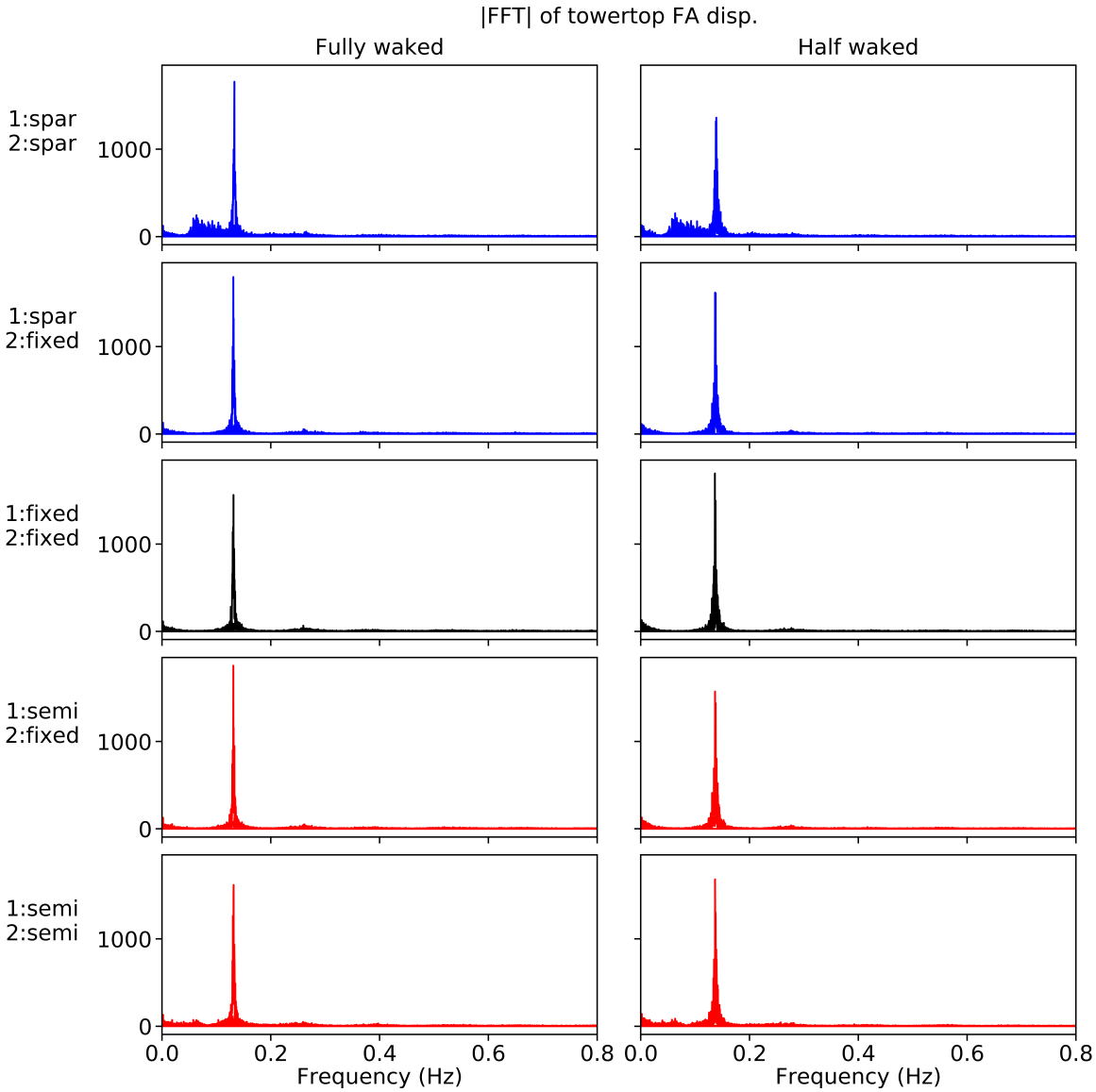

Figure 6.5. Fourier transform of the towertop fore-aft displacement time history for each simulated case, not including platform displacements.

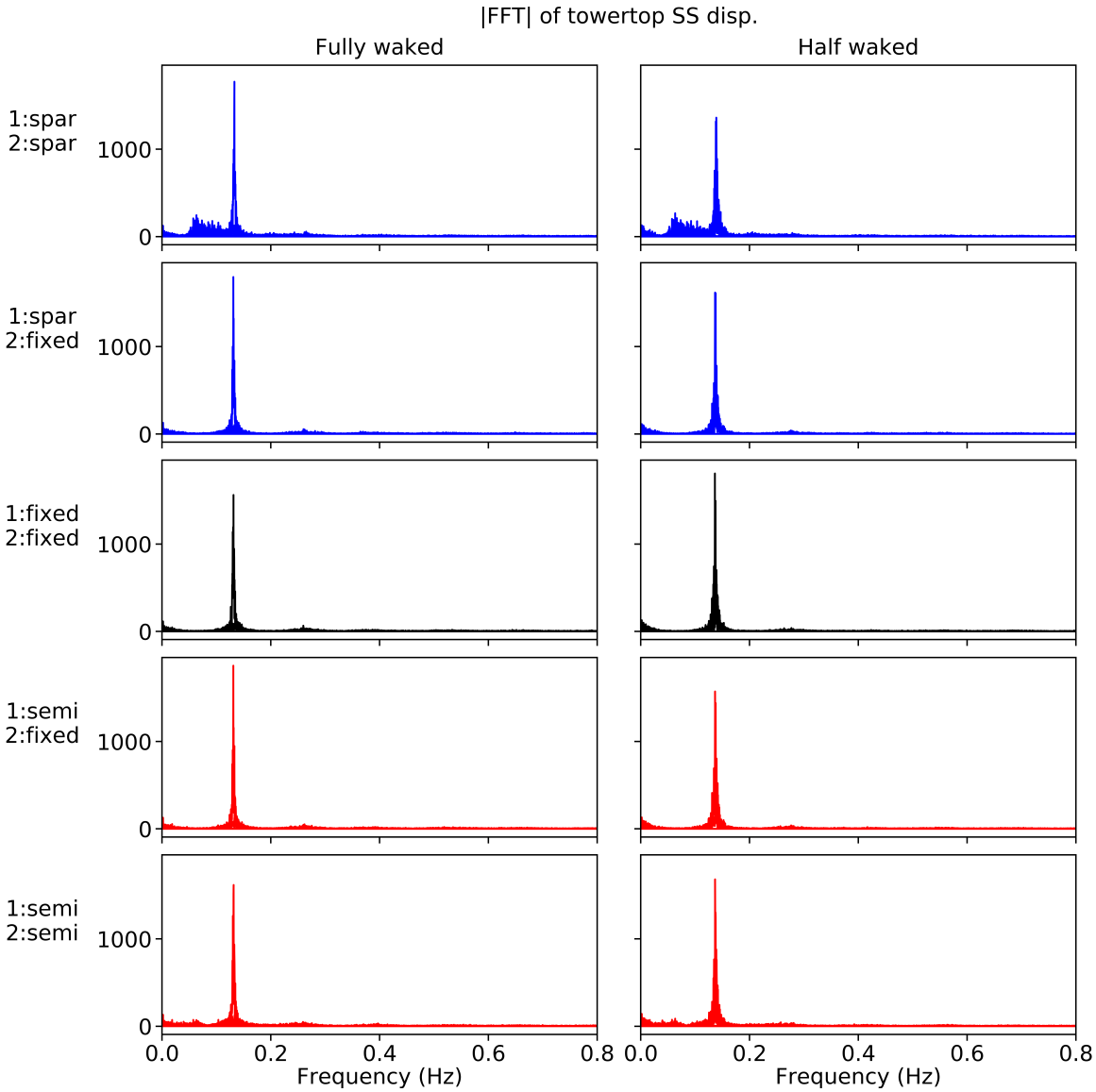

Figure 6.6. Fourier transform of the towertop side-to-side displacement time history for each simulated case, not including platform displacements.

6.3 Summary and conclusions

In summary, a two-turbine configuration of the NREL 5 MW reference turbine is simulated using OpenFAST for the downwind turbine and coupled SOWFA-OpenFAST LES for the upwind turbine. The power generation, blade root bending moments, and towertop displacements of the downwind turbine are compared between cases with spar, semisub, and fixed platforms for both turbines, as well as mixed cases with a fixed downwind turbine and a floating upwind turbine. Fully waked downwind turbines, which are located directly downwind of the first turbine, are also compared to half-waked downwind turbines, which are located $0.5D$ to the right of the first turbine.

The main finding of this study is that the downwind turbine behavior is affected much more by the downwind platform type than by the upwind platform type, and any associated changes to the wake. Specifically, the power, blade loads, and towertop displacement characteristics are fairly similar across all cases with a downwind fixed turbine, regardless of the upwind turbine type, with slight differences in average values (<4%) and somewhat larger differences in RMS values (up to 11%). The frequency content is also very similar for all cases with a fixed downwind turbine. However, any differences between floating-fixed cases and the fixed-fixed baseline are usually much smaller (i.e. from half as large, to an order of magnitude smaller) than differences between floating-floating configurations and the baseline, especially for the spar platform.

In conclusion, for both fully and half-waked downwind turbines, the platform type of the downwind turbine affects the downwind turbine behavior much more than any wake changes caused by a floating upwind turbine. Therefore, when modeling floating wind farm arrays, it may be acceptable to approximate the floating wake using fixed-bottom wake models that do not address how a floating upwind turbine changes the wake.

CHAPTER 7

WAKE CHARACTERISTICS FOR TILTED ROTORS

Wake steering is a potential control strategy to increase power generation in wind farm arrays, by reducing wake losses at downwind turbines [13]. Yaw-based wake steering, in which the wake is deflected horizontally, is the most prominent method researched to date, with many studies documenting the associated power gains [13, 126, 138, 141–144]. Several studies also document the key characteristics of the curled wakes that result from yaw-based wake steering: the wake deflecting in the opposite direction of the rotor orientation [141, 145–148], the "bean"-like curled wake shape [35, 146, 148, 149], and the cross-flow features that appear as a pair of counter-rotating vortices in the curled wake [35, 145, 148, 149].

Similarly to turbine yaw, another option to steer wakes away from downwind turbines is vertically deflecting the wake using turbine rotor tilt. Specifically, tilting the rotor top forward into the wind steers the wake downwards [11–13]. This positive rotor tilt angle may be accomplished using either downwind-style turbines with built-in tilt, or appropriately ballasted floating support structures for OWTs. The downward wake trajectory entrains high-speed air from above the wind farm, which increases the wind power available to downwind turbines, offering a potential advantage over yaw-based wake steering [11]. However, downward wake trajectories can cause wake interactions with the ground or sea surface [150], which are exacerbated by increasing rotor diameters without commensurate hub-height increases [151].

Several existing studies use high-fidelity CFD to model the wakes of tilted rotors, including LES in SOWFA by Annoni *et al.* [11] and Fleming *et al.* [12, 13], as well as

ANSYS simulations by Weipao *et al.* [126]. These studies agree that downward wake steering using rotor tilt can increase the overall power generation of a wind farm array. While these studies do reasonably capture surface effects through variants on a wall boundary condition for the bottom surface, their results focus on power generation rather than characterizing wake behavior.

Other research by Storm [150] compares high-fidelity LES of tilted rotor wakes in SOWFA to engineering wake models implemented in FLORIS, a popular wake modeling tool developed by NREL. Storm concludes that engineering models like FLORIS may overestimate power gains due to rotor tilt control, because the models lack a realistic ground model, so the wakes simply disappear into the ground [150]. Storm suggests mirroring wakes about the ground to prevent the wakes disappearing [150], although this approach does not necessarily capture surface effects accurately.

Overall, the literature indicates that rotor tilt can increase wind farm power generation, but that current approaches to modeling surface effects in engineering wake models are inadequate for tilted rotor wakes. Furthermore, while power gains from tilt-based wake steering are well-documented and tilted wakes are qualitatively described, more quantitative measures of curled wake features are needed for engineering model comparison and validation. These existing studies also establish high-fidelity LES using SOWFA as an appropriate tool to study wake effects for vertically tilted rotors. Taken together, the existing literature suggests the need to better characterize surface effects on tilted rotor wakes using high-fidelity LES, to inform future improvements to engineering wake models.

This chapter aims to describe the characteristics of vertically curled wakes from tilted rotors, and examine how these wakes interact with the ground or sea surface when they are deflected downwards. Specifically, this research addresses the following questions:

- What are the key characteristics of tilted wakes?

- How is a tilted wake affected by the ground or sea surface?
- What quantitative measures can be used to characterize curled wakes?

To answer these questions, the IEA 15 MW reference turbine [152] is simulated at several tilt angles and surface gap distances, using LES in SOWFA [104] with an ADM for the rotor. Section 7.1 describes the simulation setup, including details on the rotor model, the simulation domain, the background ABL, and case descriptions. Section 7.2 presents the simulation results for the wake geometry, downwind velocity deficits, wake circulation, and downward momentum flux from above the wake. Finally, Section 7.3 summarizes conclusions about the characteristics of wakes from tilted rotors.

7.1 Simulation setup

The wakes of tilted rotors are simulated using LES in SOWFA [104], which is described in detail in Section 4.1.2. The simulation workflow in this study consists of three main steps, similar to the workflow described in Chapter 4. First, SOWFA LES is performed for the ABL in a large domain with no rotor, which develops the wind shear profile and large background turbulence structures. Second, this initial "precursor" simulation is continued for additional simulation time, which records a time history of the flow field at the upwind domain boundary face. Third, SOWFA LES of the wind turbine wake is performed with an actuator disk model for the rotor. This third SOWFA simulation is initialized using free-stream flow field data generated by the first step, and the upwind boundary inflow is prescribed according to the boundary time history from the second step. This workflow is similar to that used by Lee *et al.* [14], among other studies.

7.1.1 Precursor atmospheric simulation

The precursor LES develops the wind profile and turbulence structures of an offshore ABL with neutral stability, capped by a stable inversion at an elevation of 750 m. The same precursor simulation used in this chapter is identical to that used in Chapters 5–6. At a hub height of 150 m, the wind speed is 8.3 m/s and the turbulence intensity is 3.4%, with a wind shear of 0.03 m/s/m and a wind veer of 0.05°/m across the height of the rotor disk. See Figure 5.1 for how these quantities vary with elevation.

7.1.2 Domain setup

Following the precursor simulation, a set of simulations is performed with an actuator disk model to represent a wind turbine. These LES cases simulate the turbine wake for 70 minutes with a timestep of 0.0625 s, using the precursor flow field as an initial condition. The simulation domain is $11D$ long by $8D$ wide by 1 km tall, with the turbine located $4D$ from the upwind boundary and centered laterally in the domain. The uniform cubic mesh has a 10 m cell size, with two additional mesh refinement regions. In the wake region, the mesh is refined to 5 m cells within a $1.875D$-wide box that starts $2D$ upwind of the rotor and extends to $6.1D$ downwind of the rotor, with height reaching from the lower boundary to 105 m above the top of the rotor disk. In the rotor region, the mesh is refined to 2.5 m cells within a $1.125D$-wide box that extends $1D$ upwind and $1D$ downwind of the rotor, with a height from the lower boundary to 30 m above the top of the rotor disk. Figure 7.1 illustrates the key features of the simulation domain, including the locations of the rotor disk and mesh refinement regions for a rotor with 150 m hub height and 30° tilt. Figure 7.1 also includes a slice through the rotor center of the instantaneous velocity field.

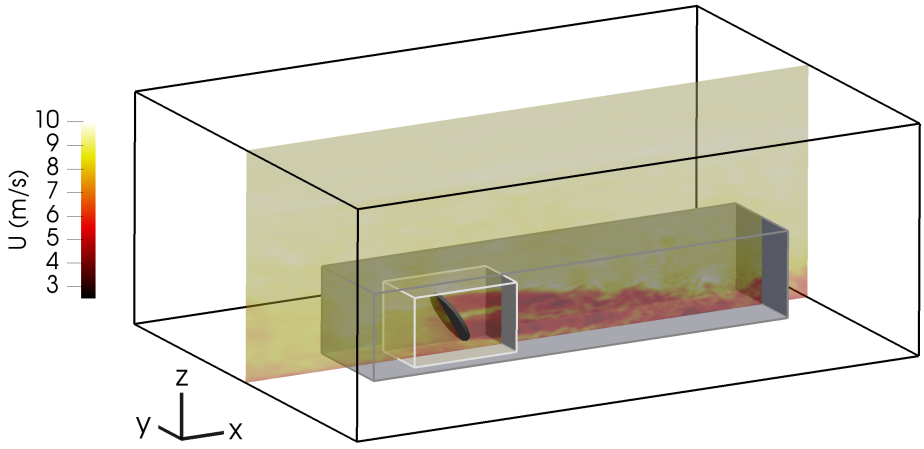

Figure 7.1. Simulation domain (outer black box) with mesh refinement regions around the wake (middle grey box) and rotor (inner white box) for a 30° tilted rotor. A snapshot of the velocity field is shown for a slice through the rotor center.

The floor boundary condition is the same rough-wall model as in the precursor simulation, while the upper boundary is an inlet/outlet condition to permit downward entrainment due to the tilted rotor. The lateral side boundaries are periodic, so that the simulation represents a row of wind turbines with $8D$ lateral spacing. The upwind side boundary uses an inflow condition with values prescribed using the precursor time histories, and the downwind side boundary uses an outflow condition with zero normal gradients. In Figure 7.1, the inflow boundary is the front left domain face.

7.1.3 Actuator disk model

For these LES cases, the wind turbine rotor is modeled using the ADM described by Martínez-Tossas *et al.* [125]. The rotor disk is discretized into a radial grid with 120 sectors from blade root to tip, similar to the ALM of Sørenson and Shen [68]. The drag and lift forces are calculated from the airfoil characteristics at each sector, and then projected onto the LES flow field as body forces in the momentum equation using a 3D Gaussian kernel at each rotor point. The width of this Gaussian projection is set

to 5.1 m, which is slightly more than twice the local cell size to maintain numerical stability, as recommended by Troldborg [116] and Churchfield *et al.* [55].

For these simulations, the wind turbine controllers are simplified to a lookup table relating the generator speed to generator torque, based on the rotor performance values from steady-state OpenFAST simulations provided in the IEA 15 MW reference turbine documentation [152]. The simulated wind speeds remain below the rated 10.59 m/s for this turbine [152], so the blade pitch remains at 0°. Yaw control is also disabled.

7.1.4 Overview of cases

Using this LES framework in SOWFA, five different cases are simulated. First, IEA 15 MW rotors with tilt angles of 0°, 15°, and 30° are simulated at a hub height of 150 m, the standard hub height for the IEA 15 MW reference turbine [152]. Second, the hub height is increased to 180 m for tilt angles of 0° and 30°, which doubles the gap between the lower boundary and the bottom of the rotor from 30 m to 60 m.

7.2 Simulation results

7.2.1 Wake location and size

For all simulated wakes, the initial 10 minutes are discarded to remove transient start-up effects, and the wake behavior is averaged over the remaining 60 minutes. First, the wake is identified using the velocity deficit $\vec{U}_d = \vec{U} - \vec{U}_\infty$. In this chapter, the wake volume is defined as all points where the x-component of the velocity deficit U_d is at least 10% of the hub-height free-stream wind speed. The edge of the wake is the outermost points of the wake volume. The wake center is calculated as the U_d-weighted coordinate average of a box around the wake. Figure 7.2 shows color contours of U_d for cross-sections of the wake at different downwind locations from

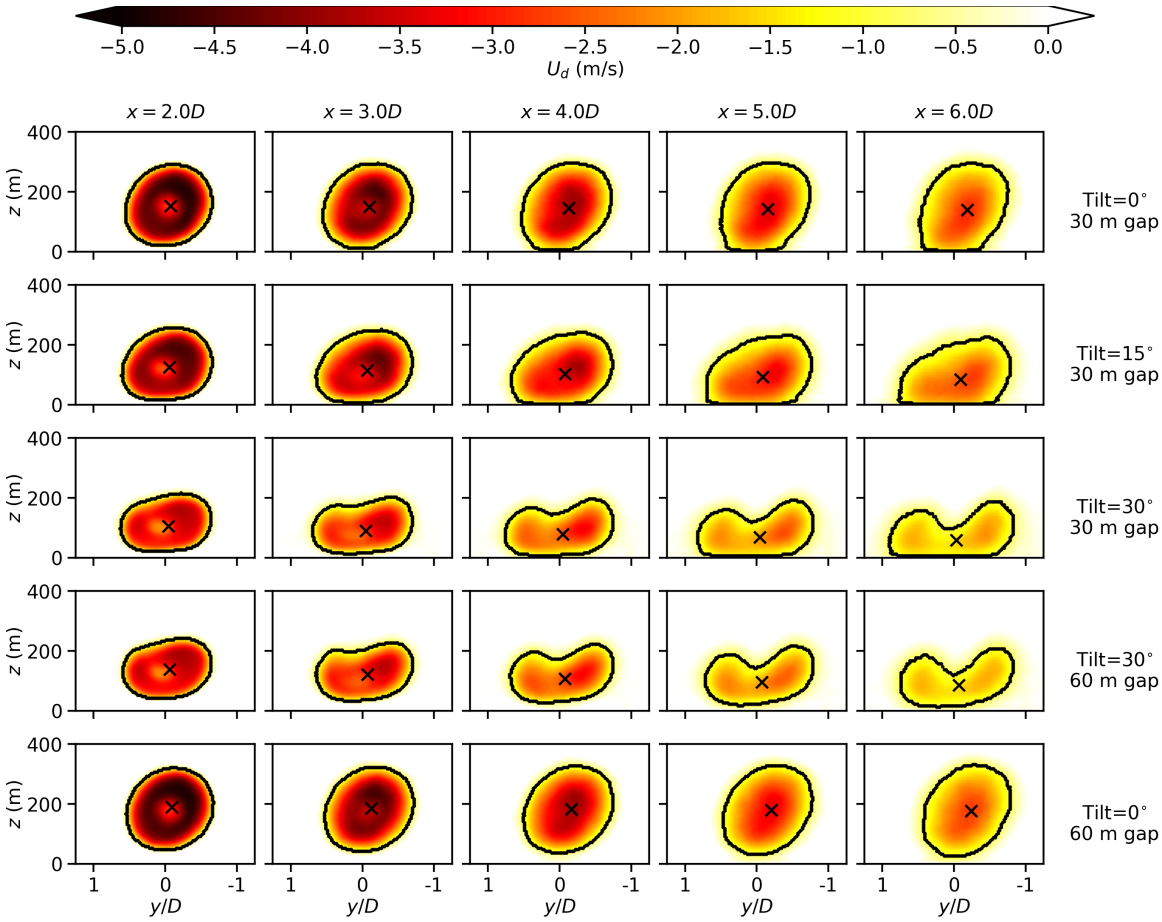

Figure 7.2. Velocity deficit contours with wake edges and wake centers marked in black, at different downwind cross-sections through the wake for each simulated case.

x=2D to x =6D, for each of the five cases. The wake edges and wake centers are also shown for each cross-section.

Figure 7.2 illustrates that the tilted wakes behave as documented in the literature [11–13, 126, 150], with positive rotor tilt causing downward wake steering and the bean-like curled wake shape. The effect of the free-stream wind veer (see Figure 5.1) is evident in the diagonal stretching and lateral asymmetry of the wake in all cases.

To more directly compare wake size and shape between the five cases, Figure 7.3 plots just the wake edges and centers for different downwind cross-sections. The top row compares the three cases with the standard hub height of 150 m across different tilt angles, while the bottom row compares the 0° and 30° tilt cases at the increased hub height of 180 m at to the corresponding tilts at the standard hub height.

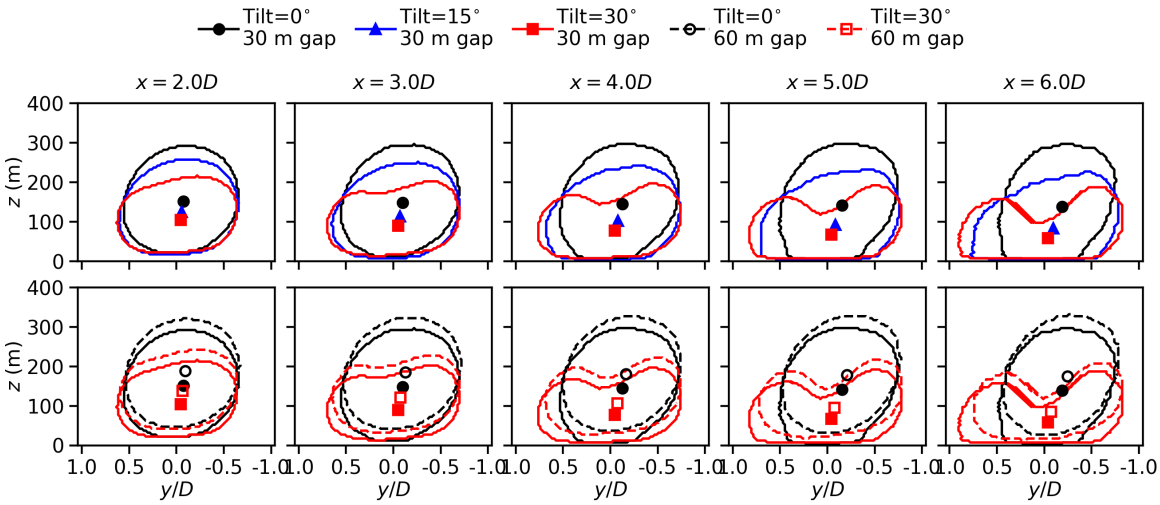

Figure 7.3. Wake edges and centers at different downwind cross-sections for different tilt angles (top) and different surface gaps (bottom).

As illustrated in Figure 7.3, larger tilt angles deflect the wake downward. For example, at $6D$ downwind, 15° tilt at a hub height of 150 m causes the wake center to move downward by $0.23D$ relative to the non-tilted case, while 30° tilt causes the wake center to move downward by $0.33D$. When the surface gap is doubled by increasing the hub height, at $6D$ downwind the wake center moves downward by $0.38D$ compared to the non-tilted case. This indicates that the presence of the surface limits the downward deflection of tilted wakes, as expected. Also, when the tilted wakes are steered downward, the free-stream wind veer causes the wake center and overall wake area to shift leftward compared to the non-tilted cases.

As shown in the top row of Figure 7.3, larger tilt angles cause shorter, wider wakes as the wake curls into the bean-like shape. For example, at $6D$ downwind, the 15° tilted wake is 25% wider and 24% shorter than the non-tilted rotor, while the 30° tilted wake is 38% wider and 39% shorter. Examining the bottom row of Figure 7.3, a larger surface gap reduces the wake shortening and widening caused by rotor tilt. For example, at $6D$ downwind, the 30° tilted wake is only 29% wider and 36% shorter than the non-tilted rotor when the hub height is 180 m, compared to 38% wider and

39% shorter when the hub height is 150 m. Physically, smaller surface gaps flatten tilted wakes more, because the surface interacts more with the wake.

7.2.2 Wake shape

In addition to changing the wake location and size, rotor tilt affects the wake shape as well. The larger 30° tilt angle results in the classic bean-shape associated with curled wakes, as illustrated in Figures 7.2 and 7.3. Although other studies have identified this bean shape qualitatively [35, 145, 148, 149], it is uncommon to quantify the shape in a way that can be compared across models or studies. To this end, an approach for quantifying curled wake shapes is proposed, based on a similar approach used by Bradshaw *et al.* for droplet characterization [153].

First, the wake edge coordinates are converted to polar coordinates r and θ, with the wake center serving as the origin and θ=0 aligned with the y-axis. Second, the polar coordinates are shifted (i.e., the wake is rotated) so that θ=0 corresponds to the minimum r-value. Third, a sixth-degree Legendre polynomial is fit to the shifted r-θ curve. Figure 7.4 shows the rotated polar coordinates of the wake edges at $2D$, $4D$, and $6D$ downwind for the three cases with a standard hub height of 150 m. The Legendre polynomial fits are overlaid in red, with vertical lines indicating the rotated θ=0 value (black dashed) and the original θ=0 value (grey dotted) for each case and downwind location.

Comparing Figures 7.3 and 7.4, sixth-degree Legendre polynomials provide a good fit for non-tilted wakes and for less extreme curled wakes, such as the 15° wake and even the 30° wake at $x = 2D$ and $4D$. The poor fit for the extremely curled wake at 30° farther downwind indicates that the wake has completely departed from a circular shape. In general, the larger the amplitude in the r-θ plots, the more bean-like the wake shape. In the future, coefficients from Legendre polynomial fits could be used to quantitatively compare wake shapes from different models, or even perhaps tune

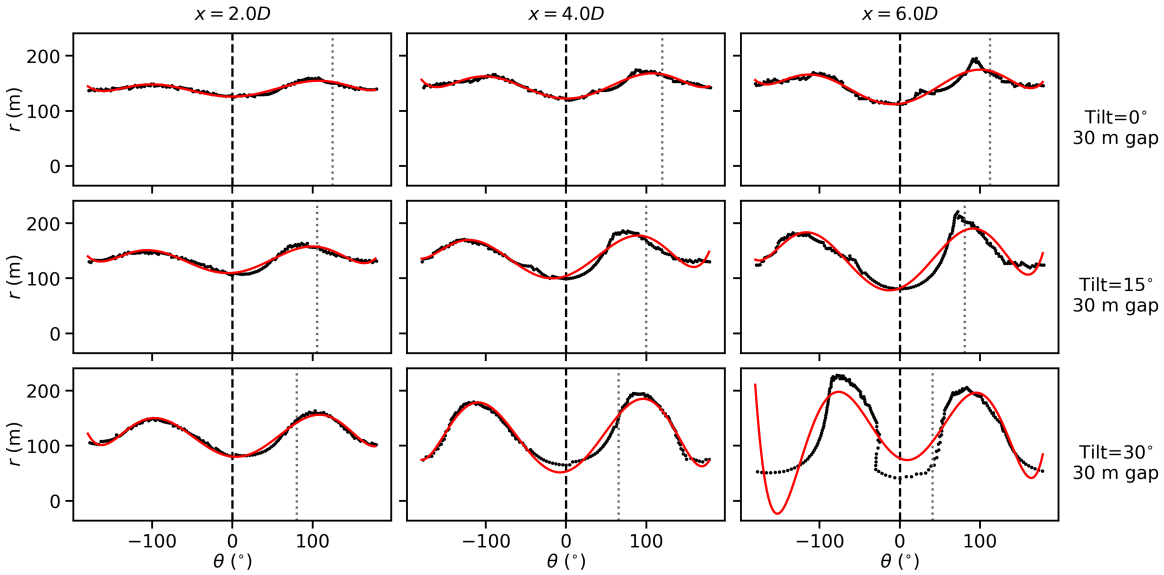

Figure 7.4. Sixth-degree Legendre polynomial fit (red) to wake edge polar coordinates (black), for a selection of downwind locations and cases. The rotated θ=0 location (black dashed) and original θ=0 location (grey dotted), are also shown.

wake shapes in an engineering model for curled wakes. Even without fitting, the polar form of the wake edges could quantify differences in wake shape between models.

7.2.3 Counter-rotating vortex pair

In addition to the bean shape, the tilted wakes also feature the counter-rotating vortex pair documented in other curled wake studies [35, 148, 149]. Figure 7.5 plots the crosswind and vertical components of the velocity deficit as arrows, on top of a color contour of the x-component of the velocity deficit to illustrate the wake location. As shown in Figure 7.5, cases with 30° tilt exhibit a pair of counter-rotating vortices in the wake, with a large downward velocity at the the center of the wake. The 15° tilt case also has a weaker counter-rotating vortex pair, although it is more asymmetrical.

Although other studies document these counter-rotating vortex pairs in curled wakes [35, 148, 149], the associated vorticity is often not quantified in a way that can be compared to results from other models or studies. To quantify the strength of these vortex pairs, the vorticity flux through a downwind rectangular surface is calculated

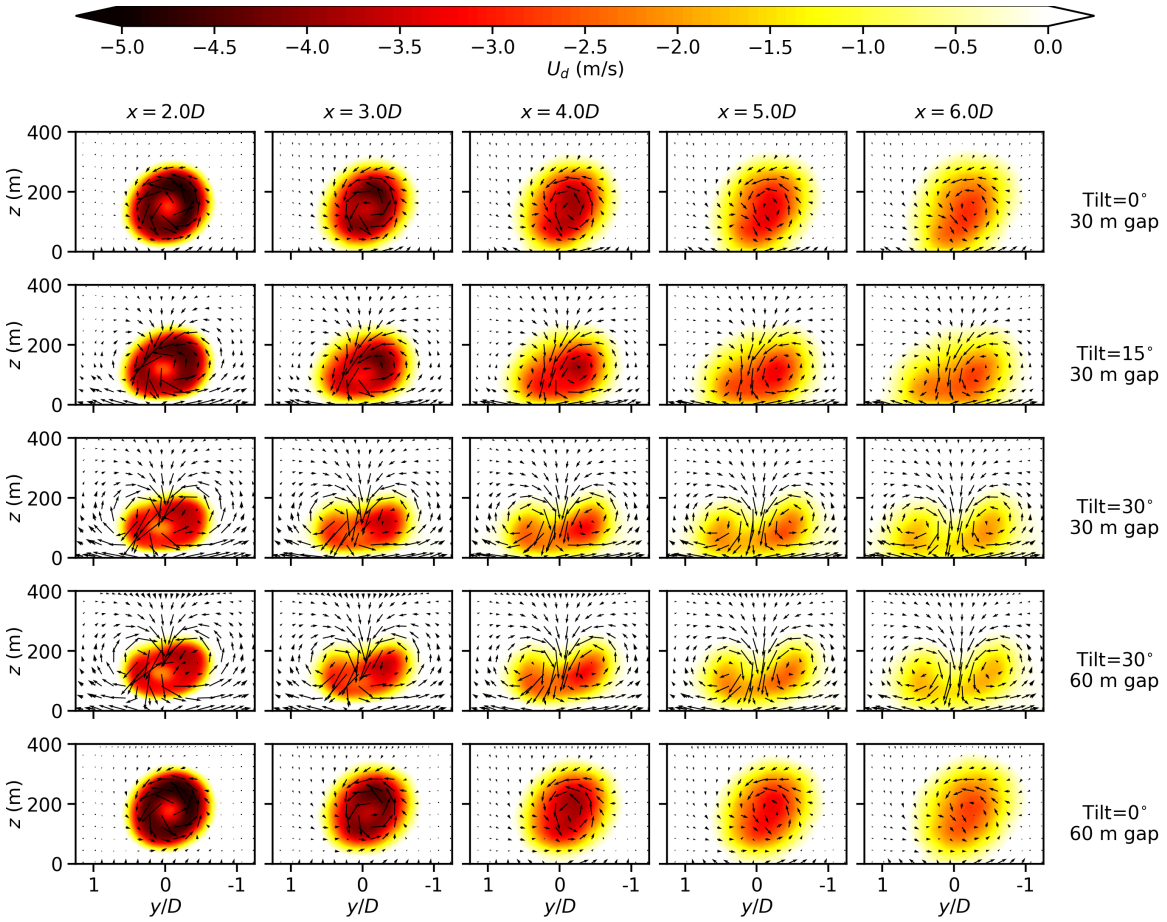

Figure 7.5. Contours of the x-component of the velocity deficit and arrows showing the y- and z-components, at different downwind cross-sections through the wake for each simulated case.

for each case, which is equivalent to the circulation Γ around the perimeter containing the wake:

$$\Gamma = \oint_L \vec{U}_d \cdot d\vec{\ell} = \oint_S (\nabla \times \vec{U}_d) \cdot d\vec{S}. \tag{7.1}$$

Because the rectangular loop encompasses both the positive and negative vortices, the total circulation is approximately zero, except for additional contribution from the rotating rotor. However, the positive and negative vorticity fluxes can be summed separately while calculating the numerical surface integral, which gives a circulation-like measure for the individual positive and negative vortices within the rectangular loop without identifying the edges of each vortex. Figure 7.6 plots these positive

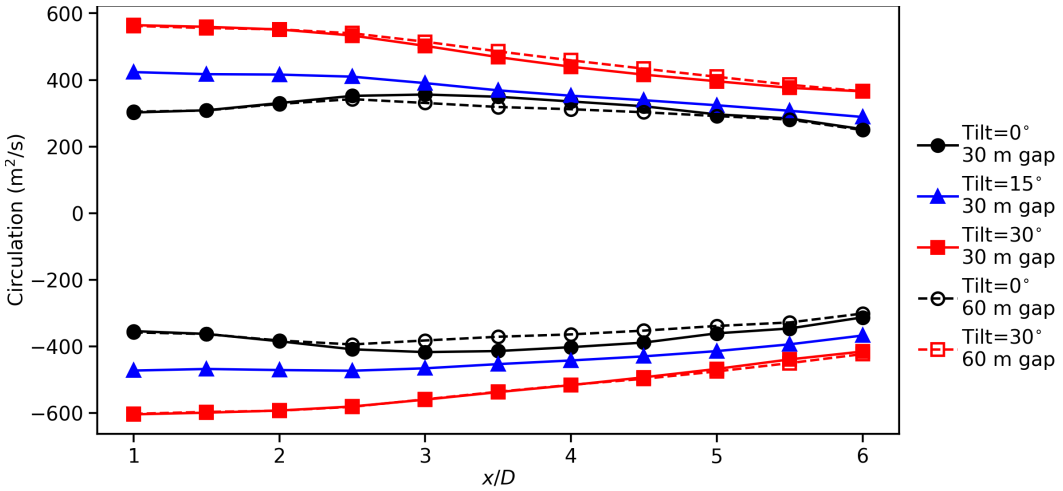

Figure 7.6. Circulation of the positive and negative vortices within the counter-rotating vortex pair, at different downwind cross-sections for each simulated case.

and negative vortex circulations at different downwind locations for the different cases. As shown in Figure 7.6, a larger tilt angle causes a larger strength of counter-rotating vortex pair, as measured by the circulations. However, this is a nonlinear relationship: the circulation difference between 0° and 15° tilt is much smaller than the circulation difference between 15° and 30° tilt. Also, the surface gap has little impact on the circulation, particularly farther downwind: surface effects do not appear to significantly affect vortex dissipation.

Although summing the positive and negative vortex circulations is a simple way to quantify the vortex strength, it does not distinguish between the counter-rotating vortex pair in curled wakes and blade root or blade tip vortices in non-tilted wakes. For example, Figure 7.6 documents significant positive and negative vortices in the 0° tilt cases, despite the lack of a counter-rotating vortex pair in these non-curled wakes (see Figure 7.5). In these cases, the positive circulation is from the blade tip vortex and the negative circulation is from the blade root vortex.

To better distinguish between the counter-rotating vortex pair in the curled wakes from the tip and root vortices in non-curled wakes, Figure 7.7 plots the total circulation (both positive and negative vorticity fluxes summed together) for the left and

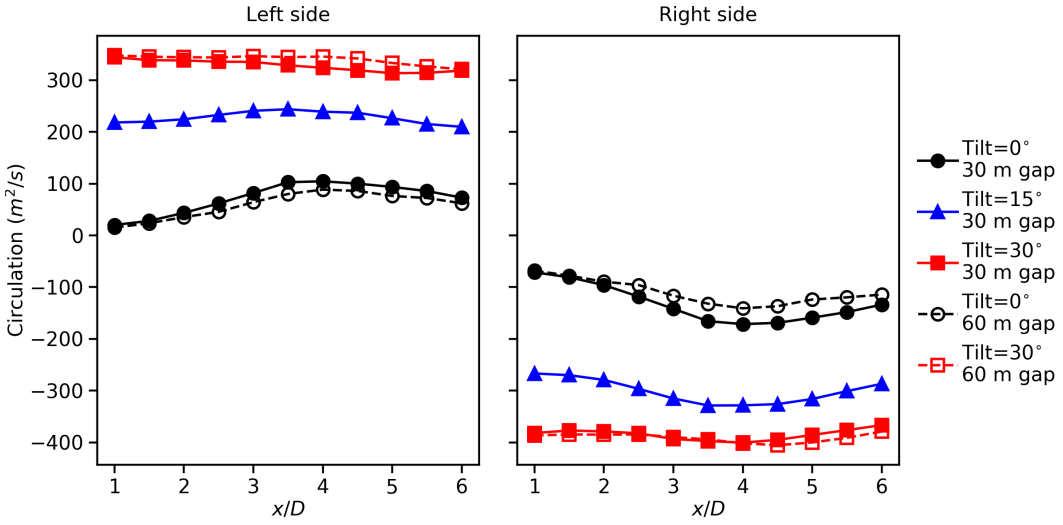

Figure 7.7. Total circulation (positive and negative) in the left and right halves of the wake, at different downwind cross-sections for each simulated case.

right halves of the rectangular loop. Although the wake is not perfectly centered between these two halves due to wind shear, this approach better captures the left-right asymmetry of the counter-rotating vortex pair, compared to the relative left-right symmetry of the tip and root vortices in the non-tilted wakes.

7.2.4 Wake deficit recovery

In addition to identifying the wake location, the velocity deficit U_d quantifies the wake recovery. For different downwind cross-sections, U_d is averaged over the wake area, as identified by the U_d cut-off at 10% U_∞ at hub height (see Figure 7.2). These wake deficit averages are then normalized by the average at x=0.5D downwind, to give the wake deficit recovery (i.e., recovery is 0 at x/D=0.5 and 1 whenever the wake recovers to the free-stream wind speed). Figure 7.8 plots this wake deficit recovery as a function of downwind location for all five simulated cases.

As shown in Figure 7.8, the wake deficit recovery is similar for all simulated cases, regardless of tilt angle. Significantly, the tilted cases do not consistently recover faster than the non-tilted cases. Wakes with larger surface gaps recover slightly faster than

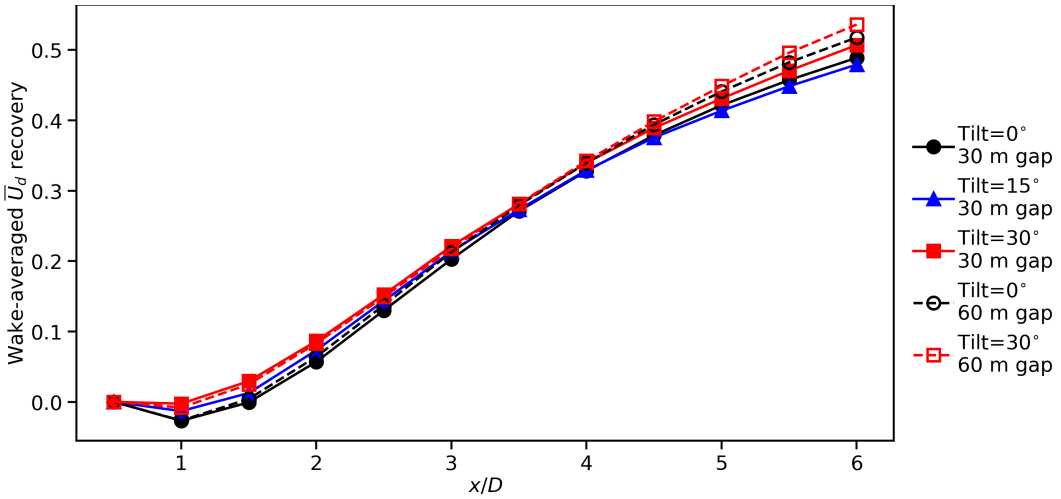

Figure 7.8. Recovery of the velocity deficit averaged over the wake area cross-section as a function of downwind location, starting from 0.5D downwind, for all simulated cases.

wakes nearer to the surface, but the surface gap does not affect the 30° wake recovery compared to the non-tilted wakes.

7.2.5 Effects on a downwind rotor

Although the literature clearly documents that tilting an upwind rotor causes a power increase to downwind rotors [11–13, 126, 150], this power gain is not caused by a faster recovery of the wake deficit (see Figure 7.8). Instead, downwind power gains appear to be caused by a combination of the reduced thrust at the upwind tilted rotor, the location of the downwind wake, and high-speed wind being pulled downward along with the wake.

To estimate how the simulated wakes would affect a downwind turbine's power generation, a circular area representing a second IEA 15 MW reference rotor is analyzed at different distances downwind, with the second rotor located directly behind the simulated upwind rotor. The downwind rotor's hub height also matches the upwind rotor for each case. First, the cube of the wind x-component is averaged over this downwind rotor area, in order to quantify the power available to the theoretical downwind turbine. Figure 7.9 plots this cubed wind speed, normalized by the power

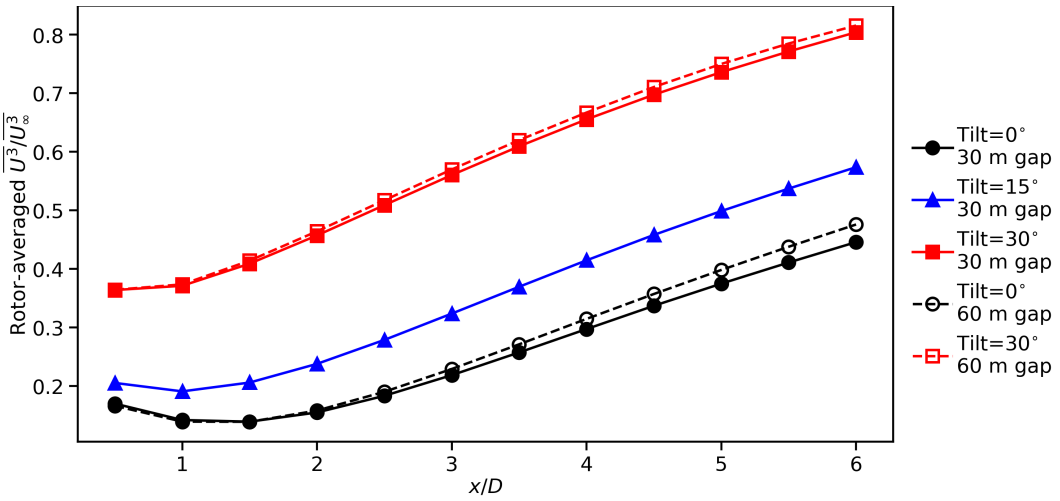

Figure 7.9. Wind power available to a second rotor at different downwind distances, normalized by the free-stream available power, for all simulated cases.

available in the free-stream wind over the same rotor area, for rotor areas at different distances downwind. The free-stream wind as a function of elevation is taken from the precursor simulation.

Comparing the cases in Figure 7.9, tilting the upwind rotor significantly increases the power available to a downwind rotor. However, a substantial portion of this downwind power gain is caused by the tilted upwind rotor extracting less power in the first place, due to the sub-optimal rotor angle. For example, at standard hub height, the rotors with 15° and 30° tilt extracted 6.6% and 24.7% less power than the non-tilted rotor, respectively.

Wake deflection also contributes to downwind power gains: a tilted upwind rotor steers the wake downward, so that the low-speed wake overlaps less with the downwind rotor area. This can be illustrated by examining the downwind power recovery from $0.5D$ downwind to $6D$ downwind: the available downwind power recovers by 37% and 44% of the free-stream power for 15° and 30° tilt, respectively, compared to the non-tilted wake only recovering 28% of the free-stream power. Larger surface gaps also allow for faster power recovery, though the effect is limited when combined with faster power recovery due to tilt: the non-tilted wake with the larger surface gap

recovers 31% of the free-stream power between $0.5D$ and $6D$, and the 30° tilted wake with the larger surface gap recovers 45% of the free-stream power. This faster power recovery due to wake location is the primary benefit of tilting rotors within a wind farm array.

Although tilted wakes provide more available power to downwind turbines, this comes at the cost of a larger effective wind shear across the downwind rotor, which can increase structural loads and fatigue [151]. To estimate the effective wind shear from tilted wakes, the x-component of the wind velocity is averaged at each elevation, across the local width of the downwind rotor disk. Figure 7.10 plots this effective wind shear across the downwind rotor's height, for all cases at different downwind locations. The top row compares the cases with the standard surface gap, while the bottom row shows cases with the larger surface gap. The free-stream wind shear profile is also included in Figure 7.10 for reference.

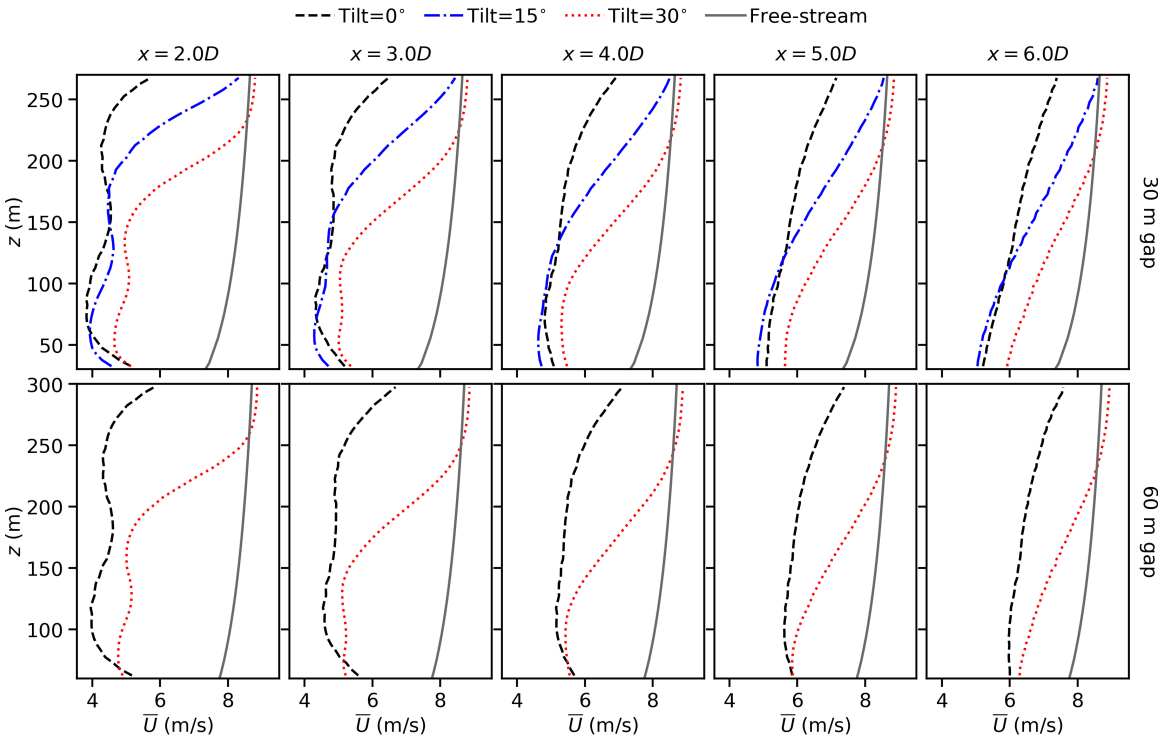

Figure 7.10. Effective wind shear profiles across a downwind rotor for tilted wakes with the standard surface gap (top) and a doubled surface gap (bottom). The free-stream wind profile is shown for comparison.

As illustrated in Figure 7.10, the effective wind shear experienced by a downwind rotor is larger for tilted wakes than for non-tilted wakes. For example, the wind speed varies by 2.17 m/s across a downwind rotor at standard hub height for a non-tilted upwind turbine, but the wind speed variations are 3.55 m/s and 2.95 m/s when the upwind rotor is tilted by 15° and 30°, respectively. The downwind effective wind shear is more severe for the 15° case than for the 30° case, because the lowest-speed regions within the 30° tilted wake are curled and steered to the sides of the downwind rotor area (see Figure 7.2). In contrast, the 15° wake is only steered downwards, to the bottom of the downwind rotor area.

Examining the effects of the surface gap size, a larger surface gap causes a smaller effective wind shear for both 0° and 30° tilt: 1.57 m/s and 2.64 m/s, respectively. However, the larger surface gap causes a slightly larger difference between the tilted and non-tilted wakes, because the tilted wake can curl away from the downwind rotor area even more with less interference from the surface.

7.2.6 Vertical momentum flux

To help illustrate where downwind rotors get the extra available energy in tilted wake cases, the vertical velocity and volume fluxes are calculated at different elevations above the wake, as stand-ins for the momentum and mass fluxes in an incompressible solver where density differences are neglected except for buoyancy terms. The velocity flux $\int_S \vec{U}\vec{U} \cdot d\vec{S}$ and volume flux $\int_S \vec{U} \cdot d\vec{S}$ are calculated through a $2D$-wide rectangular horizontal surface located from x=1D to 6D downwind, for elevations from z=400 m (just above the wake) to 850 m (above the capping inversion layer). Figure 7.11 plots these fluxes divided by the surface area for each simulated case, with positive values indicating downward flow.

Figure 7.11 indicates that tilted wakes do entrain more high-speed air from just above the wind farm than non-tilted wakes, as shown by the increased velocity and

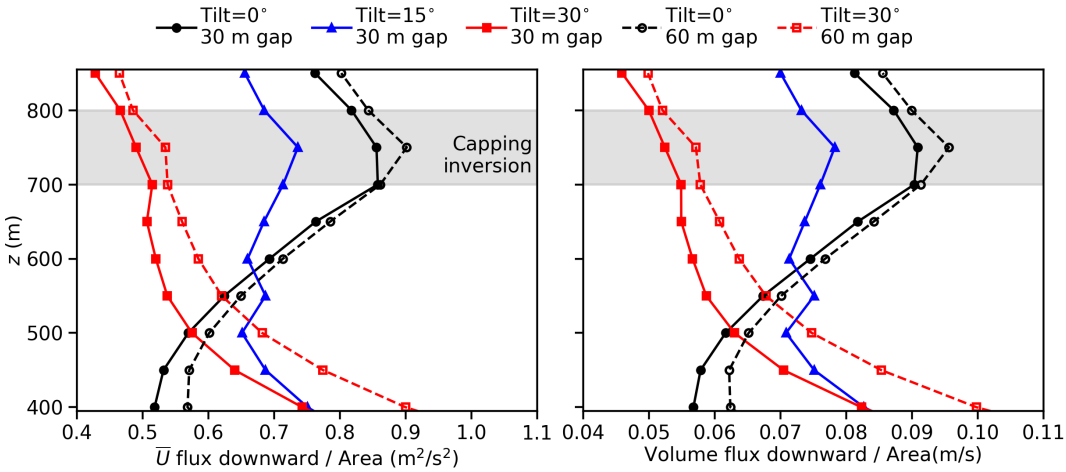

Figure 7.11. Velocity and volume fluxes through a rectangular surface above the wake at different elevations, divided by the surface area, for each simulated case. Positive values indicate downward flow.

downward volume fluxes from z=400 m to 500 m for the tilted cases. However, the tilt angle also affects the downward fluxes higher in the atmosphere, with the fluxes increasing with elevation in the non-tilted cases while the fluxes decrease with elevation in the tilted cases. These higher-elevation effects may be caused by different blockage effects due to the different rotor thrust coefficients, as well as interactions with the upper boundary condition and the capping inversion. Examining the effect of surface gap size, a larger surface gap causes larger fluxes at a given elevation, because that elevation is closer to the wake due to the increased hub height.

7.3 Summary and conclusions

In this chapter, LES of the IEA 15 MW reference turbine are performed using SOWFA with an ADM, for three different rotor tilt angles and two different surface gaps. The characteristics of the resulting curled wakes are compared and quantified, and the effects on a downwind rotor are estimated as well.

Key findings about tilted wake characteristics include:

- Larger rotor tilt angles steer wakes downward and cause shorter, wider wakes.

- Increasing rotor tilt causes a nonlinear increase in the strength of the counter-rotating vortex pair within the wake, as quantified by the vortex circulations.
- At a large tilt angle of 30°, the wake curls into classic "bean"-shaped cross-sections, which can be quantified using Legendre polynomials.

Further findings about the effect of tilted wakes on downwind rotors include:

- Increasing rotor tilt increases the power available to downwind rotors for two reasons: 1) the tilted upwind rotor extracts less power from the wind, and 2) tilting the upwind rotor allows faster power recovery because the tilted wake location and shape overlap less with the downwind rotor, allowing the downwind rotor to access high-speed air pulled down from just above the wind farm.
- Increasing rotor tilt does not cause faster recovery of the velocity deficit within the wake: downwind power recovery is caused only by wake location, and not by deficit recovery within the wake.
- Tilting the upwind rotor increases the effective wind shear across a downwind rotor, which may cause increases in loads and fatigue damage.

Finally, this research also shows that smaller surface gaps limit downward wake steering as the tilted wake collides with the surface, causing shorter, wider wakes, slower downwind power recovery, and a larger wind shear increase.

In summary, this research identifies key features of tilted wakes, including downward steering, shorter and wider wake cross-sections, stronger counter-rotating vortex pairs, and similar velocity deficit recovery within the wake. The estimated downwind power gain from tilting an upwind turbine is attributed to the wake steering away from the downwind rotor area and the reduced power extraction at the upwind rotor, but this power gain comes at the cost of increased wind shear downwind. The surface gap size is shown to influence the wake location, size, and shape, as well as the

downwind power recovery and effective wind shear. Several measures are proposed for quantitatively comparing curled wakes from different models, including circulation for the counter-rotating vortex pair as well as polar coordinate-based curve fitting for the wake shape. Future work could compare these simulated wakes to results from engineering models for curled wakes.

CHAPTER 8

CONCLUSIONS AND FUTURE WORK

This dissertation presents CFD investigations of three main topics in offshore wind energy: how breaking waves affect structural loads for fixed-bottom wind turbines; how platform motions affect power generation, wake characteristics, and downwind turbine behavior for floating wind turbines; and how rotor tilt angles affect wake characteristics when interacting with the ground or sea surface. The high-fidelity CFD simulations provide insight into physical phenomena that can be difficult to capture with current reduced-order engineering models, and expensive or inpractical to obtain from field measurements. One focus of this dissertation is quantifying context-specific metrics for flow fields and turbine behavior, so that these CFD results can help inform and validate future improvements to engineering models for wind turbine wakes, power prediction, and breaking waves. The contributions of this dissertation to the scholarly body of knowledge are summarized here, concluding with a short description of possible future directions of this research.

8.1 Contributions to knowledge

8.1.1 Breaking wave effects on OWTs

CFD simulations are performed of breaking waves with characteristics representative of potential East Coast offshore wind energy sites. The CFD model in CONVERGE is first verified and validated using both analytical solutions and experimental data for different cases. CFD simulations of shoaling and breaking waves are then used to evaluate the McCown, Miche, Battjes, and Goda breaking wave

limits. This study concludes that the Goda breaking limit is the most accurate option for seafloor slopes below 8%, which are common at fixed-bottom OWT sites on the East Coast, although the Miche and Battjes limits are acceptable conservative alternatives that perform reasonably for a wider range of seafloor slopes. Next, CFD simulations of shoaling waves breaking on monopiles for 5 and 10 MW OWTs were used to evaluate the Goda, Campbell-Weynberg, Cointe-Armand, and Wienke-Oumerachi wave slam force models. These simulations indicate that all four slam force models are conservative because they assume the "worst case" wave shape during impact, though the Goda slam model is least conservative and the Cointe-Armand and Wienke-Oumerachi models are the most.

This is the first time that breaking wave limits and slam models are evaluated for wave and site conditions specific to East Coast OWT sites. Furthermore, this research identifies that the accuracy of breaking limit models is highly impacted by how wave height and wavelength are measured in an asymmetric shoaling wave. These CFD simulations also suggest that slam force models do not account for variations in wave shape or impact timing, and also do not accurately capture the force time history after initial impact, although the VOF interface model may affect the CFD accuracy. These simulations indicate that these slam force models should only be used to generate conservative predictions of the peak breaking wave force.

8.1.2 Wake characteristics for floating turbines

Wake characteristics of floating turbines are compared to a fixed turbine wake, using LES coupled to an aeroelastic turbine model through an ALM, for different environmental conditions, rotor yaw angles, and floating platform types. This research concludes that floating OWT wakes generally have similar characteristics to wakes from fixed wind turbines, with a primary difference of floating wakes deflecting upwards by 5-10% due to mean platform pitch angles. Spar platforms produce larger

upward wake deflections than the semisubmersible because the spar has a larger pitch angle. Stable atmospheric conditions also produce larger vertical and horizontal wake deflections than neutral conditions, suggesting that the floating wake deflection interacts with wind shear and wind veer. In addition to the upwards wake deflection, floating turbines cause a 1-6% increase in peak TKE in the wake shear layer, though this effect is limited for higher wind speeds or lower wave heights. Fluctuations in the wake center location are not significantly increased by floating turbines, although horizontal fluctuations are higher in stable atmospheric conditions.

This is the first study to use LES coupled with realistic (i.e., non-prescribed) floating platform motions to study floating turbines' far wake characteristics for different combinations of atmospheric stabilities, platform types, wind speeds, wave heights, and wind-wave alignments. This research suggests that reduced-order wake models originally developed for fixed turbines can reasonably apply to most floating-turbine wakes, especially curled wake models that can capture upward wake deflection caused by platform pitch. However, additional adjustments may be necessary for vertical wake deflections interacting with wind shear and wind veer, especially in stable atmospheric conditions.

8.1.3 Power generation in floating turbines

Aeroelastic floating OWT simulations with turbulent inflow wind from LES are performed for spar and semisubmersible platforms, as well as a baseline fixed turbine, to identify how floating platform motions affect power generation in OWTs. This study concludes that overall power gains or losses in floating wind turbines are primarily caused by the balance between two competing effects: power decreases caused by a mean rotor tilt angle driven by platform pitch, and power increases caused by dynamic upwind-downwind rotor motions driven by platform surge and pitch motion. Floating platforms do not provide universally significant power gains

over fixed-bottom turbines; it depends on details in the platform dynamics. For example, the spar turbine generates 3.1-4.5% more power than the fixed turbine for this below-rated wind speed, because its lower center of mass creates larger, pitch-dominated rotor motions that outweigh its larger platform pitch angle. In contrast, the semisubmersible generates a negligible (0.1-0.2%) power gain, because its smaller rotor motions barely outweigh its smaller platform pitch angle.

Unlike most previous studies into floating OWT power generation, this research more realistically allows irregular waves and turbulent LES inflow to drive the platform motions, and also allows for non-zero time-averaged values for platform displacements. Furthermore, this set of simulations includes cases with different combinations of the six platform degrees of freedom enabled. These cases indicate that contrary to the common practice of isolating platform surge or pitch motions, surge and pitch must be enabled concurrently to accurately capture power generation in floating OWTs.

In addition, this work proposes a simple analytical model for power generation in floating OWTs in Equation 5.10, which explicitly addresses average platform pitch, rotor shaft tilt, and rotor motions upwind-downwind. This novel model reasonably predicts whether a floating platform causes a power gain or loss relative to the fixed turbine, though the magnitude of the predicted power gain or loss can be improved.

8.1.4 Floating-turbine wake effects on downwind turbines

Aeroelastic simulations of a downwind floating OWT are performed with LES wakes from an upwind OWT as the inflow flow field, for different upwind-downwind combinations of spar, semisubmersible, and fixed platforms. Configurations where the downwind turbine is fully waked and half waked are also compared. The main conclusion from these simulations is that the power, blade loads, and towertop displacements of the downwind turbine are affected much more by the downwind platform type, than

by any wake characteristics caused by a floating upwind turbine. Cases with a fixed downwind turbine had fairly similar average values, RMS values, and frequency content, regardless of upwind turbine type. Notably, differences between floating-floating configurations and the baseline fixed-fixed configuration were much larger (i.e. from doubled to an order of magnitude larger) than any differences between floating-fixed configurations and the baseline, especially for the spar.

This research is one of the few studies that addresses how floating wake characteristics affect downwind power generation, and not just downwind structural loads. Also, this study novelly compares multiple platform types for both fully waked and half-waked configurations, using high-fidelity LES for the upwind turbine's wake. Finally, this research is unusual in that it includes "mixed" configurations with floating upwind turbines and fixed downwind turbines, which is vital to isolating the floating wake's effects from any effects due to the downwind platform motion. In confirmation of the recommendation suggested by the floating wake characteristics study in Chapter 4, these simulations also indicate that when modeling floating wind farm arrays, it is likely acceptable to approximate the floating wake with fixed-bottom wake models that do not specifically address how a floating upwind turbine alters the wake.

8.1.5 Wake effects for tilted rotors

LES of tilted wind turbine rotors and their wakes is performed for three different tilt angles and two different gaps between the rotor bottom and the sea surface. These simulations agree with previous studies that increasing the tilt angle steers wakes downward, curls the wake into a shape with bean-like cross-sections, and creates a pair of counter-rotating vortices in the wake. This research further concludes that increasing the tilt angle causes shorter, wider wakes as well as a nonlinear increase in the strength of the counter-rotating vortex pair. These simulations also identify the physical phenomena behind the well-documented downwind power gains in tilted

turbine arrays: first, the titled upwind rotor simply extracts less power from the free-stream wind. More notably, the downward wake deflection and curled wake shape reduce the overlap of the wake with the downwind rotor area, allowing the downwind turbine to access high-speed air pulled down from just above the wind farm. Furthermore, rotor tilt does not cause a faster recovery of the velocity deficit within the wake, so wake recovery does not contribute to downwind power gains. These simulations also indicate that tilting the upwind rotor also increases the effective wind shear across a downwind turbine, which may increase loads and fatigue damage.

This research is the first to examine how surface gap size affects wake effects for tilted rotors, concluding that smaller surface gaps limit downward wake steering as the tilted wake collides with surface. This causes shorter, wider wakes, slower downwind power recovery, and a larger wind shear increase. Additionally, this research proposes metrics that can help quantitatively compare curled wake results from different models, including circulation of the counter-rotating vortex pair as well as polar coordinate-based curve fitting for the wake shape. Finally, this research is the first to simulate curled wakes for a larger 15 MW turbine, establishing that curled wake characteristics observed for smaller turbines are also present for larger rotors.

8.2 Future Work

Future work on the topics addressed in this dissertation should include validating these simulation results against full-scale field measurements for floating OWTs and turbines with tilted rotors, when this data is available. The simulations of wake effects and power generation for floating turbines and tilted rotors should also be repeated for additional environmental conditions, especially for above-rated wind speeds and lower wave heights. This would give a better insight into the typical wind turbine performance over longer time periods, rather than just examining the conditions where wakes and floating platform motions are expected to have the largest effects. In

addition, the effect of the tilted wake on a downwind turbine could be more precisely assessed through aeroelastic simulations of a downwind turbine, using the tilted wake LES as inflow. Finally, the tilted rotor study could be extended by using these LES wake results to evaluate and improve reduced-order curled wake models.

APPENDIX A

BREAKING WAVE LIMIT DATA

Wave parameters for breaking and non-breaking waves are listed in the following tables for the breaking wave simulations described in Section 3.3. The ratios of the simulated H/L to the predicted breaking H/L for the McCowan, Miche, Battjes, and Goda (both local L and deep water L_0) limits are presented in the last five columns. Boldface ratios indicate disagreement between the simulated wave and the breaking limit. Unless otherwise noted, the reported H and L are the average wave height H_{avg} and average wavelength L_{avg}.

Table A.1. Non-breaking wave cases' wave parameters and ratios of simulated to predicted H/L for different breaking limits.

s (%)	d (m)	H (m)	L (m)	d/L	H/L	McCowan	Miche	Battjes	Goda, L	Goda, L_0
0	10.0	4.8	111.0	0.090	0.043	0.61	0.59	0.64	0.73	–
0	25.0	10.7	227.4	0.110	0.047	0.55	0.55	0.60	0.69	–
0	30.0	17.5	253.4	0.118	0.069	0.75	0.77	0.83	0.95	–
0	5.0	2.8	40.6	0.123	0.069	0.72	0.75	0.80	0.92	–
0	50.0	28.8	391.2	0.128	0.074	0.74	0.78	0.83	0.96	–
0	45.0	21.4	281.7	0.160	0.076	0.61	0.70	0.74	0.85	–
0	40.0	21.9	249.0	0.161	0.088	0.70	0.81	0.85	0.97	–
0	20.0	10.7	120.0	0.167	0.089	0.68	0.80	0.85	0.96	–
0	35.0	18.8	202.4	0.173	0.093	0.69	0.82	0.87	0.98	–
2	54.9	34.4	409.0	0.134	0.084	0.80	0.86	0.92	1.00	0.95
2	13.0	5.8	83.0	0.157	0.069	0.57	0.65	0.68	0.74	0.70
2	36.6	13.4	203.8	0.180	0.066	0.47	0.57	0.60	0.65	0.61
3	15.7	7.2	123.7	0.127	0.058	0.59	0.62	0.66	0.69	0.64
3	69.6	40.5	515.2	0.135	0.079	0.75	0.80	0.85	0.90	0.86
3	7.1	3.2	39.3	0.180	0.081	0.58	0.70	0.74	0.77	0.73
5	27.0	16.0	130.6	0.207	0.123	0.76	1.00	**1.04**	**1.01**	0.92
8	22.3	17.3	142.1	0.157	0.122	1.00	**1.14**	**1.20**	**1.06**	0.93
8	12.3	8.4	61.2	0.202	0.137	0.87	**1.13**	**1.18**	**1.05**	0.92
12	17.8	12.7	94.3	0.189	0.135	0.92	**1.15**	**1.20**	0.98	0.80

Table A.2. Breaking wave cases' wave parameters and ratios of simulated to predicted H/L for different breaking limits.

s (%)	d (m)	H (m)	L (m)	d/L	H/L	McCowan	Miche	Battjes	Goda, L	Goda, L_0
5	21.4	25.1	329.8	0.065	0.076	1.50	1.38	1.51	1.38	1.30
5	32.1	31.5	407.5	0.079	0.077	1.26	1.19	1.29	1.21	1.14
6	12.2	17.4	206.4	0.059	0.084	1.83	1.67	1.82	1.58	1.48
6	11.6	11.3	139.4	0.083	0.081	1.25	1.19	1.29	1.16	1.08
6	18.7	18.3	208.7	0.089	0.088	1.26	1.21	1.31	1.19	1.09
6	21.7	19.7	207.9	0.104	0.095	1.16	1.16	1.25	1.15	1.07
6	2.9	2.6	25.1	0.114	0.105	1.17	1.20	1.28	1.19	1.08
8	21.7	21.8	243.4	0.089	0.090	1.29	1.24	1.35	1.12	1.02
8	42.8	45.6	451.1	0.095	0.101	1.36	1.33	1.44	1.21	1.08
8	21.6	18.0	174.8	0.124	0.103	1.07	1.12	1.20	1.04	**0.93**
9	32.9	32.1	337.4	0.098	0.095	1.25	1.23	1.32	1.07	**0.97**
9	21.6	18.8	164.6	0.131	0.114	1.12	1.19	1.27	1.07	**0.95**
9	2.4	1.8	17.2	0.140	0.104	**0.95**	1.04	1.10	**0.94**	**0.81**
9	2.3	1.8	16.0	0.143	0.110	**0.99**	1.09	1.16	**0.98**	**0.83**
9	2.9	1.8	18.0	0.159	0.102	**0.82**	**0.94**	1.00	**0.86**	**0.74**
9	15.5	10.3	84.5	0.183	0.121	**0.85**	1.04	1.09	**0.95**	**0.85**
11	12.0	12.9	148.7	0.081	0.086	1.37	1.30	1.41	1.03	**0.91**
11	33.2	31.1	286.1	0.116	0.109	1.20	1.23	1.32	1.02	**0.91**
11	36.7	32.3	287.4	0.128	0.112	1.13	1.19	1.27	1.00	**0.88**
11	39.6	36.3	238.5	0.166	0.152	1.17	1.38	1.45	1.19	**0.94**
12	3.8	4.2	40.8	0.093	0.104	1.44	1.40	1.51	1.09	**0.95**
12	18.0	20.4	191.0	0.094	0.107	1.45	1.42	1.53	1.11	**0.96**
12	20.9	23.9	200.2	0.104	0.120	1.47	1.46	1.58	1.16	1.00
12	27.9	30.9	247.2	0.113	0.125	1.42	1.45	1.55	1.16	1.00
12	13.7	12.5	90.0	0.152	0.138	1.17	1.31	1.39	1.10	**0.94**

APPENDIX B

FLOATING-TURBINE DISPLACEMENT DATA

The following tables give average, root-mean-square, minimum, and maximum values for rotor center displacements and platform displacements from the simulations described in Chapter 5, with different platform degrees of freedom enabled. The time-averaged power for simulations with both dynamic and average displacements and with average displacements only is also presented. Tables B.1 and B.2 show rotor and platform displacement data for the spar platform, while Tables B.3 and B.4 show rotor and platform displacement data for the semisubmersible platform.

Table B.1. Spar data for time-averaged power for cases with the total floating displacements and average displacements only, as well as average, root-mean-square, minimum, and maximum values for rotor displacements. Columns are organized by which platform degree of freedom (DOF) is enabled for that case.

Active DOF:		All DOF, coupled inflow	All DOF	Surge & pitch	Surge	Sway	Heave	Roll	Pitch	Yaw
Power (MW)*	Total disp.	1.712	1.678	1.679	1.611	1.606	1.606	1.606	1.599	1.606
	Avg. disp.	–	1.582	1.583	1.606	1.606	1.606	1.606	1.583	1.606
x_{RC} (m)	Avg.	12.129	12.080	12.062	5.092	–	–	–	1.717	–
	RMS	2.707	2.736	2.713	0.755	–	–	–	0.412	–
	Min.	3.010	2.853	2.911	2.335	–	–	–	0.355	–
	Max.	21.006	21.217	21.063	7.740	–	–	–	3.387	–
y_{RC} (m)	Avg.	-0.309	-0.263	–	–	-0.009	–	-0.109	–	–
	RMS	0.078	0.091	–	–	0.045	–	0.069	–	–
	Min.	-0.531	-0.547	–	–	-0.130	–	-0.280	–	–
	Max.	-0.080	-0.011	–	–	0.118	–	0.051	–	–
z_{RC} (m)	Avg.	-0.277	-0.273	-0.096	–	–	-0.072	–	-0.017	–
	RMS	0.292	0.288	0.053	–	–	0.307	–	0.008	–
	Min.	-1.201	-1.184	-0.329	–	–	-1.065	–	-0.064	–
	Max.	0.714	0.709	–	–	–	0.916	–	-0.001	–
ϕ_{RC} = Pitch (°)	Avg.	2.555	2.538	2.537	–	–	–	–	1.093	–
	RMS	0.743	0.750	0.743	–	–	–	–	0.262	–
	Min.	0.199	0.148	0.150	–	–	–	–	0.226	–
	Max.	4.962	4.961	4.904	–	–	–	–	2.157	–
θ_{RC} = Yaw (°)	Avg.	0.014	0.013	–	–	–	–	–	–	-0.006
	RMS	0.183	0.174	–	–	–	–	–	–	0.121
	Min.	-0.642	-0.594	–	–	–	–	–	–	-0.394
	Max.	0.646	0.599	–	–	–	–	–	–	0.326

*The average power for an equivalent fixed-bottom turbine is 1.661 MW for coupled inflow cases and 1.605 MW for prerecorded inflow cases.

Table B.2. Spar data for the average, root-mean-square, minimum, and maximum values for platform displacements (yaw and pitch values are reported in Table B.1). Columns are organized by which platform degree of freedom (DOF) is enabled for that case.

Active DOF:		All DOF, coupled inflow	All DOF	Surge & pitch	Surge	Sway	Heave	Roll	Pitch	Yaw
Roll (°)	Avg.	0.106	0.094	–	–	–	–	0.069	–	–
	RMS	0.025	0.029	–	–	–	–	0.044	–	–
	Min.	0.035	0.008	–	–	–	–	-0.032	–	–
	Max.	0.183	0.186	–	–	–	–	0.178	–	–
Surge (m)	Avg.	8.117	8.096	8.078	5.092	–	–	–	–	–
	RMS	1.559	1.583	1.571	0.755	–	–	–	–	–
	Min.	2.639	2.513	2.539	2.335	–	–	–	–	–
	Max.	13.400	13.570	13.490	7.740	–	–	–	–	–
Sway (m)	Avg.	-0.143	-0.115	–	–	-0.009	–	–	–	–
	RMS	0.046	0.054	–	–	0.045	–	–	–	–
	Min.	-0.275	-0.266	–	–	-0.130	–	–	–	–
	Max.	-0.018	0.040	–	–	0.118	–	–	–	–
Heave (m)	Avg.	-0.180	-0.177	–	–	–	-0.072	–	–	–
	RMS	0.290	0.287	–	–	–	0.307	–	–	–
	Min.	-1.105	-1.094	–	–	–	-1.065	–	–	–
	Max.	0.796	0.793	–	–	–	0.916	–	–	–

Table B.3. Semisubmersible data for time-averaged power for cases with the total floating displacements and average displacements only, as well as average, root-mean-square, minimum, and maximum values for rotor displacements. Columns are organized by which platform degree of freedom (DOF) is enabled for that case.

	Active DOF:	All DOF, coupled inflow	All DOF	Surge & pitch	Surge	Sway	Heave	Roll	Pitch	Yaw
Power (MW)*	Total disp.	1.664	1.608	1.604	1.630	1.606	1.607	1.606	1.694	1.606
	Avg. disp.	–	1.591	1.591	1.606	1.606	1.606	1.606	1.591	1.606
x_{RC} (m)	Avg.	8.417	8.359	8.327	5.571	–	–	–	2.729	–
	RMS	1.218	1.214	1.148	1.459	–	–	–	2.583	–
	Min.	3.092	3.102	4.147	1.259	–	–	–	-5.270	–
	Max.	12.859	12.821	12.887	10.340	–	–	–	12.147	–
y_{RC} (m)	Avg.	-0.205	-0.171	–	–	-0.010	–	-0.167	–	–
	RMS	0.062	0.072	–	–	0.038	–	0.024	–	–
	Min.	-0.373	-0.373	–	–	-0.110	–	-0.259	–	–
	Max.	-0.051	0.027	–	–	0.104	–	-0.077	–	–
z_{RC} (m)	Avg.	-0.027	-0.026	-0.051	–	–	0.033	–	-0.079	–
	RMS	0.853	0.853	0.041	–	–	0.847	–	0.098	–
	Min.	-3.206	-3.205	-0.354	–	–	-3.014	–	-0.824	–
	Max.	3.027	3.027	–	–	–	3.028	–	–	–
ϕ_{RC} = Pitch (°)	Avg.	1.773	1.746	1.754	–	–	–	–	1.738	–
	RMS	0.761	0.759	0.780	–	–	–	–	1.646	–
	Min.	-0.570	-0.580	-1.106	–	–	–	–	-3.357	–
	Max.	4.911	4.840	5.083	–	–	–	–	7.757	–
θ_{RC} = Yaw (°)	Avg.	0.009	0.011	–	–	–	–	–	–	-0.006
	RMS	0.155	0.185	–	–	–	–	–	–	0.182
	Min.	-0.453	-0.526	–	–	–	–	–	–	-0.554
	Max.	0.607	0.713	–	–	–	–	–	–	0.668

*The average power for an equivalent fixed-bottom turbine is 1.661 MW for coupled inflow cases and 1.605 MW for prerecorded inflow cases.

Table B.4. Semisubmersible data for the average, root-mean-square, minimum, and maximum values for platform displacements (yaw and pitch values are reported in Table B.3). Columns are organized by which platform degree of freedom (DOF) is enabled for that case.

Active DOF:		All DOF, coupled inflow	All DOF	Surge & pitch	Surge	Sway	Heave	Roll	Pitch	Yaw
Roll (°)	Avg.	0.113	0.105	–	–	–	–	0.106	–	–
	RMS	0.023	0.026	–	–	–	–	0.015	–	–
	Min.	0.024	0.011	–	–	–	–	0.049	–	–
	Max.	0.187	0.183	–	–	–	–	0.165	–	–
Surge (m)	Avg.	5.633	5.616	5.572	5.571	–	–	–	–	–
	RMS	1.364	1.363	1.373	1.459	–	–	–	–	–
	Min.	1.375	1.359	1.374	1.259	–	–	–	–	–
	Max.	10.180	10.200	10.110	10.340	–	–	–	–	–
Sway (m)	Avg.	-0.027	-0.006	–	–	-0.010	–	–	–	–
	RMS	0.047	0.056	–	–	0.038	–	–	–	–
	Min.	-0.129	-0.136	–	–	-0.110	–	–	–	–
	Max.	0.096	0.148	–	–	0.104	–	–	–	–
Heave (m)	Avg.	0.024	0.024	–	–	–	0.033	–	–	–
	RMS	0.849	0.849	–	–	–	0.847	–	–	–
	Min.	-3.147	-3.147	–	–	–	-3.014	–	–	–
	Max.	3.084	3.084	–	–	–	3.028	–	–	–

BIBLIOGRAPHY

[1] Fried L, Qiao L, Sawyer S, eds. *Global Wind Report: Annual Market Update 2017*. Brussels, Belgium: Global Wind Energy Council; 2018.

[2] Lee J, Zhao F. *Global Wind Report 2021*. Brussels, Belgium: Global Wind Energy Council; 2021.

[3] Manwell J, McGowan J, Rogers A. *Wind Energy Explained: Theory, Design and Application*. 2nd ed. Chichester, West Sussex: John Wiley and Sons; 2009.

[4] Hallowell S, Myers AT, Arwade SR. Variability of breaking wave characteristics and impact loads on offshore wind turbines supported by monopiles. *Wind Energy* 2015; 19: 301–312. doi: 10.1002/we.1833

[5] Veers P, Dykes K, Lantz E, *et al*. Grand challenges in the science of wind energy. *Science* 2019; 366(6464): eaau2027. doi: 10.1126/science.aau2027

[6] Thiagarajan KP, Dagher HJ. A review of floating platform concepts for offshore wind energy generation. *Journal of Offshore Mechanics and Arctic Engineering* 2014; 136(2): 021906. doi: 10.1115/1.4026607

[7] Liu Y, Xiao Q, Incecik A, Peyrard C, Wan D. Establishing a fully coupled CFD analysis tool for floating offshore wind turbines. *Renewable Energy* 2017; 112: 280–301. doi: 10.1016/j.renene.2017.04.052

[8] Tran TT, Kim DH. A CFD study of coupled aerodynamic-hydrodynamic loads on a semisubmersible floating offshore wind turbine. *Wind Energy* 2017; 21: 70–85. doi: 10.1002/we.2145

[9] Archer C, Vasel-Be-Hagh A, Yan C, Wu S, Pan Y, Brodie J, Maguire A. Review and evaluation of wake loss models for wind energy applications. *Applied Energy* 2018; 226: 1187–1207. doi: 10.1016/j.apenergy.2018.05.085

[10] Stevens R, Meneveau C. Flow structure and turbulence in wind farms. *Annual Review of Fluid Mechanics* 2017; 49: 311–339. doi: 10.1146/annurev-fluid-010816-060206

[11] Annoni J, Scholbrock A, Churchfield M, Fleming P. Evaluating tilt for wind plants. *Proceedings of the 2017 American Control Conference*. IEEE; 24-26 May 2017; Seattle, Washington: 717–722. doi: 10.23919/ACC.2017.7963037

[12] Fleming P, Gebraad P, Lee S, *et al.* Evaluating techniques for redirecting turbine wakes using SOWFA. *Renewable Energy* 2014; 70: 211–218. doi: 10.1016/j.renene.2014.02.015

[13] Fleming P, Gebraad PM, Lee S, *et al.* Simulation comparison of wake mitigation control strategies for a two-turbine case. *Wind Energy* 2015; 18: 2135–2143. doi: 10.1002/we.1810

[14] Lee S, Churchfield M, Driscoll F, *et al.* Load estimation of offshore wind turbines. *Energies* 2018; 11: 1895. doi: 10.3390/en11071895

[15] Sebastian T, Lackner M. Analysis of the induction and wake evolution of an offshore floating wind turbine. *Energies* 2012; 5: 968–1000. doi: 10.3390/en5040968

[16] Johlas HM, Hallowell S, Xie S, Lomonaco P, Lackner MA, Arwade SA, Myers AT, Schmidt DP. Modeling breaking waves for fixed-bottom support structures for offshore wind turbines. *Proceedings of ASME 2018 1st International Offshore Wind Technical Conference*. ASME; 4-7 November 2018; San Francisco, California: IOWTC2018-1095. doi: 10.1115/IOWTC2018-1095

[17] Johlas HM, Martínez-Tossas LA, Schmidt DP, Lackner MA, Churchfield MJ. Large eddy simulations of floating offshore wind turbine wakes with coupled platform motion. *Journal of Physics: Conference Series* 2019; 1256: 012018. doi: 10.1088/1742-6596/1256/1/012018

[18] Johlas HM, Martínez-Tossas LA, Lackner MA, Schmidt DP, Churchfield MJ. Large eddy simulations of offshore wind turbine wakes for two floating platform types. *Journal of Physics: Conference Series* 2020; 1452: 012034. doi: 10.1088/1742-6596/1452/1/012034

[19] Johlas HM, Martínez-Tossas LA, Churchfield MJ, Lackner MA, Schmidt DP. Floating platform effects on power generation in spar and semisubmersible wind turbines. *Wind Energy* 2021: 1–16. doi: 10.1002/we.2608

[20] Johlas HM, Schmidt DP, Lackner MA. Large eddy simulations of curled wakes from tilted wind turbines. *Renewable Energy* 2021. Under review.

[21] Betz A. *Windenergie und Ihre Ausnutzung durch Windmüllen*. Göttingen, Germany: Vandenhoeck and Ruprecht; 1926.

[22] Glauert H. Airplane propellers. In: Durand WF, ed. *Aerodynamic Theory*. Berlin, Germany: Springer; 1935: 169–360. doi: 10.1007/978-3-642-91487-4_3

[23] Sørensen J. Aerodynamic aspects of wind energy conversion. *Annual Review of Fluid Mechanics* 2011; 43: 427–448. doi: 10.1146/annurev-fluid-122109-160801

[24] Vermeer LJ, Sørensen JN, Crespo A. Wind turbine wake aerodynamics. *Progress in Aerospace Sciences* 2003; 39: 467–510. doi: 10.1016/S0376-0421(03)00078-2

[25] Crespo A, Hernández J, Frandsen S. Survey of modelling methods for wind turbine wakes and wind farms. *Wind Energy* 1999; 2: 1–24.

[26] Katic I, Højstrup J, Jensen NO. A simple model for cluster efficiency. *Proceedings of European Wind Energy Association Conference and Exhibition*. EWEA; 7-9 October 1986; Rome, Italy: 407–410.

[27] Larsen G.*A Simple Wake Calculation Procedure*. Roskilde, Denmark: Risø National Laboratory; 1988. Tech. report Risø-M-2760.

[28] Frandsen S, Barthelmie R, Pryor S, Rathmann O, Larsen S. Deficit in large offshore wind farms. *Wind Energy* 2006; 9: 39–53. doi: 10.1002/we

[29] Bastankhah M, Porté-Agel F. A new analytical model for wind-turbine wakes. *Renewable Energy* 2014; 70: 116–123. doi: 10.1016/j.renene.2014.01.002

[30] Xie S, Archer C. Self-similarity and turbulence characteristics of wind turbine wakes via large-eddy simulation. *Wind Energy* 2015; 18: 1815–1838. doi: 10.1002/we.1792

[31] Ghaisas NS, Archer CL. Geometry-based models for studying the effects of wind farm layout. *Journal of Atmospheric and Oceanic Technology* 2016; 33: 481–501. doi: 10.1175/JTECH-D-14-00199.1

[32] Sanderse B, Pijl S, Koren B. Review of computational fluid dynamics for wind turbine wake aerodynamics. *Wind Energy* 2011; 14: 799–819. doi: 10.1002/we.458

[33] Ainslie J. Calculating the flow field in the wake of wind turbines. *Journal of Wind Engineering and Industrial Aerodynamics* 1988; 27: 213–224. doi: 10.1016/0167-6105(88)90037-2

[34] Mehta D, Zuijlen vAH, Koren B, Holierhoek JG, Bijl H. Large eddy simulation of wind farm aerodynamics: A review. *Journal of Wind Engineering and Industrial Aerodynamics* 2014; 133: 1–17. doi: 10.1016/j.jweia.2014.07.002

[35] Martínez-Tossas LA, Annoni J, Fleming PA, Churchfield MJ. The aerodynamics of the curled wake: A simplified model in view of flow control. *Wind Energy Science* 2019; 4(1): 127–138. doi: 10.5194/wes-4-127-2019

[36] Martínez-Tossas LA, King J, Quon E, Bay CJ, Mudafort R, Hamilton N, Howland MF, Fleming PA. The curled wake model: A three-dimensional and extremely fast steady-state wake solver for wind plant flows. *Wind Energy Science* 2021; 6(2): 555–570. doi: 10.5194/wes-6-555-2021

[37] Calaf M, Meneveau C, Meyers J. Large eddy simulation study of fully developed wind-turbine array boundary layers. *Physics of Fluids* 2010; 22: 015110. doi: 10.1063/1.862466

[38] Larsen T, Madsen H, Larsen G, Hansen K. Validation of the dynamic wake meander model for loads and power production in the Egmond aan Zee wind farm. *Wind Energy* 2013; 16: 605–624. doi: 10.1002/we.1563

[39] Walker K, Adams N, Gribben B, *et al.* An evaluation of the predictive accuracy of wake effects models for offshore wind farms. *Wind Energy* 2016; 19: 979–996. doi: 10.1002/we.1871

[40] Barthelmie RJ, Pryor SC, Frandsen ST, *et al.* Quantifying the impact of wind turbine wakes on power output at offshore wind farms. *Journal of Atmospheric and Oceanic Technology* 2010; 27: 1302–1317. doi: 10.1175/2010JTECHA1398.1

[41] Barthelmie R, Hansen K, Frandsen S, *et al.* Modelling and measuring flow and wind turbine wakes in large wind farms offshore. *Wind Energy* 2009; 12: 431–444. doi: 10.1002/we.348

[42] Moriarty P, Rodrigo JS, Gancarski P, *et al.* IEA-task 31 WAKEBENCH: Towards a protocol for wind farm flow model evaluation, part 2: Wind farm wake models. *Journal of Physics: Conference Series* 2014; 524: 012185. doi: 10.1088/1742-6596/524/1/012185

[43] Chella M.*Breaking Wave Characteristics and Breaking Wave Forces on Slender Cylinders*. [dissertation]. Trondheim, Norway: Norwegian University of Science and Technology (NTNU); 2016.

[44] Jensen M.*Breaking of Waves Over a Steep Bottom Slope*. Aalborg, Denmark: Hydraulics and Coastal Engineering Laboratory, Aalborg University; 2004. Series paper no. 22.

[45] Rattanapitikon W, Shibayama T. Verification and modification of breaker height formulas. *Coastal Engineering Journal* 2000; 42(4): 389–406. doi: 10.1016/S0578-5634(00)00019-5

[46] Tu Y, Cheng Z, Muskulus M. A review of slamming load application to offshore wind turbines from an integrated perspective. *Energy Procedia* 2017; 137: 346–357. doi: 10.1016/j.egypro.2017.10.359

[47] Wienke J, Oumeraci H. Breaking wave impact force on a vertical and inclined slender pile – theoretical and large-scale model investigations. *Coastal Engineering* 2005; 52(5): 435–462. doi: 10.1016/j.coastaleng.2004.12.008

[48] Goda Y, Haranaka S, Kitahata M. Study on impulsive breaking wave forces on piles. *Reports of the Port and Harbour Technical Research Institute* 1966; 6(5): 1–30.

[49] Porté-Agel F, Lu H, Wu Y. A large-eddy simulation framework for wind energy applications. *Proceedings of the Fifth International Symposium on Computational Wind Engineering*. IAWE; 23-27 May 2010; Chapel Hill, North Carolina.

[50] Cabezón D, Migoya E, Crespo A. Comparison of turbulence models for the computational fluid dynamics simulation of wind turbine wakes in the atmospheric boundary layer. *Wind Energy* 2011; 14: 909–921. doi: 10.1002/we.516

[51] Farrugia R, Sant T, Micallef D. A study on the aerodynamics of a floating wind turbine rotor. *Renewable Energy* 2016; 86: 770–784. doi: 10.1016/j.renene.2015.08.063

[52] Rodriguez S, Jaworski J. Toward identifying aeroelastic mechanisms in near-wake instabilities of floating offshore wind turbines. *Journal of Energy Resources Technology* 2017; 139(5): 051203. doi: 10.1115/1.4035753

[53] Manolas DI, Papadakis GP, Chasapogiannis PI, Riziotis VA. Assessment of wake effects on floating wind turbines. *Proceedings of the 26th International Ocean and Polar Engineering Conference*. ISOPE; 26 June - 2 July 2016; Rhodes, Greece: ISOPE-I-16-635.

[54] Jeon M, Lee S, Lee S. Unsteady aerodynamics of offshore floating wind turbines in platform pitching motion using vortex lattice method. *Renewable Energy* 2014; 65: 207–212. doi: 10.1016/j.renene.2013.09.009

[55] Churchfield MJ, Lee S, Michalakes J, Moriarty PJ. A numerical study of the effects of atmospheric and wake turbulence on wind turbine dynamics. *Journal of Turbulence* 2012; 13: N14. doi: 10.1080/14685248.2012.668191

[56] Motta M, Barthelmie RJ, Vølund P. The influence of non-logarithmic wind speed profiles on potential power output at Danish offshore sites. *Wind Energy* 2005; 8: 219–236. doi: 10.1002/we.146

[57] Sathe A, Bierbooms W. Influence of different wind profiles due to varying atmospheric stability on the fatigue life of wind turbines. *Journal of Physics: Conference Series* 2007; 75: 012056. doi: 10.1088/1742-6596/75/1/012056

[58] Sathe A, Mann J, Barlas T, Bierbooms W, Bussel vG. Influence of atmospheric stability on wind turbine loads. *Wind Energy* 2013; 16: 1013–1032. doi: 10.1002/we.1528

[59] Drennan W, Taylor PK, Yelland MJ. Parameterizing the sea surface roughness. *Journal of Physical Oceanography* 2005; 35: 835–848. doi: 10.1175/JPO2704.1

[60] Lange B, Larsen S, Højstrup J, Barthelmie R. Importance of thermal effects and sea surface roughness for offshore wind resource assessment. *Journal of Wind Engineering and Industrial Aerodynamics* 2004; 92: 959–988. doi: 10.1016/J.JWEIA.2004.05.005

[61] Lee S, Churchfield MJ, Moriarty PJ, Jonkman J, Michalakes J. A numerical study of atmospheric and wake turbulence impacts on wind turbine fatigue loadings. *Journal of Solar Energy Engineering* 2013; 135(3): 031001. doi: 10.1115/1.4023319

[62] Creech A, Früh WG, Maguire AE. Simulations of an offshore wind farm using large-eddy simulation and a torque-controlled actuator disc model. *Surveys in Geophysics* 2015; 36: 427–481. doi: 10.1007/s10712-015-9313-7

[63] Tran T, Kim D. Fully coupled aero-hydrodynamic analysis of a semi-submersible FOWT using a dynamic fluid body interaction approach. *Renewable Energy* 2016; 92: 244–261. doi: 10.1016/j.renene.2016.02.021

[64] Lyu P, Park SG, Shen L, Li H. A Coupled Wind-Wave-Turbine Solver for Offshore Wind Farm. *Proceedings of the ASME 1st International Offshore Wind Technical Conference 2018*. ASME; 4-7 November 2018; San Francisco, CA: IOWTC2018-1046. doi: 10.1115/IOWTC2018-1046

[65] Quallen S, Xing T. CFD simulation of a floating offshore wind turbine system using a variable-speed generator-torque controller. *Renewable Energy* 2016; 97: 230–242. doi: 10.1016/j.renene.2016.05.061

[66] Wu Y, Porté-Agel F. Large-eddy simulation of wind-turbine wakes: Evaluation of turbine parametrisations. *Boundary-Layer Meteorology* 2011; 138: 345–366. doi: 10.1007/s10546-010-9569-x

[67] Wu Y, Porté-Agel F. Modeling turbine wakes and power losses within a wind farm using LES: An application to the Horns Rev offshore wind farm. *Renewable Energy* 2015; 75: 945–955. doi: 10.1016/J.RENENE.2014.06.019

[68] Sørensen J, Shen W. Numerical modeling of wind turbine wakes. *Journal of Fluids Engineering* 2002; 124: 393–399. doi: 10.1115/1.1471361

[69] Stevens R, Martínez-Tossas L, Meneveau C. Comparison of wind farm large eddy simulations using actuator disk and actuator line models with wind tunnel experiments. *Renewable Energy* 2018; 116: 470–478. doi: 10.1016/j.renene.2017.08.072

[70] Martínez-Tossas LA, Churchfield M, Meneveau C. Optimal smoothing length scale for actuator line models of wind turbine blades based on Gaussian body force distribution. *Wind Energy* 2017; 20: 1083–1096. doi: 10.1002/we.2081

[71] Churchfield M, Lee S, Schmitz S, Wang Z. Modeling wind turbine tower and nacelle effects within an actuator line model. *Proceedings of the 33rd Wind Energy Symposium, AIAA SciTech*. AIAA; 5-9 January 2015; Kissimmee, Florida: AIAA2015-0214. doi: 10.2514/6.2015-0214

[72] Santoni C, Carrasquillo K, Arenas-Navarro I, Leonardi S. Effect of tower and nacelle on the flow past a wind turbine. *Wind Energy* 2017; 20: 1927–1939. doi: 10.1002/we.2130

[73] Ren N, Li Y, Ou J. Coupled wind-wave time domain analysis of floating offshore wind turbine based on computational fluid dynamics method. *Journal of Renewable and Sustainable Energy* 2014; 6: 023106. doi: 10.1063/1.4870988

[74] Jonkman J, Hayman G. HydroDyn. National Renewable Energy Laboratory; 2020. https://www.nrel.gov/wind/nwtc/hydrodyn.html. Accessed 11 June 2021.

[75] Cormier M, Caboni M, Lutz T, Boorsma K, Krämer E. Numerical analysis of unsteady aerodynamics of floating offshore wind turbines. *Journal of Physics: Conference Series* 2018; 1037: 072048. doi: 10.1088/1742-6596/1037/7/072048

[76] Lin L, Wang K, Vassalos D. Detecting wake performance of floating offshore wind turbine. *Ocean Engineering* 2018; 156: 263–276. doi: 10.1016/J.OCEANENG.2018.03.028

[77] Burmester S, de Ridder EJ, Wehmeyer C, Asp E, Gujer P. Comparing different approaches for calculating wave impacts on a monopile turbine foundation. *Proceedings of the ASME 2017 36th International Conference on Ocean, Offshore and Arctic Engineering*. ASME; 25-30 June 2017; Trondheim, Norway: OMAE2017-61182. doi: 10.1115/OMAE2017-61182

[78] Hallowell S. Large scale modeling of breaking waves. *International Offshore Wind Partnering Forum*. Business Network for Offshore Wind; 3-6 April 2017; Princeton, New Jersey.

[79] de Ridder EJ, Bunnik T, Peeringa JM, Paulsen BT, Weyhmeyer C, Gujer P, Asp E. Summary of the joint industry project wave impact on fixed foundations (WIFI JIP). *Proceedings of the ASME 2017 36th International Conference on Ocean, Offshore and Arctic Engineering*. ASME; 25-30 June 2017; Trondheim, Norway: OMAE2017-62040. doi: 10.1115/OMAE2017-62040

[80] Bredmose H, Mariegaard J, Paulsen BT, Jensen B, Schløer S, Larsen TJ, Kim T, Hansen AM. *The Wave Loads Project*. Roskilde, Denmark: Technical University of Denmark; 2013. Tech. report E-0045.

[81] Stansby PK, Devaney LC, Stallard TJ. Breaking wave loads on monopiles for offshore wind turbines and estimation of extreme overturning moment. *IET Renewable Power Generation* 2013; 7(5): 514–520. doi: 10.1049/iet-rpg.2012.0205

[82] Marino E, Borri C, Peil U. A fully nonlinear wave model to account for breaking wave impact loads on offshore wind turbines. *Journal of Wind Engineering and Industrial Aerodynamics* 2011; 99(4): 483–490. doi: 10.1016/j.jweia.2010.12.015

[83] Luck M, Benoit M. Wave loading on monopile foundation for offshore wind turbines in shallow-water areas. *Coastal Engineering 2004, Proceedings of the 29th International Conference*. ASME; 19-24 September 2004; Lisbon, Portugal: 3992-4004. doi: 10.1142/9789812701916_0322

[84] Irschik K. *Loading of Slender Cylindrical Piles Due to Non-Breaking and Breaking Waves*. [dissertation]. Braunschweig, Germany: Technical University of Braunschweig (TU Braunschweig); 2012.

[85] Richards KJ, Senecal PK, Pomraning E.*CONVERGE v2.4 Manual*. Madison, Wisconsin: Convergent Science; 2018.

[86] Fenton JD. The numerical solution of steady water wave problems. *Computers and Geosciences* 1990; 14(3): 357–368. doi: 10.1016/0098-3004(88)90066-0

[87] Whitman GB.*Linear and Nonlinear Waves*. New York: John Wiley and Sons; 1974.

[88] Fenton JD. A fifth-order Stokes theory for steady waves. *Journal of Waterway, Port, Coastal, and Ocean Engineering* 1985; 111(2): 216–234. doi: 10.1061/(ASCE)0733-950X(1985)111:2(216)

[89] Fenton JD. Nonlinear wave theories. In: Méhauté BL, Hanes DM, eds. *The Sea: Ocean Engineering Science, Part A*. New York, New York: Wiley; 1990: 3–25.

[90] Yeoh GH, Barber T. Assessment of interface capturing methods in computational fluid dynamics (CFD) codes – A case study. *Journal of Computational Multiphase Flows* 2009; 1(2): 201–215. doi: 10.1260/175748209789563946

[91] Niedzwecki JM, Duggal AS. Wave runup and force on cylinders in regular and random waves. *Journal of Waterway, Port, Coastal, and Ocean Engineering* 1992; 118(6): 615–634. doi: 10.1061/(ASCE)0733-950X(1992)118:6(615)

[92] Velarde J.*Design of Monopile Foundations to Support the DTU 10 MW Wind Turbine*. [master's thesis]. Trondheim, Norway: Delft University of Technology (TU Delft) and Norwegian University of Science and Technology (NTNU); 2016.

[93] de Vries W.*Support Structure Concepts for Deep Water Sites*. Delft, Netherlands: Project UpWind; 2011. Deliverable D4.2.8 (WP 4.2 final report).

[94] Sarpkaya T.*Wave Forces on Offshore Structures*. Cambridge: Cambridge University Press; 2010.

[95] Wang J, Wang C, Castañeda OD, Campagnolo F, Bottasso CL. Large-eddy simulation of scaled floating wind turbines in a boundary layer wind tunnel. *Journal of Physics: Conference Series* 2018; 1037: 072032. doi: 10.1088/1742-6596/1037/7/072032

[96] Liu Y, Xiao Q, Incecik A, Peyrard C. Aeroelastic analysis of a floating offshore wind turbine in platform-induced surge motion using a fully coupled CFD-MBD method. *Wind Energy* 2019; 22: 1–20. doi: 10.1002/we.2265

[97] Rockel S, Peinke J, Hölling M, Cal R. Dynamic wake development of a floating wind turbine in free pitch motion subjected to turbulent inflow generated with an active grid. *Renewable Energy* 2017; 112: 1–16. doi: 10.1016/J.RENENE.2017.05.016

[98] Robertson AN, Jonkman JM. Loads analysis of several offshore floating wind turbine concepts. *Proceedings of the 21st International Offshore and Polar Engineering Conference*. ISOPE; 19-24 June 2011; Maui, Hawaii: ISOPE-I-11-204.

[99] Sebastian T, Lackner M. Characterization of the unsteady aerodynamics of offshore floating wind turbines. *Wind Energy* 2013; 16: 339–352. doi: 10.1002/we.545

[100] Bachynski EE, Kvittem MI, Luan C, Moan T. Wind-wave misalignment effects on floating wind turbines: Motions and tower load effects. *Journal of Offshore Mechanics and Arctic Engineering* 2014; 136: 041902. doi: 10.1115/1.4028028

[101] Xie S, Archer CL. A numerical study of wind-turbine wakes for three atmospheric stability conditions. *Boundary Layer Meteorology* 2017; 165: 87–112. doi: 10.1007/s10546-017-0259-9

[102] Abkar M, Porté-Agel F. Influence of atmospheric stability on wind-turbine wakes: A large-eddy simulation study. *Physics of Fluids* 2015; 27: 035104. doi: 10.1063/1.4913695

[103] Wu YT, Porté-Agel F. Atmospheric turbulence effects on wind-turbine wakes: An LES study. *Energies* 2012; 5(12): 5340–5362. doi: 10.3390/en5125340

[104] Churchfield M, Lee S. SOWFA: Simulator fOr Wind Farm Applications. National Renewable Energy Laboratory; 2020. https://www.nrel.gov/wind/nwtc/sowfa.html. Accessed 11 June 2021.

[105] OpenFOAM: The Open Source CFD Toolbox. OpenCFD Ltd; 2021. https://www.openfoam.com. Accessed 11 June 2021.

[106] Jonkman J. FAST. National Renewable Energy Laboratory; 2020. https://www.nrel.gov/wind/nwtc/fast.html. Accessed 11 June 2021.

[107] Doubrawa P, Martínez-Tossas LA, Quon E, Moriarty P, Churchfield MJ. Comparison of mean and dynamic wake characteristics between research-scale and full-scale wind turbines. *Journal of Physics: Conference Series* 2018; 1037: 072053. doi: 10.1088/1742-6596/1037/7/072053

[108] Martínez-Tossas L, Churchfield M, Yilmaz A, Sarlak H, Johnson PL, Sørensen J, Meyers J, Meneveau C. Comparison of four large-eddy simulation research codes and effects of model coefficient and inflow turbulence in actuator-line-based wind turbine modeling. *Journal of Renewable and Sustainable Energy* 2018; 10(3): 033301. doi: 10.1063/1.5004710

[109] Mirocha JD, Churchfield MJ, Muñoz-Esparza D, *et al.* Large-eddy simulation sensitivities to variations of configuration and forcing parameters in canonical boundary-layer flows for wind energy applications. *Wind Energy Science* 2018; 3: 589–613. doi: 10.5194/wes-2017-33

[110] Churchfield MJ, Lee S, Moriarty PJ, Hao Y, Lackner MA, Barthelmie R, Lundquist JK, Oxley G. A comparison of the dynamic wake meandering model, large-eddy simulation, and field data at the Egmond aan Zee offshore wind plant. *Proceedings of the 33rd Wind Energy Symposium, AIAA SciTech*. AIAA; 5-9 January 2015; Kissimmee, Florida: AIAA2015-0724. doi: 10.2514/6.2015-0724

[111] Issa R. Solution of the implicitly discretised fluid flow equations by operator-splitting. *Journal of Computational Physics* 1986; 62(1): 40–65. doi: 10.1016/0021-9991(86)90099-9

[112] Rhie CM, Chow WL. Numerical study of the turbulent flow past an airfoil with trailing edge separation. *AIAA Journal* 1983; 21(11): 1525–32. doi: 10.2514/3.8284

[113] Moeng CH. A large-eddy-simulation model for the study of planetary boundary-layer turbulence. *Journal of the Atmospheric Sciences* 1984; 41(13): 2052–2062.

[114] Schumann U. Subgrid-scale model for finite-difference simulations of turbulent flow in plane channels and annuli. *Journal of Computational Physics* 1975; 18(4): 376–404. doi: 10.1016/0021-9991(75)90093-5

[115] Monin AS, Obukhov AM. Basic laws of turbulent mixing in the atmospheric surface layer. *Transactions of the Geophysics Institute of the Academy of Sciences of the USSR* 1954; 24: 163–187.

[116] Troldborg N.*Actuator Line Modeling of Wind Turbine Wakes*. [dissertation]. Lyngby, Denmark: Technical University of Denmark (DTU); 2009.

[117] Jonkman JM, Buhl ML.*FAST User's Guide*. Golden, Colorado: National Renewable Energy Laboratory; 2005. Tech. report NREL/TP-500-38230. doi: 10.2172/15020796

[118] OpenFAST Documentation. National Renewable Energy Laboratory; 2021. https://openfast.readthedocs.io/. Accessed 11 June 2021.

[119] Jonkman J, Butterfield S, Musial W, Scott G.*Definition of a 5-MW Reference Wind Turbine for Offshore System Development*. Golden, Colorado: National Renewable Energy Laboratory; 2009. Tech. report NREL/TP-500-38060. doi: 10.2172/947422

[120] Robertson A, Jonkman J, Masciola M, Song H, Goupee A, Coulling A, Luan C.*Definition of the Semisubmersible Floating System for Phase II of OC4*. Golden, Colorado: National Renewable Energy Laboratory; 2014. Tech. report NREL/TP-5000-60601. doi: 10.2172/1155123

[121] Jonkman J.*Definition of the Floating System for Phase IV of OC3*. Golden, Colorado: National Renewable Energy Laboratory; 2010. Tech. report NREL/TP-500-47535. doi: 10.2172/979456

[122] *IEC 61400-3 Wind Turbines – Part 3: Design Requirements for Offshore Wind Turbines*. International Electrotechnical Commission; 2009.

[123] Türk M, Emeis S. The dependence of offshore turbulence intensity on wind speed. *Journal of Wind Engineering and Industrial Aerodynamics* 2010; 98: 466–471. doi: 10.1016/j.jweia.2010.02.005

[124] Beare RJ, Macvean MK, Holtslag AAM, *et al*. An intercomparison of large-eddy simulations of the stable boundary layer. *Boundary Layer Meteorology* 2006; 118: 247–272. doi: 10.1007/s10546-004-2820-6

[125] Martínez-Tossas LA, Churchfield MJ, Leonardi S. Large eddy simulations of the flow past wind turbines: actuator line and disk modeling. *Wind Energy* 2015; 18: 1047–60. doi: 10.1002/we.1747

[126] Weipao M, Chun L, Jun Y, Yang Y, Xiaoyun X. Numerical investigation of wake control strategies for maximizing the power generation of wind farm. *Journal of Solar Energy Engineering* 2016; 138: 034501. doi: 10.1115/1.4033110

[127] Eliot Q. SAMWICH Box: Simulated And Measured Wake Identification and CHaracterization Toolbox. GitHub; 2019. https://github.com/ewquon/waketracking. Accessed 11 June 2021.

[128] Huang Y, Wan D. Investigation of interference effects between wind turbine and spar-type floating platform under combined wind-wave excitation. *Sustainability* 2020; 12: 246. doi: 10.3390/SU12010246

[129] Karimian Aliabadi S, Rasekh S. Effect of platform disturbance on the performance of offshore wind turbine under pitch control. *Wind Energy* 2020: 1210–1230. doi: 10.1002/we.2482

[130] Sant T, Bonnici D, Farrugia R, Micallef D. Measurements and modelling of the power performance of a model floating wind turbine under controlled conditions. *Wind Energy* 2015; 18: 811–834. doi: 10.1002/we.1730

[131] Shen X, Hu P, Chen J, Zhu X, Du Z. The unsteady aerodynamics of floating wind turbine under platform pitch motion. *Proceedings of the Institution of Mechanical Engineers, Part A: Journal of Power and Energy* 2018; 232(8): 1019–1036. doi: 10.1177/0957650918766606

[132] Wen B, Tian X, Dong X, Peng Z, Zhang W. Influences of surge motion on the power and thrust characteristics of an offshore floating wind turbine. *Energy* 2017; 141: 2054–2068. doi: 10.1016/j.energy.2017.11.090

[133] Wen B, Dong X, Tian X, Peng Z, Zhang W, Wei K. The power performance of an offshore floating wind turbine in platform pitching motion. *Energy* 2018; 154: 508–521. doi: 10.1016/j.energy.2018.04.140

[134] Wen B, Tian X, Dong X, Peng Z, Zhang W. On the power coefficient overshoot of an offshore floating wind turbine in surge oscillations. *Wind Energy* 2018; 21: 1076–1091. doi: 10.1002/we.2215

[135] Micallef D, Sant T. A review of wind turbine yaw aerodynamics. In: Aissaoui AG, Tahour A, eds. *Wind Turbines - Design, Control and Applications*. Intech; 2016: 27–53. doi: 10.5772/63445

[136] Wen B, Tian X, Zhang Q, Dong X, Peng Z, Zhang W, Wei K. Wind shear effect induced by the platform pitch motion of a spar-type floating wind turbine. *Renewable Energy* 2019; 135: 1186–1199. doi: 10.1016/j.renene.2018.12.034

[137] Roddier D, Cermelli C, Weinstein J, Byklum E, Atcheson M, Utsunomiya T, Jorde J, Borgen E. State-of-the-art. In: Cruz J, Atcheson M, eds. *Floating Offshore Wind Energy*. Springer; 2016: 271–331. doi: 10.1007/978-3-319-29398-1_6

[138] Fleming P, Annoni J, Shah JJ, *et al*. Field test of wake steering at an offshore wind farm. *Wind Energy Science* 2017; 2: 229–239. doi: 10.5194/wes-2-229-2017

[139] Schepers JG.*Engineering Models in Wind Energy Aerodynamics: Development, Implementation and Analysis Using Dedicated Aerodynamic Measurements*. [dissertation]. Delft, Netherlands: Delft University of Technology (TU Delft); 2012. doi: 10.4233/uuid:92123c07-cc12-4945-973f-103bd744ec87

[140] Wise AS, Bachynski EE. Wake meandering effects on floating wind turbines. *Wind Energy* 2020: 1266–1285. doi: 10.1002/we.2485

[141] Gebraad PMO, Teeuwisse FW, Wingerden vJW, Fleming PA, Ruben SD, Marden JR, Pao LY. Wind plant power optimization through yaw control using a parametric model for wake effects – a CFD simulation study. *Wind Energy* 2016; 19: 95–114. doi: 10.1002/we.1822

[142] Howland MF, Lele SK, Dabiri JO. Wind farm power optimization through wake steering. *Proceedings of the National Academy of Sciences of the United States of America* 2019; 116(29): 14495–14500. doi: 10.1073/pnas.1903680116

[143] Howland MF, González CM, Martínez JJP, Quesada JB, Larrañaga FP, Yadav NK, Chawla JS, Dabiri JO. Influence of atmospheric conditions on the power production of utility-scale wind turbines in yaw misalignment. *Journal of Renewable and Sustainable Energy* 2020; 12: 063307. doi: 10.1063/5.0023746

[144] Adaramola MS, Krogstad PÅ. Experimental investigation of wake effects on wind turbine performance. *Renewable Energy* 2011; 36(8): 2078–2086. doi: 10.1016/j.renene.2011.01.024

[145] Vollmer L, Steinfeld G, Heinemann D, Kühn M. Estimating the wake deflection downstream of a wind turbine in different atmospheric stabilities: an LES study. *Wind Energy Science* 2016; 1: 129–141. doi: 10.5194/wes-1-129-2016

[146] Fleming P, Annoni J, Martínez-Tossas LA, Raach S, Gruchalla K, Scholbrock A, Churchfield M, Roadman J. Investigation into the shape of a wake of a yawed full-scale turbine. *Journal of Physics: Conference Series* 2018; 1037: 032010. doi: 10.1088/1742-6596/1037/3/032010

[147] Jiménez Á, Crespo A, Migoya E. Application of a LES technique to characterize the wake deflection of a wind turbine in yaw. *Wind Energy* 2009; 13: 559–572. doi: 10.1002/we.380

[148] Bastankhah M, Porté-Agel F. Experimental and theoretical study of wind turbine wakes in yawed conditions. *Journal of Fluid Mechanics* 2016; 806: 506–541. doi: 10.1017/jfm.2016.595

[149] Howland MF, Bossuyt J, Martínez-Tossas LA, Meyers J, Meneveau C. Wake structure in actuator disk models of wind turbines in yaw under uniform inflow conditions. *Journal of Renewable and Sustainable Energy* 2016; 8: 043301. doi: 10.1063/1.4955091

[150] Storm RM. *Wake Control Using Rotor Tilting*. [master's thesis]. Delft, Netherlands: Delft University of Technology (TU Delft); 2018.

[151] Barthelmie RJ, Shepherd TJ, Aird JA, Pryor SC. Power and wind shear implications of large wind turbine scenarios in the US central plains. *Energies* 2020; 13(6): 4269. doi: 10.3390/en13164269

[152] Gaertner E, Rinker J, Sethuraman L, *et al.Definition of the IEA 15-Megawatt Offshore Reference Wind Turbine*. Golden, Colorado: National Renewable Energy Laboratory; 2020. Tech. report NREL/TP–5000–75698. doi: 10.2172/1603478

[153] Bradshaw RC, Schmidt DP, Rogers JR, Kelton KF, Hyers RW. Machine vision for high-precision volume measurement applied to levitated containerless material processing. *Review of Scientific Instruments* 2005; 76(12): 125108. doi: 10.1063/1.2140490